Master-Thesis

Christian Löffler Matr.-Nr.1106492

Comparison of mechanical concepts for Nb_3Sn high field accelerator magnets

Hamburger Fern Hochschule, CERN TE-MSC-LMF

Supervisor at the University
Prof. Dr.-Ing Peter Schmolz

Supervisor at CERN
M. Eng. Frederic Savary

working period of the thesis:
01-10-16 to 31-03-17

Acknowledgements

I would like to thank my two advisers, Peter Schmolz and Frederic Savary, for giving me the opportunity to write this thesis. For helping me find the topic for this thesis, I would like to thank Luca Bottura, Gijs De Rijk, and Davide Tommasini.

On the technical side, I would like to thank Paolo Ferracin for his input about the design of the MQXF magnet. I am thankful to Bernhard Auchmann and Charilaos Kokkinos (Harris) for their marvellous previous finite element work with the DS11T. Their work was my foundation for learning the ways of finite element modelling, which started almost three years ago. Special thanks go to Mikko Karppinen, not only for designing the DS11T magnet, but also for the fruitful discussion we had, even though agreement was not always achieved. I also thank Gerard Willering, not only for his more than useful technical input but also for being around always. A big thank you goes to David Smekens for his positive view of things in general, for the coffee, and for being all in all a great guy.

For taking the pictures with the electron microscope, I owe a big thank you to Ana Teresa Perez Fontenla. Finite element analysis is nothing without proper material data. Michael Daly with the manufacturing, planning, designing of the 10-Stack samples; and Oscar Sacristan De Frutos and Michael Guinchard with the material testing made great efforts in providing the dearly needed mechanical data for the coil composite. Even though it was a bit late for this thesis, a big thank you to all of you. Glyn Kirby, thank you for your work to determine the thermal behaviour of the materials.

A special thank you goes to my girlfriend, parents, and friends for putting up with me during the time while I was working on this thesis!

Contents

Nomenclature **I**

List of Tables **II**

List of Pictures **III**

List of Equations **VIII**

1 Introduction **1**
1.1 Methodology . . . 1
1.2 The HL-LHC Project . . . 1
1.3 Magnets . . . 2
1.4 Superconductivity . . . 3

2 Nb_3Sn Accelerator Magnets **7**
2.1 Conductor . . . 7
2.1.1 Wire . . . 7
2.1.2 Cable . . . 9
2.1.3 Cable Insulation . . . 11
2.2 Mechanical Design of Superconducting Magnets . . . 12
2.3 Coils . . . 15
2.4 Magnets . . . 17
2.4.1 DS11T . . . 17
2.4.2 MQXF . . . 19
2.4.3 SMC-11T . . . 20
2.5 Failure Modes of Nb_3Sn-magnets . . . 21
2.5.1 Heat-Related Quench . . . 21
2.5.2 Strain-Related Quench . . . 21
2.5.3 Short circuit . . . 22

3 Material Characteristics **23**
3.1 Material Properties . . . 23
3.1.1 Wire . . . 23
3.1.2 Insulation . . . 24
3.1.3 Metals . . . 25
3.2 Theoretical Stiffness of the Coils . . . 28
3.3 Conductor-Insulation Composite . . . 30
3.3.1 Material Tests on Composite Cable Stacks . . . 30
3.3.2 Theoretical Stiffness of the 10-Stack . . . 32
3.4 Finite Element Analysis of the 10-Stack . . . 33
3.4.1 Hardening Behaviour of the Coil Composite . . . 33
3.4.2 10-Stack FE models . . . 33
3.5 Strain Dependency of Nb3Sn . . . 35

4 Excitation of the Coils **41**
4.1 Electromagnetic Forces . . . 42
4.2 Induced Cable Stress by EM-forces . . . 44

5 Comparison of the Mechanical Structures **49**
5.1 DS11T . . . 50
5.1.1 Load Steps (LS) . . . 51
5.1.2 Nominal Case . . . 53
5.1.3 Collaring Process (LS 1&2) . . . 54
5.1.4 Welding of the Shell (LS 3) . . . 56
5.1.5 Cool Down to 1.9K (LS 4) . . . 57
5.1.6 Powering 12.8kA (LS 5) . . . 58
5.2 MQXF . . . 60
5.2.1 Load Steps (LS) . . . 61
5.2.2 Nominal Case . . . 62
5.2.3 Pressurisation of the Bladders (LS 1) . . . 63
5.2.4 De-pressurisation Bladders and placing of the Keys (LS 2) . . . 64
5.2.5 Welding of the Shell (LS 3) . . . 65
5.2.6 Cool Down to 1.9K (LS 4) . . . 65
5.2.7 Powering 19.1kA (LS 5) . . . 66
5.3 SMC-11T . . . 68
5.3.1 Load Steps (LS) . . . 69
5.3.2 Nominal Case . . . 70
5.3.3 Pressurisation of the Bladders (LS 1&2) . . . 71
5.3.4 De-pressurisation Bladders and placing of the Keys (LS 3) . . . 72
5.3.5 Cool Down to 1.9K (LS 4) . . . 73
5.3.6 Powering 15.1kA (LS 5) . . . 74

6 Comparison of the Coil-Stress and Strain **77**
6.1 Influence of the Structure on the Coil Stress . . . 77
6.2 Cable Stresses during Assembly and Operation . . . 78
6.3 Plasticity in the Cable . . . 79
6.4 Possible Reduction of the Critical Current . . . 80

7 Conclusion **83**

Bibliography **85**

Appendices **I**

A Table Appendix **III**
A.1 FEA of the structures . . . IV
A.1.1 Contacts . . . IV

B Graph Appendix **IX**
B.1 FEA of the strand . . . IX
B.2 FEA of the coils . . . IX

C Figure Appendix **XI**
C.1 FEA of 10-Stacks . . . XI
C.2 FEA of the strand . . . XV
C.3 Electro Magnetic Force plots . . . XV
C.4 FEA of the coils . . . XX
C.5 FEA of the structures . . . XXII
C.5.1 DS11T . . . XXII
C.5.2 MQXF . . . XXVII
C.5.3 SMC-11T . . . XXX
C.5.4 convergence plots . . . XXXII
C.6 Geometrical Dimensions . . . XXXVI

Nomenclature

μ	Friction Coefficient
B_{c1}	Lower Critical Magnetic Field
B_{c2}	Upper Critical Magnetic Field
$B_{c2}(\varepsilon, T=0)$	Superconducting Upper Critical Field, depending on Strain and Temperature
B_c	Critical Magnetic Field
B_{op}	Operational Magnetic Field
E_a	Moduli of Elasticity
E_e	Elastic Modulus
E_t	Tangential Modulus
EQV	von Mises stress
J_c	Critical Current Density
J_{op}	Operational Current Density
T_c	Critical Temperature
T_{op}	Operational Temperature
IL	inner layer of the coil
OL	outer layer of the coil

List of Tables

2.1 Comparison of conductors 8
2.2 Overview of cable geometry parameters 10
2.3 Overview of coil geometry parameters 16
2.4 Overview of magnet parameters 17

3.1 Material data of the Nb_3Sn composite wire 24
3.2 Material data of the **Insulation** 25
3.3 Material data of **G10** 25
3.4 Material data of **Kapton®** 25
3.5 Material data of the **austenitic steel** 26
3.6 Material data of the **aluminium** 26
3.7 Material data of the **Magnetil** 26
3.8 Material data of the **titanium alloy Ti-6Al-4V** 27
3.9 Material data of the **ODS copper** *Glidcop* 27
3.10 Material data of the **copper stabilizer** 27
3.11 Elastic modulus and volume fractions of the coils—calculated modulus 29
3.12 Elastic modulus and volume fractions of the coils—calculated modulus without the interstitial epoxy 30
3.13 10-stack measurements from literature 30
3.14 10-stack measurements on the DS11T cable, carried out in September 2015 31
3.15 10-stack measurements on the DS11T cable, carried out in January 2017 32
3.16 Elastic modulus and volume fractions of the 10-stack—calculated modulus 32
3.17 Response from the 10-stack simulations modulus 34
3.18 Response from the 10-stack simulations stress and average stress on the cable, with the minimum and maximum values 36
3.19 Material data for the FEA of the 108/127 RRP strand 37

4.1 Current and peak magnetic fields for a load line of 90% at 1.9K 41
4.2 Electromagnetic Forces of the Cross-section Summary in N/mm 42
4.3 Stresses in the coil, only under the EM Force 46

5.1 FE-Models Overview 49
5.2 Load Steps used in the FE-Simulation 50

A.1 Tensile tests at different temperatures, samples from longitudinal and transversal rolling directions[37] III
A.2 Electro magnetic forces summary in N/mm III
A.3 Contacts for the DS11T model, first table IV
A.4 Contacts for the DS11T model, second table V
A.5 Contacts for the MQXF, first table VI
A.6 Contacts for the MQXF, second table VII
A.7 Contacts for the SMC-11T VIII

List of Figures

1.1 Pure dipole configurations: two infinite slabs (left), intersecting ellipses (center), and cylinder with cos-θ azimuthal current density distribution (right)[2] . . . 2
1.2 Pure quadropole configurations: four infinite slabs (left) and two intersecting ellipses (center) with constant current density, and cylinder with cos-2θ azimuthal current density distribution (right)[2] 2
1.3 Schematics of the Shubnikov phase. The magnetic field and the supercurrents are shown only for two flux lines. [3] . . . 3
1.4 Schematic overview of the superconducting states in type-2 superconductors . . . 4
1.5 Shubnikov phase in the presence of a transport-current density j. The flus lines experience a force F driving them along the y-direction. The magnetic-field distribution around the flux lines is indicated by the hatching. [3] . . . 4
1.6 Schematic of the critical surface of a superconductor . . . 5
1.7 Illustration of a magnets loadline . . . 5

2.1 Critical current density of superconducting materials, courtesy of the Applied Superconductivity Centre . . . 7
2.2 Elementary cell of a A15-structure, Nb_3Sn [9] . . . 8
2.3 Schematic presentation of the three main Nb_3Sn wire fabrication techniques. From top to bottom: The bronze process, the internal Sn (IT) process (RRP), and the Powder-in-Tube (PIT) process. To the right are SEM cross sections of actual wires manufactured according to the specific processes[6] 9
2.4 *Top*: Cross sections of different RRP strands. *Bottom*: Cross sections of keystoned cable made with 150/169 RRP strands and a stainless-steel core 11-mm wide and 25μm thick. Picture taken from[12] . . . 9
2.5 Main geometrical cable parameters . . . 10
2.6 Cable insulation on the DS11T, with 108/127 RRP® strand . . . 11
2.7 Rutherford cable with the mica foil and the S2-Glas, as used in DS11T . . . 11
2.8 Coil layout of the main bending magnet in the LHC, magnetic field-yellow, direction of the current-green, direction of the particle beam-red[14] . . . 12
2.9 Flow chart for the mechanical design of superconducting magnets[15] . . . 13
2.10 (a) Cos-theta dipole winding; (b) field map on the coil (c) electromagnetic forces [16] . . . 14
2.11 Layout of the coils and naming of the coil blocks . . . 15
2.12 Flow chart of the coil manufacturing . . . 16
2.13 all three magnets powered at roughly 90% of their load line at 1.9K, black vectors are the current flow, plots are to different scale . . . 17
2.14 Cross section of the DS11T, only one half of the magnet shown . . . 18
2.15 One collared coil of the DS11T, detailed view on the right focusing on the collar key and the interleaving of the collars . . . 19
2.16 Cross section of the MQXF . . . 19
2.17 Cross section of the SMC-11T . . . 20
2.18 Specific heat of materials[23] . . . 22

3.1 108/127 OST-RRP strand in a cable used for the DS11T. The non-conductive materials are not visible and the surface was gold-coated . . . 23
3.2 Stress-strain curves of copper wire cold-drawn and after subsequent 695C ° heat treatment, published in [28] . . . 28
3.3 Loading direction composite, axial loading: Voigt model; transverse loading: Reuss model . . . 28
3.4 Dimensions of the 10-stack used for the compression tests performed at CERN in September 2015 30
3.5 10-stack compression test . . . 31
3.6 10-stack modulus as a variation of the material modulus . . . 33

3.7 10-stack geometries used in the FEA . . . 34
3.8 Boundaries and mesh of the M3 model for the transverse loading case. For the horizontal loading, the boundaries are applied to the surfaces turned by 90 degrees . . . 35
3.9 Stress-strain curve loading and unloading—response from the 10-stack simulations E_t/E_e . . . 35
3.10 B_{c2} values at 4.2K for the Furukawa, VAC, OKSC, and OST strand samples, from [46] . . . 36
3.11 a.) Geometry used and the assigned materials b.) Detail of the mesh on the filament c.) Von Mises strain on the filaments under a compression of 150MPa . . . 38
3.12 Simulation results for 108/127 RRP strand . . . 38
3.13 Simulation results comparing the three 10-stack models on their critical current reduction response 39

4.1 magnetic field strength, same scale, values over 13T are white . . . 41
4.2 BH-curve of the yoke material, Low-Carbon Magnetic Steel . . . 41
4.3 MQXF magnetic field and force vectors at 19.1kA, coordinate systems origin is in the centre of the aperture . . . 42
4.4 Geometries for the extraction of the EM forces . . . 43
4.5 MQXF EM force, at 19.1kA, projected on a cartesian and cylindrical coordinate system, projected on the outer radius 113mm . . . 43
4.6 DS11T-EM force, at 12.8kA, projected on a Cartesian and cylindrical coordinate system, projected onto the outer radius 60.8mm . . . 44
4.7 SMC-11T-EM force, at 15.1kA, projected onto the vertical and horizontal coordinate . . . 44
4.8 naming of the cable surfaces, DS11T coil block 4 pole turn inner layer . . . 45
4.9 Magnetic field of the MQXF magnet in the conductor of a coil in T, at 19.1kA, and the cable of interest . . . 46
4.10 Stresses in the inner layer of the three coils at excitation compared with the difference between a movable pole and a fixed pole . . . 47

5.1 Materials used in the DS11T-model . . . 50
5.2 Materials used in the DS11T-model, focus coil . . . 50
5.3 Meshing used in the DS11T-model . . . 51
5.4 Detailed meshing, Kapton & Shim . . . 51
5.5 DS11T: overview of the contacts; b-bonded, f-frictional, fl-frictionless, ns-no separation, r-rough . 52
5.6 DS11T response for the lateral shim, collared coil to yoke shime at 0.4mm . . . 53
5.7 DS11T unloading of the collar “nose” as a function of the lateral shim at 12.8kA . . . 53
5.8 DS11T response for the collared coil to yoke shim, lateral shim at 0.2mm . . . 54
5.9 EQV stress in the collared coil during collaring, at LS 1 . . . 54
5.10 EQV stress in the collars during collaring, shown for the collar pack with two long collars . . . 54
5.11 EQV stress in the collaring shoe during collaring . . . 55
5.12 Radial stress in the coil, with the maximum longitudinal deviation . . . 55
5.13 DS11T EQV stress during the maximum collaring displacement, at LS 1 . . . 55
5.14 EQV stress in the collared coil after collaring, LS 2 . . . 56
5.15 EQV stress in the collaring key, top in contact with two long collars, bottom with one long collar . 56
5.16 DS11T EQV stress in the coil after collaring while the collared coil is at rest state, at LS 2 . . . 56
5.17 Contact pressure between the collared coil shim and the yoke after the welding, LS 3 . . . 57
5.18 EQV stress in the magnet after welding, LS 3 . . . 57
5.19 DS11T welding operation influence on the azimuthal stress in the coil, delta between LS 2 and LS 3 57
5.20 Azimuthal stress difference between 295K and 1.9K . . . 58
5.21 Displacement between 295K and the cool down to 1.9K . . . 58
5.22 DS11T EQV stress in the coil after the cool down to 1.9K, at LS 4 . . . 58
5.23 Contact pressure between the collared coil shim and the yoke during powering, LS 5 . . . 59
5.24 Radial normal stress in the collared coil during powering, LS 5 . . . 59
5.25 DS11T EQV stress in the coil during powering 12.8kA, at LS 5 . . . 59
5.26 DS11T azimuthal normal stress in the coil during powering 12.8kA, at LS 5 . . . 60
5.27 Materials used in the MQXF-model . . . 60
5.28 Materials used in the MQXF-model, focus coil . . . 60
5.29 Meshing used in the MQXF-model . . . 61
5.30 Detailed meshing, Kapton & key . . . 61
5.31 MQXF: overview of the contacts; b-bonded, f-frictional, fl-frictionless, ns-no separation, r-rough . 62

5.32 the eight locations for the the pressurization of the bladders . . . 62
5.33 MQXF response of the average transversal stress per cable for the vertical and horizontal shim . . 63
5.34 Total deformation, bladder pressure of 50MPa, LS 1 . . . 63
5.35 EQV stress during the bladder pressurisation, LS 1 . . . 63
5.36 MQXF EQV stress in the coil during pressurisation of the bladders at LS 1 . . . 64
5.37 Total deformation, keys placed, bladders de-pressurised, LS 2 . . . 64
5.38 EQV stress, keys placed, bladders de-pressurised, LS 2 . . . 64
5.39 MQXF EQV stress in the coil during pressurisation of the bladders at LS 2 . . . 65
5.40 MQXF EQV stress in the coil after the welding of the shell at LS 3 . . . 65
5.41 Total deformation, at 1.9K LS 4 . . . 66
5.42 EQV stress, at 1.9K, LS 4 . . . 66
5.43 MQXF EQV stress in the coil after the cool down to 1.9K at LS 4 . . . 66
5.44 Deformation due to the EM-forces at 19.1kA, LS 5 . . . 67
5.45 MQXF azimuthal stress in the coil at 19.1kA at LS 5 . . . 67
5.46 Materials used in the SMC-11T-model . . . 68
5.47 Materials used in the SMC-11T-model, focus coil . . . 68
5.48 Meshing used in the SMC-11T-model . . . 68
5.49 Detailed meshing . . . 68
5.50 SCM-11T: overview of the contacts; b-bonded, f-frictional, fl-frictionless, ns-no separation, r-rough 69
5.51 the six locations for the the pressurization of the bladders . . . 69
5.52 SMC11T response of the average transversal stress per cable for the vertical and horizontal shim . 70
5.53 SMC11T response of the average EQV stress per cable for the vertical and horizontal shim . . . 71
5.54 Pressurization of the vertical bladder, LS 1 . . . 71
5.55 Pressurization of the horizontal bladder, LS 2 . . . 71
5.56 EQV stress in the magnet, vertical bladder pressurization, LS 1 . . . 72
5.57 EQV stress in the magnet, horizontal bladder pressurization, LS 2 . . . 72
5.58 SMC-11T EQV stress in the coil during horizontal compression at LS 2 . . . 72
5.59 Total displacement, after the pressure is released from the bladders, LS 3 . . . 73
5.60 EQV stress in the magnet, after the pressure is released from the bladders, LS 3 . . . 73
5.61 SMC-11T EQV stress in the coil during horizontal compression at LS 3 . . . 73
5.62 Total displacement, after the cool down to 1.9K, LS 4 . . . 74
5.63 EQV stress in the magnet, after the cool down to 1.9K, LS 4 . . . 74
5.64 SMC-11T EQV stress in the coil after the cool down to 1.9K, LS 4 . . . 74
5.65 Horizontal stress delta due to the EM-forces between LS 4 and LS5 . . . 75
5.66 EQV stress in the magnet, powering with 15.1kA, LS 5 . . . 75
5.67 SMC-11T EQV stress in the coil, powering with 15.1kA, LS 5 . . . 75

6.1 average transversal cable stress, comparison between the single coil and the coils in the structure . 77
6.2 change in average transversal cable stress, comparison between the single coil and the coils in the structure . . . 77
6.3 EQV stress in the pole and midplane cables . . . 78
6.4 transversal stress in the pole and midplane cables . . . 79
6.5 Plastic strain in the cable after the assembly of the magnet at room temperature, LS 3 . . . 79
6.6 Plastic strain in the cable after the cool down to 1.9K, LS 4 . . . 80
6.7 Plastic strain in the cable, excitation of the coils, LS 5 . . . 80
6.8 respond of the strain function s(ε), during operation, LS 5 . . . 81
6.9 critical current reduction, during operation, LS 5 . . . 81

B.1 Simulation results for 108/127 RRP Strand . . . IX
B.2 Stresses in the MQXF-coil with the pole at 19.1kA, azimuthal position is 0 at the midplane . . . IX
B.3 Stresses in the MQXF-coil with a free pole at 19.1kA, azimuthal position is 0 at the midplane . . . X
B.4 Stresses in the DS11T-coil at 12.8kA, azimuthal position is 0 at the midplane . . . X
B.5 Stresses in the SMC-coil at 15.1kA, vertical position is 0 at the midplane . . . X

C.1 Vertical loading of the M2 10-Stack model to 150MPa in compression . . . XI
C.2 Horizontal loading of the M2 10-Stack model to 150MPa in compression . . . XII
C.3 Vertical loading of the M3 10-Stack model to 150MPa in compression . . . XIII
C.4 Horizontal loading of the M3 10-Stack model to 150MPa in compression . . . XIV

C.5 critical current reduction, 108/127 RRP Strand, 12T at 1.9K XV
C.6 Radial and Azimuthal Forces - DS11T at 12.8 kA XVI
C.7 Horizontal and Vertical Forces - DS11T at 12.8 kA XVI
C.8 Radial and Azimuthal Forces - MQXF at 19.1 kA XVII
C.9 Horizontal and Vertical Forces - MQXF at 19.1 kA XVII
C.10 Horizontal and Vertical Forces - SMC-11T at 15.1 kA XVIII
C.11 11T magnetic field an force vectors at 12.8 kA, coordinate systems origin is in the center of the bore XVIII
C.12 SMC-11T magnetic field an force vectors at 15.1 kA, coordinate systems origin is in the center of the coil XIX
C.13 MQXF - only full coil - EQV and Azimuthal Stress at 19.1kA XX
C.14 MQXF - only half coil - EQV and Azimuthal Stress at 19.1kA XX
C.15 MQXF - half and full coil model - critical current degradation at 19.1kA XX
C.16 DS11T - EQV and Azimuthal Stress at 12.8kA XXI
C.17 DS11T - critical current degradation at 12.8kA XXI
C.18 SMC - only full coil - EQV and Azimuthal Stress at 15.1kA XXI
C.19 SMC - only half coil - EQV and Azimuthal Stress at 15.1kA XXI
C.20 SMC - half and full coil model - critical current degradation at 15.1kA XXII
C.21 Meshing used on the cable and insulation XXII
C.22 Meshing of the collaring key and the three interleaving collars XXII
C.23 Collaring Surfaces Top Collar-Pack XXII
C.24 Collaring Surfaces Lower Collar-Pack XXII
C.25 EQV Plastic Strain in the long collar after collaring XXIII
C.26 Displacement vector during the maximum collaring displacement, note that the max. displacement is due to the contact offset of 0.2mm XXIII
C.27 Total deformation after collaring, LS 2 XXIII
C.28 Deformation due to spring back, LS 2 XXIII
C.29 “pulling” on the shell to simulate the welding, deformation scaled by factor 50, LS 3 XXIII
C.30 Contact pressure of the yoke on the tapered edge, after welding, LS 3 XXIII
C.31 EQV stress in the magnet at 1.9K XXIV
C.32 Delta between 295K and 1.9K in radial pressure, CS center of the magnet XXIV
C.33 Body force map of the DS11T at 12.8kA XXIV
C.34 EQV stress in the collared coil during powering, LS 5 XXIV
C.35 Vertical normal stress in the collared coil during powering, LS 5 XXIV
C.36 Horizontal normal stress in the collared coil during powering, LS 5 XXIV
C.37 DS11T radial coil stress, LS 1 XXV
C.38 DS11T azimuthal coil stress, LS 1 XXV
C.39 DS11T radial coil stress, LS 2 XXV
C.40 DS11T azimuthal coil stress, LS 2 XXV
C.41 DS11T radial coil stress, LS 3 XXV
C.42 DS11T azimuthal coil stress, LS 3 XXV
C.43 DS11T radial coil stress, LS 4 XXVI
C.44 DS11T azimuthal coil stress, LS 4 XXVI
C.45 Radial normal stress in the coil during powering, LS 5 XXVI
C.46 Longitudinal normal stress in the coil during powering, LS 5 XXVI
C.47 DS11T radial coil stress, LS 5 XXVI
C.48 DS11T azimuthal coil stress, LS 5 XXVI
C.49 Meshing used on the cable and insulation XXVII
C.50 Meshing of the vertical and horizontal keys XXVII
C.51 Radial stress at maximum bladder pressure, LS 1 XXVII
C.52 Azimuthal stress at maximum bladder pressure, LS 1 XXVII
C.53 MQXF radial coil stress, LS 1 XXVIII
C.54 MQXF azimuthal coil stress, LS 1 XXVIII
C.55 MQXF radial coil stress, LS 2 XXVIII
C.56 MQXF azimuthal coil stress, LS 2 XXVIII
C.57 MQXF radial coil stress, LS 3 XXVIII
C.58 MQXF azimuthal coil stress, LS 3 XXVIII
C.59 MQXF radial coil stress, LS 4 XXIX

C.60 MQXF azimuthal coil stress, LS 4 . . . XXIX
C.61 MQXF radial coil stress, LS 5 . . . XXIX
C.62 MQXF azimuthal coil stress, LS 5 . . . XXIX
C.63 Magnetic field in the condutor and body force map of the MQXF at 19.1kA . . . XXIX
C.64 SMC-11T horizontal stress, LS 1 . . . XXX
C.65 SMC-11T vertical stress, LS 1 . . . XXX
C.66 SMC-11T body force density of the EM-forces . . . XXX
C.67 SMC-11T magnetic field at 15.1kA . . . XXX
C.68 SMC-11T horizontal stress, LS 4 . . . XXXI
C.69 SMC-11T vertical stress, LS 4 . . . XXXI
C.70 SMC-11T horizontal stress, LS 1 . . . XXXI
C.71 SMC-11T vertical stress, LS 1 . . . XXXI
C.72 SMC-11T horizontal stress, LS 2 . . . XXXI
C.73 SMC-11T vertical stress, LS 2 . . . XXXI
C.74 SMC-11T horizontal stress, LS 3 . . . XXXII
C.75 SMC-11T vertical stress, LS 3 . . . XXXII
C.76 SMC-11T horizontal stress, LS 4 . . . XXXII
C.77 SMC-11T vertical stress, LS 4 . . . XXXII
C.78 SMC-11T horizontal stress, LS 5 . . . XXXII
C.79 SMC-11T vertical stress, LS 5 . . . XXXII
C.80 convergence of the five loading steps of the nominal shimming DS11T-simulations . . . XXXIII
C.81 convergence of the five loading steps of the nominal shimming SMC-11T-simulations . . . XXXIV
C.82 convergence of the five loading steps of the nominal shimming MQXF-simulations . . . XXXV
C.83 Dimension of the DS11T, SMC-11T and the MQXF coil . . . XXXVI
C.84 Dimensions of the DS11T . . . XXXVII
C.85 Dimensions of the MQXF . . . XXXVIII
C.86 Dimensions of the SMC-11T . . . XXXIX

List of Equations

1.2.1 Luminosity function . . . 1
1.3.1 Beam energy dependency on the magnetic field . . . 2
2.2.1 force density of a conductor in a field . . . 13
2.2.2 body Lorenz force $\vec{F}_L$ . . . 13
2.2.3 magnetic pressure, p_m . . . 13
2.2.4 polar components of the magnetic field, B_{ri} . . . 13
2.2.5 polar components of the magnetic field, $B_{\phi i}$ . . . 14
2.2.6 polar components of the Lorentz force density, f_r . . . 14
2.2.7 polar components of the Lorentz force density, f_θ . . . 14
2.2.8 Cartesian components of the Lorentz force density, F_x . . . 14
2.2.9 Cartesian components of the Lorentz force density, F_y . . . 14
3.2.1 rule of mixtures, transverse, combination of matrix and fibre modulus . . . 29
3.2.3 rule of mixtures, transverse, n-components . . . 29
3.2.4 rule of mixtures, transverse, n-components . . . 29
3.5.4 strain function to calculate the critical current reduction . . . 36
3.5.5 critical temperature, $T_c(\varepsilon)$ . . . 36
3.5.6 calculation of the critical magnetic field, $B_{c2}(T,\varepsilon$ . . . 37
3.5.7 calculation of the pinning force $F_p(T,\varepsilon)$ and $F_p(T,0)$ . . . 37
3.5.8 critical current degradation of one element, R_i . . . 37
3.5.9 critical current degradation, $\frac{I_c}{I_{c0}}$ . . . 37

1 Introduction

For the development of future circular particle accelerators to get energy and luminosity levels higher than the current ones, magnets providing fields above 11T are required. The most widely used super-conductor, Nb-Ti, is not sufficient for this purpose. In fact, Nb_3Sn will be widely used in future accelerator magnets. Several magnets using this conductor are currently being developed at CERN; these magnets are either slated for future updates of the LHC or for research purposes relating to future accelerators. The mechanical structure is one of the most challenging aspects of superconducting high-field magnets. The main purpose of the mechanical structure is to keep the coils in compression till the emergence of the highest electromagnetic forces that are developed in the ultimate field of the magnet. Any loss of pre-compression during the magnet's excitation would cause too large deformation of the coil and possibly a quench in the conductor owing to relative movements of strands in contact associated with excessive local heat release. However, too high pre-compression would overstrain the conductor and thereby limit the performance of the magnet. This thesis focuses on the mechanical behaviour of three of these magnets. All of them are based on different mechanical designs for the support of the coils.

In this thesis, different mechanical structures are studied by means of finite element modelling (FEM). Different designs are compared by using the same methodology for the analysis to list the advantages and the disadvantages of different designs. All calculations for the FEM have been carried out using the software *ANSYS 17.2*.

1.1 Methodology

Based on the experience of already built magnets, a matrix of parameters is defined to assess the performance of each structure. These parameters are: the maximal transversal and equivalent stress during the assembly and the powering of the magnet; the loss of pre-compression of the conductor during the powering; the overstraining of the conductor and by thus limiting the critical current.

The assessment of these parameters also focuses on the variation in these parameters and the influence on different mechanical designs. With this, the robustness of individual designs can be established. In a more refined analysis, non-linear material parameters are used. It has been observed that the geometry of the impregnated coils changes after assembly and cold test. Material tests on cable blocks have shown that the stress strain relation of the impregnated cable block is non-linear and has a hysteretic behaviour. The influence of these non-linearities of the impregnated coil material on magnet performance is analysed in this study. This approach can be extended to different components that are exposed to high mechanical stresses. A chapter in this thesis is dedicated to defining important parameters that determine the performance of the superconducting magnet. To give an example, the critical current of the superconductor is determined by the strain on the strand, the current density, temperature, and the magnetic field. This can be used to compare different mechanical concepts. Beyond using the uni-axial strain as a criterion, comparative strain formalism needs to be developed. Using the strain intensity or the equivalent von Mises strain as comparative formalism is not practical for superconductors. Another parameter for comparing the different mechanical concepts is the maximum stress in the impregnated coils during assembly at room temperature or stress distribution in the coil. These and more parameters are evaluated in this thesis to ensure the comparability between the different concepts.

1.2 The HL-LHC Project

The Large Hadron Collider (LHC), based in Geneva, Switzerland, is one of the largest scientific instruments ever. Since the 2010 the LHC is operational and is delivering scientific results for the global community of 7000 physicist. To extend its potential for future discoveries, a major upgrade is predicted in the 2020s. With this, the rate of collisions (luminosity) will be increased by a factor of five compared to its designed value and the integrated luminosity by a factor of 10. The luminosity can be expressed in the luminosity function:

$$L = F\frac{n_b N_b^2 f_{rev}}{4\pi\sigma^{*2}} \tag{1.2.1}$$

where n_b is the number of particle bunches circulating in the machine, N_b is the number of proton per bunch, f_{rev} is the revolution frequency of the machine and σ^{*2} is the transverse RSM beam size at the collision point. F is factor expressing the crossing angle of the particle bunches at the collision point. The nominal value of the LHC, prior to the upgrade is $10^{34} cm^{-2} s^{-1}$.

Such a major upgrade needs careful planning and development of new technology. This requires about 10 years to be implemented and finished. The novel machine configuration will be called high-luminosity LHC (HL-LHC). The upgrade will rely on several key innovation technologies representing exceptional technological challenges such as 11-12 Tesla superconducting magnets, compact superconducting cavities for beam rotation with ultra-precise phase control, and the new technology for beam collimation and 300-meter-long high-power superconducting links[1].

1.3 Magnets

This Thesis will focus on the magnets mentioned in section 1.2,which are needed for the HL-LHC. Three high-field magnets have been chosen for this DS11T, MQXF, and SMC-11T. The DS11T and MQXF will be installed in the accelerator ring for the HL-LHC. The SMC-11T is considered a research magnet that investigates the behaviour of superconducting coils under different loading concepts. The SMC can host two coils, but can also be adapted to host coils made from the same cable as the DS11T. Only the placement of one coil is possible in this configuration. The DS11T is a dipole magnet that produces a vertical magnetic field perpendicular to the particle direction. Dipoles are used to deflect particle motions to circular trajectories. The magnetic field needs to be adapted to the beam energy. After the injection phase of the LHC (particle energy 450GeV), the energy of particles constantly increases to up to 7TeV. This requires the magnetic field strength to be constantly adapted. The relationship is given in Equation 1.3.1, where mv is the particle momentum, B the dipole field, and ρ the accelerator curvature.

$$\frac{mv}{e} = B\rho \tag{1.3.1}$$

Quadropoles, like the MQXF, produce a field that is null at the centre of the beam tube. The field is linearly dependent on the distance of the centre, with the purpose of focusing the beam . The field is expressed as a gradient, and the LHC quadropoles have a gradient of 223 T/m.

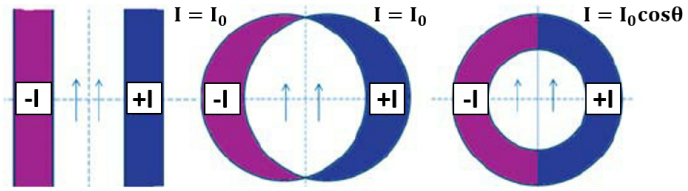

Figure 1.1: Pure dipole configurations: two infinite slabs (left), intersecting ellipses (center), and cylinder with cos-θ azimuthal current density distribution (right)[2]

The definition of an ideal field is that only one multipole (dipole, quadrupole, etc.) is present and all other harmonics are theoretically zero. To generate a perfect dipole field two infinite tall conductor blocks, with opposing direction of electrical current, would form a perfect field in between them. This kind of conditions are infeasible in reality. Another approach is a current distribution of two intersecting circles with a constant current density, as shown in Figure 1.1 for a dipole field. Manufacturing a coil with this kind of current distribution in the cross-section is also rather difficult.

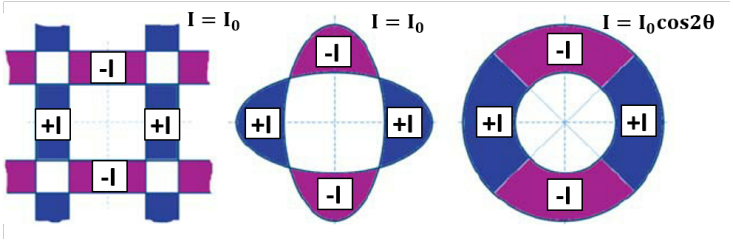

Figure 1.2: Pure quadropole configurations: four infinite slabs (left) and two intersecting ellipses (center) with constant current density, and cylinder with cos-2θ azimuthal current density distribution (right)[2]

Coils can be wound into cylinder shaped forms. The current density can be changed by replacing current carrieng conductor with spacers, there fore decreasing the current density in this local region. Varying the current

density over a full cylinder with $I_o * \cos(\theta)$ a near perfect dipole field can be generated, Figure 1.1 right. The same principle can be applied to generate n-pole fields. For a quadropole field four infinite slabs are needed, Figure 1.2. The needed current distribution for the quadropole is given by $I_o * \cos(2\theta)$ for a full cylinder. The formula for the current distribution is also the name giver to the two coil designs shown here, $\cos(\theta)$ for the dipole and $2\cos(\theta)$ for the quadrople. Of course is the field quality in the aperture limited by such fixed parameters like cable width and thickness or wind ability. This rather interesting problem of the receivable field quality is not part of this thesis and will be therefore not discussed.

1.4 Superconductivity

Superconductivity is a phenomenon which in its fundamentals describes the loss of electrical resistance as a function of temperature, magnetic field and current density. Although superconductivity is a complex quantum physics phenomenon which is still not fully understood, its macroscopic behaviour can be put to use in modern day technology. Applied superconductivity is mainly found in magnet technologies. These range from medical appliances (MRI[1] scanners), material and biology science (NMR[2] machines) to high energy physics in particle accelerators. Superconductivity can be found in a variety of compounds and metals. The first discovery of superconductivity was found in mercury by Kamerlingh-Onnes in 1911. This discovery revealed that a state of electrons exists below a certain temperature. In this state the electrons form so called cooper-pairs. This formation allows a tunnelling effect to transport current without electrical resistance.

Superconductivity is a phenomenon, which fundamentally describes the loss of electrical resistance as a function of temperature, magnetic field, and current density. Although super- conductivity is a complex quantum physics phenomenon that is yet to be understood fully, its macroscopic behaviour can be used in modern-day technology. Applied superconductivity is mainly found in magnet technologies that range from medical appliances (MRI[3] scanners) and material and biology science (NMR[4] machines) to high-energy physics in particle accelerators. Superconductivity can be found in a variety of compounds and metals. The first discovery of superconductivity was found in mercury by Kamerlingh-Onnes in 1911-this revealed that a state of electrons exists below a certain temperature. In this state, the electrons form the so-called cooper pairs. This formation allows a tunnelling effect to transport current without electrical resistance.

Superconducting materials can be separated by their ability to expel the magnetic field. The first type, referred to as Type-1 superconductors, expels the magnetic field up to a maximum value of B_c, the critical field. If the field is larger than B_c,the sample reverts to its normal conducting state. B_c is a function of temperature and normally increases with lower temperatures. Pure mercury and lead are examples of Type-1 superconductors. The second type, referred to as Type-2 superconductors, shows ideal diamagnetic for magnetic fields smaller than the “lower critical field”, B_{c1}, and the superconducting effect completely vanishes at fields higher than the “upper critical field”, B_{c2}. Both fields reach zero at critical temperature T_c. The phase for Type-1 below B_c and for Type-2

[1] Magnetic resonance imaging
[2] Nuclear magnetic resonance
[3] Magnetic resonance imaging
[4] Nuclear magnetic resonance

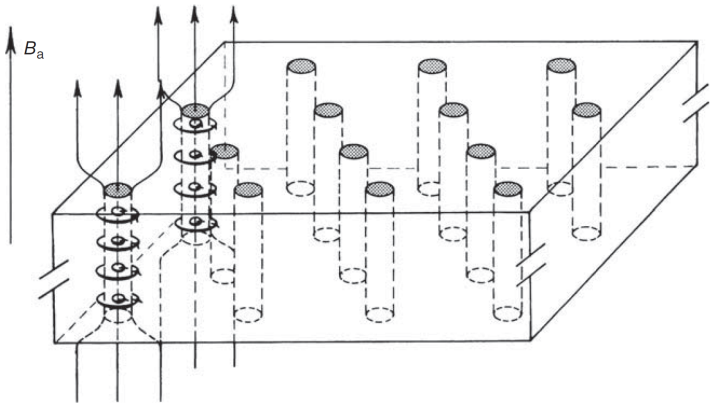

Figure 1.3: Schematics of the Shubnikov phase. The magnetic field and the supercurrents are shown only for two flux lines. [3]

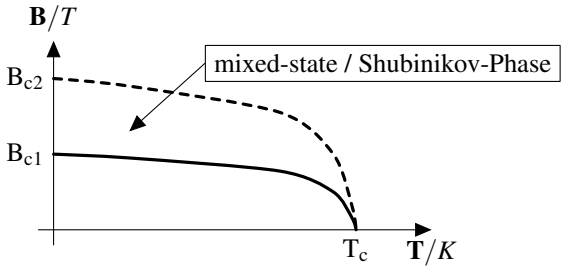

Figure 1.4: Schematic overview of the superconducting states in type-2 superconductors

below B_{c1} is called the Meissner phase. AboveB_{c1} and below B_{c2}, for Type-2 superconductors, this phase is called the mixed phase (or "Shubnikov phase") because both normal and superconducting states are present in this region. In the mixed phase of the Type-2 superconductor between B_{c1} and B_{c2}, the magnetic field only partially penetrates the sample. Shielding currents are formed around the magnetic field lines penetrating the sample. This happens in such a way that a system of flux lines, also called Abrikosov vortices, is generated. Figure 1.3 schematically shows a Shubinikov phase structure. Each flux line consists of a system of circular currents, which, in Figure 1.3, is indicated by two flux lines. With an increase of B_a,the distance between the flux lines decreases [3].

As previously described, the difference between a Type-1 superconductor and a Type-2 superconductor is that the magnetic field can penetrate the sample above Bc1 without losing the superconducting properties of the material. In this intermediate state, both superconducting and normal conducting states persist simultaneously. The transition schematic is shown in Figure 1.4. This allows the superconductor to reach higher magnetic fields. To increase the maximum magnetic flux density, the flux lines need to be hindered from creeping or migrating from their position and the movement causes power dissipation. Hence, the flux lines are pinned with material impurities-this makes it energetically favourable for the flux to fix its position.

Lorentz force acting on the vortices increases the current density J-this mechanism is shown in Figure 1.3. When the Lorentz force exceeds the pinning force, the vortices start to move, resulting in electrical resistance. This explains why, apart from Tc and Bc2,the transition point of the superconductor is also determined by critical current density J_c. J_c is defined as the current density, J, at which the specific resistivity exceeds $10^{-14}\Omega m$, after which the superconductor has a steep ascend in resistivity [4]. Such pinning of the vortices can indeed be achieved by incorporating suitable "pinning centres" into the material.

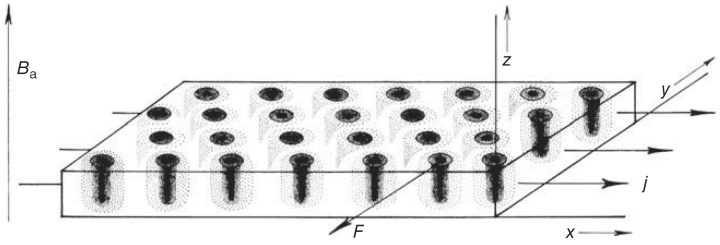

Figure 1.5: Shubnikov phase in the presence of a transport-current density j. The flus lines experience a force F driving them along the y-direction. The magnetic-field distribution around the flux lines is indicated by the hatching. [3]

Considering all three parameter, the limitation of the Type-2 superconductor can be shown schematically in Figure 1.6. The shown surface is representing the bounds between the superconducting and the normal conducting state. When the superconductor crosses this surface, it looses it superconducting properties and becomes normal conducting. This can be reversible in a magnet if only a very small portion of the total conductor can cross the critical surface. In most cases, this happens owing to a local increase in temperature near the critical temperature T_c. When the temperature exceeds the local T_c,the conductivity of the material decreases to its normal conductivity and the resistance increases rapidly with an order of magnitude. If a source that is finite in time and duration deposits heat in a superconductor, it will recover only if the cooling of the conductor locally exceeds the heat generation[5].

Within the normal use of a magnet, current and magnetic field are coupled. The operating temperature T_{op} is decoupled and can be assumed constant. Hence, the operating domain is reduced to a single dimension, which is called the load line of a magnet. The design of a magnet must always account for sufficient margin. This margin is represented by the ration of operational current density J_{op} and critical current density J_c. In Figure 1.7, the

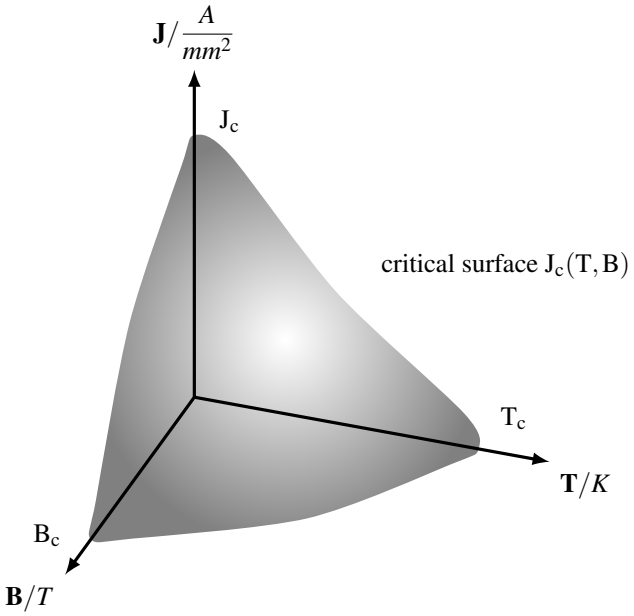

Figure 1.6: Schematic of the critical surface of a superconductor

load line for a fictive magnet is shown where the superconducting regime enclosed by the two-dimensional critical surface is schematically represented by a circle. What is not shown in Figure 1.7 is the sensitivity to mechanical strain on the super conductor itself, this will be discussed in detail in a later part of this Thesis. The main cause for the strain is the electro mechanical force which is acting on the coils itself, high field magnets generate forces in the kN range per mm of magnet length. This strain can be reduced and managed by the design of the coils and the mechanical support structure of the magnets.

Most magnets which are designed to be used in an particle accelerator have a margin of more than 20% at the operating current. This margin includes the reduction in critical current due to the keystoning of the cable. But the imperfections resulting from the production process are not included in such design. Imperfections could be local stress concentrations due to an local excess of material, bad strand arrangement in the cable, a displaced turn and many more. This should be kept in mind that magnets which should have a large margin are possibly operating very close to their critical surface.

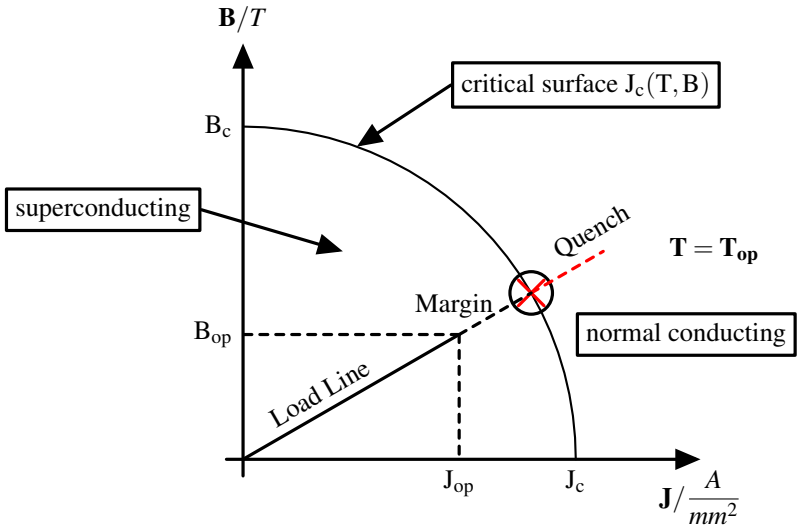

Figure 1.7: Illustration of a magnets loadline

2 Nb_3Sn Accelerator Magnets

In this chapter, the Nb3Sn magnet will be introduced. The MQXF, DS11T, and SCM-11T will be presented to explain how they differ them from each other. All these magnets use Nb_3Sn as a superconductor. The production of the coils follows the same steps for all three coil designs. Nb_3Sn is formed during a 10-day heat treatment with temperature up to 700° C. After the very brittle Nb_3Sn-phase is formed , the cable cannot be wound afterwards, therefore the coils need to be reacted in their final geometry. The next step is the impregnation of the coils, which provides mechanical stability and a improved electrical insulation between the cables.

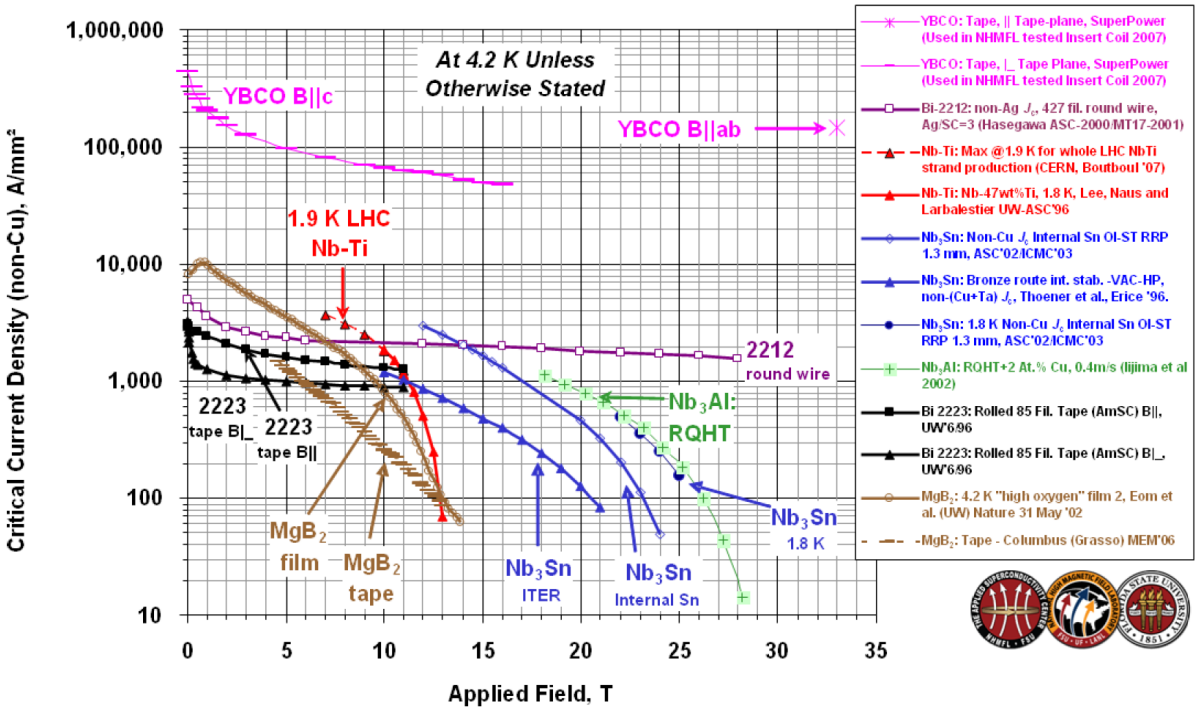

Figure 2.1: Critical current density of superconducting materials, courtesy of the Applied Superconductivity Centre

Nb_3Sn is the superconductor that is needed to fulfil the requirements of the MQXF and the DS11T for the HL-LHC project. Nb_3Sn has much higher superconducting properties than the more generally used Nb-Ti. For a J_c equal to 1000 A/mm^2, Nb-Ti reaches its peak field at 11T at 1.9K, whereas with Nb_3Sn 17T at 4.2K can be achieved. The reduction in the peak field is much more gradual for Nb_3Sn than for Nb-Ti, see Figure 2.1.

Pure superconductors tend to be unstable and generally not suitable for practical use in applications with high current density. A stable operation of superconductors in a high magnetic field requires superconducting filaments embedded in a well-conducting matrix, in most cases made from copper [5]. In most wires used for accelerator magnets, the filament number in one wire ranges from 20 to 400. The function of the matrix is manifold: it allows for current redistribution between the filaments, for example, during current sweep or due to an interrupted filament. It also carries away any heat caused by mechanical energy release or an incipient flux jump [3].

2.1 Conductor

2.1.1 Wire

For future accelerators where fields above 10T are needed, Nb_3Sn will be used as a superconductor. NbTi, which was used for the LHC construction, is not capable of reaching the needed fields for HL-LHC. Nb_3Sn is a superior conductor to NbTi, see Table 2.1. Nb_3Sn exists in a cubic A15 lattice, shown in Figure 2.2. It undergoes a cubic-to-tetragonal phase transition at a temperature of $T_m \cong 43K$, at about 24.5 % Sn. The A15 lattice is formed through solid-state diffusion. Apart from the sensitivity to the Sn content and the grain size and boundaries[6], the performance of Nb_3Sn is also highly sensitive to strain.

The A15 Nb_3Sn needs to be stabilized electrically and thermally in a normal conducting matrix. Also, for stabilization reasons, the A15 conductor is distributed in fine filaments, preferably smaller than 50μm, which need

Table 2.1: Comparison of conductors

conductor	$J_e/\frac{A}{mm^2}$	I/A	B/T
Copper	5	3	2
NbTi	600-700	300-400	8-9
Nb_3Sn	600-700	300-400	12-13

This is an example comparison of the typical operation conditions for 0.85mm diameter wires.

to be twisted along the wire axis. In most applications of Nb_3Sn, the wire length exceeds 1km in length and the diameter is below 1mm. For the fabrication process, the single components of the wire are stacked in about 5–30cm diameter billets. These are extruded and drawn into wires. This is done before the forming of the A15 phase with a thermal treatment. The wire at this stage is still ductile since the A15 is not formed yet [7]. The thermal treatment of the wire happens normally after the wire is drawn and after coil winding. The formation of the A15 lattice is a solid-state diffusion at temperature around 650 ° C under a protective atmosphere.

The industrial process relies on the fact that, when the niobium/tin/copper composite is heated to a temperature of 650 ° C, Sn atoms selectively diffuse into the niobium. This solid-state diffusion process is slow and a full reaction can require several hundreds of hours. This heat treatment is normally performed in vacuum or in an inert gas atmosphere to prevent oxidation of stabilizing copper[8].

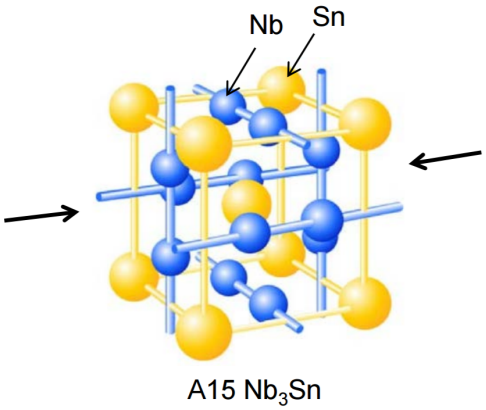

Figure 2.2: Elementary cell of a A15-structure, Nb_3Sn [9]

Currently, the two most advanced technologies for the manufacturing of Nb_3Sn-wire are PIT (*Powder in Tube*) and RRP® (*Restack Rod Process, Internal Sn process*)[10]. In Figure 2.3, the schematics of the different manufacturing techniques are shown. Following the manufacturing, the wire is a composite of Copper (Cu), Niobium (Ni), and Tin (Sn) [11]. All of the magnets used in this thesis use an RRP wire. Studies are ongoing at the moment to use PIT fabricated conductors for these magnets. Since this is still in the R& D phase, only RRP-made cable will be considered for the analysis.

It is very important to point out that, after the heat treatment to form the A15-phase, the copper content of the wire is fully annealed and soft. Other residual components other than copper need to carry the mechanical load. The material properties for the annealed copper will be shown in subsection 3.1.3.

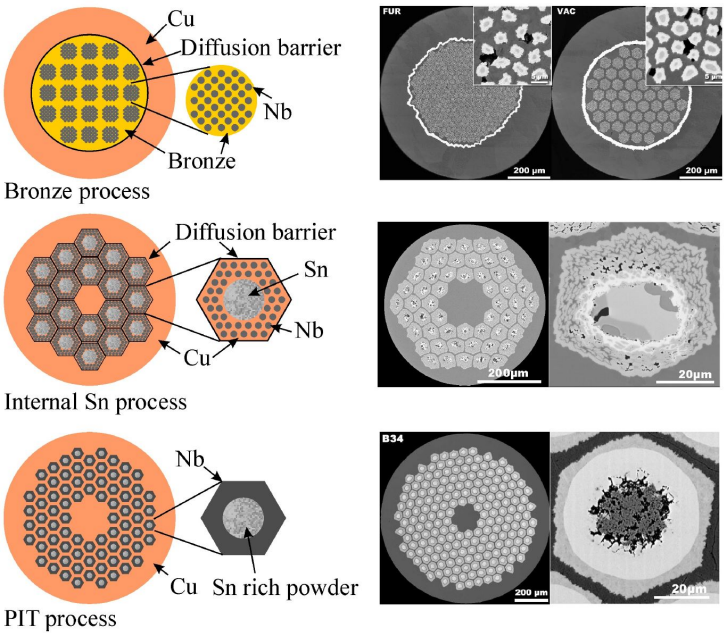

Figure 2.3: Schematic presentation of the three main Nb_3Sn wire fabrication techniques. From top to bottom: The bronze process, the internal Sn (IT) process (RRP), and the Powder-in-Tube (PIT) process. To the right are SEM cross sections of actual wires manufactured according to the specific processes[6]

2.1.2 Cable

To mitigate inductance and improve cable windability, the wires are formed into the so-called Rutherford-type cable. All cables are made in the Rutherford fashion, from several tens of superconducting wires formed into a rectangular shape [10]. In Figure 2.4, three Nb_3Sn strands and a keystoned cable cross section are shown. The cables of the three magnets, MQXF, SMC-11T, and DS11T, use the Nb_3Sn superconductor, the SMC-11T, and the DS11T and the same strand and insulation scheme. All cables have a core in the middle. This core is a $25\mu m$ thick stainless-steel sheet. The core is effective to reduce field distortions and ramp rate dependencies. It controls the inter-strand resistance to allow current sharing and avoid large eddy currents. The core prevents sintering of the strands during heat treatment.

The Rutherford-type cable cross section can be either rectangular or, more generally, trapezoidal. In the latter case, the main dimensional cable parameters are the mid-thickness, the width, and the keystone angle, as illustrated in Figure 2.5. The cable of a trapezoidal shape is also called keystoned cable. This geometry is produced with a forming process after the cabling of the Rutherford-type cable. The cable is passed between two rollers which

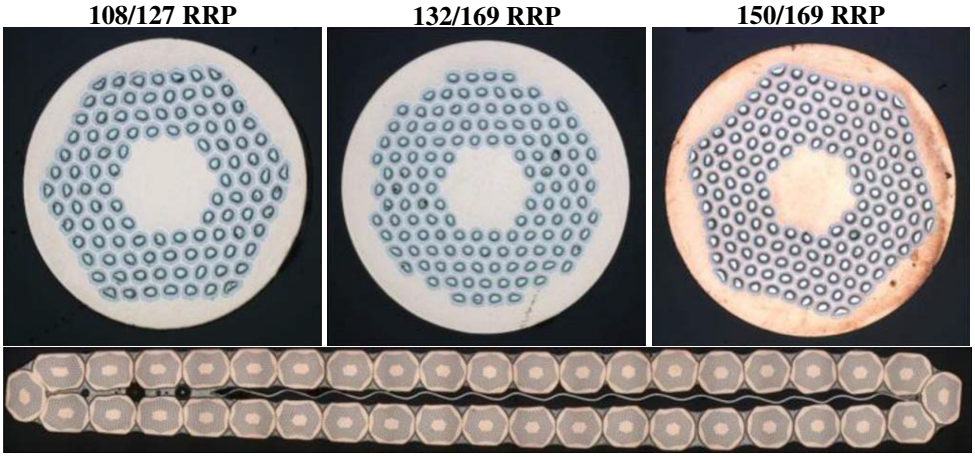

Figure 2.4: *Top*: Cross sections of different RRP strands. *Bottom*: Cross sections of keystoned cable made with 150/169 RRP strands and a stainless-steel core 11-mm wide and $25\mu m$ thick. Picture taken from[12]

Table 2.2: Overview of cable geometry parameters

	DS-11T dipole	MQXF	SMC-11T
number of strands	40	40	40
keystone angle / deg	0.78±0.15	0.55±0.15	0
	cable parameters after heat treatment		
strand diameter / mm^2	0.71	0.86	0.71
cable width / mm	14.85	18.15	14.85
mid thickness / mm	1.31	1.53	1.31
	this results in the following areas per cable		
cable area / mm^2	19.39	27.68	19.39
strand area / mm^2	15.84	23.24	15.84
interstitial epoxy area / mm^2	2.77	3.45	2.77
core area / mm^2	0.3	0.3	0.3
muscovite area / mm^2	0.5	0	0.5
mica E-Glas area / mm^2	1.5	0	1.5
S2-Glas area / mm^2	3.51	10.21	3.35

All values are after thermal treatment
The values for the DS-11T and SMC-11T cables are the same. The possible change in the interstitial epoxy content is not taken into account. The required information is currently not available.

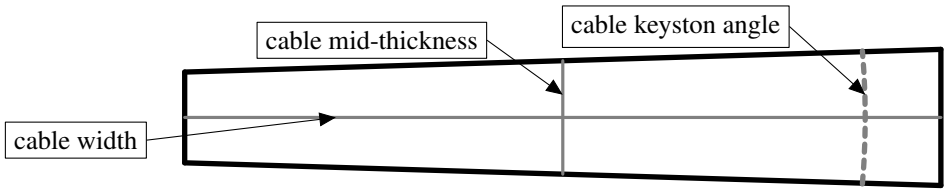

Figure 2.5: Main geometrical cable parameters

plastically deform the cable to the needed keystone angle.

The main advantages of Rutherford-type cables are the high packing factor, transposition of strands, good control of dimensions ($\pm 6\mu$m on thickness), and good windability. The main cable parameters. for the MQXF, DS11T and the SMC-11T, are shown in Table 2.2. This thesis focuses on the global mechanical behaviour of the coils and the mechanical structure of the magnets, which is why the detailed composition of the wire itself will not be discussed. Nevertheless, it should be mentioned that the main difference between different types of cables made by the RRP®process lies in the number of Nb_3Sn-filaments per wire. The amount and size of the said filaments can have an impact on the mechanical stability of the cable. In Figure 2.4, three different wires are shown with a different number of filaments. It should be noted that for this thesis the 108/127 RRP®wire is used for all three magnets.

2.1.3 Cable Insulation

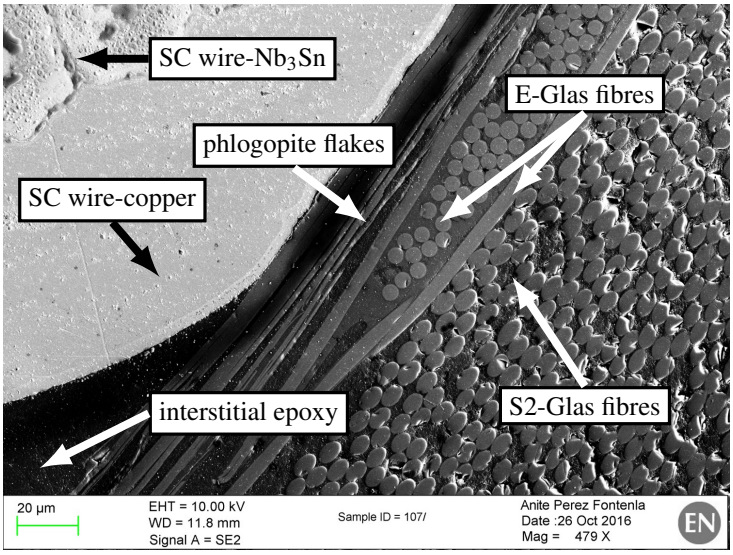

Figure 2.6: Cable insulation on the DS11T, with 108/127 RRP® strand

The cable needs to be wound in sharp radii for all three magnets. This cannot be done with the already reacted, and therefore brittle, Nb_3Sn cable. This gives rise to a very stringent requirement on the cable insulation system, which must be able to sustain the high temperatures during the heat treatment while retaining its insulation capabilities and avoiding the formation of deleterious carbon compounds[8]. In Figure 2.6, the insulation system of the DS11T is shown. The picture represents the state after the heat treatment and impregnation of the coil. The wire is covered by pure epoxy, here called interstitial epoxy. Between the impregnated S2-Glass fibres and the cable, a layer of E-Glas and phlogopite flakes is shown. Called a “mica sheet”, it is only used for the 11T cable. Phologopite is a member of the mica family of phyllosilicates. Mica is a silicate that can be found in nature in the form of large flake-like crystals formed into a rock.

All magnets use for the impregnation an epoxy called CTD-101K by *Composite Technology Development* is used. It was chosen because of its long pot life and low viscosity. This epoxy is designed to withstand high radiation and can be used for cryogenic applications.

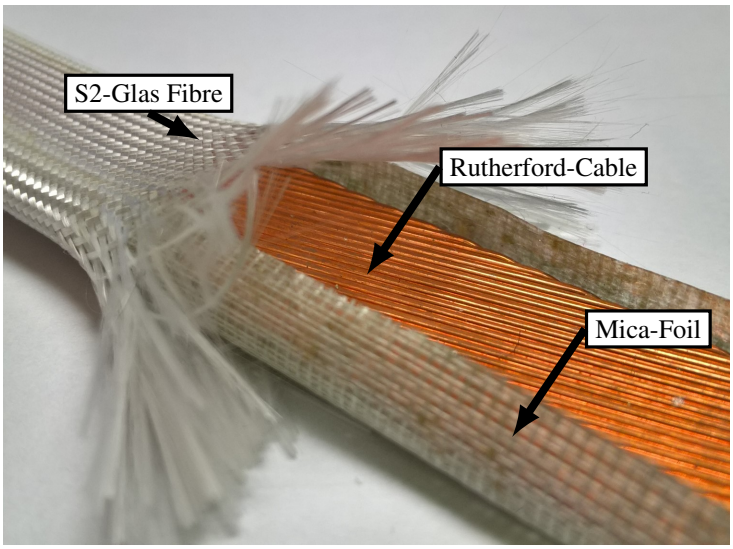

Figure 2.7: Rutherford cable with the mica foil and the S2-Glas, as used in DS11T

11T-cable The DS11T magnets and the SMC-11T use a sheet of mica around the bare cable supported by a braided S2 glass as insulation with a thickness $75 \pm 15 \mu$m. The mica sheet is wrapped around the cable in a C

shape, with a length of 25mm and a thickness of $80 \pm 15 \mu$m[1]. It covers 78% of the cable. The mica sheet consists of 60μm E-Glas for stabilizing the Phlogopite flakes in sheet form, which is 20μm in thickness. The E-Glas sheet is impregnated with a high temperature–resistant silicone elastomer. The remains of this elastomer can be seen in Figure 2.6 surrounding the E-Glas fibres. The mica sheets used for the insulation of the cable can be found under the commercial name "FIROX 63P24A". This sheet is held in place by a S2-Glass insulation braiding. The total thickness of these layers is around 150μm. In Figure 2.7, the Rutherford cable of the 11T is shown with its partially removed insulation. The mica foil is kept close to the cable with S2-Glas fibre braiding.

MQXF The cable used for the MQXF is 18.15mm wide, with mid thickness of 1.5mm and 40 $0.85 \pm 4 \mu m$ wide strands. In the current design, the cable used is an RRP-manufactured 132/169. Moreover, the cable, like the 11T, has a stainless-steel core of 25μm thickness and 10–12mm width to reduce the inter strand coupling. The cable is insulated by braided S2-Glass with a thickness of 146μm. The MQXF cable has a keystone of 0.55 degrees. [13]

2.2 Mechanical Design of Superconducting Magnets

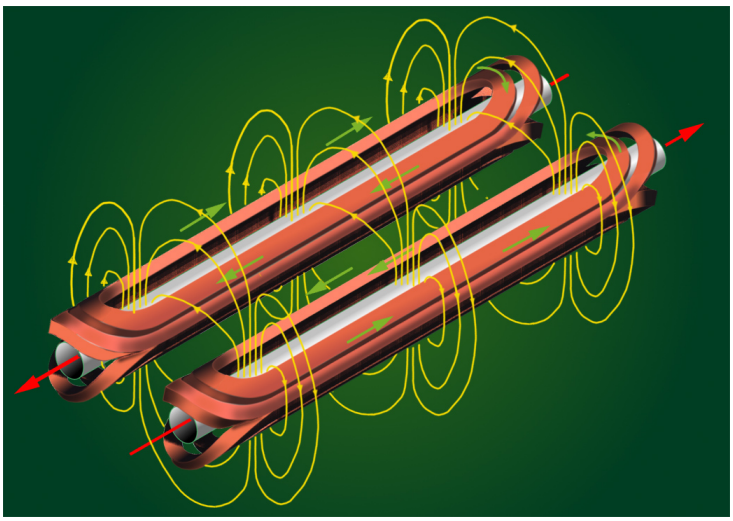

Figure 2.8: Coil layout of the main bending magnet in the LHC, magnetic field-yellow, direction of the current-green, direction of the particle beam-red[14]

In Figure 2.8 the coil layout for the main bending dipole in the LHC is shown, this magnet has two apertures. One magnet uses four dipole coils, two are needed for each aperture. This 180 degree cylinder shaped design is called cos-theta. For a quadropole the coils would be four per aperture and shaped in 90 degree increments, called cos-2 theta coils. The beam passes through both aperture but in opposite directions. The direction of the current is in such a way that the magnetic field of one aperture is not counter acting the one of the other. The extremities of the coils are very difficult to design and manufacture, this thesis is focusing on the straight section of the magnets, therefore this part of the coil will not be further investigated.

In this section, a brief overview will be given of the challenges and goals of the mechanical design of superconducting accelerator magnets. In short, the design needs to accomplish a very good magnetic field quality, allowing the magnet to prevent mechanical failure of the coils and keep the coils compressed at all times. Superconducting accelerator magnets are characterized by large fields and current densities. These factors result in high stresses in the coils with the following effects. Quenches can be triggered by the sudden release of stored elastic energy, such as when part of the coil moves or a crack is formed in the resin. Due to the low heat capacity of the materials at low temperatures, the resulting energy deposition can increase the temperature of the superconductor above its critical value. Mechanical degradation can also be a result of excessive stresses in the coil, the most sensitive parts to suffer being the Nb_3Sn-filaments. Under the large magnetic force and resulting deformation, the field quality can suffer. In Figure 2.9, the principal strategy for the design chart of a superconducting accelerator magnet is shown.

[1] from the company's website COGEBI http://www.fkaeng.com/userfiles/Firox%20P%20-%20UK%20-%20mv-.pdf

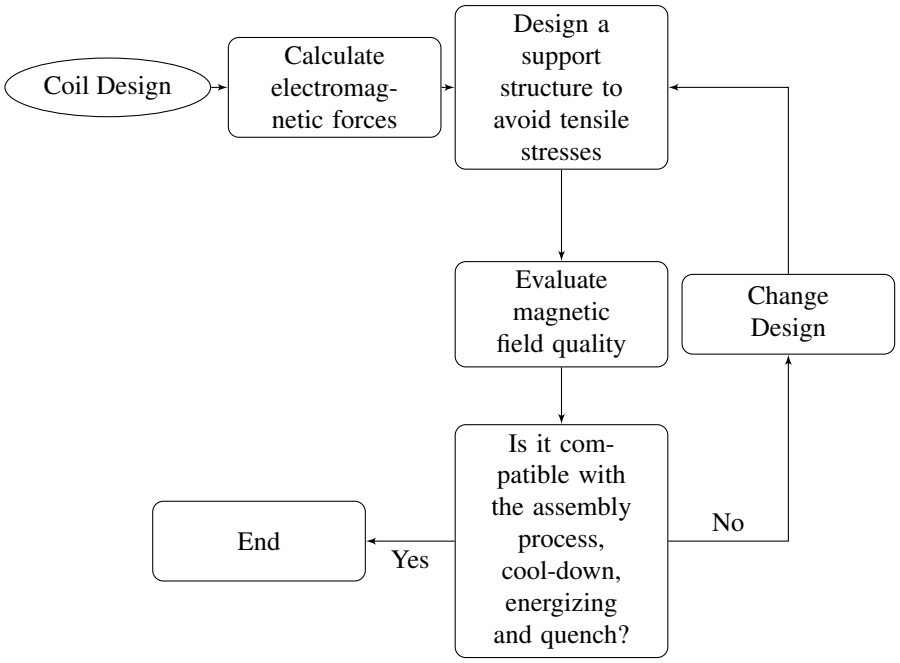

Figure 2.9: Flow chart for the mechanical design of superconducting magnets[15]

Some basic concepts of electromagnetism will be presented in the following. A conductor element carrying a current density j in the presence of a magnetic field B will experience the force density.

$$\vec{f_L}[N*m^{-3}] = \vec{j} \times \vec{B} \tag{2.2.1}$$

The Lorentz force is a body force, i.e. it acts on all parts of the conductor. The total force on a given body can be computed by integration:

$$\vec{F_L}[N] = \int\int\int \vec{f_L} dv \tag{2.2.2}$$

The total stored energy density in the coil may be understood as a "magnetic pressure", p_m in a current loop, the magnetic field line density is higher inside : The field lines try to expand the loop, much like a pressurized gas container. The magnetic pressure is given by

$$p_m[N*m^{-2}] = \frac{B^2}{2\mu_0} \tag{2.2.3}$$

The most common coil design for accelerator magnets is of the cos-theta type. The efficiency of the superconductor is very high (the current distribution is close to the aperture) and permits high magnetic fields to be achieved. The drawback is the relative complex geometry of the windings. The Lorenz forces in an n-pole magnet tend to push the coils towards the mid plane in the vertical/azimuthal direction ($F_<, F_\theta < 0$) and outwards in the radial-horizontal direction ($F_x, F_r > 0$). At the extremities, the forces tend to elongate the coils ($F_> 0$). To calculate the forces without the presence of an iron koke and a uniform current density perpendicular to the cross-section plane $J = J_0$, with the inner radius a_1, outer radius a_2, a span angle ϕ such that the first allowed field harmonic is null (i.e. $\phi = 60^\circ$ for a dipole), the polar components of the magnetic field inside the aperture are [16] as follows :

$$B_{ri} = -\frac{2\mu_0 J_0}{\pi}\left[(a_2-a_1)sin\phi sin\theta + \sum_{n=1}^{\infty}\frac{r^{2n}}{(2n+1)(2n-1)}\left(\frac{1}{a_1^{n-1}} - \frac{1}{a_2^{n-1}}\right)sin(2n+1)\phi sin(2n+1)\theta\right] \tag{2.2.4}$$

$$B_{\phi i} = -\frac{2\mu_0 J_0}{\pi}\left[(a_2-a_1)sin\phi cos\theta + \sum_{n=1}^{\infty}\frac{r^{2n}}{(2n+1)(2n-1)}\left(\frac{1}{a_1^{n-1}} - \frac{1}{a_2^{n-1}}\right)sin(2n+1)\phi cos(2n+1)\theta\right] \tag{2.2.5}$$

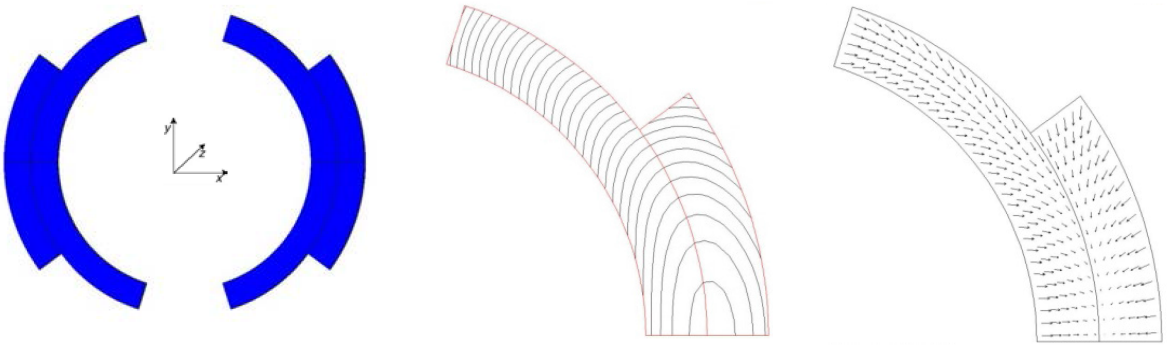

a.) b.) c.)

Figure 2.10: (a) Cos-theta dipole winding; (b) field map on the coil (c) electromagnetic forces [16]

In the case of a dipole, the polar components of the Lorentz force density are given by

$$f_r = -B_\phi J = +\frac{2\mu_0 J_0^2}{\pi} sin\phi \left[(a_2 - r) - \frac{r^3 - a_1^3}{3r^2}\right] cos\theta \tag{2.2.6}$$

$$f_\theta = -B_\phi J = +\frac{2\mu_0 J_0^2}{\pi} sin\phi \left[(a_2 - r) - \frac{r^3 - a_1^3}{3r^2}\right] sin\theta \tag{2.2.7}$$

The Cartesian components of the total force acting on the coil per unit length are given by

$$F_x = +\frac{2\mu_0 J_0^2}{\pi}\frac{\sqrt{3}}{2}\left[\frac{2\pi - \sqrt{3}}{36} a_2^3 ln\frac{a_2}{a_1} a_1^3 + \frac{4\pi + \sqrt{3}}{36} a_1^3 - \frac{\pi}{6} a_2 a_1^2\right] \tag{2.2.8}$$

$$F_y = -\frac{2\mu_0 J_0^2}{\pi}\frac{\sqrt{3}}{2}\left[\frac{1}{12} a_2^3 + \frac{1}{4} ln\frac{a_1}{a_2} a_1^3 - \frac{1}{12} a_1^3\right] \tag{2.2.9}$$

Applying the formulas for F_x and F_y to the parameters of the DS11T coil $a_1 = 29.9mmmm$, $a_2 = 60.8mm$ and $J_overall = 535A/mm^2$, from Figure 2.13, a force of $F_x/F_y = 2520/2230$N per one millimetre coil cross-section can be calculated.

This thesis does not focus on the coil ends. Hence, this will not be discussed in detail. But to provide some insights, the formulas for the axial force F_z, if the coil is approximated as a thin shell, may be written as

$$F_z = \frac{\mu_0 \pi}{4n}\left[1 + \left(\frac{a}{R}\right)^{2n}\right] J_0^2 a^2 = \frac{B_y^2}{\mu_0}\pi a^2 \tag{2.2.10}$$

The axial force in a dipole increases with the square of the magnetic field and the aperture. For the same current density, the end forces on a quadrupole coil are hald those measured in a dipole.

Pre-stress The main goal of pre-stressing the coils is to avoid the build-up of tensile stresses in the coils during the powering stage. In the case of the cos-theta winding configuration, the external mechanical structure usually applies a radial compression, which is transformed into an azimuthal compression inside the coil. This pre-stress counteracts the formation of tensile stresses during powering. It is believed when tensile stresses are present in the coil during excitation that coil is more prone to quench. Most likely due to the loss of compression the conductor is able to move which generate heat and result in a quench. But it is not said that when the conductor is in tension, in the azimuthal direction, this would inevitably lead to an quench.

2.3 Coils

This section will focus on the comparison of the three different coil designs. The coils differ in their global designs like coil shape, number of wedges, pole geometry and number of turns. The different coil cross sections are shown in Figure 2.11, only one half of the cross-section of the full coil is shown, also known as an arc of the coil. Furthermore the position of the midplane for the DS11T and the MQXF-coil is indicated, the midplane is the surface where, later in the full magnet, the coil is in contact with another coil. The pole pieces are represented in gray, the pole piece of the DS11T is not shown. The pole is a part which connects the two arcs of the coils. Making the MQXF and the SMC-11T-coil one closed piece without any recesses.

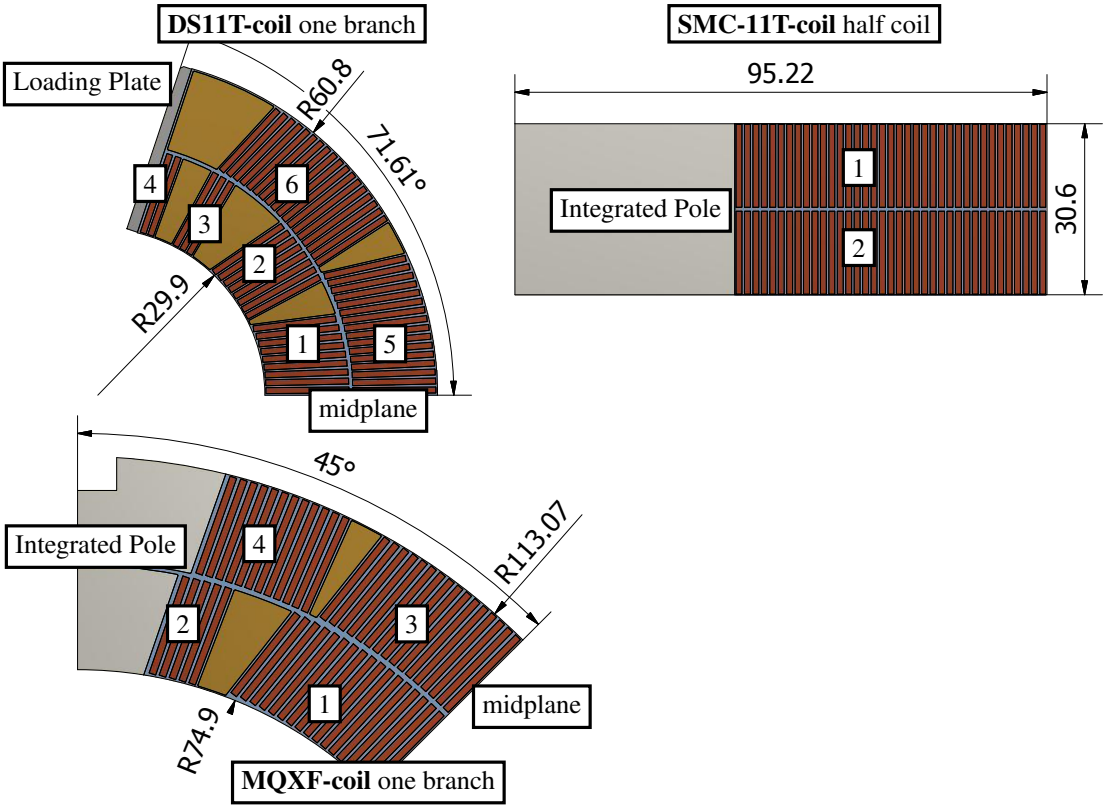

Figure 2.11: Layout of the coils and naming of the coil blocks

DS11T-coil The coil used for the DS11T magnet is segmented in six different coil blocks over two layers, the position and size of these coil blocks is designed in such a way to give the best dipole field quality in the aperture. To separate the coils blocks so called wedges are used, yellow colour in Figure 2.11. This wedges carry no current and only serve the purpose as a separator. In Table 2.3 the number of wedges and cable turns is given. One of the very distinct design features of the DS11T coil is the removable pole piece. The so called Loading Plate is impregnated with the coil and hence "glued" to the coil, during the assembly of the magnet a pole piece is inserted in the gap between the Loading Plates. This allows for relative movement between the pole and the coil.

MQXF-coil The MQXF-coil is a cos2-theta design. The coil has two wedges and four coil blocks spread out over two layers. The integrated pole is split in two pieces, pone piece per layer. The whole coil is impregnated, hence all parts are glued together. The contact surface, on the inner and outer diameter, of the pole is epoxy free.

SMC-11T-coil The SMC-11T-coil is a so called block-coil, the cable can be rectangular and does not require to be keystoned. No wedges are used in this coil, the pole piece is one solid piece that connects the two sides of the coil. The whole coil is impregnated, fixing all parts relative to each other. The winding of such a coil is less complex than the winding of a cos-theta coil.

Table 2.3: Overview of coil geometry parameters

	DS-11T	MQXF	SMC-11T
number of turns	56	50	74
number of wedges	5	2	0
	cross section of the coil without removable parts		
coil area / mm^2	3647.44	5521.48	5827.46
wedges area / mm^2	930.33	437.01	0.00
pole area / mm^2	0.00	1364.37	2408.22
	conductor matrix area = coil area - wedges area - pole area		
conductor matrix area / mm^2	2717.11	3720.10	3419.24

the loading pole of the DS-11T is not considered since it can be removed from the coil
the area is calculated for a full cross section of the coils

Coil Manufacturing

To better understand the challenges of producing Nb_3Sn-coils, a short summary of the manufacturing steps is given. In Figure 2.12, the different manufacturing steps are shown in the flow chart. The coil manufacturing does not differ much between the three designs. As mentioned, the MQXF does not have the mica sheet for the cable insulation and compensates for this with a thicker layer of S2-Glass. The winding for all coils is done with a ceramic binder in between the turns. This binder helps to confine the winding and needs to be cured after one layer is finished. In the reaction process, the coils are enclosed in an atmosphere tight tool that confines the coils close to the nominal geometry. These tools need to be flushed with argon to prevent any kind of reaction with oxygen during the heat treatment. The heat treatment is done on multiple plateaus of temperature and holding time to achieve the best possible formation of Nb_3Sn. The reaction process requires several temperature plateaus up to 650°C during which the homogeneity of temperature in the coil shall be better than $\pm 3^\circ$ C. After the heat treatment, the "leads", which are the connecting cables of the coil, need to be spliced, which is a soldering process, to Nb-Ti superconducting Rutherford cables. This needs to be done since the Nb_3Sn cable is too brittle to allow for manipulation and bending, which is required for the assembly of the multiple coils. For the impregnation process, the reacted coils are enclosed in a tool which can be vacuumized. The epoxy resin is injected with atmospheric pressure and afterwards cured. After the impregnation, all coils need to be measured. With the current manufacturing techniques, a size variation of $\pm 0.15mm$ in azimuthal length is achievable. The metrology, of the coils, is important to determine the shimming for the magnet, larger coils need less additional shims than smaller coils to create the same pre-stress. The assembly of the magnet differs in all three designs and is described in the previous section. The last manufacturing step is quality control, where the electrical integrity of the magnet at room temperature is controlled.

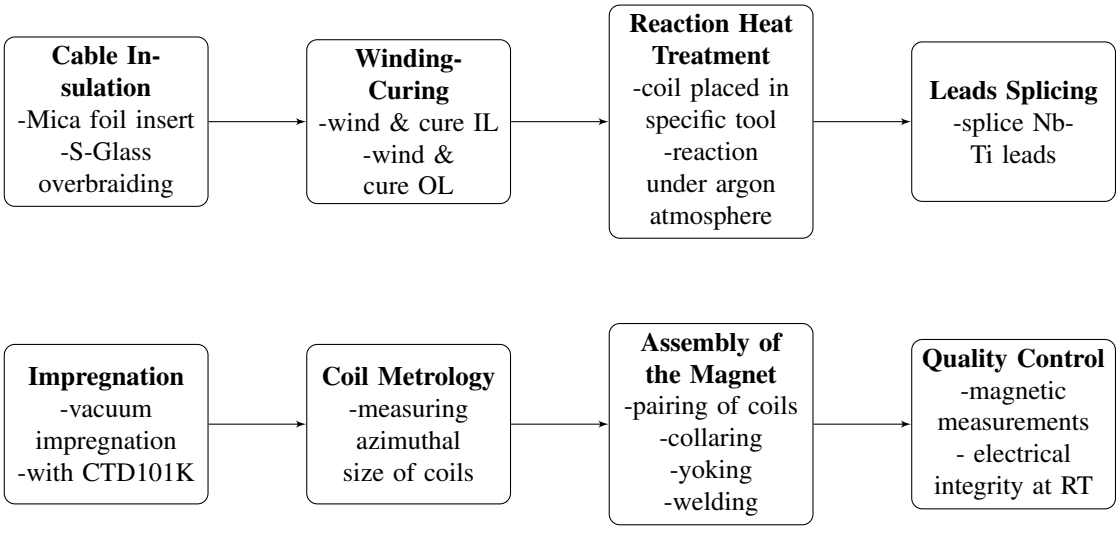

Figure 2.12: Flow chart of the coil manufacturing

2.4 Magnets

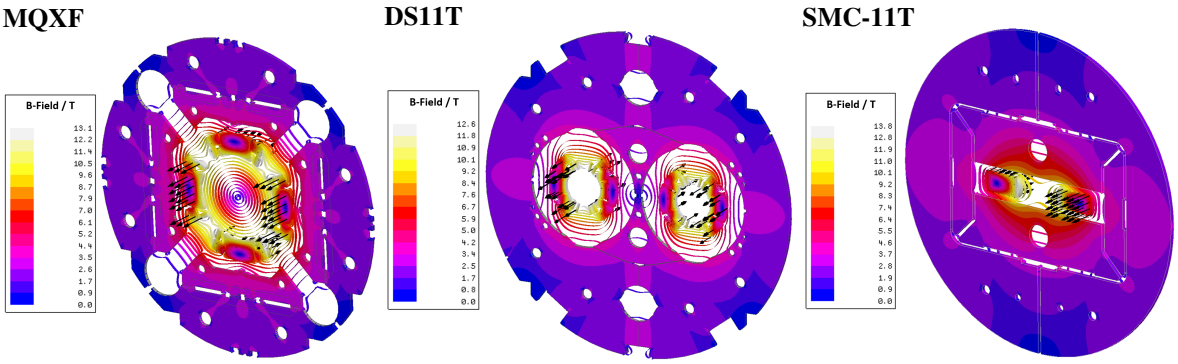

Figure 2.13: all three magnets powered at roughly 90% of their load line at 1.9K, black vectors are the current flow, plots are to different scale

In this section, the individual design of the magnets will be discussed, mainly focusing on the mechanical aspects. To give a brief overview in Figure 2.13 the magnetic field the three magnets are producing is shown, the black arrows indicate the current flow. The MQXF is producing a quadropole field, which has its minimum in the center of the aperture and is increasing outwards. The DS11T and the SMC-11T are producing a dipole field, which is uniform in the aperture and the field lines are parallel. The coil is the most important part of a magnet, which is why the coils will be discussed in a separate part. In Table 2.4, the main properties of the DS11T and the MQXF are listed and compared with the standard LHC MB-dipole.

Table 2.4: Overview of magnet parameters

	LHC-MB dipole	DS-11T dipole	MQXF
Field/Gradient in the aperture at $I_{nom}(B_0)$, T or T/m)	8.3	11.2	132.6
Peak field in the conductor at $I_{nom}(B_p)$, T	8.6	11.6	11.4
Engineering current density at $I_{nom}(J_{eng})$, A/mm^2	475/616	770	726
Overall current density at $I_{nom}(J_{overall})$, A/mm^2	356/442	523	469
Current density, copper at $I_{nom}(J_{cu})$, A/mm^2	763/932	1440	1330
Stored energy, conductor volume I_{nom}, MJ/mm^3	71	130	129
Stored energy, coil volume I_{nom}, MJ/mm^3	52	88	83
Magnetic length, m	14.3	2x5.3	4.2/7.15

These values are for nominal operation in the LHC.

2.4.1 DS11T

In the LHC, collimators are used for beam cleaning and machine protection by safely intercepting and absorbing beam losses. In the LHC, collimators are used to reduce the spatial cross section of the beam to become smaller, with this reducing the risk of uncontrolled beam loss, minimizing the proton/ion beam halo, and reducing the activation of downstream components in the machine.

In order to cope with intensities that are larger than nominal, e.g. in the High Luminosity LHC (HL-LHC) Project [1], additional collimators [17] are installed in the Dispersion Suppressor (DS) region at the location of selected 14.3m long, 8.3T Nb-Ti LHC main bending dipoles. This becomes possible if these main bending magnets are replaced by two shorter 11T dipoles (MBH). These will be installed around the centre of the replaced bending magnet. With their shorter length, space for the additional warm collimator will be made. These MBHs need to be compatible with the LHC lattice and the main system. They will be connected in a series with the main bending dipoles and will operate at an integrated field of 119Tm at 11.85kA [18]. A joint research and development (R&D) programme was initiated in October 2010 at FNAL and CERN with the goal of developing the necessary technology for the fabrication of a 5.5m two-in-one aperture Nb3Sn dipole prototype suitable for installation in the LHC.

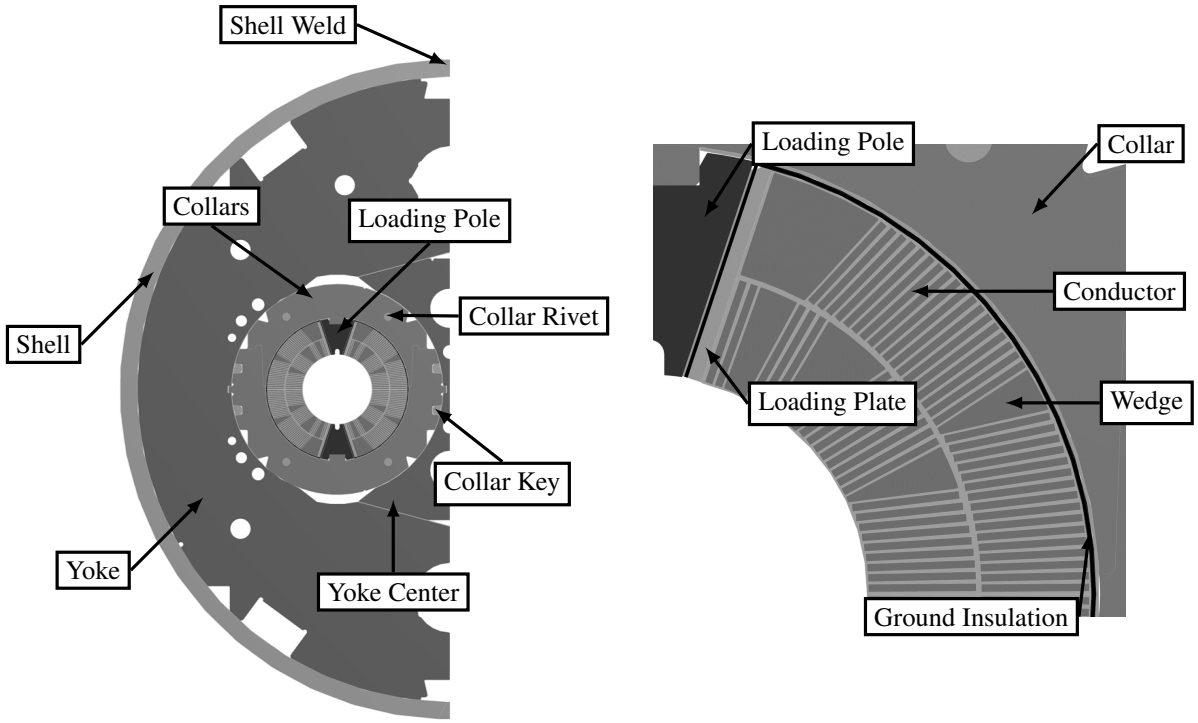

Figure 2.14: Cross section of the DS11T, only one half of the magnet shown

Mechanical Magnet Design The design of the DS11T dipole magnet features two-layer Nb_3Sn half-shell-type coils, $\cos\theta$ design, stainless-steel collars, and a vertically split iron yoke surrounded by a stainless-steel skin. The collars are laminated pieces 3mm thick, the yokes are also laminated with a thickness of 6mm. The coils have an outer and inner diameter of 121.6 and 59.8mm, one coil. The DS11T has two separate collared coils, for each aperture one, a collared coil is two assembled coils in the collars. To avoid curving the magnet, like the main bending magnets in the LHC, the aperture was increased from 56mm to 60mm. Therefore, a bending of the whole magnet is not necessary. The coils are divided into six coil blocks separated by ODS-copper wedges. At the operating current of 11.85kA, the central field is 11.23T. Under operation conditions, the magnet has a load line margin of 20%. The heaters to protect the coils after a quench are glued on the outer diameter, the heater is made from copper and stainless steel strips which are fixed on a Kapton®-foil. This Kapton®-foil extends from the diameter on the midplane of each coil to insulate them from each other. To insulate the coils electrically from the mechanical structure, four layers of Kapton®-foil are placed around the coils. These layers also extend between the removable pole and the coil. To protect this, so called, ground insulation from getting pierced by the collars, a 0.4mm thick stainless steel sheet is placed between the collars and the outer layer of the Kapton®.

The coils in the DS11T-magnet are pre-stressed at room temperature with a fixed displacement on the coils. This is done in two steps, first the collaring of the coils and then the welding of the shell around the yokes. Pre-compression is created by an excess of material in a given enclosure. The collars are designed to "lock" the given pre-stress by an external force, in such a way that the stand alone system is pre-stressed without external intervention. In the collaring process 3mm laminated half tube like stainless steel sheets are displaced around the two coils. The collars are interleaved to each other, they are put in place from alternating directions. There are two type of collars one load carrying and one space filling. In Figure 2.15 the interleaving of the collars is shown on the right. This interleaving of the long collars requires the missing space to be filled up by the short collars. During the assembly of the two coils are placed with the insulation and the loading pole in the collars, at this stage the collars are "open". The whole assembly is placed under a hydraulic press where forces up to 10MN, per one meter length, are needed to displace the upper and lower collars enough to place the collar key. With the removal of the external force the coils are pushing the upper and lower collars apart, but are hindered by the collar key which now connects the lower and upper collars. In the second stage of the assembly the two collared coils are placed in the yokes, Figure 2.14, apart from its magnetic properties the purpose of the yoke-shell system is to give the collared coil additional support. This is needed to with stand the EM-forces which are pushing the coils apart in the horizontal plane. To displace the yokes around the collared coils the assembly is moved under a hydraulic press,

which compresses the whole assembly to ensure a firm contact in-between the single components. The yokes in the The weld-shrinkage of the shell causes it to contract, this contraction is further compressing the whole assembly. After the welding the process of pre-stressing the coils is finished.

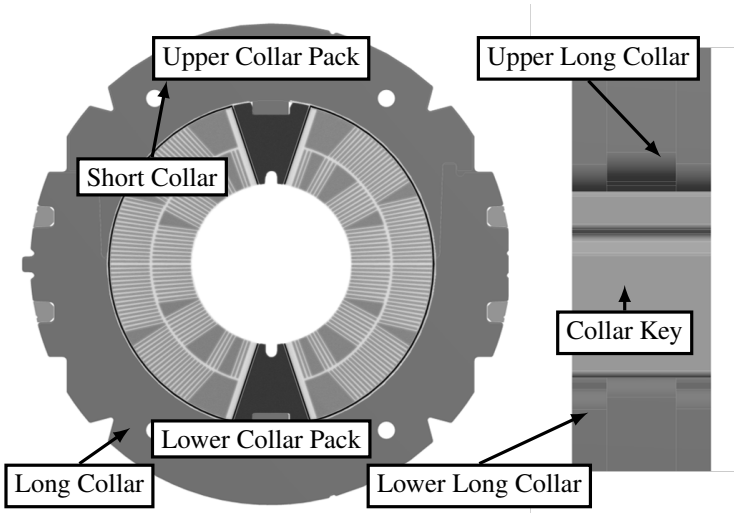

Figure 2.15: One collared coil of the DS11T, detailed view on the right focusing on the collar key and the interleaving of the collars

2.4.2 MQXF

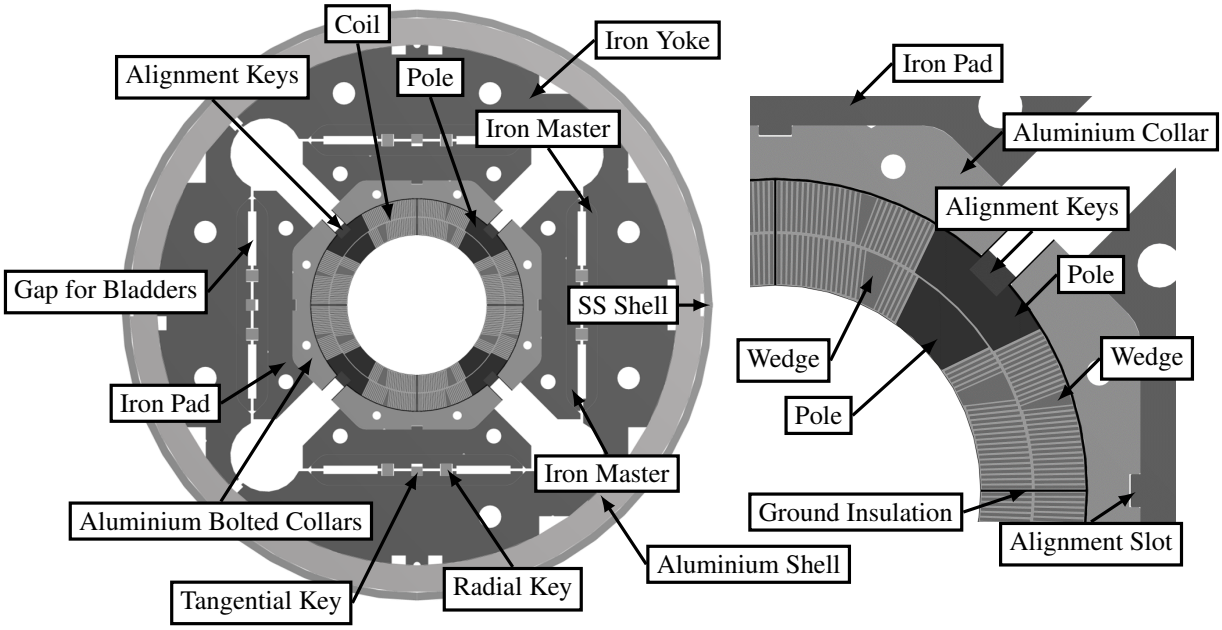

Figure 2.16: Cross section of the MQXF

On each side of the four experiments of the LHC (Atlas, Alice, CMS, and LHCb), a string of quadrupole superconducting magnets are installed. Called the inner triplets, they realize the final focusing of the two beams of protons prior to collision. In terms of the HL-LHC, the inner triplets around ATLAS and CMS are also foreseen to receive a major update. A Nb_3Sn 150mm aperture quadrupole called MQXF will be installed. The development program is carried out as a joint effort between CERN and the US-based laboratory LARP[2] The magnet

[2]The US LHC Accelerator Research Program (LARP) comprises four US laboratories—BNL, FNAL, LBNL and SLAC—which collaborate with CERN in the context of the High Luminosity LHC program.

will be produced in two lengths, MQXFA and MQXFB with a magnetic length of respectively 4.2m and 7.15m. The MQXF relies on an aluminium shell and bladder & key pre-load mechanism, allowing for an easy and fast disassembly and adaptive control of the pre-stress.

Mechanical Magnet Design The bladder & key concept was first developed at LBNL by S. Caspi[19]. It involves pre-compressing the coils against an external cylinder, also called the shell. The first loading of the coils is at room temperature. The structure needs to be fully assembled. In foreseen gaps in the structure, the so-called *bladders* are inserted. These are pressurized, with the resulting force deforming and compressing the coils and the structure. To fix this pre-compression, *keys* are inserted, which are oriented on the same plane as the bladders. These keys are slightly smaller than the resulting gap from the pressurization but larger than the gap in the rest state. With the insertion of the keys and the depressurization of the bladders, the pre-stress is created. In this state, all the load is carried by the coil and the shell. Due to different thermal contractions of the single components, the pre-stress of the coil increases. With the higher thermal contraction of the aluminium shell, a second pre-loading takes place. This allows for *moderate* pre-loading at room temperature compared to the gain in pre-loading after the cool down to cryogenic temperature. The stainless steel shell surrounding the whole magnet is used as a leak tight helium vessel. The shrinking shell made from aluminium has some recesses spread out over the length of the magnet.

2.4.3 SMC-11T

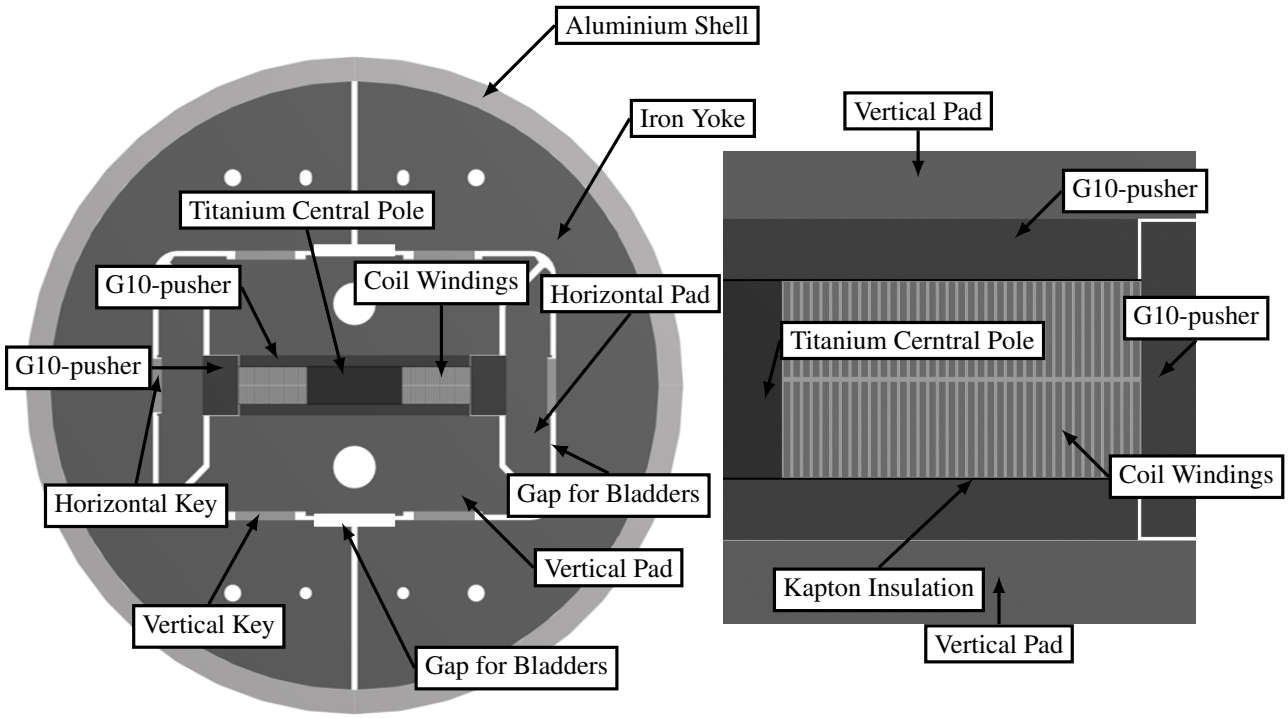

Figure 2.17: Cross section of the SMC-11T

The Short Model Coil (SMC) was designed in the framework of the Next European Dipole (NED) in order to develop a short-scale model of a Nb_3Sn dipole magnet. The groups involved in this project are: CERN/TE-MSc group (CH), CEA/IRFU (FR), RAL (UK), and LBNL (US). In the original design, the magnet was foreseen to reach a field of 13T on the conductor, using PIT-wire. The aim was to study the degradation of the cable by applying different levels of pre-stress.

The short model coil (SMC) is a magnet for purposes of tests and research. It was designed and constructed in the framework of the European project EuCARD as a test bed for Nb_3Sn magnet R&D. It enables the testing of the coil fabrication methods and of Nb_3Sn Rutherford-type cables. SMC coils are subscale planar racetrack dipoles. The design of the SMC allows different sizes of cables to be tested. This allows two coils with two layers each to be mounted in the SMC structure. The SMC is also used to test the same cable as the DS11T magnet does,

with the only difference being that the cable for the SMC is not keystoned. The cable used in the DS11T is wider than the standard cable used in the SMC. Therefore, only one coil with two layers can be mounted in the SMC. When the SMC is equipped with the 11T cable, it is called SMC-11T[20]. The SMC-11T will be used in this thesis for comparing the mechanical concepts. Sharing nearly the exact same cable with the DS11T gives a good foundation for this comparison.

Mechanical Magnet Design The SMC was designed in such a way that changing the pre-stress is rather easy and time efficient using the same concept (bladder & key) as the MQXF. For longitudinal pre-loading of the structure, two rods over the full length are used. These rods can push via the end-support of the coil in the longitudinal direction of the coil. The rods, made from aluminium, can be pre-tensioned with a nut and apply additional pre-stress with the help of the thermal contraction[21]. The loading operation of the SMC starts with the full assembly, apart from the keys, of all the components in the aluminium shell. The inflation of the bladders can happen sequential or in parallel, depending on the loading strategy. If a sufficient opening of the gaps is achieved the keys are inserted. The size of these keys determines the final pre-stress in the magnet. Larger keys require a higher pressure from the bladders. After the depressurization of the bladders the load is transmitted from the coil in the shell via the keys.

2.5 Failure Modes of Nb_3Sn-magnets

A quench is defined as the sudden and irreversible transition of a superconductor into its normal conducting state. Normally, a training behaviour is observed, whereby the quench magnetic field improves after consecutive current test cycles of the magnet [5]. Since every quench puts the magnet under thermal strain and the cost resulting from the needed cools after the quench, the number of quenches needed to reach the full performance needs to be limited. When a magnet quenches, single or multiple strands lose the superconducting properties, resulting in a heat build-up since the current now flows through the copper of the strand. To dissipate the stored energy in the magnet, the whole coil needs to lose its superconductivity. Only then is the stored energy dispersed on the full coil, decreasing the maximum temperature reached in the conductor. This sudden loss of superconductivity is achieved by heating the coil above its critical temperature T_c. This stainless-steel foils are placed on the outer surfaces of the coils, with electrical heating these strips heating up the coil fast enough to dissipate the stored energy in the helium bath.

Magnet training is a major issue in large-scale magnet systems such as the LHC. The 1232 LHC main dipole magnets were tested and trained prior to installations in the ring, with an average training number of 0.9 quenches per dipole, the reach the design current and magnetic field of 8.33T [22]. Most superconducting magnets show a training behaviour. In some cases, the maximum current reached becomes stagnant for multiple powering. In this case, one speaks of a limitation. Another observed behaviour is a decreasing maximum current with continuous powering. This is called a de-training. The maximum current can decrease irreversibly with each powering due to a permanent damage in the conductor. When the magnetic field increases, three important characteristics of the cable stability change as a function of the magnetic field. These are the temperature margin T_m, the magnetic field margin B_m, and the current density margin J_m. The last two are directly linked in a magnet.

2.5.1 Heat-Related Quench

The critical temperature T_c of the conductor cannot be exceeded by insufficient cooling of the magnet. At the operating temperature, the specific heat of the used materials drops drastically, roughly by a factor of 2000. In Figure 2.18, the specific heat of some commonly used materials is shown as the function of temperature.

At 1.9K, a very small amount of energy is required to change the temperature drastically. In high-field magnets, the electromagnetic forces cause the coil and mechanical structure to deform and move. Sudden movements due to stick-slip effects would cause a local rise in temperature. Besides, the epoxy can form cracks, which could also lead to a rise in the temperature. It is assumed that these mechanisms cause a magnet to quench.

2.5.2 Strain-Related Quench

The performance of the superconductor Nb_3Sn depends on the strain on the superconducting phase. The intrinsic strain moves the lattice from a optimum position for superconductivity, leading to a decrease in I_c. This is an important design consideration for the design of superconducting magnets. Strain builds up in the strand due to the different thermal contraction factors of the wire materials. During the excitation of the magnet, the electromagnetic

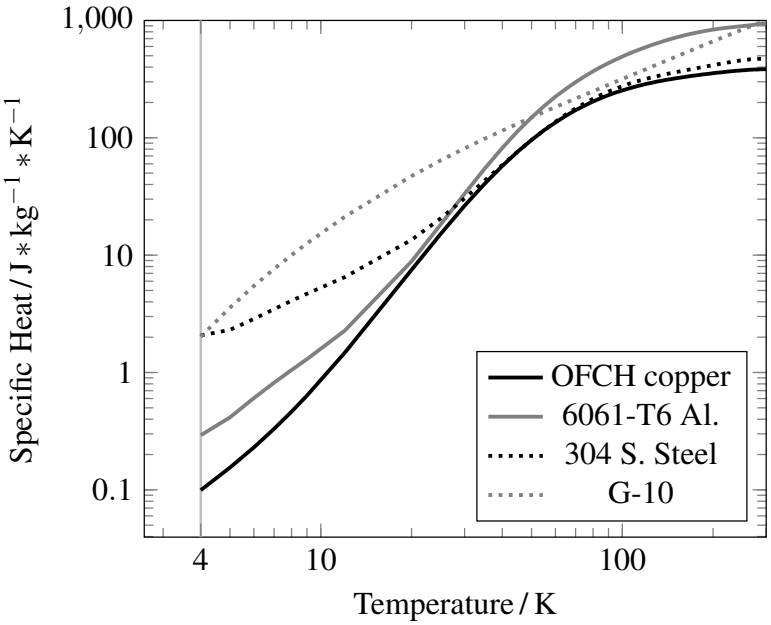

Figure 2.18: Specific heat of materials[23]

forces are acting on the conductor. In certain locations of the coils, these forces are added up and decrease the I_c. If these regions are also submitted to a high magnetic field, the over-straining can lead to a quench. Limitations of this sort cannot be overcome normally with a continuous training of the magnet[24].

2.5.3 Short circuit

A short circuit in the coils could cause that the current travels from turn to turn or in the mechanical structure. The former is called an inter-turn short, while the latter is known as a short to ground. The inter-turn insulation is required to withstand the thermal treatment of the coil. It can not be placed after the thermal reaction. Therefore heat resistive materials like glass-fibre are used. The insulation between the coil and the structure can be placed after the thermal treatment of the coil. Therefore, heat sensitive materials like Kapton® and G10/11 can be used. They can either be impregnated with the coil directly or placed around the impregnated coil.

3 Material Characteristics

3.1 Material Properties

All of the Nb_3Sn-based coils in the three different magnets use similar materials to form the coils and the mechanical structure. For the DS11T and the SMC-11T, the insulation scheme of the cable and the used Nb_3Sn wire differ from the MQXF. In this section, the properties of the individual materials of the coils and the mechanical structure will be discussed.

3.1.1 Wire

At the current stage of the three magnet projects, the only strand used is made by RRP. For this reason, the PIT wire will not be taken into account. Furthermore, a potential influence on the mechanical properties of the texture and size of the wire will be neglected. The material data for single wires is scarce; therefore, this thesis will only use the data presented in *Elastic Anisotropy in Multifilament Nb3Sn Superconducting Wires* by C. Scheuerlein et al. [25]. Using the technique of the rule of mixture (Voigt and Reuss), the grain orientation and the single crystal elastic constant of Nb_3Sn has been taken into account. Furthermore, tensile tests had been carried out on the composite wire. The moduli of elasticity (E_a) of the entire composite wire determined the engineering stress-strain curve under a decreasing load. The calculated value for the polycrystalline Nb_3Sn in the RRP wire #7419[1] is $E_{axial} = 140$GPa and $E_{trans} = 129$ and, at 4.2K, $E_{axial} = 127$ and $E_{trans} = 104$. The result of the tensile tests, which have only been performed at room temperature, is $E_{axial} = 124 \pm 1.7$. Tensile tests have not been carried out at 4.2K. In a different experiment, it was found that the non-copper E-modulus of a PIT wire decreased by 30% after the wire was cooled down to 4.2K [26]. The reason for the difference between the calculated value and the measured value might result from the porosity of the Nb_3Sn, the not well-connected grains, and the uncertainty relating to the individual material data.

Poisson's ratio of Nb_3Sn wires was measured by A. Nyilas[2] and K. P. Weiss[3]. These measurements were carried out on different Nb_3Sn wires. It was found that Poisson's ratio depends on the temperature. Values between

[1] Wire diameter of 0.537mm and with 54 filaments
[2] Cryogenic Engineering & Materials Expertise, CEME 76249 Stutensee, Germany
[3] Forschungszentrum Karlsruhe, Institute for Technical Physics, 76344 Eggenstein-Leopoldshafen, Germany

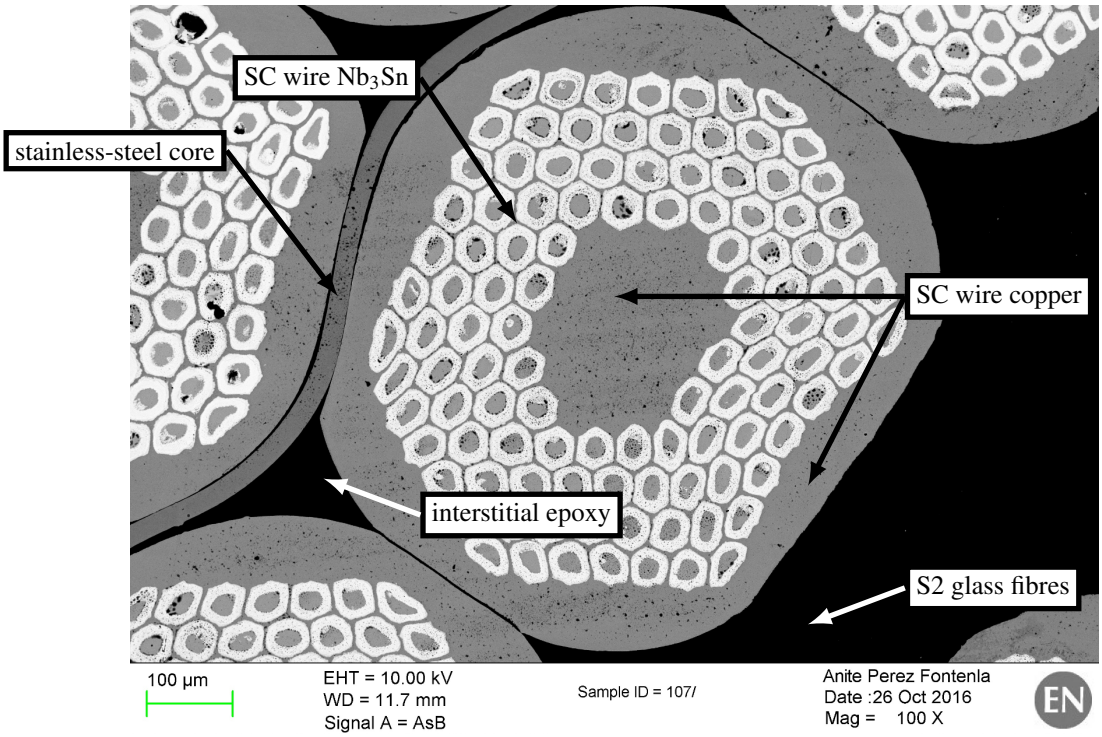

Figure 3.1: 108/127 OST-RRP strand in a cable used for the DS11T. The non-conductive materials are not visible and the surface was gold-coated

Table 3.1: Material data of the Nb_3Sn composite wire

E_{axial} / GPa	$E_{transversal}$ / GPa	Poisson's Ratio	Secant Coefficient of Thermal Expansion
124(295K) / 112(4.2K)	114(295K) / 92(4.2K)	0.35	$1.031e^{-5}$

0.31 and 0.39 where measured at room temperature; at 7K, the values ranged from 0.39 to 0.26 [27]. This shows that Poisson's ratio is highly dependent on the type of cable used. Currently, no measurements are available for the cable that is used in the magnets that are the subject of this thesis. Therefore, 0.35 will be used as Poisson's ratio for the wire composite.

For this thesis, one set of material parameters needs to be fixed. Therefore, the measured modulus of the RRP wire [25] will be used: $E_{axial} = 124$. For the elasticity at 4.2K, the relative reduction from the calculated value (from the rule of mixture) will be taken (4.2K, 9.3%). The transversal elasticity will also be reduced by the relative values from the calculated value (RT, 7.8%; 4.2K, 25.7%).

In 2014, the thermal contraction of Nb_3Sn wires and Nb_3Sn cables was measured by Glyn Kirby and Vladimir Ivanovich Datskov at CERN. Their work has not been published yet. It was found that the secant coefficient of thermal expansion is $1.031e^{-5}$ for the full cable and $1.013e^{-5}$ for single wires, ranging between a temperature range of 295 to 10K. Both values are only available in the axial direction. For the analysis presented in this thesis, the value for the full cable will be used in all three dimensions, knowing that, in reality, the thermal contraction might be orthotropic.

During the heat treatment, to form the Nb_3Sn phase in the wire, the copper stabilizer is fully annealing. This results in a very soft copper matrix after the reaction, which shows strong plastification even at very low levels of stress [28]. Unfortunately, the characteristics of this behaviour were not dealt with in previous publications. This material behaviour will be later discussed in subsection 3.3.1.

All material data used for the composite wire is shown in Table 3.1. This will be used for the finite element analysis (FEA) to represent the cable.

3.1.2 Insulation

In this section, all the insulating materials will be presented. The cable insulation will be covered in a single paragraph. The insulation can be divided into the impregnated and the "external" insulation. The inter-turn insulation of the coils is submitted to the heat treatment and the impregnation process. Currently, the impregnated insulation scheme is not fully analysed in terms of mechanical properties. Therefore, the impregnated materials are summarized under the section entitled "Impregnated Cable Insulation". The external insulation refers to the components that are added after the impregnation of the coils. Like multiple layers of Kapton® foil, which forms the insulation between the coils and the mechanical structure, this is also called the "ground insulation". Blocks made from G10 are used in the MQXF and the SMC-11T to shield the coils from the mechanical structure.

Impregnated Cable Insulation

As shown in subsection 2.1.3, the insulation scheme consists of three components: the CTD-101K epoxy, the S2 glass fibre, and the mica sheet for the 11T cable. This section will present the single material parameters and the resulting properties for the insulation composite. The mica sheet is part of the impregnated insulation. The pure phlogopite flake has an E-modulus of 150 ± 30GPa. The large range is because phlogopite is a natural occurring material.

G10

G10 is a lightweight insulation material. It is made of glass fabric impregnated with an epoxy resin. It is created by stacking multiple layers of glass cloth, which are impregnated under compression with an epoxy resin. It is used because of its high strength and excellent electrical insulating properties. For cryogenic application, it is preferred because of its beneficial thermal expansion. On account of its layered structure, G10 shows high orthotropic behaviour with regard to the modulus and the thermal contraction factor.

Table 3.2: Material data of the **Insulation**

Component	Young's Modulus / GPa	Yield Strength / MPa	Shear Strength / MPa	Secant Coefficient of Thermal Expansion
CTD-101K + S2 glass	12.9(295K) / 19.7(4K)	compression 790(295K) / 1260(4K)	108(77K) / 120(4K)	$6.5e^{-6}$
S2 glass fibre	86.9(295K)	4890(295K) / 2400(825K)		$2.8e^{-6}$
E glass fibre	72.3(295K)	3445(295K)		$5.4e^{-6}$
Mica sheet Firox	<35(295K)	>60(295K)		
CTD101K	4(295K) / 6.5(4K)			$4.14e^{-05}$
Phlogopite flake	150 ± 30(295K)			

Values for CTD-101K + S2 glass are with 50% V_f satin weave S2 glass fibre [29]
Data for mica sheet Firox 63P24A supplied by the manufacturer
Data for the fibres taken from [30]
Values for the pure CTD101K published in [31] and [32]; the modulus at 4K is extrapolated from [33]
Thermal contraction of the resin composite materials measured by Glyn Kirby and Vladimir Ivanovich Datskov at CERN

Table 3.3: Material data of **G10**

G10 Direction	Young's Modulus / GPa	Yield Strength / MPa	Poisson's Ratio	Secant Coefficient of Thermal Expansion
normal	10(295K) / 10(4.2K)	350(295K)	0.3	$2.44e^{-5}$
layer	30(295K) / 30(4.2K)	350(295K)	0.3	$8.39e^{-6}$

Values from [34]

Kapton®

Kapton® possesses a unique combination of properties that make it ideal for a variety of applications in many different industries. The key ability is that Kapton® keeps its properties over a large spectrum of temperature values. Kapton® is synthesized by polymerizing an aromatic dianhydride and an aromatic diamine [35]. The main reason for using Kapton® in cryogenic applications is its excellent electrical insulation, without degradation at cryogenic temperatures.

Table 3.4: Material data of **Kapton®**

Young's Modulus / GPa	Yield Strength / MPa	Poisson's Ratio	Secant Coefficient of Thermal Expansion
2.5(295K) / 8.96(4.2K)	207(295K) / 346(4.2K)	0.34(295K)	$1.51e^{-5}$

Thermal expansion measured by Glyn Kirby and Vladimir Ivanovich Datskov at CERN
Values at cryogenic temperature from [36]
Values at room temperature from [35]

3.1.3 Metals

Austenitic Steels

For the construction of the magnets, two types of austenitic steel are used: the common-grade 316L (1.4435 / X2CrNiMo18-14-3) and YUS-130 (X8CrMnNiN19-11-6). YUS-130 is only used for the collars of the DS11T. It has been specifically developed for the collars of the MB dipoles by Nippon Steel Corporation. It has a low

magnetic permeability and high strength, which is obtained by an adequate balance of manganese and nickel content [37]. The magnetic permeability μ_r must be below 1.003 and for $H \geq 4$ 8x10A/m at 1.9K, the yield strength ($R_{p0.2}$) needs to be between 400–500MPa. The 316L grade is used for the other components of the magnets that do not require these high specifications. Like the shell, rivets are used for holding the collar packs together or for the collaring shoe. The used material properties are shown in Table 3.5.

Table 3.5: Material data of the **austenitic steel**

Type	Young's Modulus / GPa	Yield Strength / MPa	Poisson's Ratio	Secant Coefficient of Thermal Expansion
YUS-130	190(295K) / 202(4.2K)	415(295K) / 1360(4.2K)	0.3	$8.93e^{-6}$
316L	193(295K) / 210(4.2K)	324(295K) / 1360(4.2K)	0.3	$9.97e^{-6}$

Values for YUS-130 taken from [37]
316L values taken from [34]

Aluminium

Aluminium alloys are mainly used because of their different thermal contraction compared to steel. In the magnets based on the bladder and key concept, the shell is manufactured from aluminium. While cooling down, the shell shrinks more than the other bodies, thus creating additional pre-compression. In addition, the very low magnetic permeability of the aluminium is also beneficial for use. The shells of the MQXF and the SMC-11T are made from Al-6061. The collars of the MQXF are made from Al-6082.

Table 3.6: Material data of the **aluminium**

Type	Young's Modulus / GPa	Yield Strength / MPa	Poisson's Ratio	Secant Coefficient of Thermal Expansion
Aluminium-6061	70(295K) / 79(4.2K)	340(295K)	0.3	$1.44e^{-5}$
Aluminium-6082	70(295K) / 79(4.2K)	320(295K) / 450(4.2K)	0.3	$1.44e^{-5}$

Values from [34]

Low-carbon Magnetic Steel

For the magnetic yoke of the magnets, a special type of steel is used. The yoke of the magnet provides the return path for the magnetic flux and contributes to the mechanical rigidity for the superconducting magnets. Over 6,700,000 units of 6mm-thick sheets, called laminations, were produced for the construction of the LHC. The steel is best known under its trade name MAGNETIL^{TM}[4]. The steel has a density of $7858 kg/dm^3$ at 24.5C. The integrated thermal contraction between 295K and 11.5K is $2.1 * 10^{-3}$ [37]. The data from tensile tests is shown in Table A.1. For this thesis, the material parameters shown in Table 3.7 will be used.

Table 3.7: Material data of the **Magnetil**

Young's Modulus / GPa	Yield Strength / MPa	Poisson's Ratio	Secant Coefficient of Thermal Expansion
205(295K) / 210(4.2K)	115(295K) / 820(4.2K)	0.3	$7.22e^{-6}$

Values taken from [37]

[4] Patent EP 0 681 031 A1-B1 "Procédé de production d'acier doux".

Titanium

In all three magnets, the titanium alloy Ti-6Al-4V is used. It serves as the pole pieces of the coils, mainly due to its preferable thermal contraction but also for its high tensile strength. The material properties are presented in Table 3.8.

Table 3.8: Material data of the **titanium alloy Ti-6Al-4V**

Young's Modulus / GPa	Yield Strength / MPa	Poisson's Ratio	Secant Coefficient of Thermal Expansion
115(295K) / 125(4.2K)	868(295K)	0.33	$5.8459e^{-6}$

Values for Young's modulus and thermal contraction taken from [34], yield strength from [28], and Poisson's ratio from [38]

ODS Copper

Oxide dispersion-strengthened copper (ODS copper) is produced by the simple mechanical mixing of copper and oxide powders. Compared to "normal" copper alloys, it retains the typical properties of copper—high strength, high thermal conductivity, and high electrical conductivity after exposure to elevated temperatures. ODS copper has excellent resistance to softening after exposure to high temperatures close to the melting point of pure copper. The aluminium oxide particles in the copper matrix are stable at these temperatures, and retain their original size and spacing. These particles block dislocation and grain-boundary motion, thus preventing recrystallization, which is normally allocated with softening.

The wedges used in the coil are made from ODS copper to prevent the softening of these parts during the heat treatment of the coils. The ODS copper used for the manufacturing of the wedges is found under the trade name *Glidcop*. The material data used in this analysis is presented in Table 3.9.

Table 3.9: Material data of the **ODS copper** *Glidcop*

Young's Modulus / GPa	Yield Strength / MPa	Poisson's Ratio	Secant Coefficient of Thermal Expansion
88(295K) / 95(4.2K)	332	0.33	$1.114e^{-5}$

Values for Young's modulus and yield strength at room temperature taken from [28] and thermal contraction from [34]. The Young's modulus at 4.2K is assumed

Copper Stabilizer of the Wire

The stabilizer for the Nb_3Sn filaments is made from pure copper, which anneals during the heat treatment of the coils. It loses most of its strength; therefore, it cannot carry high loads after the annealing [26]. Owing to the plastification even at low levels of stress, this effect cannot be neglected for the analysis in this thesis. In Figure 3.2, the stress-strain curve of a pure copper wire is shown, before and after the heat treatment. It illustrates the reduction of strength and the yielding at very low levels of stress of the annealed copper wire. Only tensile tests were performed. The behaviour in pure compression is not known but is assumed to be similar to that in tension. In [28], a tensile test has been performed on pure copper wires. In Table 3.10, the results are shown for the cold-worked and annealed wire.

Table 3.10: Material data of the **copper stabilizer**

	Young's Modulus / GPa	Yield Strength / MPa	Tensile Strength / MPa
Cold-worked copper wire	127 ± 0.8	397 ± 15	427 ± 5.9
Annealed copper wire	108 ± 2.1	46.2 ± 2.6	204 ± 1.6

Data published in [28]

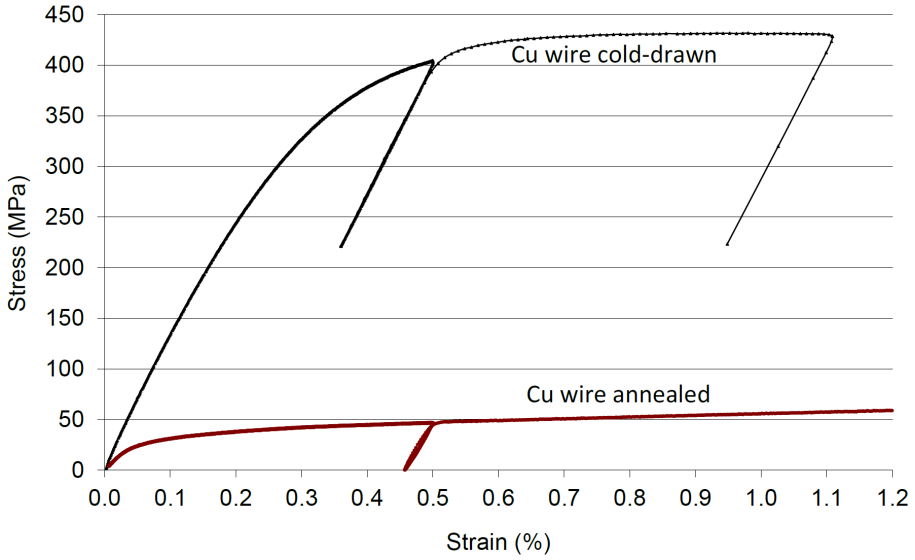

Figure 3.2: Stress-strain curves of copper wire cold-drawn and after subsequent 695C ° heat treatment, published in [28]

3.2 Theoretical Stiffness of the Coils

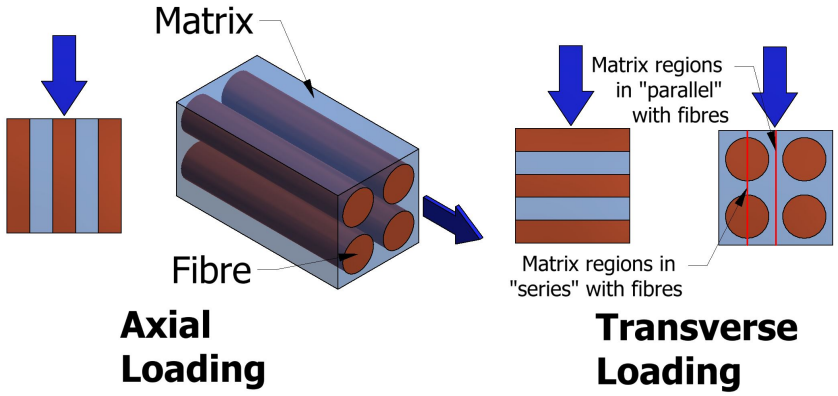

Figure 3.3: Loading direction composite, axial loading: Voigt model; transverse loading: Reuss model

A theoretical approach to determine the influence of the single components of the conductor matrix is the rule of mixtures. It is a weighted mean and can be used to determine the mechanical properties of a composite, based on the knowledge of the mechanical properties of the single components. There are two models for composites with long fibres, one for axial loading, along the fibre, (Voigt model) [39], and one for transverse loading (Reuss model) [40]. When the fibre strain is equal to the matrix strain, the Voigt model is applicable. If the fibre stress is equal to the matrix stress, the Reuss model is applicable. The main direction of the mechanical load in the magnets is in the transverse direction; therefore, the Reuss model will be applied for the conductor-insulation composite. For applying the rule of mixtures, a number of assumptions must be made: Fibres are uniformly distributed throughout the matrix, there is perfect bonding between the matrix and the fibres, and the matrix is free of voids. The modulus of the coil is detrimental for controlling the stress in the conductor during assembly and excitation. In the series production of the magnets for the accelerator, no mechanical instrumentation will be available to measure the strain on the structural components. This can only be done if the stiffness of the coils is well known, since both the DS11T and the MQXF rely on a displacement-driven pre-loading of the coils. For the following, the fibre/cable is considered to be homogeneous in the axial direction, along the fibre/cable. The effect of the woven fibre/cable cannot be determined with the methods used.

The theoretical modulus of a two-component composite (E_c) can be calculated with Equation 3.2.1, where E_f is the elastic modulus of the fibre and E_m is the elastic modulus of the matrix.

Table 3.11: Elastic modulus and volume fractions of the coils—calculated modulus

	Strand	Core	Inter. Epoxy	Phlogopite	E Glass +Epoxy	S2 Glass +Epoxy	Wedges	Pole		
Modulus/GPa	114	195	4	150	12.9	12.9	88	115		
Coil Fractions/%									**Coil Stiff./GPa** trans.	axial.
DS11T	48.63	0.92	8.69	1.54	4.61	10.11	25.51	0	**25**	**84**
MQXF	42.08	0.54	6.25	0	0	18.5	7.91	24.71	**27**	**87**
SMC-11T	38.05	0.72	6.8	1.2	3.6	8.3	0	41.33	**30**	**96**

Values extracted from the CAD models of the coils in combination with the cable data from Table 2.2 and Table 2.3.

$$E_c = fE_f + (1-1f)E_m \tag{3.2.1}$$

where, in Equation 3.2.1 f, the volume fraction of the fibre is:

$$f = \frac{V_f}{V_f + V_m} \tag{3.2.2}$$

For applying the rule of mixtures in the transverse loading case (perpendicular to the cable surface) on multiple components of the composite, the following formula, based on the work of Reuss, needs to be applied, using the fractions from all materials. This assumes that all materials are in a series to the loading direction, as shown in Figure 3.3.

$$E_{trans} = \left[\sum_{n=1}^{n}\left(\frac{f_n}{E_n}\right)\right]^{-1} \tag{3.2.3}$$

For the axial-loading case, the formula from Voigt needs to be applied:

$$E_{axial} = \sum_{n=1}^{n}(E_n * f_n) \tag{3.2.4}$$

To calculate the theoretical coil stiffness, the elastic moduli from section 3.1 are used. In Table 3.11, the fractions of the material are shown with the used moduli. With the use of Equation 3.2.3, the resulting modulus can be calculated, as is also shown in Table 3.11. This method assumes that all materials are under the same stress. This would only be possible if all materials are layered perpendicular to the loading direction. This case is unlikely and it is assumed that the contribution of the interstitial epoxy is negligible. The interstitial epoxy is surrounded by the composite wire, which is 28 times stiffer than the pure epoxy. Under the assumption that no relative movement between the wire and the epoxy takes place, the same strain is encountered by both components. Owing to the different degrees of stiffness, barely no load is carried by the epoxy. Therefore, it might not be considered for the calculation of the stiffness of the coils. This is shown in Table 3.12, where the interstitial epoxy was removed for the calculation.

Conclusion on the theoretical coil stiffness Using the available material properties, the theoretical stiffness of the coils can be calculated. This was done for two extreme cases: for all materials in the parallel or axial direction, using the formalism of Voigt, and for all materials in a series or transverse direction, using the formalism of Reuss. The results in the axial direction are dominated by the materials with a high modulus. In the transverse direction, the materials with a low modulus determine the stiffness of the coils. The transverse case neglects the contribution of the regions that are "parallel" to each other. The actual contribution of the interstitial cannot be determined with this method. The results need to be handled carefully. The transverse stiffness varies by a factor of two whether the interstitial epoxy is considered or not. This case might be more realistic.

Table 3.12: Elastic modulus and volume fractions of the coils—calculated modulus without the interstitial epoxy

	Strand	Core	Phlogopite	E-Glass +Epoxy	S2 Glass +Epoxy	Wedges	Pole		
Modulus/GPa	114	195	150	12.9	12.9	88	115		
Coil Fractions/%								**Coil Stiff./GPa** trans.	axial.
DS11T	53.26	1.01	1.68	5.04	11.07	27.93	0	**49**	**92**
MQXF	44.89	0.58	0	0	19.73	8.44	26.36	**44**	**93**
SMC-11T	40.82	0.77	1.29	3.87	8.91	0	44.34	**57**	**102**

Values extracted from the CAD models of the coils in combination with the cable data from Table 2.2 and Table 2.3.

3.3 Conductor-Insulation Composite

3.3.1 Material Tests on Composite Cable Stacks

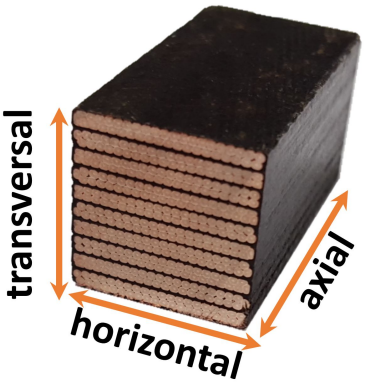

Figure 3.4: Dimensions of the 10-stack used for the compression tests performed at CERN in September 2015

To determine the material characteristics of the impregnated cable composite, compression tests have been performed in the past. These tests mainly focused on measuring the stiffness of the cable composite. This was done because the stiffness has the largest impact on the mechanical behaviour of the coils in the final magnet. Other mechanical tests—like tension or three-point bending tests—on the cable composite have not been conducted. In Table 3.13, the results from previous publications are summarized. This information needs to be handled with caution since the specimens were never identical. They differ in cable type and geometry, size, and the used epoxy. For this thesis, the latest results from 10-stack measurements employing the DS11T cable configuration will be used to obtain the material data. The samples were produced to be as representative of the DS11T coils as possible. The keystoned cables were placed to alternate the keystone position in order to obtain a square block. This test campaign was carried out in September 2015.

Table 3.13: 10-stack measurements from literature

	Loading Type, all values in *GPa*			
	monotonic		**cyclic**	
D. R. Chichili [41]	18(300K)	26(4.2K)	39(300K)	40(4.2K)
M. Reytier [42]			33(293K)	45(4.2K)
R. Bossert [43]	17(293K)		37(293K)	
D. Dell Orco [44]	38(293K) & 43(77K) *Loading Type not specified*			

Values obtained only for compression

In Figure 3.4.2, the dimensions of the used 10-stack are shown. The compression tests involved monotonic and cyclic loading up to 200MPa in the *azimuthal* or *transverse* direction. This has been done at 293K and 77K. The results will not be presented in further detail and the discussion will focus on two samples. In Figure 3.5, the stress-strain curve of two samples is shown with the same loading parameters but at different temperatures. Three cycles have been performed at 50, 100, and 150MPa. Overall, the behaviour of the samples is in line with the

Table 3.14: 10-stack measurements on the DS11T cable, carried out in September 2015

	Loading Type, all values in *GPa*			
	monotonic loading		cyclic loading	
	Up Slope	**Down Slope**	**Lin. Modulus**	**Sec. Modulus**
Average	9.60	26.68	19.85	19.37
STDEV $(\mathbf{1}\sigma)$	0.15	6.32	0.99	1.91

Four samples have been used for the monotonic loading to 50, 100, 150, and 200MPa. For the cyclic loading, five samples have been used with three cycles to 50,100 and 150MPa.

previous results stated in Table 3.13. The first loading always exhibits a lower stiffness than the unloading. All loadings to the same stress level have a similar high stiffness. In the stress-strain curve, non-linear behaviour is seen up to 25MPa, followed by linear behaviour to 125MPa. Beyond 150MPa, the behaviour is again non-linear. The dependency of the load cycle and the previous applied loads is distinct. In general, the initial loading curve is less steep than the subsequent loadings by a factor of two. The stiffness of the sample remains high even after removing the entire load. It has been observed that the sample experiences a reduction in height of roughly 1%, after a compression to 150MPa. This has an important implication for the coils since some of the mechanical pre-load systems are purely displacement-driven.

In Table 3.14, the measured values for the samples are shown. There were no significant differences between the tests done at room temperature and at 77K. A permanent deformation of the test samples in the compression region was observed. After loading the samples to 150MPa, the height was reduced by $0.25 \pm 0.1\%$.

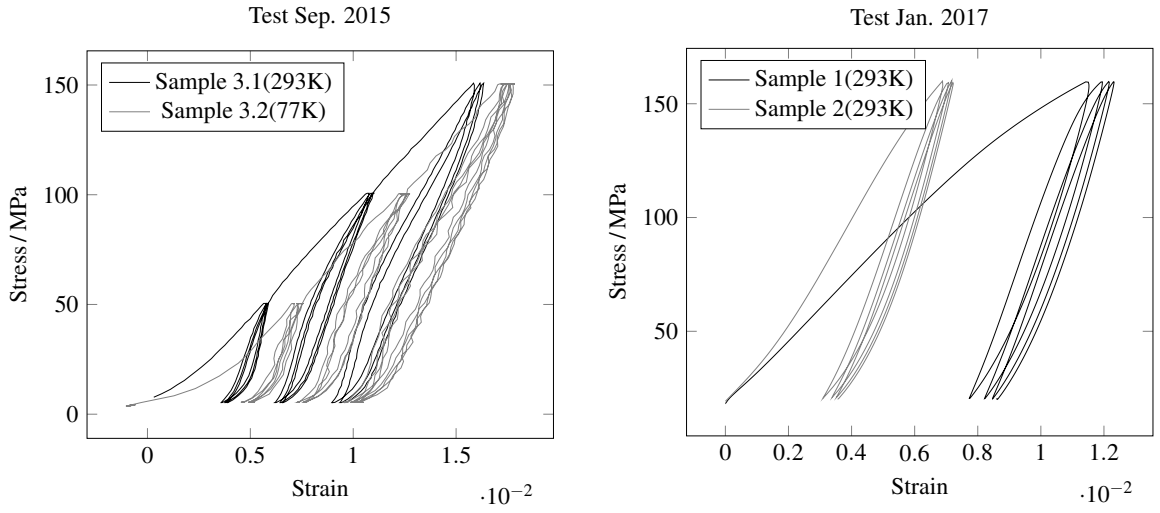

Figure 3.5: 10-stack compression test

In a test carried out in January 2017, the same behaviour of the 10-stack was observed. But the stiffness of the samples changed by roughly a factor of two. For the first compression, a value of 20GPa was measured for the cyclic loading of 40GPa. It is assumed that the tooling for the first test was not sufficiently calibrated. The new values are more in line with the measured values from the literature (see Table 3.13). Owing to a more precise calibration and more effort spent on the design of the measurement equipment, it was decided to use these new values for the analysis in this thesis (see Table 3.15). At the time of compiling this thesis, the results were under analysis; therefore, no statistical values can be shown. A larger fluctuation than in the previous test is not expected.

Table 3.15: 10-stack measurements on the DS11T cable, carried out in January 2017

	Loading Type, all values in *GPa*			
	monotonic loading		cyclic loading	
	Up Slope	**Down Slope**	**Lin. Modulus**	**Sec. Modulus**
Average	21	46	42	39

Table 3.16: Elastic modulus and volume fractions of the 10-stack—calculated modulus

	Strand	Core	Inter. Epoxy	Phlogopite	E-Glass +Epoxy	S2 Glass +Epoxy		
Modulus/GPa	114	195	4	150	12.9	12.9		
10-Stack Fractions / %							**10-Stack Stiff. / GPa**	
							trans.	axial.
11T	69.46	1.32	12.41	2.19	6.58	8.04	**20.6**	**87.5**
MQXF	78.92	1.02	11.72	0	0	8.33	**23.4**	**93.5**
10-Stack Fractions / %, no interstitial epoxy								
11T	79.3	1.5	0	2.5	7.51	9.18	**49.6**	**99.25**
MQXF	89.41	1.15	0	0	0	9.44	**65.7**	**105.4**

Values extracted from the CAD models of the coils in combination with the cable data from Table 2.2 and Table 2.3.

3.3.2 Theoretical Stiffness of the 10-Stack

The rule of mixture (see section 3.2) can be applied to determine the expected stiffness of the 10-stack. For this, the ratios of the single materials of the cable are used in combination with the material properties shown in section 3.1. In Table 3.16, the ratios with the used material properties are shown. These values were determined using the same technique as in section 3.2 used for the coils. The values for the stiffness were obtained by using the rule of mixtures for the transverse direction.

Following the same method as in section 3.2, the theoretical stiffness of the 10-stack was calculated. Here, two cases were studied—one with the contribution of the interstitial epoxy and one without. The results are shown in Table 3.16. In both cases, the 10-stack made from the MQXF cable is stiffer. This is due to the higher fraction of conductor compared to the 11T cable. The effect of removing the interstitial epoxy is larger for the 10-stack than for the full coil. The difference in stiffness is bigger for the MQXF case by a factor of 2.8. Some of the material parameters are not well known and are based on sophisticated assumptions or have a large scatter. For a better understanding about the sensitivity of the 10-stack modulus to the variations in the material properties, the elastic modulus was varied for the single materials. In Figure 3.6, the response to different elastic moduli is shown, with the linear fitted gradients displayed in the legend of the graphs. The base value for the modulus is the same as in the previous calculations. This value was varied by $\pm 50\%$. For the case without the interstitial epoxy, the biggest influence on the stiffness has the strand and the two glass-epoxy moduli. With the interstitial epoxy considered the main driving factor, for the overall stiffness, is the interstitial epoxy itself.

Conclusion on the stiffness of the 10-stack The values obtained with the analytical model depend significantly on whether the interstitial epoxy is considered or not. The experimental results are between the two calculated extreme scenarios. The analytical model cannot precisely predict the stiffness of the 10-stack without further knowledge of the ratios between the regions in "series" or "parallel" with the fibres or cable. The baseline for this thesis will be the values obtained in the transversal direction, for the first loading a modulus of **20GPa**, and for consecutive loadings **40GPa**.

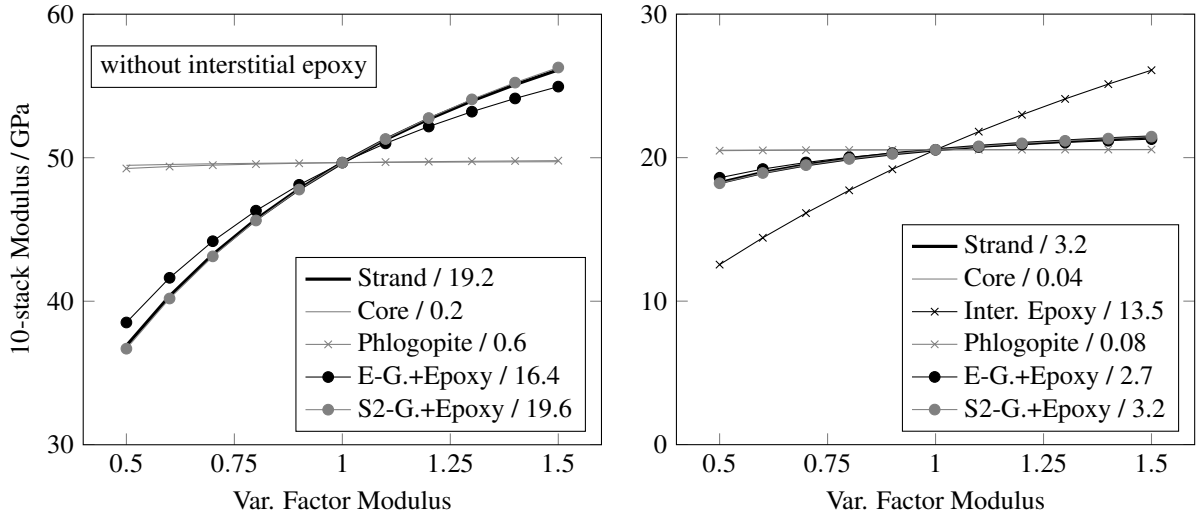

Figure 3.6: 10-stack modulus as a variation of the material modulus

3.4 Finite Element Analysis of the 10-Stack

Recreating the measured non-linear behaviour and the correct stiffness in a finite element (FE) model is an important step to validate the assumptions for the coil geometry. The validation of the FE model will be done by comparing the results from the material test in section 3.3 with the results obtained by the FE model using the material properties from section 3.1. To analyse the effect of the geometry and the detail of the model, three simulations will be performed with different degrees of detail. The different geometries will be called M1, M2, & M3, with an increasing level of detail. For the modelling of the 2D 10-stack, the PLANE183 shell element was used in the Tri6 or Quad8 option. The minimum size of the element is 11μm while 57μm is the maximum. The model M3 consists of three types of bodies: a simplified conductor, a fibre-saturated region, and pure epoxy resin in-between the strands. For the conductor, a single smeared material property will be assumed. For M2, two bodies will be used: one conductor model, which will be a square representing all of the 40 strands, with the same area than the strands in the model M3, and a fibre-saturated region. The model M1 will be one body with one smeared material property representing the full conductor-insulation composite. For the simulation of full coils, the degree of detail of the cable needs to be adapted. The results from the 10-stack simulation should give a clearer understanding on the influence of the different degrees of detail.

3.4.1 Hardening Behaviour of the Coil Composite

In most cases, the hardening behaviour of a material can be neglected for the analysis of a structural problem since hardening or yielding will only take place at stress levels that are above the normal usage. But for the Nb_3Sn coil composite, this cannot be ignored. In Figure 3.5, the hysteric behaviour during the compression test of the 10-stack is reported. This hardening behaviour starts at stresses below 20MPa. The coils are subjected to stresses beyond 100MPa during the assembly and excitation. Furthermore, permanent plastic deformation was observed in the compression direction during the compression tests in subsection 3.3.1. To determine the correct stress levels in the coils, these two phenomena cannot be neglected. It is assumed that all non-linear effects will be caused by the copper content of the composite wire. The copper is assumed to be fully annealed after the thermal treatment. Currently, not enough measurements have been carried out to quantify the hardening under compression. Therefore, the material properties used in the FEA will be adapted to represent the measured values from the 10-stack in subsection 3.3.1. The hardening of the cable composite will be assumed to be purely kinematic.

3.4.2 10-Stack FE models

The three FE models will be used to validate the modulus measurements carried out on the 10-stack from subsection 3.3.1. For the simulation of the full magnets, it is important to understand what effect the different simplifications have in terms of geometry. All FE models are made in the same way, only varying by the material properties and the internal geometry of the 10-stack. The directional designation from will be used. In the transverse and horizontal directions, the 10-stack values are 14.5mm and 14.9mm, respectively. All models are two-dimensional. The plain

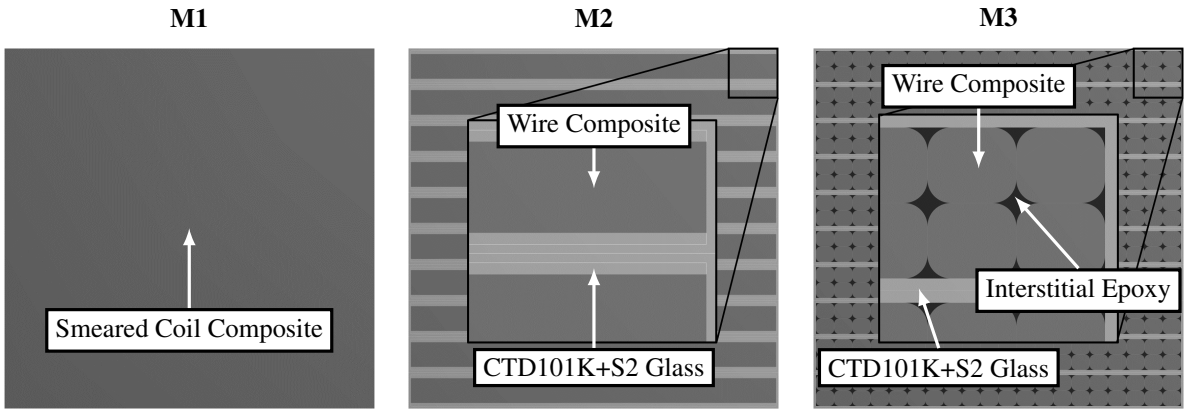

Figure 3.7: 10-stack geometries used in the FEA

Table 3.17: Response from the 10-stack simulations modulus

Modulus / GPa	**M1**	**M2$_{trans.}$**	**M2$_{hor.}$**	**M3$_{trans.}$**	**M3$_{hor.}$**	**M1$_{p.Stress}$**
$E_{tangential}$	24.6	21.6	22.7	21.7	21.5	20.1
$E_{elastic}$	45.6	43.8	85.9	55.4	77.1	40.0

strain condition is assumed, meaning that no strain is exhibited in the axial direction. One surface will be exposed to a pressure of 150MPa. This pressure will be cycled twice to assess the hysterical behaviour of the 10-stack. The applied boundaries are shown in Figure 3.8, including the mesh used for the model M3. The opposite surface will be supported in a frictionless manner and the node on the edge will be fixed to fully constrain the model. The main focus is on the global stiffness of the model in the direction of compression. The material properties for M2 and M3 are taken from Table 3.1 and Table 3.2. The material properties for M1 are set to the modulus of the measured 10-stack. The elastic modulus is $E_e = 40$GPa. To represent the hardening behaviour, the yield limit was set to 2MPa with a tangential modulus of $E_t = 20$GPa. Poisson's ratio is assumed to be 0.35.

For the models M2 and M3, the assumption is that the only component with a hardening behaviour is the wire composite. As mentioned, the hardening behaviour is not fully characterized with material tests. Therefore, the kinematic hardening parameters of the wire composite were adjusted to give for the first compression on the 10-stack in the transverse direction, the response of $E_{tangential} = 20$GPa.

The response from the simulation is shown in Figure 3.9 for the three models in the transverse direction. The calculated modulus from the simulation results in the transverse and horizontal directions is shown in Table 3.17. For the purposes of comparison, the response of the M1 model under plain stress conditions was included. The difference is due to the missing support in the longitudinal direction for the plain stress case. The anisotropy of the models can be explained by the additional support of the cable in the horizontal direction. In the transverse direction, most of the components are in series. Meanwhile, in the horizontal direction, the cable geometry is parallel to the loading direction. Therefore, the stiffer cable dominates the overall stiffness of the 10-stack. For the first compression where the copper is assumed to "stiffen", the difference is not so drastic. This is because the difference in stiffness between cable and epoxy matrix is not large. After the first loading, the 10-stack in the horizontal direction is much stiffer than in the vertical direction. This is because the cable is parallel to the insulation matrix and, therefore, under the same strain conductions. On account of the higher modulus of the cable, more load is taken by it.

For the two loading conditions, the strain and stress in equivalent von Mises, vertical and horizontal, are shown in full FE plots in Figure C.1 to Figure C.4. To provide a better overview, the average, minimum, and maximum stresses on the cable are shown in Table 3.18. For the model M1, the whole area was considered. The model is one isotropic square; therefore, it has no minimum or maximum value. The maximum equivalent stresses occur in the M3 model. This is caused by the complex geometry of the single strands. Also, the anisotropy based on the cable orientation to the loading direction is visible. The horizontal loading causes a higher normal stress in the same direction as the transversal loading. Through the confinement in the longitudinal direction, with the plain strain condition, the equivalent stress is lower than the primary normal stress; for the plain stress condition, the equivalent stress would be the same.

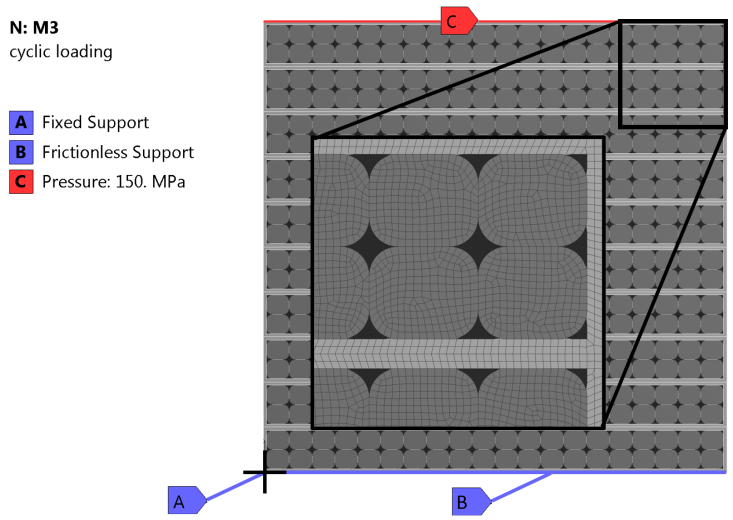

Figure 3.8: Boundaries and mesh of the M3 model for the transverse loading case. For the horizontal loading, the boundaries are applied to the surfaces turned by 90 degrees

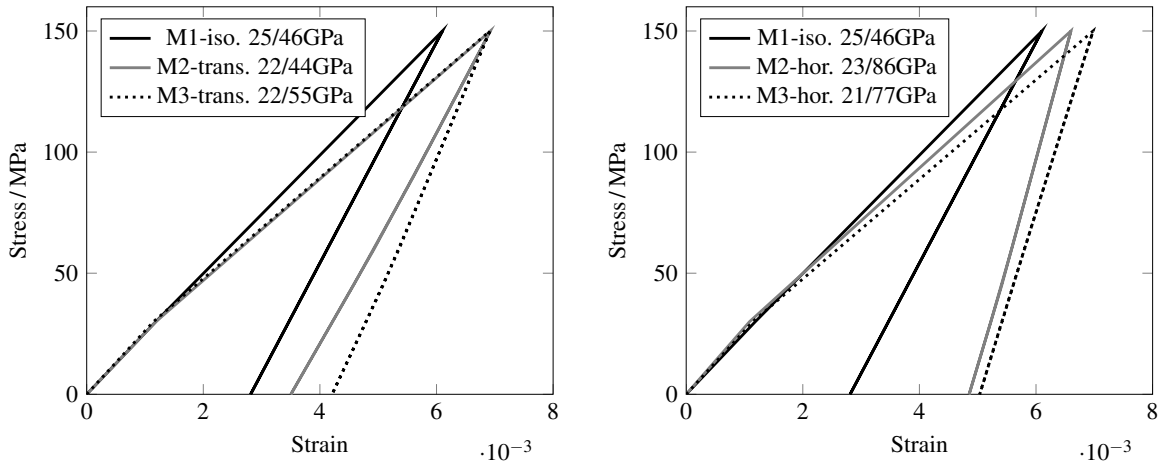

Figure 3.9: Stress-strain curve loading and unloading—response from the 10-stack simulations E_t/E_e

Conclusion on the 10-stack modelling With three different geometries for the 10-stack FE model, it was shown that on using single material properties, the overall stiffness of the 10-stack in the transverse direction is similar to the measured values in subsection 3.3.1. The anisotropy in the M2 and M3 depends on the loading direction compared to the cable orientation. This is currently not confirmed by experimental results, but it will be assumed to be a realistic effect. From the overall stiffness, there seems to be no need to use the refined M3 model for the modelling of the full-magnet cross-section, although the stress levels are different on the cable level.

3.5 Strain Dependency of Nb3Sn

The two important challenges with Nb_3Sn are the brittleness of the material after the thermal reaction and the dependency of the critical current density on the strain on the cable and the lattice [45]. To investigate the strain dependency, the conventional material laws, like von Mises or strain intensity, are not suitable.

In many of the models available in the literature (e.g. [47], [48], [49]), the strain sensitivity of Nb_3Sn is generally parameterized using the strain function $s(\varepsilon)$ [24]. Here, $B_{c2}(\varepsilon, T=0)$ is the superconducting upper critical field, depending on strain and temperature.

$$s(\varepsilon) = \frac{B_{c2}(\varepsilon, T=0)}{B_{c2}(0, T=0)} \tag{3.5.1}$$

In this thesis, the scaling law from Bordini will be applied [46]. This scaling law is based on critical current

Table 3.18: Response from the 10-stack simulations stress and average stress on the cable, with the minimum and maximum values

Stress / MPa	$\mathbf{M1_{trans.}}$	$\mathbf{M1_{hor.}}$	$\mathbf{M2_{trans.}}$	$\mathbf{M2_{hor.}}$	$\mathbf{M3_{trans.}}$	$\mathbf{M3_{hor.}}$
EQV	130	130	132 (130,162)	146 (132,178)	149 (76,169)	155 (76,170)
horizontal	0	-150	2 (-5,11)	-170 (-196,-150)	8 (-83,28)	-170 (-229,-82)
transversal	-150	0	-150 (-188,-146)	-2 (-18,33)	-163 (-225,-74)	8 (-81,30)
longitudinal	-63	-63	-71 (-93,-66)	-82 (-103,-56)	-75 (-148,-28)	-78 (-148,-32)

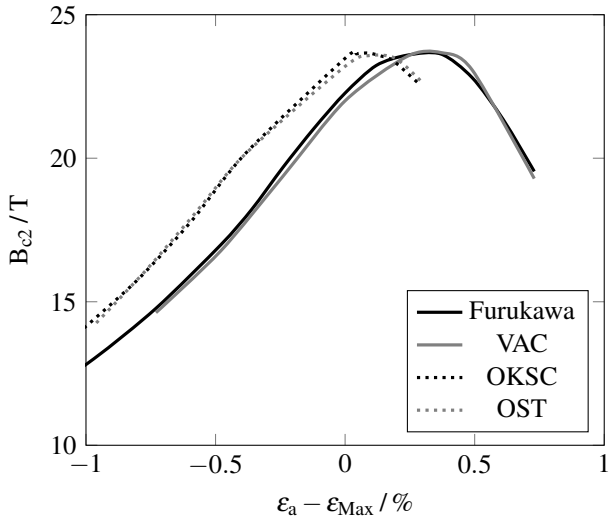

Figure 3.10: B_{c2} values at 4.2K for the Furukawa, VAC, OKSC, and OST strand samples, from [46]

measurements of cable samples under applied axial stress. The measurements of four strand samples are shown in Figure 3.10. The strain function is based on the strain tensors of the superconductor [50]. On the basis of the principal strains $\varepsilon_1, \varepsilon_2, \varepsilon_3$, the two needed invariants can be written as follows:

$$I_1 = \varepsilon_1 + \varepsilon_2 + \varepsilon_3 \tag{3.5.2}$$

$$J_2 = \frac{1}{6}[(\varepsilon_1 - \varepsilon_2)^2 + (\varepsilon_2 - \varepsilon_3)^2 + (\varepsilon_3 - \varepsilon_1)^2] \tag{3.5.3}$$

In the scaling law based on the work of Bordini, when assuming a Poisson ratio equal to 0.36 for the lattice, the proposed strain function is:

$$s(\varepsilon) = \frac{e^{-C_1 \frac{J_2+3}{J_2+1} J_2} + e^{-C_1 \frac{I_1^2+3}{I_1^2+1} I_1^2}}{2} \tag{3.5.4}$$

In this exponential function, the strain dependency is ruled by the hydrostatic and deviatory components of the elastic strain. The parameter C_1 is a fitting parameter that needs to be adapted to the type of strand used.

To calculate the critical current degradation, even the temperature and the magnetic field need to be taken into account. The following is based on [51], where the same calculation was performed for the PIT192 and PIT288 FE models. In this calculation, multiple wire-specific constants are necessary. These constants are currently not available for the RRP wire used for the magnets presented here. Nevertheless, the calculation of the critical current degradation is a useful tool to compare the three magnets with each other.

The $s/(\varepsilon)$ function has already been shown. To calculate the critical temperature $T_c(\varepsilon)$, where T is the temperature of the conductor and w the constant 3:

$$T_c(\varepsilon) = T_c(0) s(\varepsilon)^{1/w}; t = \frac{T}{T_c(\varepsilon)} \tag{3.5.5}$$

Table 3.19: Material data for the FEA of the 108/127 RRP strand

Material	Behaviour	Young's Modulus / GPa	Yield Modulus / MPa	Plastic Tangent Modulus / MPa
Copper	Elasto-Plastic	110	1	1300
Nb_3Sn	Elastic	90		
Bronze	Elastic	110		
Epoxy	Elastic	4		
Epoxy + S2-Glass	Elastic	12.9		

The second critical magnetic field $B_{c2}(T,\varepsilon)$ and the normalized magnetic field b can be calculated by the following, where v is 1.5 and B is the background field.

$$B_{c2}(T,\varepsilon = B_{c2}(0,0s(\varepsilon)(1-t^v);b = \frac{B}{B_{c2}(0,0)} \tag{3.5.6}$$

For the calculation of the pinning force $F_p(T,\varepsilon)$ and $F_p(T,0)$, where p is 0.5 and q is 1.91:

$$F_p(T,\varepsilon) = J_c(T,\varepsilon) \times B = B * s(\varepsilon)(1-t^2)(1-t^{1.52})b^p(1-b)^q \tag{3.5.7}$$

To calculate the critical current degradation of one element i:

$$R_i = \frac{F_p(T,\varepsilon)}{F_p(T,0)} \tag{3.5.8}$$

Finally, to obtain the current degradation of the strand, where A is the surface:

$$\frac{I_c}{I_{c0}} = \sum_{n=1}^{N} A_i R_i / \sum_{n=1}^{N} A_i \tag{3.5.9}$$

This approach is discussed in detail in [51], where a 2D plain strain FE model of a PIT strand, including a surrounding layer of epoxy, was used to validate the FE approach with experimental results. In reality and in the FE model, the strand was compressed to a certain level and the critical current was measured or calculated. This thesis will not go into such detail as regards simulating the single filaments in a full-magnet model. The cable needs to be simplified to one smeared material property, which includes the Nb_3Sn, copper, and bronze. In the following, an FE simulation will be shown using the geometry of an RRP-manufactured strand with the geometry corresponding to a 108/127 type strand.

FE simulation of the strand The simulation consists of one strand cut in the vertical symmetry plane. It is enclosed by epoxy resin—pure epoxy for the bottom half and epoxy with S2 glass on top. In the axial direction, symmetry is assumed and the model is 50μm thick. The bottom surface is fixed in the vertical direction, which means sliding in the horizontal direction is allowed. The pressure is applied on the top surface. Material data is taken from [51], apart from the values for the epoxy and the bronze, which are presented in Table 3.19. The main purpose of the model is to determine if the strain on the full cable is linked to the strain on the Nb_3Sn filaments. More details about the model are shown in Figure 3.11. In the model, all nodes of the mesh are merged. Meanwhile, three layers of elements are used in the longitudinal direction. Therefore, the current degradation due to the principal strains will be calculated for the strain of the filaments and the full cable cross-section.

The first comparison is a function of the pressure applied on the numerical model. The background field is 19T and the temperature 4.2K. The used elements are SOLID186 in 90% Hex8 and 10% Wed6 configuration. The minimum size is 0.6μm and the maximum is 3μm. The current degradation is being calculated using Equation 3.5.9 and the elastic principal strains. The result is shown in Figure 3.12. The largest difference between the full cable and the filaments is at 200MPa. The full cable overestimates the reduction by 13% compared to just the filaments. In the magnet, the background field is generated by the conductor itself, thus operating at much higher current densities. This case would be similar to 12T and 1.9K, where the reduction of the critical current is

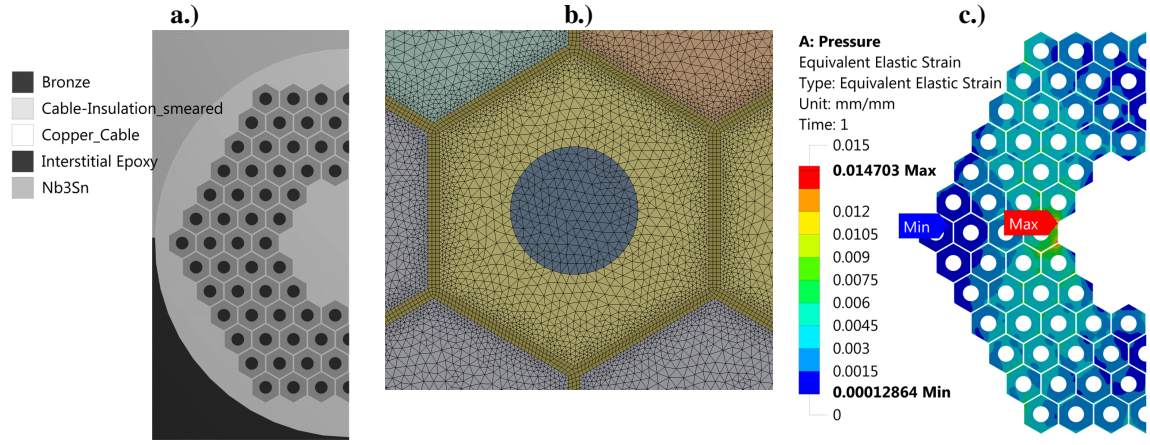

Figure 3.11: a.) Geometry used and the assigned materials b.) Detail of the mesh on the filament c.) Von Mises strain on the filaments under a compression of 150MPa

much less. Also, in this case, the results for the filaments and the strand area are very similar. In Figure B.1, the influence of the background field and the temperature is shown for the same model under 150MPa of compression.

To integrate the scaling law into the analysis of a full-magnet cross-section, where it also would be possible to link the local magnetic field to the conductor degradation, the scaling law needs to be applied on the conductor geometry used in these simulations. As a representative for this, the M2 10-stack model from subsection 3.4.2 with the square cable geometry will be used. In Figure 3.13, left, the comparison between all three 10-stack models is shown at 12T and 1.9K. The models M2 and M3 show similar results, while model M1 shows very different results. This can be explained by the different degrees of stiffness used for the material in the model. Model M1 is one isotropic material with an elastic modulus of 40GPa, while the cable in M2 and M3 has the value 114GPa. On the right in Figure 3.13, the comparison between the Nb_3Sn filaments from the strand model and the M2 10-stack model are shown. The response from the 10-stack model underestimates the current degradation. In the strand model, the degradation is around 25% at 200MPa, while in the 10-stack model it is 13%. Overall, a factor of two is present. In the square cable of the 10-stack, no strain concentration is present due to the abundance of the filament. This effect can be compensated by applying a correction factor of two to the calculation of $s(\varepsilon)$. So, $s_{fac}(\varepsilon) = s(\varepsilon) - 2(1 - s(\varepsilon))$. This is not the most elegant solution, but it delivers comparable results between the 10-stack and the strand model. In Figure 3.13, right, the results of the 10-stack model M2 with the correction factor are shown under *10-stack M2S2*.

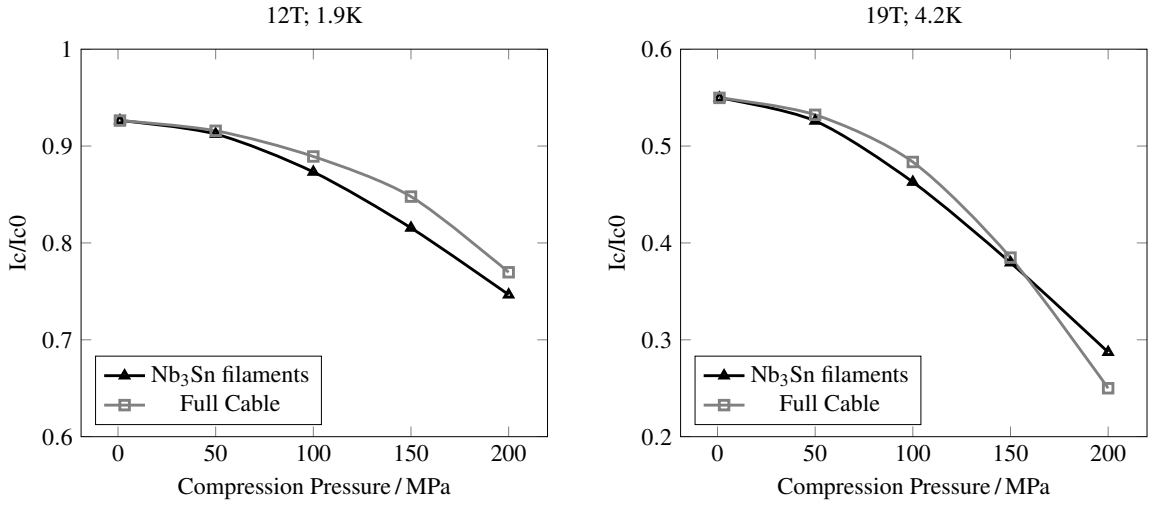

Figure 3.12: Simulation results for 108/127 RRP strand

Conclusion on the strand modelling The application of the scaling law based on the work of Bordini [46] seems to be feasible for the modelling of a full-magnet cross-section. Even though the exact cable parameters that

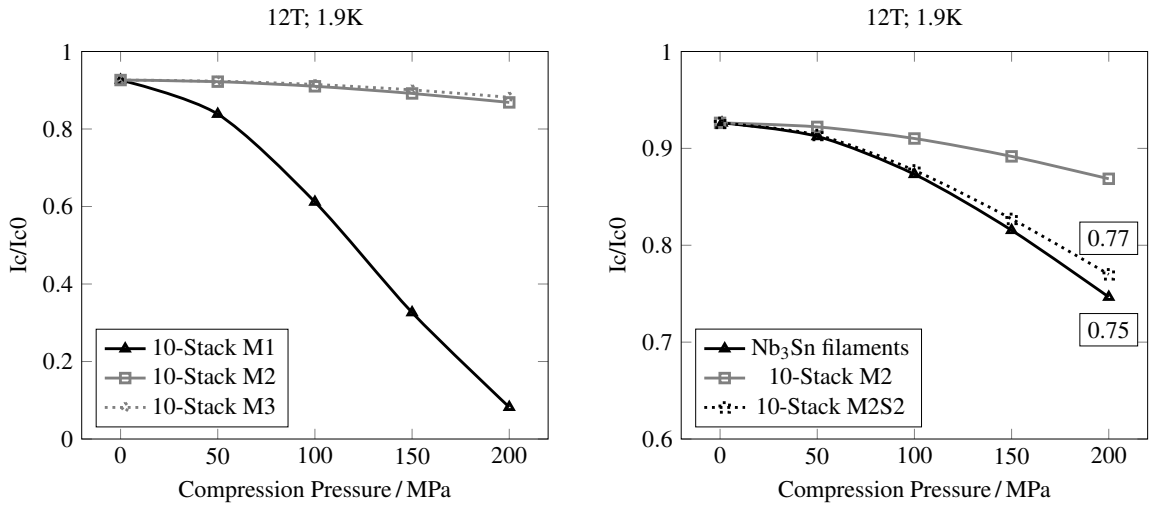

Figure 3.13: Simulation results comparing the three 10-stack models on their critical current reduction response

need to be applied for the calculation are not known at the moment, the scaling law provides a good indication about the performance of the conductor in the mechanical assembly. Obviously, the accuracy of the results is diminished by the used simplification, going from the filament to the full strand and simplifying this by a square cable. But the overall trend is consistent, comparing the full-square cable 10-stack model with the filament model.

4 Excitation of the Coils

Table 4.1: Current and peak magnetic fields for a load line of 90% at 1.9K

		MQXF	DS11T	SMC-11T
powering current	I_{pow} / kA	19.1	12.8	15.1
max. field conductor	B_{max} / T	13.1	12.6	13.8

all computations were done on *ANSYS® Electronics Desktop 2016.2.0* using the same geometry shown in Figure C.83

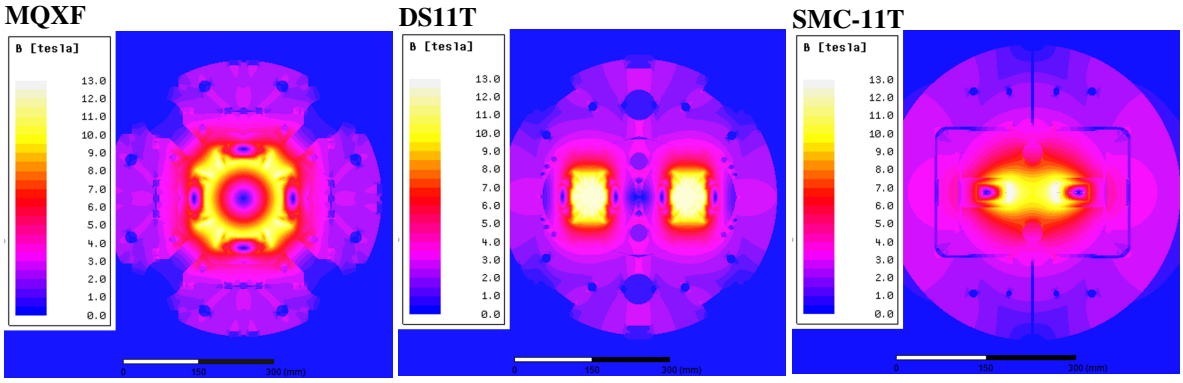

Figure 4.1: magnetic field strength, same scale, values over 13T are white

This chapter will focus on electromagnetic forces (EM forces) on the coils. Prior to analysing the mechanical behaviour of the coils, the EM forces are summarized. The main purpose of the mechanical structure of the magnets is to absorb the forces emitted by the coils while keeping the coils under compression. The EM forces were calculated using the software *ANSYS® Electronics Desktop 2016.2.0*. The geometries were extracted from the CAD models, the details of which are shown in Figure C.83. The BH curve of the Low-Carbon Magnetic Steel used for the yoke is shown in Figure 4.2. The conductor has a relative permeability of 1. Only the yokes and the cable where considered in this analysis. For the calculation of the magnetic field, nominal geometry was used without taking any deformation into account. For the powering of the magnets, it was decided to pick a current equivalent to the magnet load line of 90% at 1.9K, see Table 4.1, the resulting magnetic field strength is shown in Figure 4.1.

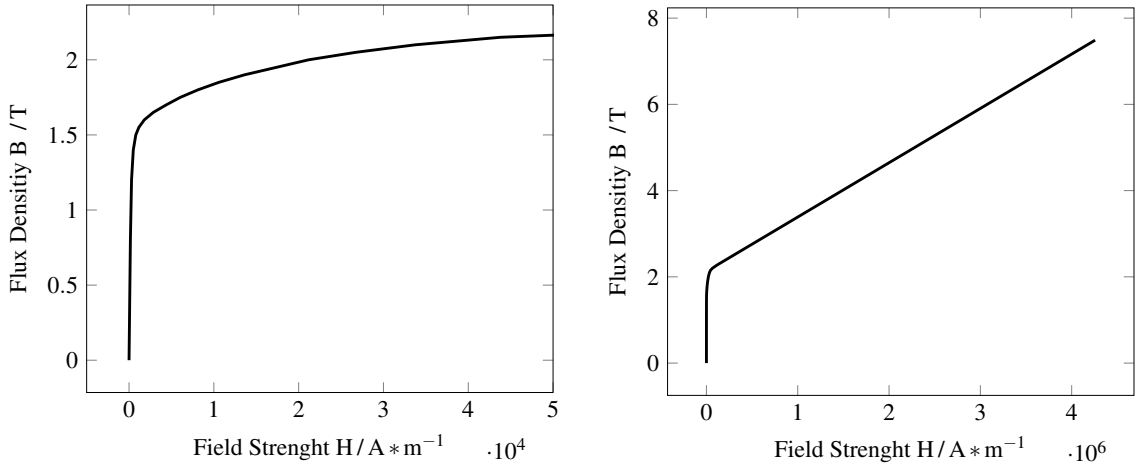

Figure 4.2: BH-curve of the yoke material, Low-Carbon Magnetic Steel

Table 4.2: Electromagnetic Forces of the Cross-section Summary in N/mm

	Horizontal / X	*Vertical* / Y	*Radial*	*Azimuthal*
MQXF	3120	-4536	1266	-5235
DS11T	3561	-1832	1639	-3484
SMC-11T	1697	-1825		

for the DS11T and MQXF one coil half was considered
the data for the SMC-11T is shown for one quarter of the coil

4.1 Electromagnetic Forces

Figure C.11 illustrates the magnetic field strength and the direction of the force vectors. The coordinate system will be used for future referencing. In Table 4.2, the sum of the EM forces at ultimate current is shown; the forces acting on the single coil blocks are shown in Table A.2. The midplanes of the DS11T and the MQXF are parallel in horizontal direction, X, while the winding axis of the SMC-11T is parallel in vertical direction, Y. To better understand which forces were transmitted to the structure and which were “left” in the coils, the absolute force vector was divided into its radial and azimuthal components. This is shown in the appendices from Figure C.6 to Figure C.10. In Table 4.2, the SMC-11T is shown for a quarter coil or one coil block. This was done to show the vertical force acting in the coil. It is similar for the DS11T and the MQXF, but in their case the vertical forces cancel out between two different coils.

In Figure 4.3, the direction of the force vectors and the magnetic field of the MQXF at 19.1 kA are shown. For the 11T, see Figure C.11 and for the SMC-11T Figure C.12. All three coils have a “zero field” region, where the magnetic field drops close to zero in the coil, in local proximity the force vectors point to the center of this region.

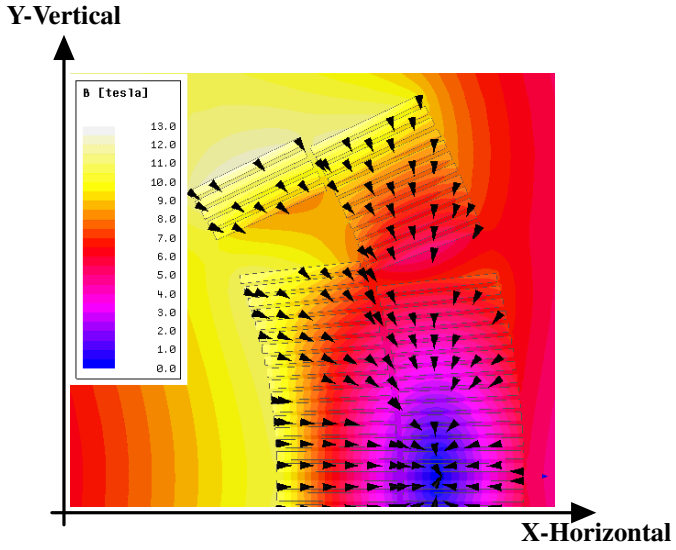

Figure 4.3: MQXF magnetic field and force vectors at 19.1kA, coordinate systems origin is in the centre of the aperture

For the calculation of the forces, a current corresponding to roughly 90% of the load line was assumed. Well knowing that the load line of a magnet also depends on the used type of cable. In the following plots, the forces acting on the coils’ cross sections are shown, Figure 4.5, Figure 4.6, and Figure 4.7. The forces were extracted from one branch of the magnet, as shown in Figure 4.4. The origin of the coordinate system is in the centre of the magnet. They are plotted in two dimensions, either in the vertical and horizontal, or in the radial and azimuthal direction. The forces are given in N/mm, meaning that the force is given for one unit of distance. The forces are given for a 1mm thick cross section. To calculate the total force acting on the mechanical support structure, the integral of the curve needs to be calculated.

For all coils, the vertical and azimuthal forces are symmetric, which is due to the field asymmetry over the horizontal axis. The zero for all axes corresponds to the centre of the aperture.

In Figure 4.5-**A**, the vertical and horizontal force densities for the MQXF are shown. The dips on both

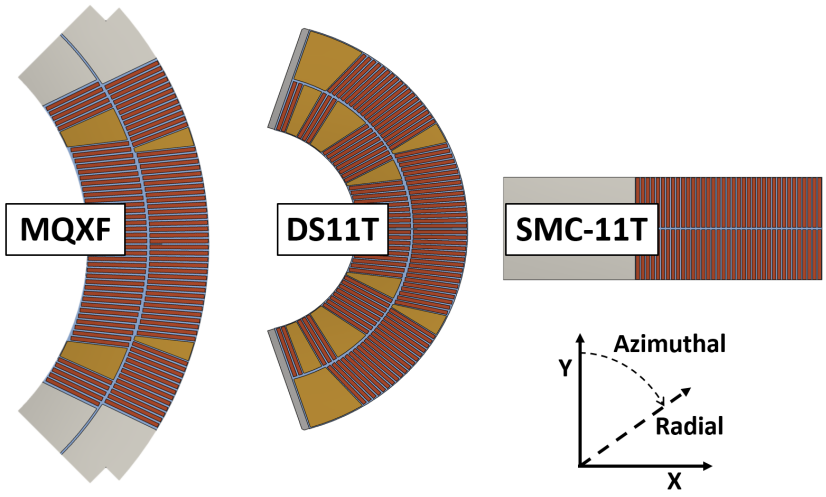

Figure 4.4: Geometries for the extraction of the EM forces

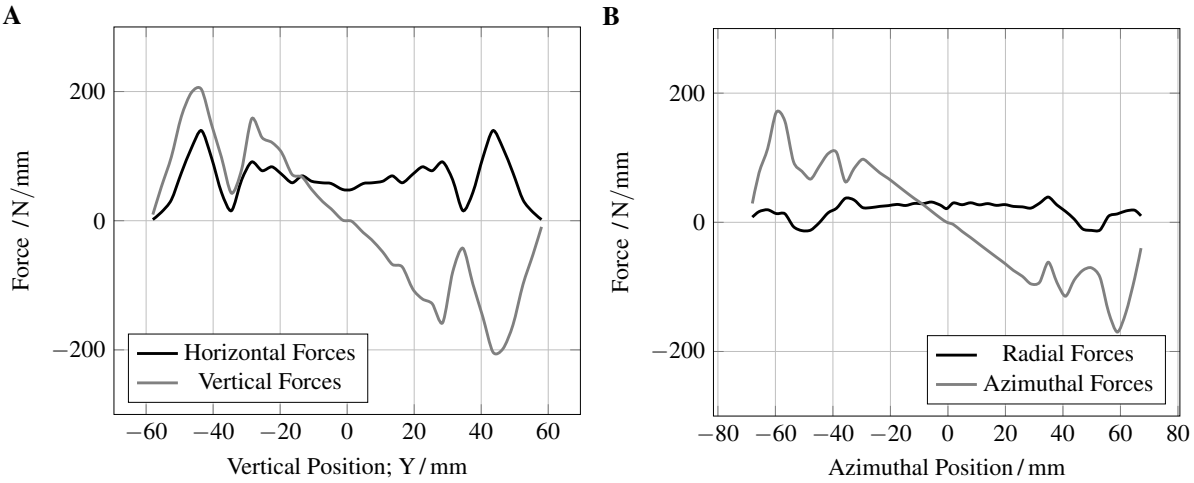

Figure 4.5: MQXF EM force, at 19.1kA, projected on a cartesian and cylindrical coordinate system, projected on the outer radius 113mm

curves at around ±35mm come from the wedges in the coil. The vertical force decreases to 0 at the midplane of the magnet. In this position, the resulting forces are only horizontal. In Figure 4.5-**B**, the forces are projected onto the outer radius of the coil and plotted in azimuthal and radial directions. One needs to consider that the circular length is longer than the vertical in **A**. Therefore, the shown force is smaller. A large margin of the EM forces is kept in the coil itself. This is shown when comparing the azimuthal forces and the radial forces in **B**.

Like the MQXF, the force field of the DS11T coil is also interrupted by the presence of the wedges. The distribution of force is similar to the MQXF, with the sole difference that in the vertical position the horizontal force of the DS11T is larger than the vertical force, **C**, which is not the case for the MQXF. In the azimuthal direction, the distribution between radial and azimuthal forces is similar, **D**.

The SMC-11T differs strongly from the previously shown cos-theta coils. In the vertical plane, **E** in Figure 4.7, the horizontal force is evenly distributed over the short edge of the coil. The reduction at the centre of the coil results from the increased layer of insulation in between the two coil layers. The horizontal forces decrease towards the centre, just as in the cos-theta coils. In the horizontal plane, the vertical forces are zero, meaning that the mechanical structure is not loaded by the EM force in the vertical direction. The forces in horizontal direction are decreasing toward the centre of the coil. Only a small portion of the coil after 80mm in **F** counteracts these forces.

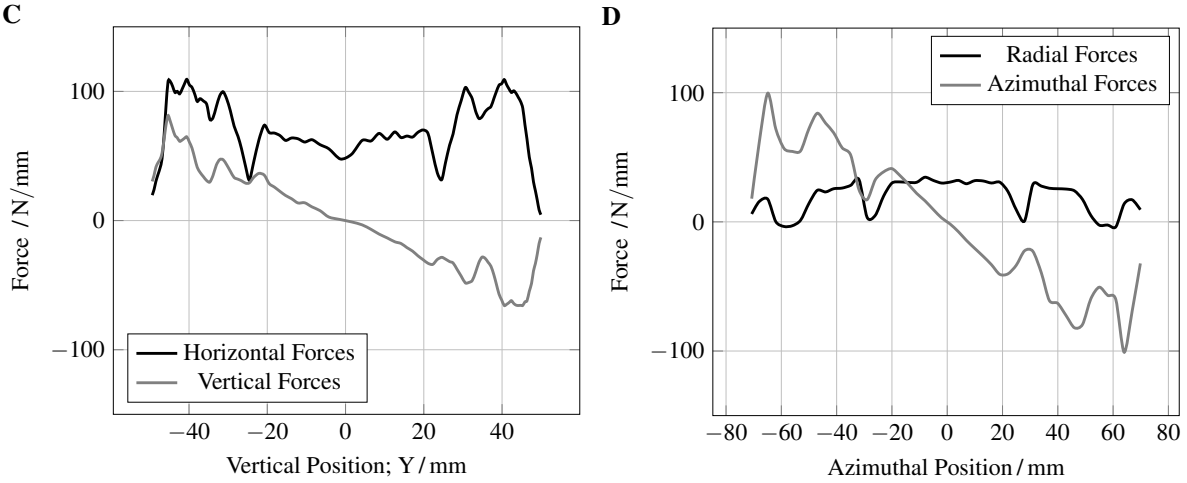

Figure 4.6: DS11T-EM force, at 12.8kA, projected on a Cartesian and cylindrical coordinate system, projected onto the outer radius 60.8mm

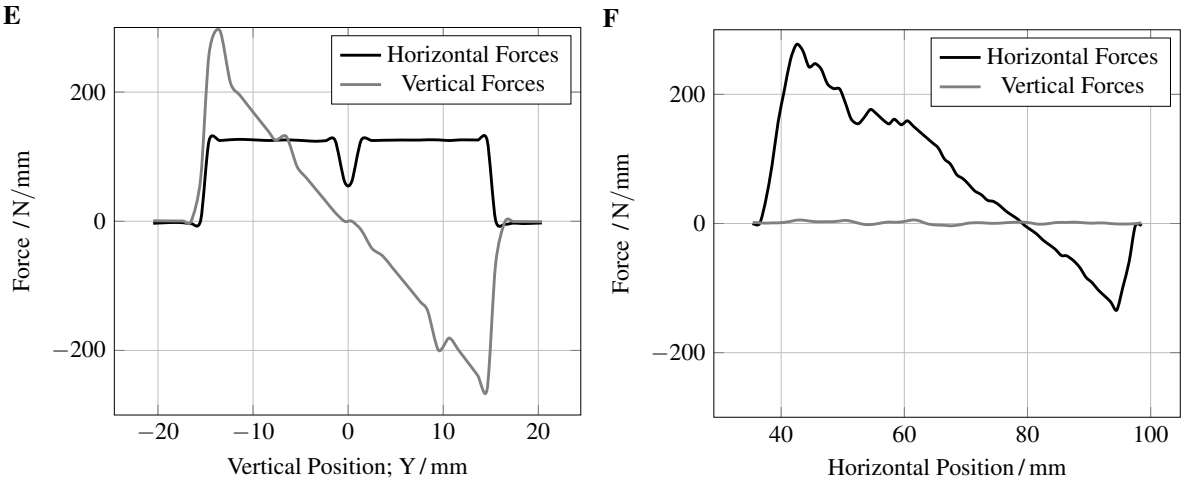

Figure 4.7: SMC-11T-EM force, at 15.1kA, projected onto the vertical and horizontal coordinate

Conclusion on the EM Force Map of the Coils The SMC-11T sees the highest forces in terms of forces by unit length, for example in vertical and horizontal direction. The highest internal force of the coils is in the MQXF coil. The azimuthal forces, which cannot be taken by the mechanical structure, are stored in the coils. Concerning the mechanical structure, the forces emitted radially by the DS11T-coil are 23% higher than those of the MQXF coil. In addition, the radial length is shorter for the DS11T. The SMC-11T-coil transmits the highest forces to the structure with 3.5% more than the DS11T.

4.2 Induced Cable Stress by EM-forces

In order to make a fair comparison between the different mechanical structures, a base line of the stresses and strains in the coils needs to be established. To achieve this, the coil will be supported by an infinite, rigid, frictionless support and then submitted to the EM force. With this only the non-suppressible stresses and strains by the mechanical structure will be visible. For the MQXF and DS11T coils, the frictionless support will be on the outer diameter and the midplane, the SMC-11T, will be supported on all outer surfaces. All models are 6mm thick, but for this analysis one layer of elements was used in the longitudinal direction. The meshing consisted of SOLID186 elements in mainly Hex20 elements. It was ensured that the cable has three elements over the thickness. The coil was one body where all nodes merged.

The faces of the model in the longitudinal direction have a symmetry boundary, which means no displacement in the longitudinal axis is allowed. The influence of the thermal contraction will be skipped in this analysis.

The two coils with an integrated pole (MQXF, SMC-11T) will be analysed in two ways-once with the pole “glued” to the coils, also called an impregnated pole, and once with a free moving half coil. This was done by “cutting” the coil in half to have a single branch.

For the analysis three output parameters will be used-the azimuthal stress, to give an overview of the compression of the turns; the von Mises equivalent stress (EQV. Stress), to assess the risk of classical material failure; and the critical current reduction due to strain, by applying the same formalism as in section 3.5. Special attention will be paid to the outer cable of the coils, i.e. the turns next to the pole and next to the midplane, since those are the turns which are exposed either to the highest equivalent stresses or to the highest tensile stresses. To describe the face of the cable, the letters A, B, and C are used. A is the surface that is perpendicular to the azimuthal axis facing either to the pole or to the midplane, B is perpendicular to the longitudinal axis, and C to the radial axis facing out of the coil. In Figure 4.8 the three surfaces are shown of the first cable of the inner layer pole turn of the 11T. To ease understanding, the cables will be referred to by their positions, inner layer pole cable (ILPC), outer layer pole cable (OLPC), inner layer midplane cable (ILMC), and outer layer midplane cable. For the SMC-11T, both layers will be referred to as outer layer.

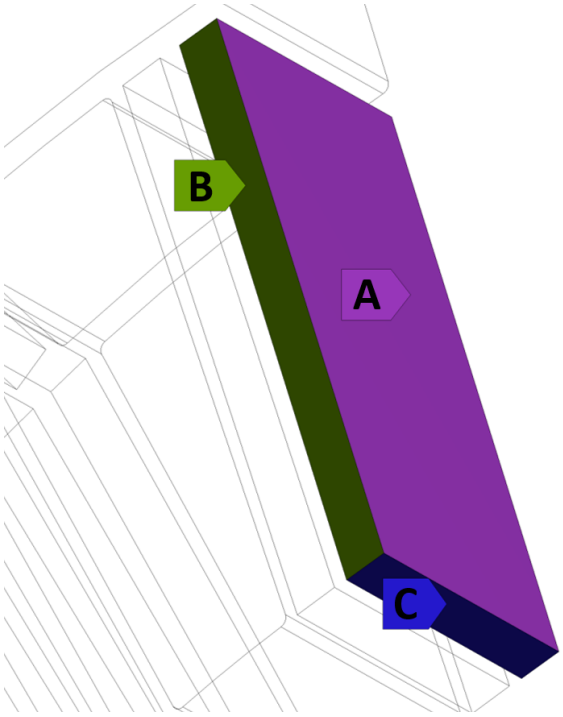

Figure 4.8: naming of the cable surfaces, DS11T coil block 4 pole turn inner layer

MQXF In Figure 4.9 the magnetic field and the cables of interest are shown for the full MQXF coil. The analysis was done using two different approaches. In both cases, the only boundary conditions are the EM force and the frictionless support of the outer diameter and the midplane. In one approach, the full coil with two arches was considered, while in the other only half of the coil with a cut at 45 degrees was considered. This was done to allow the coil arch to move freely without being over-constrained by the pole in the azimuthal direction.

For the full and the so-called half coil, the data was extracted for three surfaces per cable. The data is the average of the EQV stress and the azimuthal stress over the full surface, as shown in Table 4.3. The average value gives a clearer view of the overall behaviour, since it is not strongly influenced by singularities or stress concentrations and is mostly present at sharp corners of the model. In the appendix, the full stress plot is shown in Figure C.13 for the EQV stress and the azimuthal stress at 19.1kA. The EQV stresses in the cables next to the midplane are up to 67MPa on the B-surface for the half-coil model. In general, the EQV stresses for the midplane are higher on the half coil model by roughly a factor of two. For the pole turns the opposite is the case, for the half coil all EQV stresses are below 10MPa, for the full coil between 18 and 34MPa. For the azimuthal stresses, a similar behaviour is observed. The midplane turns in the half coil model are within -154MPa of compression on surface B on the cable in the outer layer midplane cable. The stresses for the full coil model are lower than the half-coil model, for example, in the inner layer midplane cable, the stress is lower by 68MPa for surface B. In

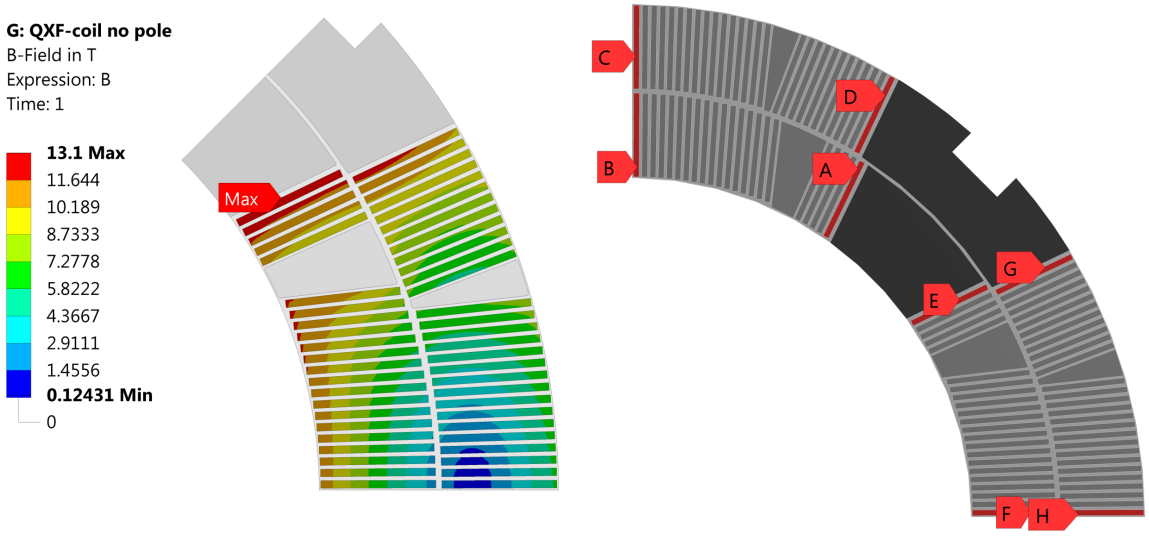

Figure 4.9: Magnetic field of the MQXF magnet in the conductor of a coil in T, at 19.1kA, and the cable of interest

the pole turns, all the turns are in tension in the full-coil model, with the minimum at 37MPa. The maximum in tension for the half-coil model is 1MPa; the other cables are all in compression. The stress in all three dimensions over the inner and outer layers is shown in Figure B.2 for the fixed pole and Figure B.3 for the free pole. The plots represent the stress of the centre line of each layer.

DS11T Since the pole of the DS11T is by design not fixed to the coil, only one scenario was analysed. Stresses for the four cables are shown in Table 4.3. The pattern and the deviation of the stress are similar to those of the MQXF coil, although all EQV stresses are lower than in the MQXF coil, with a maximum of 45MPa on the C-side in the inner layer. This is different for the stresses in the azimuthal axis. Like the MQXF coil, the DS11T coil is more compressed on the inner layer in the midplane. On the outer layer, the opposite is the case. The maximum azimuthal stresses of -126MPa are on the outer layer. The stress in all three dimensions over the inner and outer layers is shown in Figure B.4. The plots represent the stress of the centre line of each layer.

Table 4.3: Stresses in the coil, only under the EM Force

	inner l. midplane			inner l. pole			outer l. midplane		outer l. pole	
EQV Stress / MPa	MQXF	DS11T	SMC	MQXF	DS11T	SMC	MQXF	DS11T	MQXF	DS11T
Side A full	61		11	18		**35**	22		**25**	
Side A half	60	40	**39**	7	3	4	**53**	**37**	5	7
Side B full	17		15	**34**		24	21		23	
Side B half	**67**	29	29	8	**6**	4	47	21	7	**8**
Side C full	18		13	**34**		31	21		19	
Side C half	58	**45**	37	9	**6**	8	41	27	5	6
Trans. Stress / MPa										
Side A full	-32		-19	**76**		82	-76		**64**	
Side A half	-84	-110	-108	-4	**-1**	-7	-137	-117	1	**-3**
Side B full	-32		-25	42		**90**	-76		62	
Side B half	**-100**	**-113**	**-123**	-6	-2	-10	**-154**	**-126**	-6	-8
Side C full	-20		-17	37		84	-59		59	
Side C half	-66	-50	-99	-7	-6	6	-116	-95	-1	-6

maximum values ins EQV. Stress in bold
maximum compression for the midplane and maximum tension for the pole cables in bold

SMC-11T For the SMC coil, only one layer was analysed, as all four layers are symmetric. Again, with regard to the MQXF coil. One analysis was done with the pole glued to both coil halves and one with the pole cut in half and made freely movable. Overall, the lowest EQV stresses are present in the SMC coil compared to other designs, Table 4.3. In terms of azimuthal stresses, the SMC coil has the highest tensile stresses with the fixed poles. 90MPa on average over the cable are present in the pole turn. The same cable with a free pole is under -10MPa in compression. Furthermore, it is the same cable with 6MPa in tension and with the same configuration on surface C.

The inner layer of the cos-theta coils is more critical to the performance than the outer layer. This is mainly due to the presence of a higher field and, in case of the DS11T, the number of wedges. In Figure 4.10, the stress along the centre line of the inner layer is plotted. In this plot, only the azimuthal stress is shown. The axes are normalized to the specific length of the layer. For the SMC coil, one layer is shown with the 0 at the midplane. Considering the "glued" pole, starting from the midplane, the SMC and the MQXF coil are fully in compression. For the SMC coil, the compression increases until the field minimum in the coil is reached. At this location, the force vectors turn in the opposite direction, Figure 4.7 at around 80mm. The peak of compression is shifted for the MQXF coil directly on the midplane. This is because the location where the force vectors turn is also in the midplane for the cos-theta coils. The two plateaus in the azimuthal stress of the MQXF coil due to the presence of the wedge and the half of the pole. It is remarkable that 50% of the MQXF coil is under compression. This is greater for the SMC coil, but the maximum tensile stresses are higher than in the MQXF coil.

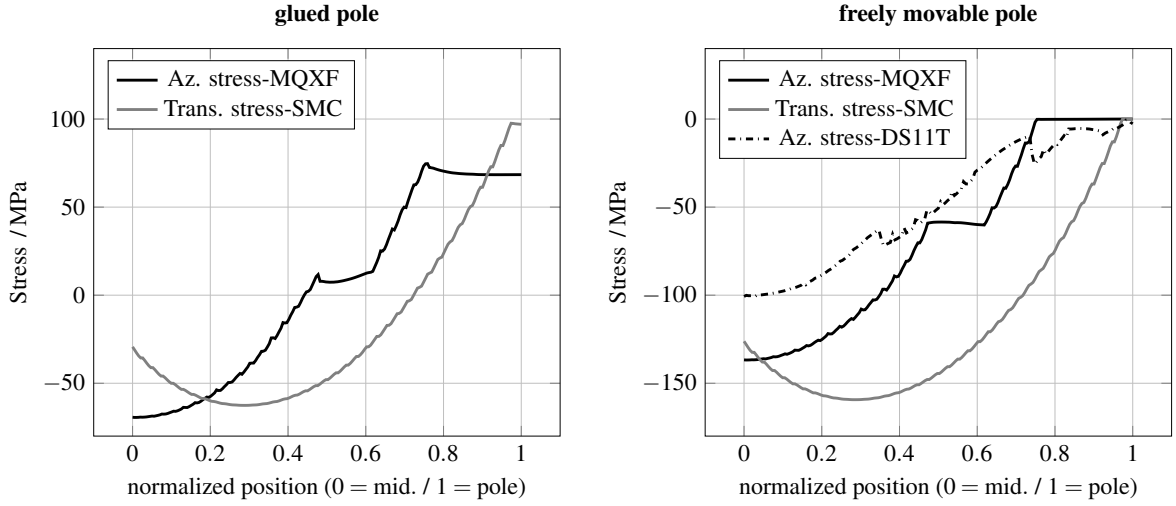

Figure 4.10: Stresses in the inner layer of the three coils at excitation compared with the difference between a movable pole and a fixed pole

Removing the constraint from the poles increases the overall compression in the coils. In the right graph of Figure 4.10, the comparison of the three coils for this case is shown. When the poles are allowed to move, all the coils are nearly complete in compression. In the transversal direction of the SMC coil, the highest compressions are achieved even though the pressure at the midplane is lower.

Conclusions on the Stresses in the Coils Induced by EM Forces In all three coils, the EQV stresses are below 70MPa, which should be sufficient to avoid damaging the impregnated fibre or the conductor itself. The peak EQV stress is always found in the midplane. Besides, in the midplane the level of hydrostatic pressure is higher than in the rest of the coil, see Figure B.2 to Figure B.5. Close to the midplane, the stress in all three directions is in compression and around the same level, which is useful if the von Mises equivalent stress is considered as a failure criterion. In the present study, it has been demonstrated that, even with a perfect support, a full coil with an impregnated pole will be exposed to high tensile stresses. If the pole is not fixed to both arches of the coil, as in the DS11T coil, the coil sees minimal tensile stresses in the first pole turns. This tension can be reduced by pre-compressing the coil before excitation. Maintaining this pre-compression is one of the main challenges of the mechanical structure.

5 Comparison of the Mechanical Structures

In the previous chapters, the basic principals of the mechanical design of the three magnet designs has been shown. In this chapter, more details will be given based on the explanation of the finite element model for the full magnets. In section 4.2 a base line of the expected stresses in the coils was given, this will be used to establish the influence of the mechanical structure on the stresses and strains in the coils. In the first part of this chapter the three mechanical designs will be analysed. The analysis will be structured in such a way that it represents the different assembly steps and conditions, like the cooling to 1.9K and the excitation of the the coils. For the coils the EQV-Stress, the azimuthal stress and the critical current reduction will be used as output parameters. The components of the mechanical structure will be assessed on their structural integrity. To ease the naming of directions the terms vertical and horizontal will be used, these always refer to the orientation of the magnets in the plots and figures.

All three models are three dimensional with a thickness of 6mm. The collars of the DS11T have a thickness of 3mm, to simulate at least two collars interacting with each other a thickness of 6mm is required. The MQXF and SMC-11T are represented with a full cross-section. The DS11T was split in the center vertically, so that only two coils are used. This was done to reduce the computing time and because the effect of one aperture on the other can be neglected. In the longitudinal direction both sides of the models are constrained by a symmetry condition. To avoid creating artificial stress during the cool down, no thermal shrinkage in the longitudinal direction is allowed by the used material. For all models the materials from section 3.1 were used. All three simulations have five different load steps, in which the assembly procedures, the cool down and the powering of the coil will be simulated, see Table 5.2. All of this is done in one simulation to ensure consistency through out the simulation. This was achieved by disabling certain contacts and revoking them when needed. An overview of the geometries is shown in Figure C.84, Figure C.85 and Figure C.86.

Table 5.1: FE-Models Overview

	DS11T	**MQXF**	**SMC-11T**
Total Nodes	948610	635942	907684
Solid Elements	4966916	170307	125281
Contact Elements	156514	39840	20622
Average Computation Time	13h 52m	2h 22m	50m 35s
Memory Used	12.8GB	23.9GB	37.4GB

The meshing strategy for the three different coil designs was to have at least three layers of elements on the cable in transverse direction, which lead to an element size of 0.45mm on the cross-section of the coil. The meshing in longitudinal direction was different for the coils, the DS11T has three layers in the longitudinal direction, MQXF and SMC-11T coil have one layer, mesh numbers given in Table 5.1. All nodes in the coils, cable, insulation, wedges and poles are merged. The model of the DS11T represents the interleaving collars which cause non uniform loads along the longitudinal axis. The MQXF and SMC-11T model are in the longitudinal plane uniform, therefore one layer of elements is sufficient. All elements are SOLID186, for the coils Hex20 and Wed15 are used, for the structural components Hex8 and Wed6 were used. The dropped midside node for the structural components was necessary to achieve a reasonable computation time. The meshing of the structural components will be shown in the detailed sections of the the magnets. The meshing for all models was refined to such an extend that the achieved results are mesh size independent, never the less singularities at sharp corners, especially at transitions between a soft to a stiff material, can not be completely avoided. Five types of contacts were used *frictionless*, *frictional*, *no separation*, *rough* and *bonded contacts*. *Frictionless* contacts allow for parallel movement between two surfaces and for detachment, the tangential stiffness is zero. *Frictional* contacts are similar to *frictionless* contacts but the tangential stiffness is depending on the normal force and the friction coefficient μ. The linear version of the *frictionless* contact is the *no separation* contact, it allows for free sliding but no detachment of the surfaces. A *rough* contact is the the opposite, no tangential sliding is allowed but detachment, when the contact is detached the surfaces can move relative to each other. A *bonded* contact fixes the position of the two surfaces to each other. For all contacts the "Augmented Lagrange method"-algorithm was used, the contact detection was done using gauss integration points. It should be noted that one contact can reach over multiple surfaces, the surfaces do not need to be connected. The initial contact stiffness for all models is give from Table A.3 to Table A.7.

In order to compare the mechanical structures with each other a "nominal"-shimming case needs to be defined. For this a perfect coil geometry is used. The shimming is altered in such a way that the pole turns are under at least **-10MPa** in compression, on average over the full cable cross-section, at the defined maximum current. With this goal reached, the stresses and strains in the coils can be compared between the different designs.

Table 5.2: Load Steps used in the FE-Simulation

Load Step	DS11T	MQXF	SMC-11T
1	collars move vertical; contacts are engaged	pressure is applied at the location of the bladders	pressure is applied for the vertical bladders
2	collars are displaced vertically; collar key contact is activated	key contacts are activated; pressure is removed	pressure is applied for the vertical bladders; vertical keys placed
3	contact collars to yoke active; welding of the shell	welding of the shell	pressure from bladders removed; keys in contact
4	cool down of all components to 1.9K		
5	powering 12.8kA	powering 19.1kA	powering 15.1kA

5.1 DS11T

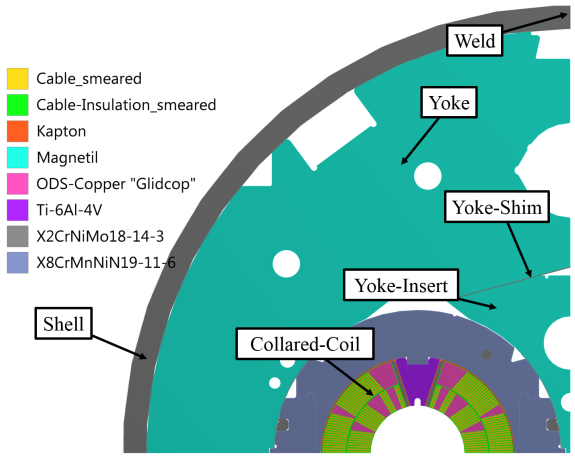

Figure 5.1: Materials used in the DS11T-model

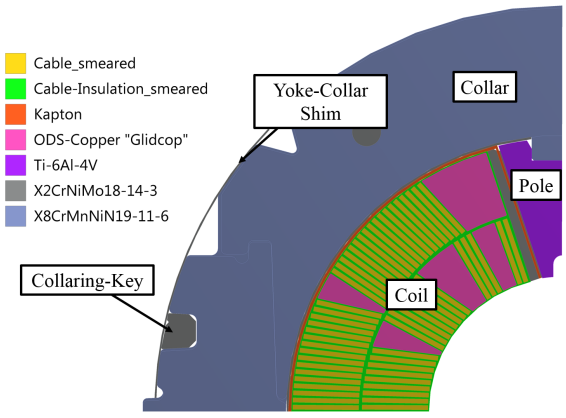

Figure 5.2: Materials used in the DS11T-model, focus coil

Geometry The geometry used is the full cross-section, split in half in the vertical plane. With this only one collared coil is simulated. In Figure 5.1 the used geometry and material is shown, the actual model is one half of the magnet. Figure 5.2 shows the detail of the collared coil. The coils are surrounded by the ground insulation, Figure 5.4, which intrudes between the coil and the pole. On the outer diameter of the ground insulation the collaring shoe surrounds the both coils. It should be mentioned that all shims in the DS11T are made from stainless steel[1]. The lateral shim between the ground insulation and the loading pole can be varied in thickness to tune the pre-stress to a desired level. Also a shim can be placed in-between the pole and the collar for a finer tuning. The set of collars, upper or lower, is fixed together with a collar rivet. Between the contact of yoke and the collared coil another shim is placed, Figure 5.3, also this shim can be varied in size to tune the pre-stress. The DS11T has a vertically split yoke and a yoke insert, bot shown in Figure 5.1. The yoke-shim is between the yoke-insert and the yoke. The large yoke laminations in the DS11T have a tapered vertical contact surface. During the welding operation the shrinkage of the weld compresses the assembly. Due to the tapered surfaces of the yoke laminations, with an angle of 0.04 degree, the first contact between the two yokes on the inner edge, close to the center of the magnet. With increasing shrinkage of the weld the yokes begin to close by bending around the longitudinal axis. At the end of the welding operation the yokes are closed over nearly the whole contact surface. With this method, of storing energy in the mechanical system, the risk of an opening of the yokes during the excitation of the magnet can be minimized.

[1] X2CrNiMo18-14-3

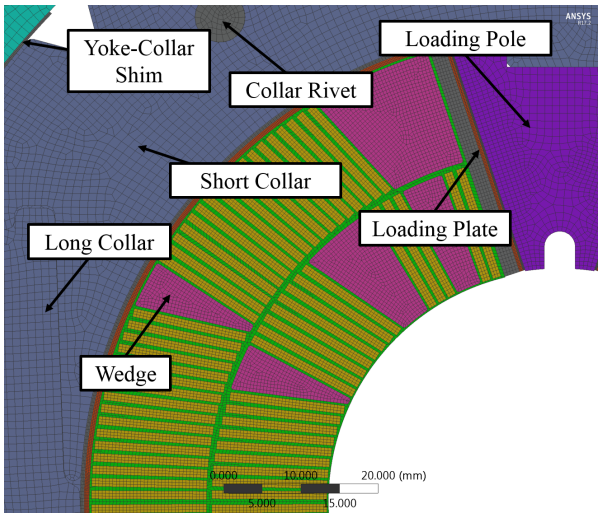

Figure 5.3: Meshing used in the DS11T-model

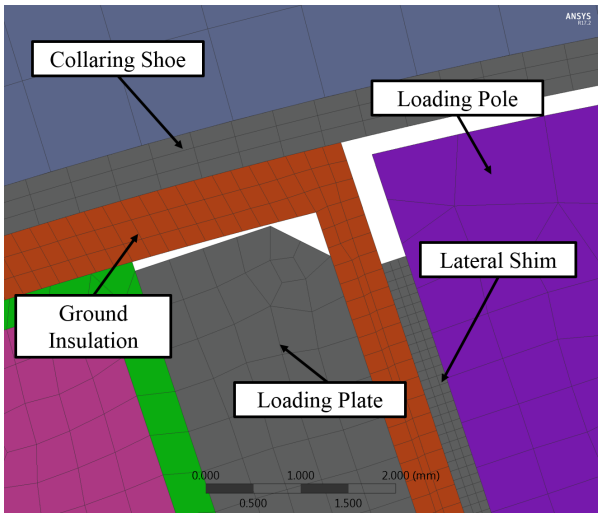

Figure 5.4: Detailed meshing, Kapton & Shim

Mesh The meshing of the coil is shown in detail in Figure C.21, three layers of elements in transverse direction and three layers in longitudinal direction. All sheet parts, like the ground insulation, collaring shoe or the shims, have at least three elements in thickness. All sheets in direct contact with the coil have three layers in longitudinal direction. 15 layers are needed for the collaring shoe, loading pole, yoke collar shim and the collaring key, these components are in direct contact with the interleaving collars, therefore a finer mesh is required in longitudinal direction. Four layers are required for the collars, in Figure C.22 the first and last collar are cut in the longitudinal center and the central ones are represented accurately, this was needed to create a correct symmetry boundary. The element size for the yoke and shell is 2mm, decreasing to 0.5mm at the contact with the collared coil.

Contacts The contact details of the DS11T-model are given in Table A.3 and Table A.4, a graphical overview is shown in Figure 5.5. The contact number (CN) will be given to each mentioned contact. For the contact between ground insulation and coil a *bonded* (CN 3) contact was used. The collaring shoe has a *frictional* (CN 8 & 9) contact with $\mu = 0.2$ to the ground insulation and the collars, this was needed to stabilize the simulation. If one contact is without tangential stiffness one of the bodies would be under constrained. With this it was avoided to create additional artificial boundaries, needed to solve the simulation. The lateral shim *bonded* (CN 4) to the ground insulation. While the contact from the lateral shim to the loading pole is *frictional* (CN 11-14), but μ is for the standard case 0. This was done to simulate the potential influence of friction of this contact. The vertical surfaces of the pole are connected to the collar with a *non separation* (CN 23) contact, the horizontal surface is *frictionless* (CN 16). The upper or lower collar packs are only connected with each other via a *bonded* (CN 2) contact to the rivet. The collaring-keys have a *bonded* (CN 1) contact to the collars on one side and a *rough* (CN 24) on the other, the bonded contact is deactivated for the first 2 loading steps. A *frictionless* (CN 20 & 21) contact is used between the collared coil shim and the collared coil. The collared coil shim is connected with a *bonded* contact with the yoke. The yoke shims are using a *bonded* (CN 5) contact for the yoke insert, the connection between the yoke and the yoke shims is *frictionless* (CN 17). The contact between the yoke and the shell is *frictional* (CN 10), this was done to ease the convergence of the simulation, since a tangential stiffness of zero would allow for too many degrees of freedom, μ was set to 0.2.

5.1.1 Load Steps (LS)

The conditions for each of the five load steps will be shown, including the boundaries and the active contact. The force convergence plot of the DS11T-simulation is shown in Figure C.80.

Load Step 1 - collaring For the first load step all contacts between the collared coil and the yoke are disabled. The collaring-keys are only fixed to one collar pack, which allows the collars to freely move in the vertical direction. The collars are getting displaced towards the center of the aperture by 0.1mm, the interacting surfaces are shown Figure C.23 and Figure C.24. This displacement represents the “over-collaring” which is needed for insertion of the collaring keys. The displacement boundary fixes the interacting surfaces in all three dimensions. To simulate

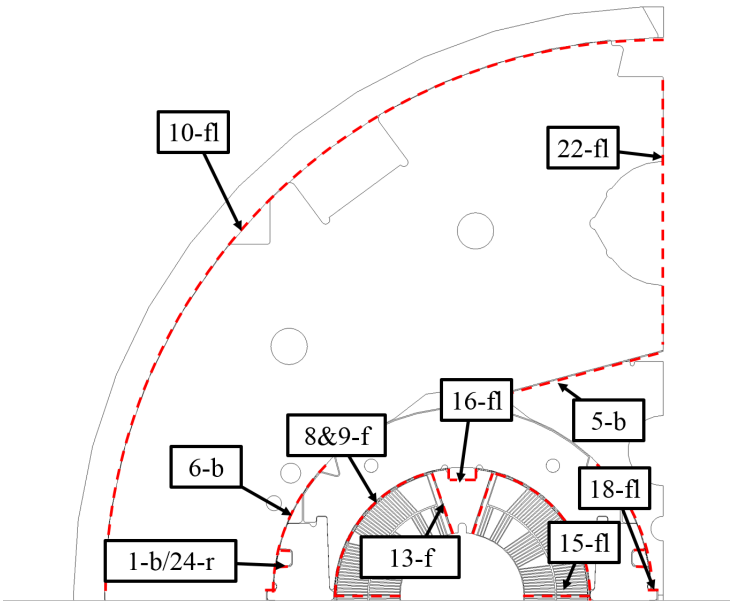

Figure 5.5: DS11T: overview of the contacts; b-bonded, f-frictional, fl-frictionless, ns-no separation, r-rough

the shimming, the purposely created excess of material to generate pre-stress, the contact between the pole and the lateral shim is getting offset. Meaning, that for a fixed value all contact elements are moved in the normal direction to the contact surface (CN 11 to 14). During the first load step the initiation of all contacts takes place, in this particular case the contacts between the pole and the lateral shims are getting of set by there defined shimming value. Depending on the needed pre-stress this value can range from 0 to 0.4mm. After the final iteration the collars are vertically displaced by an total of 0.2mm. The contacts of the lateral shim have reached their offset. This is load step is representing the state of the real coil where the assembly is under the collaring press at maximum force of the press.

Load Step 2 - spring back The displacement of the collars is now in reverse direction. Reaching the original position where the geometry was initiated. This is called the spring back of the collared coil, where the induced stress by the shimming and the locking of the collaring-keys causes the collars to “spring back” after pressure of the collaring press is released. The contact of the collaring key (CN 24) is activated with the first iteration of the 2nd load step. This contact is now validating with each iteration the distance of the open contact and if the contact is engaged, this is done for each single contact element. At the end of the loading step the collared coil is in its free state, containing the created pre-stress by the lateral shims.

Load Step 3 - welding In the first iteration the contact between the yoke shim and the collars is activated (CN 20 & 21). The position of the collared coil is now only influenced by the yoke. The shrinkage of the welded shell due to the weld is assumed to be 1.2mm per weld. In the simulations this is done by displacing the welds of the shell in the horizontal direction by 0.6mm, the weld is free in vertical direction. During all of the reaming load steps the weld remains being displaced by 0.6mm compared to the initial geometry. In the nominal case the shim between the collared coil and the yoke is 0.4mm thick, which is the case for the geometry used in this simulation. The thickness of this shim can be changed by offsetting the contact, this would also take place load step 3.

Load Step 4 - cool down to 1.9K Apart from the change in temperature the only active boundaries are the horizontal symmetry on the yoke insert, the vertical fixed center node of the yoke insert and the welding displacement. The thermal condition causes all parts to shrink according to the thermal contraction of the individual material.

Load Step 5 - excitation of the coils The imported body force is now applied on the bodies of the cable. For the DS11T the body force is corresponding to a powering with 12.8kA.

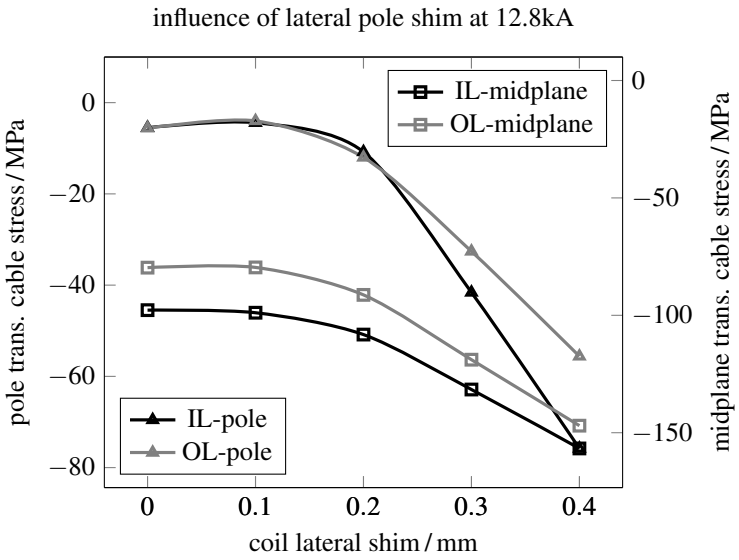

Shim / mm	IL-pole	OL-pole	IL-midplane	OL-midplane
0.0	-6	-6	-98	-80
0.1	-4	-4	-99	-80
0.2	-11	-12	-108	-91
0.3	-42	-33	-132	-119
0.4	-76	-56	-157	-147

Values are for average transversal stress per first cable

Figure 5.6: DS11T response for the lateral shim, collared coil to yoke shime at 0.4mm

5.1.2 Nominal Case

The DS11T has two ways to adjust the pre-stress in the coils, the lateral shims, on the pole, acting directly on the coils and the yoke-collared coil shims compressing the collared coil on a 90 degree arc from both sides. To define the "nominal case" for the shimming, the behaviour of the magnet during excitation of the coils was studied. All stresses shown here are the average transversal stresses of one cable. The lateral shim on all four coils was varied in a range of 0 to 0.4mm thickness, the response from the magnet is shown in Figure 5.6. Between 0 and 0.2mm minimal changes can be observed in the transversal stress of the cable. From a thickness of 0.2 to 0.4mm a nearly linear behaviour of the stress is observed. If the shimming is not sufficient the coils are detaching from the pole. Observing the stresses in the collar, the collar "nose" is in vertical direction unloading below 0.1mm lateral shim thickness. As a result of this the pole is no longer compressing the coils, in Figure 5.7 the stress in the collar nose is shown. For a shimming smaller than 0.2mm the collar nose is partially in tension. The shimming case with a lateral shim of 0.2mm full fills the goal of keeping the two cables, of both layer, close to the pole under a compression of -10MPa.

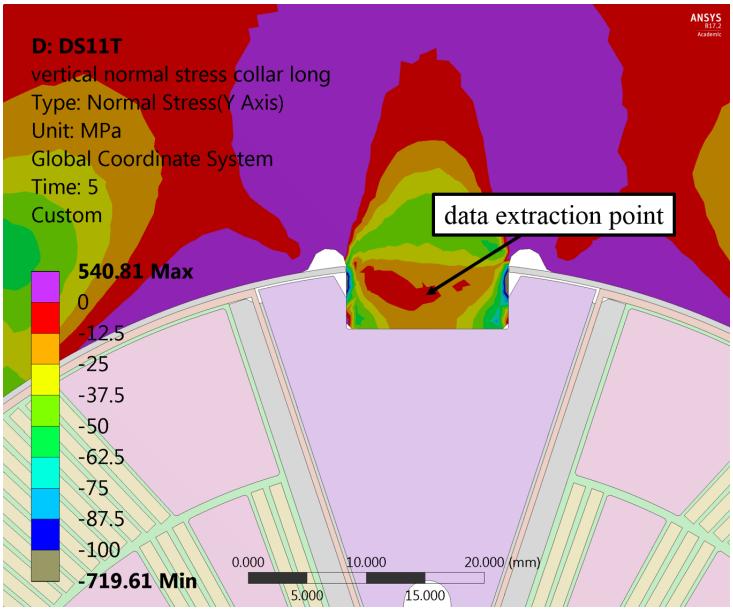

Shim / mm	normal stress in vertical direction collar nose
0.0	5.2
0.1	5.6
0.2	**-6.0**
0.3	-84.9
0.4	-179.1

- normal vertical stress in the top collar
- shown plot is for a lateral shim of 0.2mm
- asymmetries between the left and right part are due to the asymmetric yoke support

Figure 5.7: DS11T unloading of the collar "nose" as a function of the lateral shim at 12.8kA

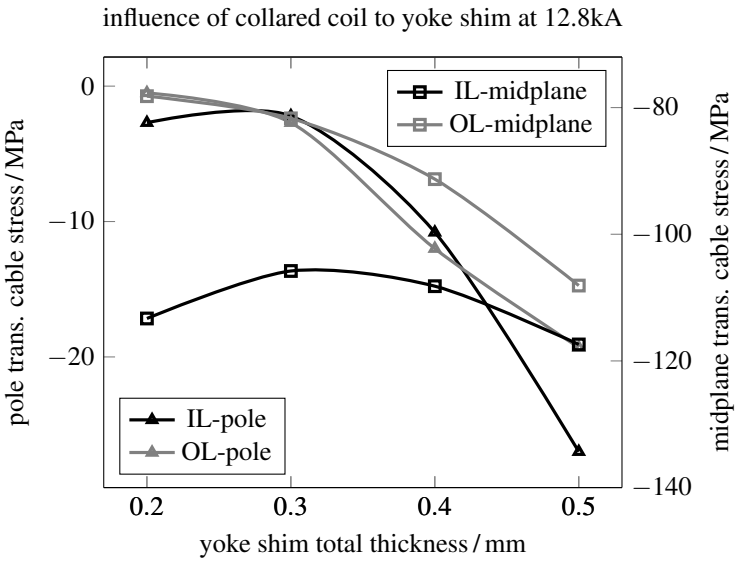

Shim / mm	IL-pole	OL-pole	IL-midplane	OL-midplane
0.2	-3	-1	-113	-78
0.3	-2	-3	-106	-82
0.4	-11	-12	-108	-91
0.5	-27	-19	-117	-108

Values are for average transversal stress per first cable

Figure 5.8: DS11T response for the collared coil to yoke shim, lateral shim at 0.2mm

The same analysis was carried out to test the effect of the collared coil to yoke shim. In Figure 5.8, the shim was varied between 0.2 and 0.5mm in total thickness, the nominal value is 0.4mm. A shim of 0.4mm would create the same inner diameter as the outer diameter of the collars. The lateral pole shim was set to 0.2mm. To reach the goal of -10MPa in compression in the pole turns the nominal shim is adequate. The pre-stress in the coil can be increase with the collared coil to yoke shim, this might be useful if the stress created during the collaring process needs to be reduced.

5.1.3 Collaring Process (LS 1&2)

During the collaring of the two coils, the collars are transmitting all of the load from the hydraulic press to the coils. The contact surfaces on the collars are rather small, which leads to intense stresses in the contact regions with the press. The collaring process will be here described as a combination of LS 1 and LS 2, the maximum displacement during collaring and the spring back. During LS 1 EQV-stresses above 400MPa are reached in the collars in Figure 5.10 the contact surface of the collars is shown. The two long collars with half the thickness are shown with the short collar in between. In Figure 5.9 the full collared coil during the maximum displacement of 0.2mm is shown.

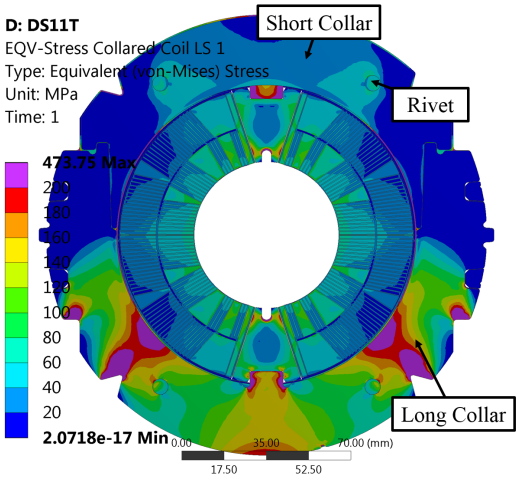

Figure 5.9: EQV stress in the collared coil during collaring, at LS 1

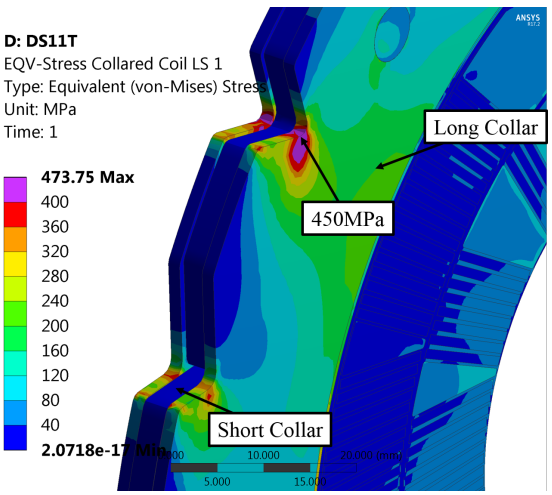

Figure 5.10: EQV stress in the collars during collaring, shown for the collar pack with two long collars

The excessive stress causes the long collar to yield in the edges of the contact surface, the plastic strain is shown in Figure C.25. The short and long collars are displayed, the short collar is interacting with the rivets, which are connecting the short with the long collars, and the collaring shoe on the inner diameter. The hydraulic press is not acting on the short collar, therefore the stresses are much lower than in the long collar. The displacement vectors during the collaring are shown in Figure C.26. The collaring shoe, a thin stainless steel sheet place between the collars and the ground insulation, is submitted to EQV-stresses beyond its yield limit. The pattern of the long collars is visible in the stress concentration on the collaring shoe, Figure 5.11. The pattern of the transferred force, from the collars via the collaring shoe, is visible directly on the coil in radial compression, Figure 5.12. The maximum difference between the region with the short and long collar is 13MPa on the outer diameter. This anisotropy, along the longitudinal axis, is not noticeable in the coil closer to the center.

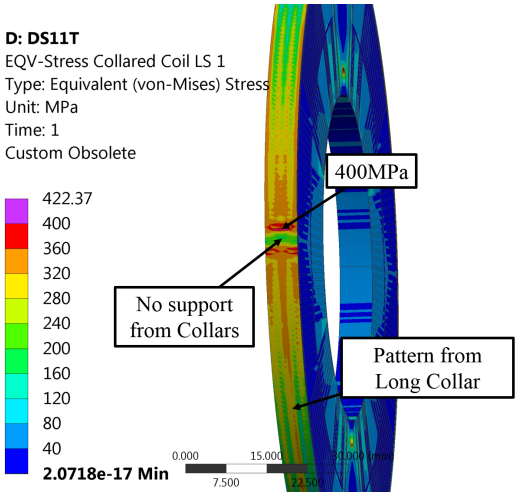

Figure 5.11: EQV stress in the collaring shoe during collaring

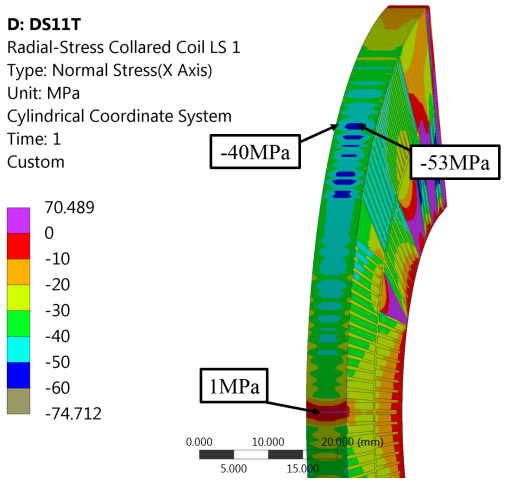

Figure 5.12: Radial stress in the coil, with the maximum longitudinal deviation

The average stresses per cable in the transversal direction reach an maximum of -75MPa on the inner layer cable. The EQV-stresses reach an maximum on the inner layer midplane cable close to the inner radius at 75MPa.

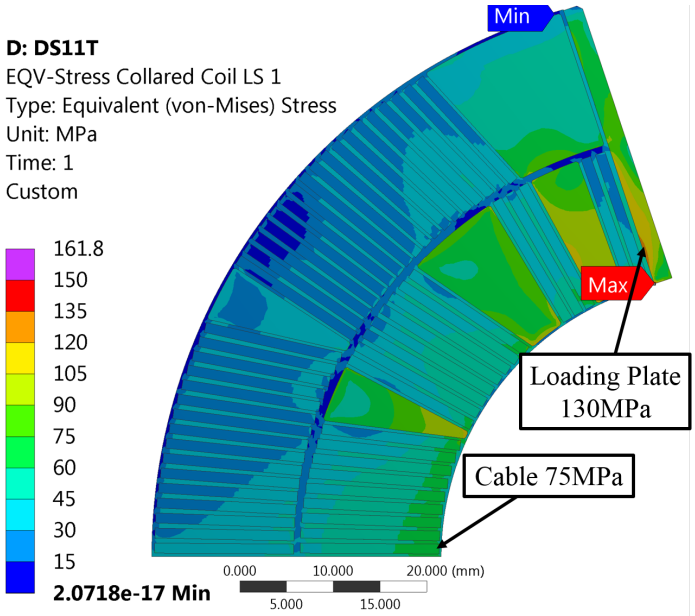

Stress / MPa	IL-pole	OL-pole	IL-midplane	OL-midplane
Trans.	-75	-67	-74	-56
EQV	30	28	48	40

- shown plot is for a lateral shim of 0.2mm
- stress concentration on the lower edge of the loading plate

Figure 5.13: DS11T EQV stress during the maximum collaring displacement, at LS 1

After the convergence of LS 1 the contacts for the collaring keys are activated. In LS 2 the forced displacement on the long collars is removed to the initial position of the collars and removed. At LS 2 the collared coil is completely self supporting with no external force acting on it. The long collars are interlocked with the collaring

key. In Figure 5.14 the EQV stress in the long collars around the collaring key is resulting from this interlocking. The interleaved long collars are acting upon the collaring key in a scissor motion. The resulting EQV stress is shown in Figure 5.15, the iso-surface plot is showing stress greater than 40MPa.

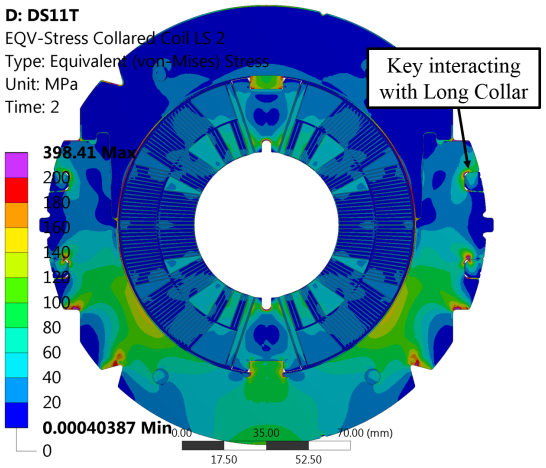

Figure 5.14: EQV stress in the collared coil after collaring, LS 2

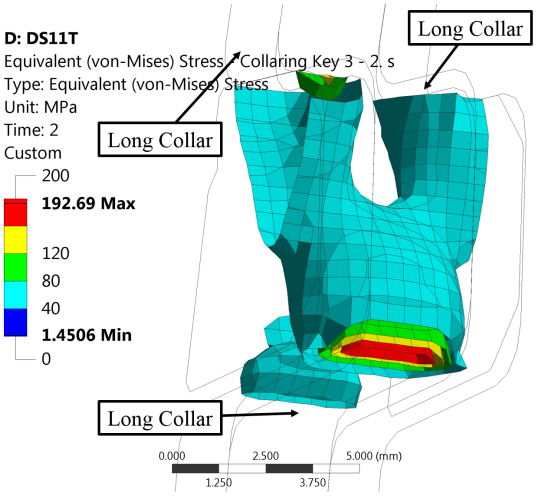

Figure 5.15: EQV stress in the collaring key, top in contact with two long collars, bottom with one long collar

The remaining stress in the coil is much below the stress during the collaring process. The transversal and EQV stress on the cable has decrease by approximately 30MPa and 15MPa compared to the maximum stress during collaring, Figure 5.16. The total deformation and the deformation due to the spring back are shown in Figure C.27 and Figure C.28.

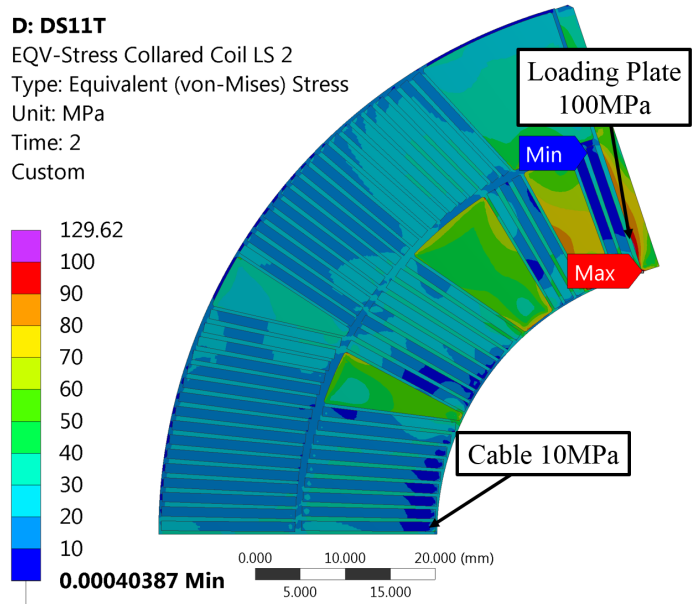

Stress / MPa	IL-pole	OL-pole	IL-midplane	OL-midplane
Trans.	-45	-40	-35	-40
EQV	13	19	22	26

- shown plot is for a lateral shim of 0.2mm
- note the changed scale compared to Figure 5.13

Figure 5.16: DS11T EQV stress in the coil after collaring while the collared coil is at rest state, at LS 2

5.1.4 Welding of the Shell (LS 3)

The vertical displacement on the shell welds is used to simulate the shrinkage of the weld during the welding operation. In Figure C.29 the deformation of the shell is shown. Due to the shell shrinkage the compression from the yoke on the collared coil is build up. In Figure 5.17 the contact between the collar coil shim and the yoke

is shown. During the welding the gap between the two yoke laminations is closing, in the simulation only one yoke lamination is present. The yoke laminations are tapered on this surface, the effect of this can be seen in Figure C.30, where the pressure reaches a maximum close to the center of the magnet and continuously decreases outwards. The maximum EQV stress in the shell is in the weld, Figure 5.18. In the yoke insert a maximum of 420MPa is reached in the alignment groove for the collar notch.

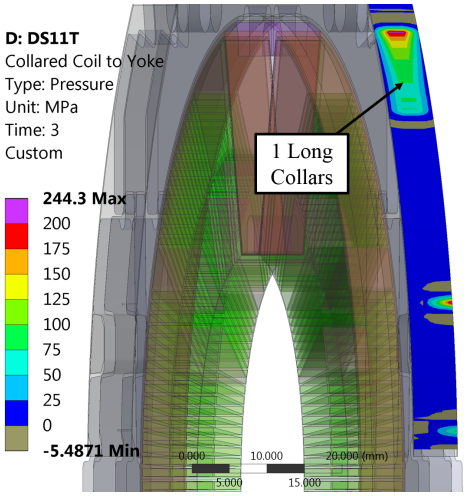

Figure 5.17: Contact pressure between the collared coil shim and the yoke after the welding, LS 3

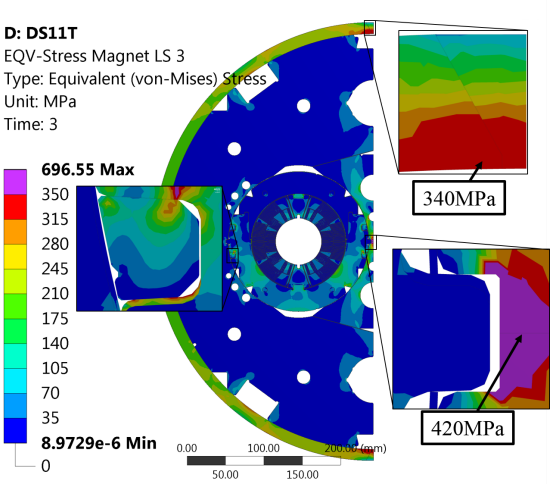

Figure 5.18: EQV stress in the magnet after welding, LS 3

The coil stresses do not change to a big extend due to the welding of the shells. In Figure 5.26 the delta in azimuthal stresses due to the welding operation is shown. Close to the midplane, the inner layer of the coil is getting stretched while the outer layer is more compressed. Due to the asymmetry in the yoke the stresses in the coil are no longer uniform when comparing the left and right branch. The influence is minimal with its strongest impact on the outer layer pole cable which is compressed by 5MPa more in the right branch.

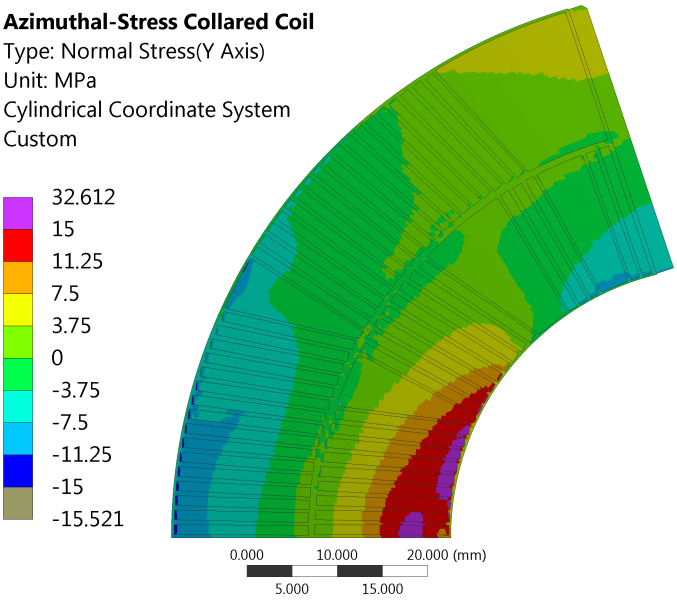

Stress / MPa	IL-pole	OL-pole	IL-midplane	OL-midplane
Left Branch				
Trans.	-45	-40	-35	-40
EQV	13	20	22	30
Right Branch				
Trans.	-46	-45	-32	-44
EQV	10	26	22	28

- shown plot is for a lateral shim of 0.2mm
- plot is showing the left branch

Figure 5.19: DS11T welding operation influence on the azimuthal stress in the coil, delta between LS 2 and LS 3

5.1.5 Cool Down to 1.9K (LS 4)

The change in temperature from 295K to 1.9K causes all components to shrink according to their thermal contraction coefficient. The stainless steel shell with a thermal secant coefficient of $9.97e^{-6}$ shrinks more than the yoke

made from *Magnetil* with a coefficient of $7.22e^{-6}$, the difference is around 26%. The thermal contraction of the collared coil is larger than the one of the yoke. This balance of collared coil and shell shrinkage compared to the yokes' shrinkage results in similar stress levels between 295K and 1.9K in the coil. The difference in azimuthal stress of the magnet can be seen in Figure 5.20, where the stress caused by the change of temperature is shown. Compared to the state at 295K the tension stress in azimuthal direction in the shell is increased, while the yoke is more compressed. In Figure C.32 and Figure C.31 the change in radial stress and the EQV stress is shown. The effect of the thermal shrinkage is shown in Figure 5.21.

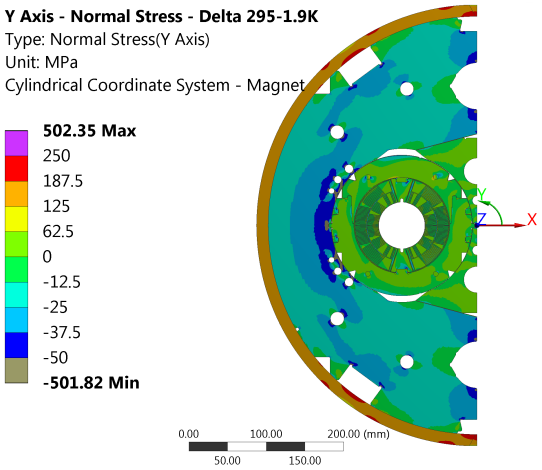

Figure 5.20: Azimuthal stress difference between 295K and 1.9K

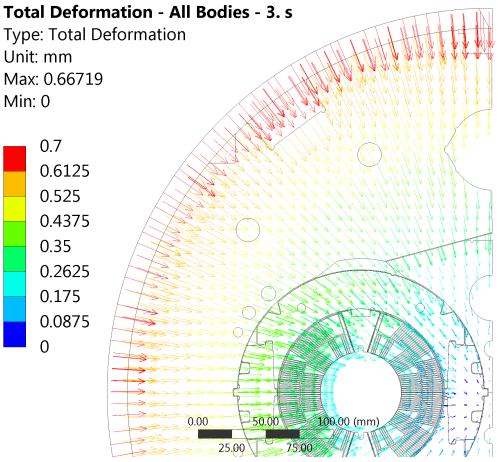

Figure 5.21: Displacement between 295K and the cool down to 1.9K

As described before the stresses in the coil itself do not change by a large margin. The maximum change in EQV stress per cable is in the right branch inter layer cable with an increase of 12MPa, the azimuthal compression is increased by -7MPa on the left branch in the outer layer cable.

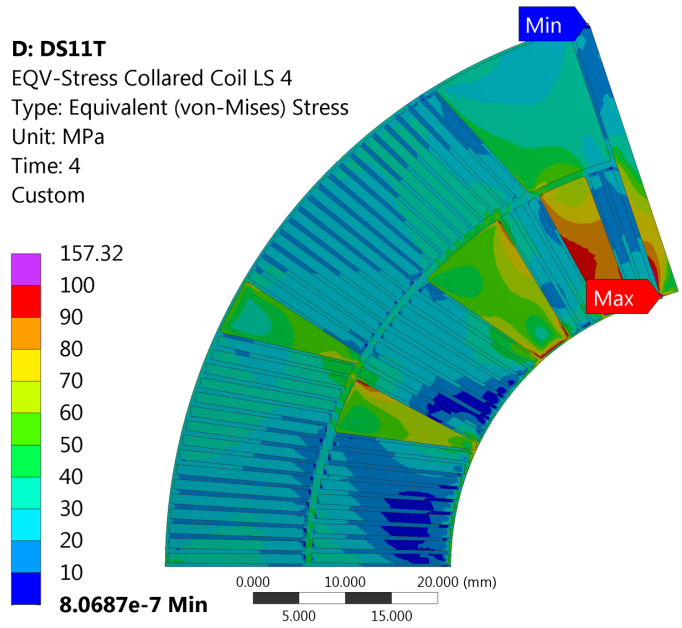

Stress / MPa	IL-pole	OL-pole	IL-midplane	OL-midplane
Left Branch				
Trans.	-49	-30	-30	-47
EQV	23	24	31	38
Right Branch				
Trans.	-50	-37	-32	-44
EQV	22	28	31	33

- shown plot is for a lateral shim of 0.2mm
- plot is showing the left branch

Figure 5.22: DS11T EQV stress in the coil after the cool down to 1.9K, at LS 4

5.1.6 Powering 12.8kA (LS 5)

The final and most important loading step is the excitation of the coils, in case of the DS11T with a current of 12.8kA. The additional boundary condition of this load step is the mapping of the body force, Figure C.33,

representing the EM-forces acting on the coil. The EM-Force are acting on the conductor and forcing the two coil arches apart. The coil pushing horizontally on the collars causes them to deform in such a way that the collared coil is fully in contact with the yoke. In Figure 5.23 the pressure between the yoke and the collars is shown, if compared to Figure 5.17 it is clearly visible how the collars are supported by the yoke. The radial stresses in the collared coil show, Figure 5.24, that the collars are in compression where they are in contact with the yoke. The coil, apart from the wedges, is in radial compression. In Figure C.35 and Figure C.36 the horizontal and vertical normal stresses are shown, here the contribution on carrying the load by the short collars in the horizontal direction is visible. Between the two rivits the short collar is in tension.

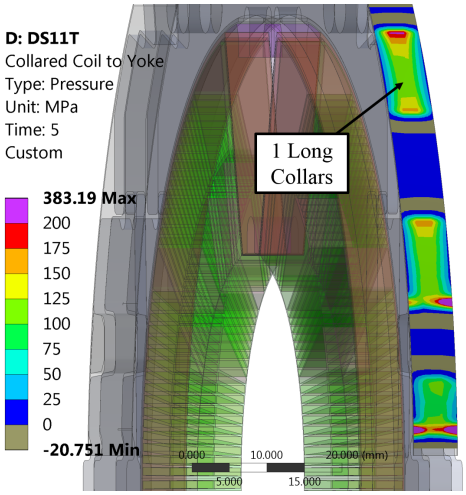

Figure 5.23: Contact pressure between the collared coil shim and the yoke during powering, LS 5

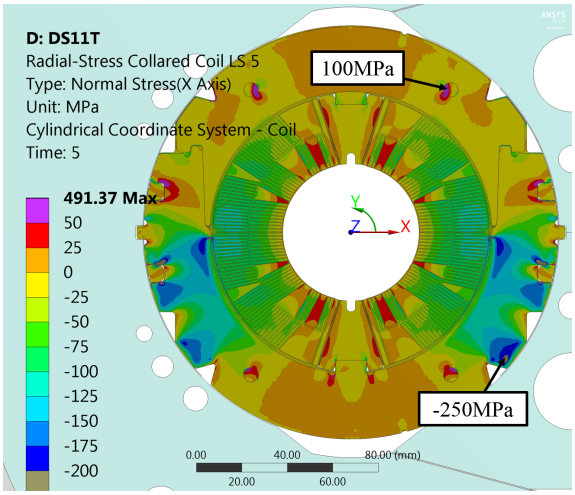

Figure 5.24: Radial normal stress in the collared coil during powering, LS 5

Due to the EM-forces the EQV stresses reach a local maximum on the inner layer midplane cable of 95MPa, the maximum stress is in the wedge of the coil, Figure 5.25. All cables are on average under compression, due to the asymmetry of the yoke the outer layer pole cable is more compressed on the left branch than on the right. The transversal compression reaches an overall maximum of -116MPa on the inner layer midplane.

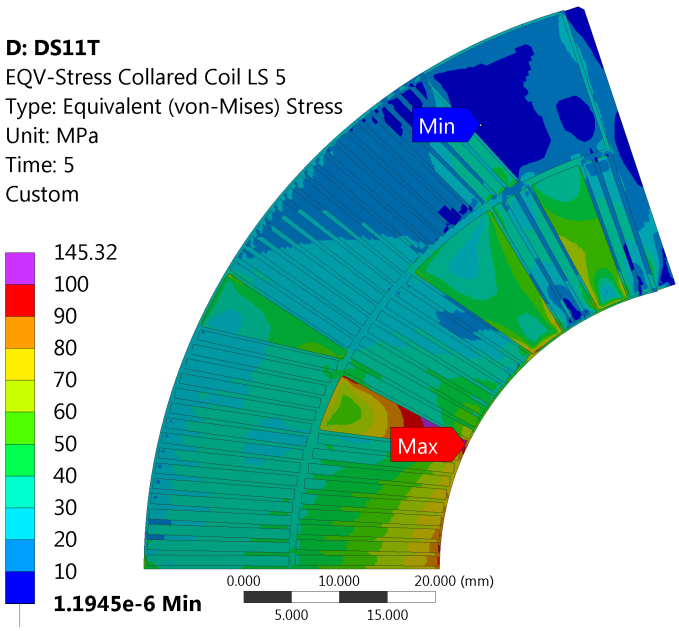

Stress / MPa	IL-pole	OL-pole	IL-midplane	OL-midplane
Left Branch				
Trans.	-13	-20	-113	-87
EQV	14	12	48	44
Right Branch				
Trans.	-11	-9	-116	-85
EQV	16	34	50	43

- shown plot is for a lateral shim of 0.2mm
- plot is showing the left branch

Figure 5.25: DS11T EQV stress in the coil during powering 12.8kA, at LS 5

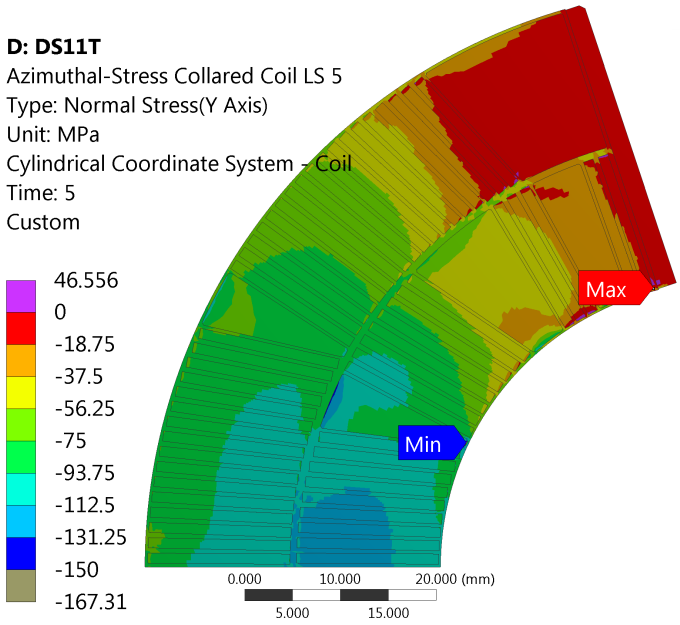

The DS11T coil is at 12.8kA almost fully under compression. In local segments close to the cable short edge tension is present. The azimuthal compression reaches its maximum on the inner layer close to the outer layer.

Figure 5.26: DS11T azimuthal normal stress in the coil during powering 12.8kA, at LS 5

conclusion Multiple parts of the DS11T structure are exposed to stresses high enough to reach the yielding limit of the components. The contacts surfaces of the collars, with the collaring tool, reach limits over 450MPa. The collaring shoe reaches levels of stress above 350MPa. A similar case is the yoke insert, on the small alignment groove for the collars the stress is above 400MPa during the welding operation. A critical component, the collaring key, is not exposed to stresses above its yielding limit.

5.2 MQXF

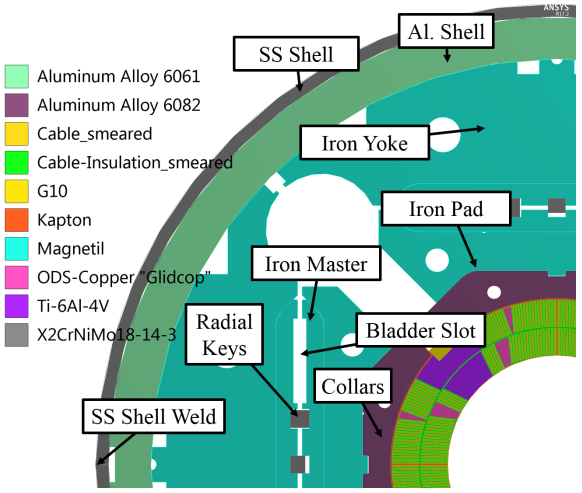

Figure 5.27: Materials used in the MQXF-model

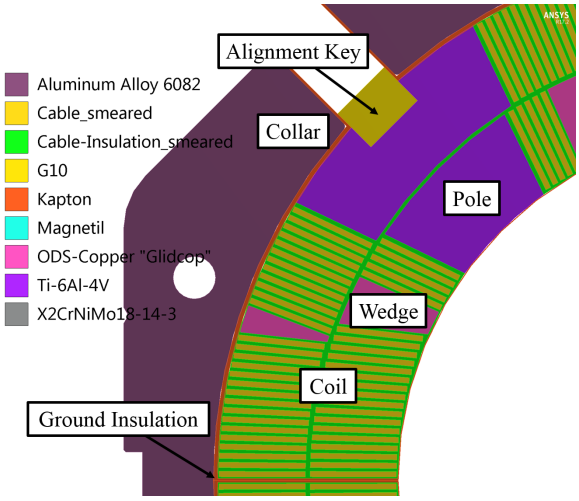

Figure 5.28: Materials used in the MQXF-model, focus coil

Geometry For the MQXF the full cross-section was used, with four independent coils, Figure 5.27. Each coils is surrounded by its own layer of Kapton made ground insulation. The coils poles are tangentially aligned with the collars by the G10 made alignment key, Figure 5.28. The coils are directly in contact via the ground insulation with the collars. The collars are pushing on the iron pad which is in contact with the iron master. The iron master packs are the ones displaced by the bladders to generate the pre-stress. The iron yoke connects directly the aluminium

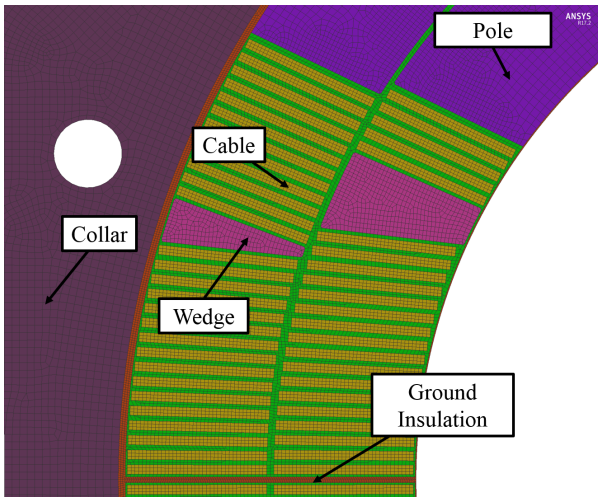

Figure 5.29: Meshing used in the MQXF-model

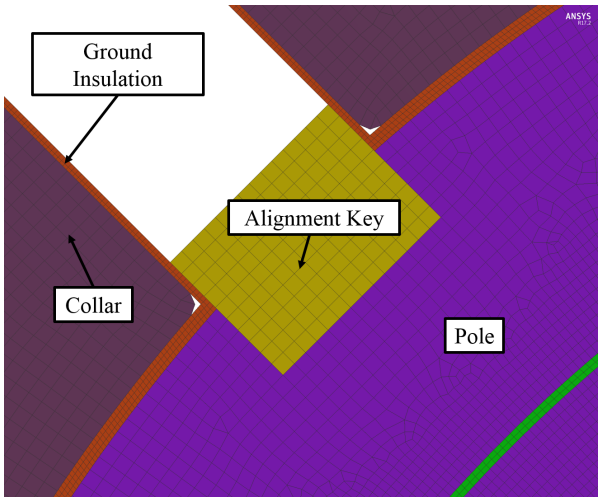

Figure 5.30: Detailed meshing, Kapton & key

shell with the iron master.

Mesh Similar to the DS11T magnet model the coils are a uni-body with all nodes merged, this also includes the pole for the MQXF, the meshing is shown in Figure 5.29 and in more detail Figure C.49. In the longitudinal direction the whole model is made from one layer of elements. Only one layer is needed to represent the magnet cross-section since the model is uni-form in the depth. The mesh size transition between the iron masters and the adjacent pads seems to be harsh but has no effect due to the increase of contact elements.

Contacts The contact details of the DS11T-model are given in Table A.5 and Table A.6, a graphical overview is shown in Figure 5.31. The coils are *bonded* (CN 1) to the ground insulation. The only solvable configuration has been found to be with a *no separation* (CN 17) contact between the ground insulation and the collars, even though a frictionless contact would be more representative. Also the collar to the iron pad contact is done with a *no separation* (CN 19) contact. The radial inner and outer side of the iron master are *bonded* (CN 2 & 5) to the next yoke part. The aluminium shell has a *frictional* (CN 6 & 7) contact with the yoke and the stainless steel shell, $\mu = 0.2$. Concerning the keys of the iron master, the contact of the tangential keys is though out the whole simulation active. The tangential key has *bonded* (CN 4) contact to the outer iron master, the contact with the inner iron master is a *no separation* (CN 20).

5.2.1 Load Steps (LS)

Load Step 2 - de-pressurisation bladders, placing of the keys The pressure in the bladders gap is continuously reduced during this load step. Before the first iteration the contact for the radial keys are activated. The "thickness" of the radial key can be changed with the contact offset of CN 13 - 16. The initial geometry with an offset of 0 would generate no pre-stress at room temperature.

Load Step 3 - welding of the stainless steel shell Similar to the welding of the shell in the DS11T, the weld is cut in the center and two resulting surfaces are getting displaced to simulate the welding shrinkage. For the MQXF a total weld shrinkage of 0.6mm is foreseen. It is half of the DS11T due to half the thickness of the shell.

Load Step 4 - cool down to 1.9K The only remaining boundaries acting is the vertical and horizontal fixed displacement of the stainless steel shell quadrants. Which allow the assembly to shrink and grow but not to rotate. The thermal condition causes all parts to shrink according to the thermal contraction of the individual material. Which in case of the MQXF causes the aluminium shell to shrink more than the assembly surrounded by the shell. There fore the pre-stress in the magnet is increasing during the cool down.

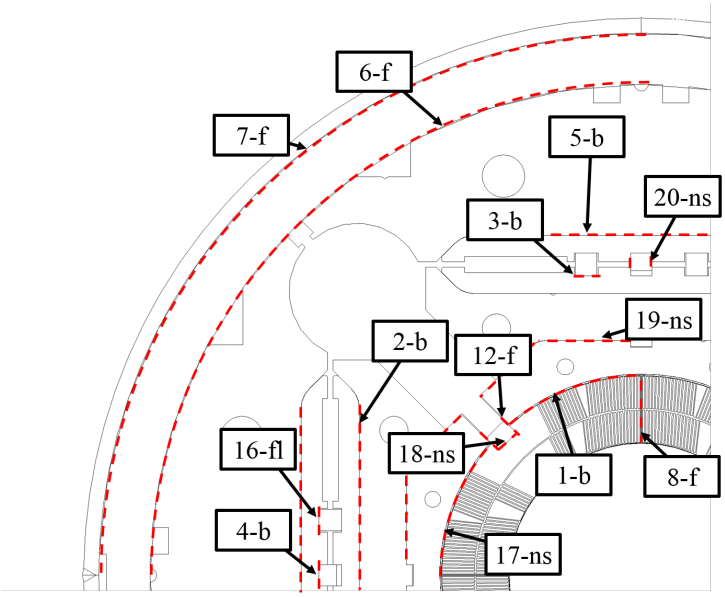

Figure 5.31: MQXF: overview of the contacts; b-bonded, f-frictional, fl-frictionless, ns-no separation, r-rough

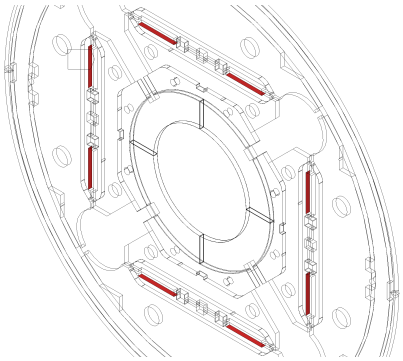

Figure 5.32: the eight locations for the the pressurization of the bladders

Load Step 1 - pressurisation bladders The contact of the radial keys (CN 13-16) is deactivated. The coils and the collar assembly are only constrained by the use of weak springs and the tangential keys. The stainless steel shell is fixed in The contact between the coils can be offset to simulate a different thickness of the midplane. Pressure is applied to the 16 surfaces which belong to the eight bladder slots of the MQXF. This pressure is widening the gap between the iron masters. The modelling of a detailed bladder was not considered, the application of hydrostatic pressure in the gap on the concerning surfaces is for this approach simplified enough. It needs to be ensured that the gap opening due to the pressurisation is big enough to host the radial key.

Load Step 5 - excitation of the coils The imported body force is now applied on the bodies of the cable. For the MQXF the body force is corresponding to a powering with 19.1kA.

5.2.2 Nominal Case

To adapt the pre-stress of the coil the radial key size in the MQXF can be altered. In Figure 5.33, the response for the transversal cable stress to the change of shim thickness on the radial keys is shown during powering. The sensitivity of the inner layer pole cable, compared to the outer layer pole cable, to the change of shim on the key is five times bigger. On average, over the range of 1mm, for the change of 0.1mm in shim thickness the transversal stress on the inner layer pole cable changes by 14MPa for the outer layer it is 3MPa, during powering. If the key excess is changed by 0.7mm the goal of keeping the pole cable compressed by 10MPa during powering is reached. Therefore a shim with the thickness of 0.7mm was chosen for the nominal case.

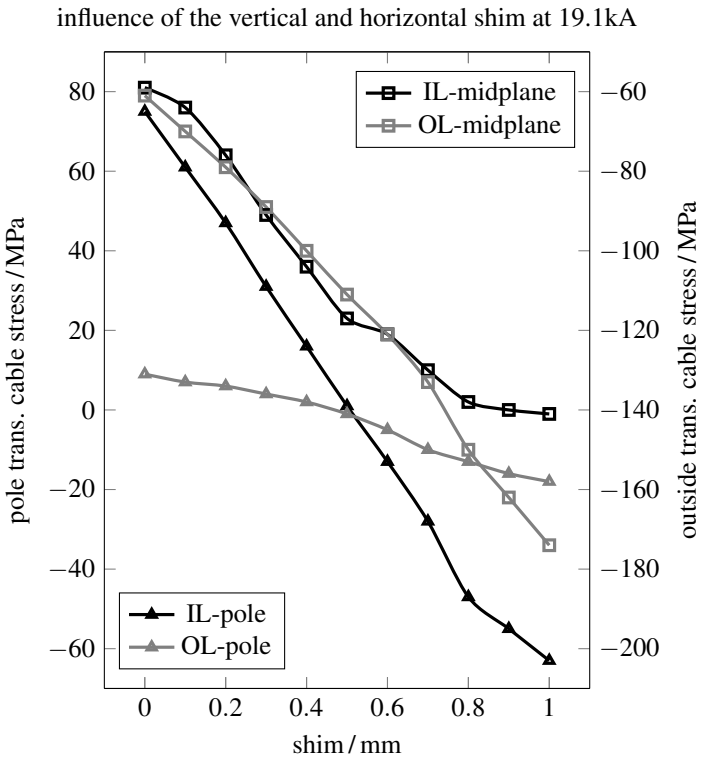

Shim / mm	IL-pole	OL-pole	IL-midplane	OL-midplane
0	75	9	-59	-61
0.1	61	7	-64	-70
0.2	47	6	-76	-79
0.3	31	4	-91	-89
0.4	16	2	-104	-100
0.5	1	-1	-117	-111
0.6	-13	-5	-121	-121
0.7	-28	-10	-130	-133
0.8	-47	-13	-138	-150
0.9	-55	-16	-140	-162
1	-63	-18	-141	-174

Values are the average transversal stress of the cable next to the pole and on the outer sides of the coil

Figure 5.33: MQXF response of the average transversal stress per cable for the vertical and horizontal shim

5.2.3 Pressurisation of the Bladders (LS 1)

The pressure representing the bladder is applied on the eight slots shown in Figure 5.32, in the normal direction of the surface of iron masters. A pressure of 50MPa is needed to open the key slot wide enough to fit the keys with 0.7mm excess, the minimum gap opening is 0.33 and maximum 0.59mm, in Figure 5.34 the total displacement at maximum pressure is shown. During the pressurisation the distance between the single collars is decreasing, the alignment key made from G10 is trapped. This causes a EQV stress build up to 280MPa.

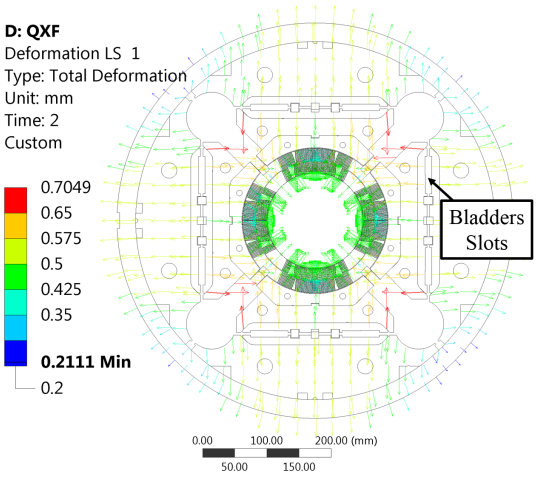

Figure 5.34: Total deformation, bladder pressure of 50MPa, LS 1

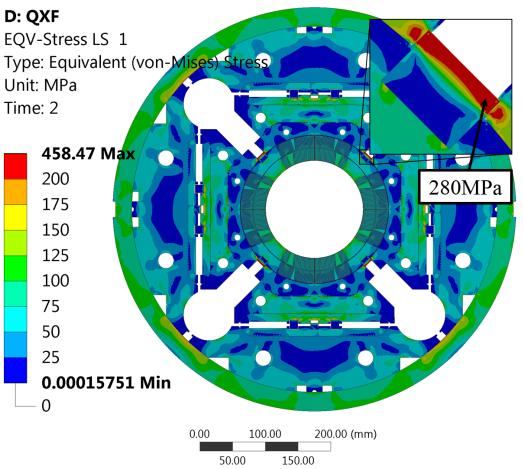

Figure 5.35: EQV stress during the bladder pressurisation, LS 1

In Figure C.51 and Figure C.52 the radial and azimuthal pressure of the magnet during pressurization is shown, the shell is on average by 110MPa in tension while the coils are compressed by 88MPa. This was calculated using the azimuthal normal stress over the entire respective body. The average EQV stress in the cable is reached in the inner layer midplane 87MPa.

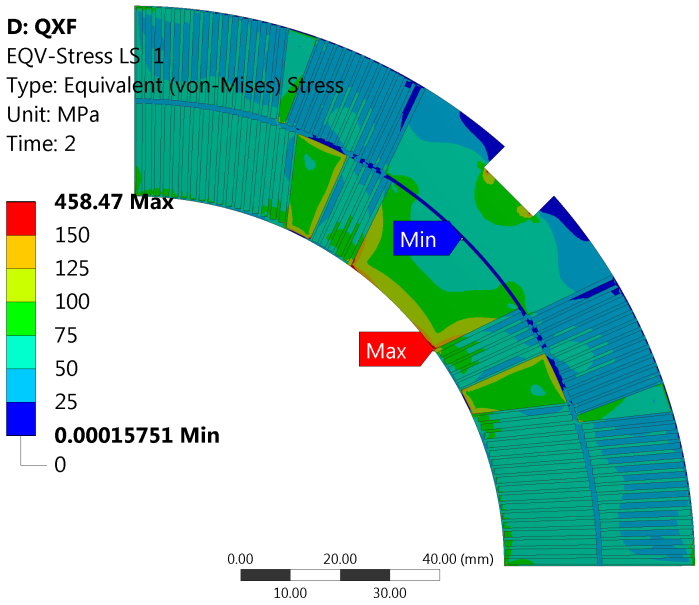

Stress / MPa	IL-pole	OL-pole	IL-midplane	OL-midplane
Trans.	-78	-61	-80	-79
EQV	62	25	87	55

- shown plot is for a radial key excess of 0.7mm

Figure 5.36: MQXF EQV stress in the coil during pressurisation of the bladders at LS 1

5.2.4 De-pressurisation Bladders and placing of the Keys (LS 2)

The pressure in the locations of the bladders is removed to 0MPa. In the first iteration of this loading step the contact between the radial keys and the iron master is activated. With the decreasing pressure the contact is closed. The EQV Stress in the radial keys reaches up to 300MPa on the edges and in the center of the key 130MPa.

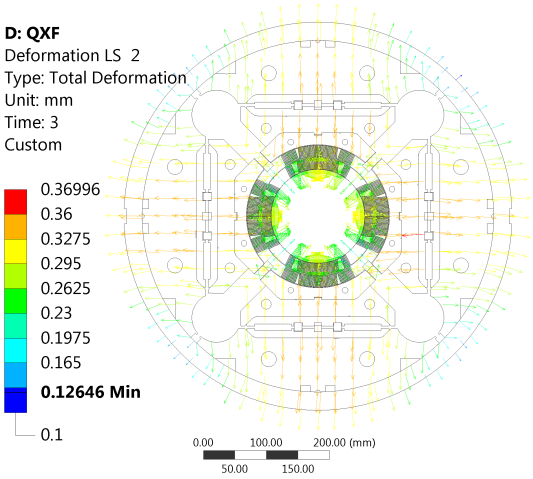

Figure 5.37: Total deformation, keys placed, bladders de-pressurised, LS 2

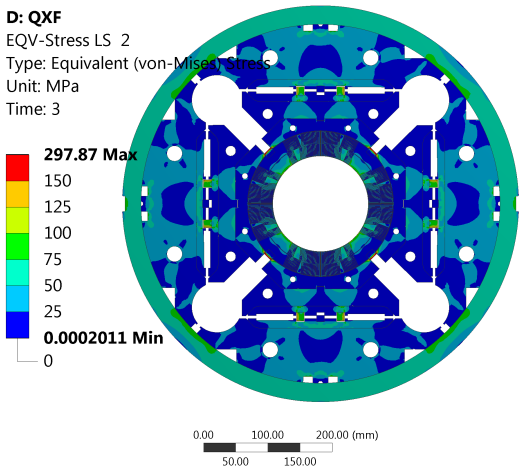

Figure 5.38: EQV stress, keys placed, bladders de-pressurised, LS 2

The stresses in the coils decrease after the de-pressurisation. The largest difference, is the average transversal stress in the inner layer midplane cable by 65MPa and the EQV stress by 68MPa.

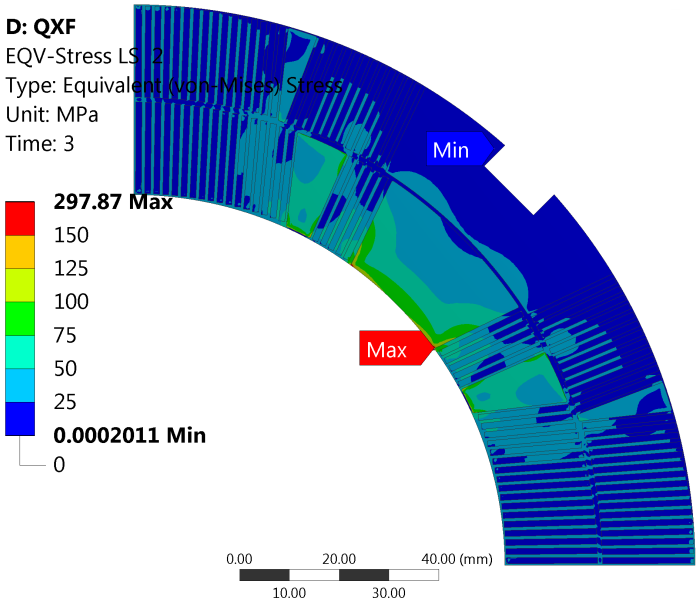

Stress / MPa	IL-pole	OL-pole	IL-midplane	OL-midplane
Trans.	-52	-9	-15	-28
EQV	38	11	19	17

- shown plot is for a radial key excess of 0.7mm

Figure 5.39: MQXF EQV stress in the coil during pressurisation of the bladders at LS 2

5.2.5 Welding of the Shell (LS 3)

The welding of the stainless steel shell helps to further compress the magnet and the coils. The transversal compression in the cable further increases and reaches a maximum of -80MPa on the inner layer pole in compression. After the welding the average azimuthal stress in the shell is 230MPa, the stress in the aluminium shell decreases from 65 to 35MPa after the welding. The average coil compression is in creasing from -38MPa to -59MPa after the welding.

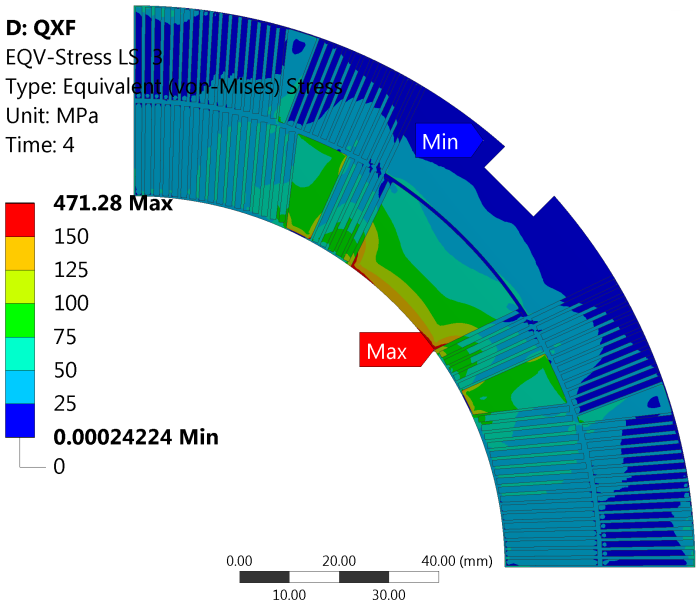

Stress / MPa	IL-pole	OL-pole	IL-midplane	OL-midplane
Trans.	-80	-12	-36	-48
EQV	66	15	26	29

- shown plot is for a radial key excess of 0.7mm

Figure 5.40: MQXF EQV stress in the coil after the welding of the shell at LS 3

5.2.6 Cool Down to 1.9K (LS 4)

During the cool down the aluminium shell shrinks around the assembly. The thermal secant coefficient of the shell is 1.44e^{-5} which is twice as large as the thermal coefficient of the yoke made from *Magnetil*. The total deformation

after the cool down is shown in Figure 5.37, the difference between the two layers of the irons masters is due to the interfering keys (0.7mm). The EQV stress in the radial keys reaches up to 350MPa in the center and 490MPa locally. The total deformation after the cool down is shown in Figure 5.41, resulting EQV stresses in Figure 5.42. The EQV stress in the stainless steel decrease.

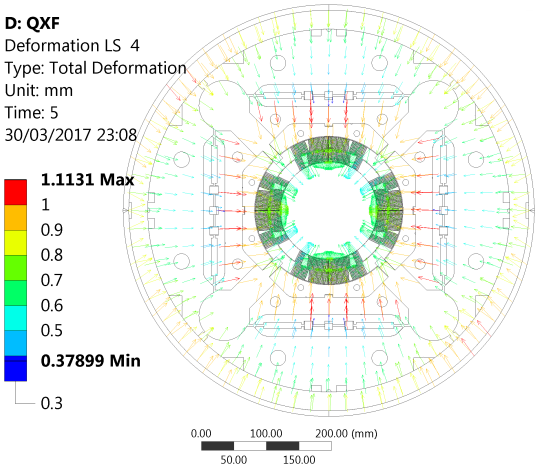

Figure 5.41: Total deformation, at 1.9K LS 4

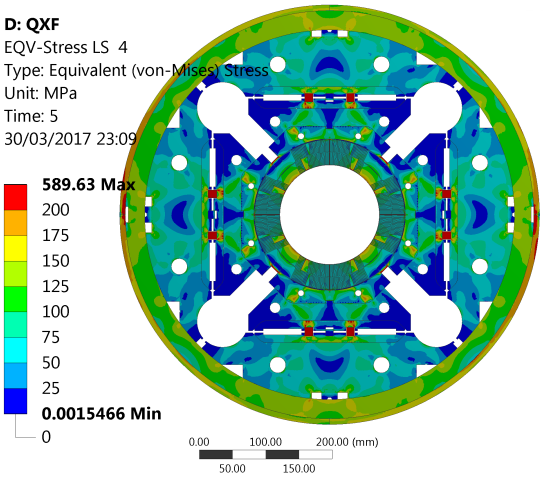

Figure 5.42: EQV stress, at 1.9K, LS 4

The compression of the coils reach a maximum after the cool down of the magnet. Up to -157MPa on average transversal compression is present on the inner layer pole cable, the EQV stress is 128MPa. This is an increase of -77MPa in compression.

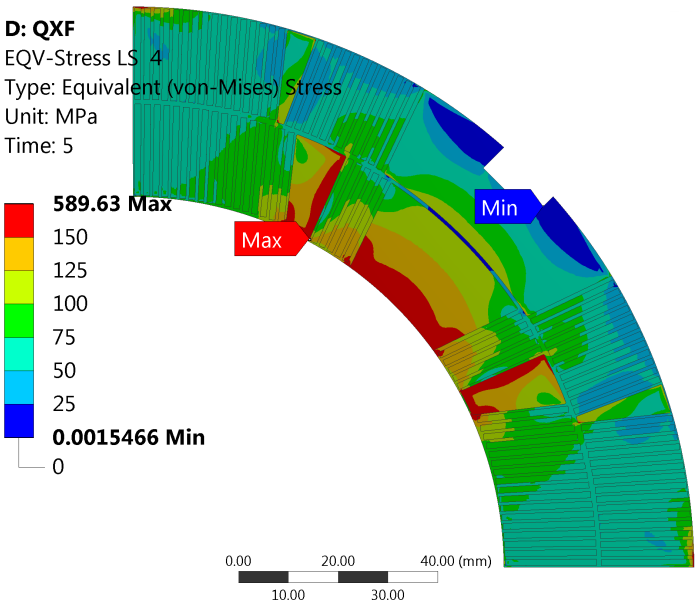

Stress / MPa	IL-pole	OL-pole	IL-midplane	OL-midplane
Trans.	-157	-31	-64	-93
EQV	128	50	61	68

- shown plot is for a radial key excess of 0.7mm

Figure 5.43: MQXF EQV stress in the coil after the cool down to 1.9K at LS 4

5.2.7 Powering 19.1kA (LS 5)

In the final load step the elector mechanical forces are mapped as body forces on the conductor, field and body forces are shown in Figure C.63. The EM-forces are causing the coil branches to compress against each other and are pulling the cables away from the pole. The resulting deformation is shown in Figure 5.44. This outward bending motion of the coil around the pole causes the compression on the inner layer to decrease, Figure 5.45.

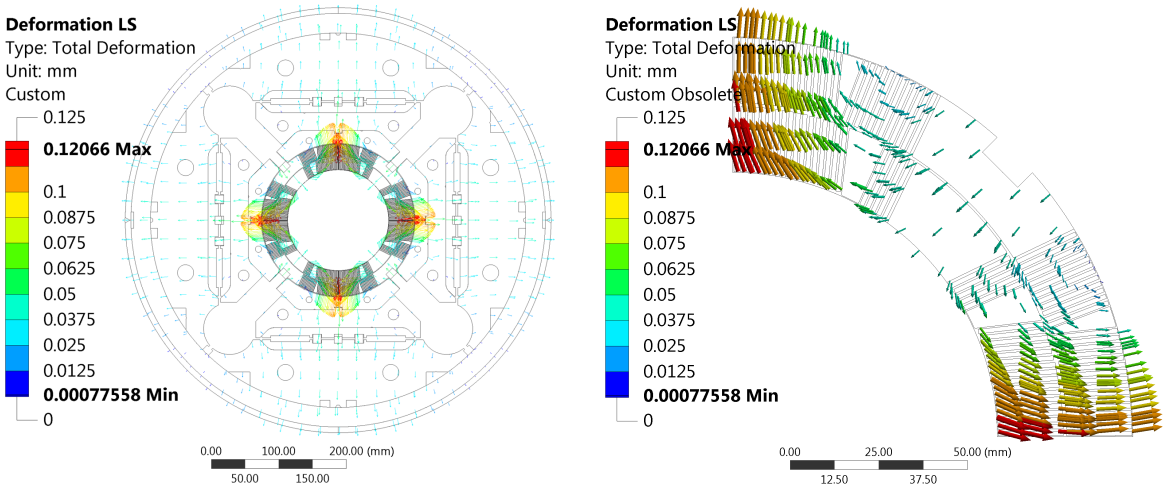

Figure 5.44: Deformation due to the EM-forces at 19.1kA, LS 5

Due to the powering the transversal stress is decreased by -129MPa on the inner layer pole cable. The change for the outer layer pole cable is only -21MPa. The inner radius of the pole is completely in tension during the powering.

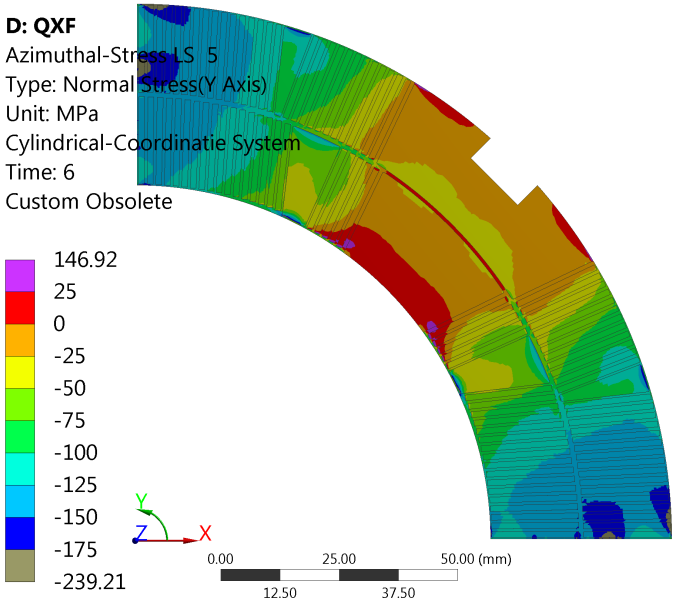

Stress / MPa	IL-pole	OL-pole	IL-midplane	OL-midplane
Trans.	-28	-10	-130	-133
EQV	18	34	109	64

- shown plot is for a radial key excess of 0.7mm

Figure 5.45: MQXF azimuthal stress in the coil at 19.1kA at LS 5

conclusion The coil of the MQXF is fully compressed during the excitation. The midplane is under a high compression of 130MPa. The keys, transmitting the forces from the shell to the coil, are possible exposed to yielding, stresses of 400MPa are reached. The alingment key of the coils is compressed by the collars during the inflation of the bladders, compression stresses of 280MPa are reached. These components should be carefully examined, after a test of the magnet.

5.3 SMC-11T

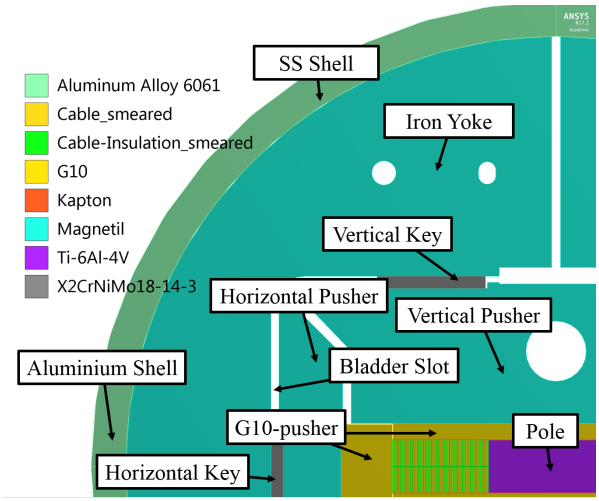

Figure 5.46: Materials used in the SMC-11T-model

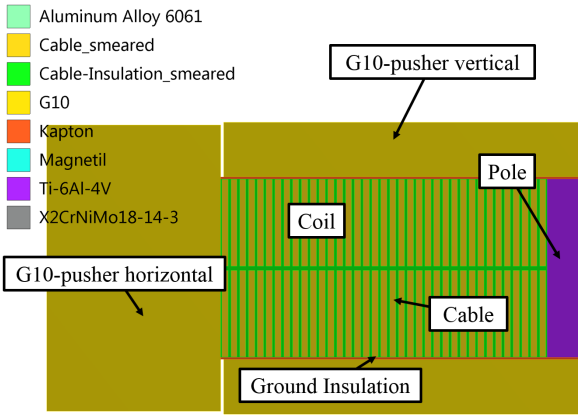

Figure 5.47: Materials used in the SMC-11T-model, focus coil

Geometry Similar to the MQXF, for the simulation of the SMC-11T the full cross-section geometry was used. The coil is represented by its complete coil consisting out of four coil blocks, and the pole in the center, the SMC coils have no wedge. The coil is one body, where all nodes are merged. Adjacent to the coil the ground insulation is present on the top and bottom of the coil, separating the vertical G10-pusher from the coil. The horizontal pad is pushing directly via the horizontal G10-pusher on the coil. The vertical pad and the horizontal pad are similar to the MQXF floating in the structure and are held in place by the inserted keys. Two gaps for the bladders per horizontal pad and one for the vertical pad are foreseen. All of the bladders are pushing via the iron yoke directly onto the aluminium shell.

Mesh The meshing of the SMC-11T model is very similar to the one applied for the MQXF model. The cable is represented by four layers in the transverse direction and two for the insulation. in longitudinal direction only one layer of elements is used.

Contacts The contact details of the DS11T-model are given in Table A.7, a graphical overview is shown in Figure 5.50. Also in this model the ground insulation is *bonded* (CN 1) to the coil. Both contacts of the vertical and horizontal pushers on the coils are *frictionless* (CN 6 & 7). The pushers are *bonded* (CN 2 & 3) to the respective

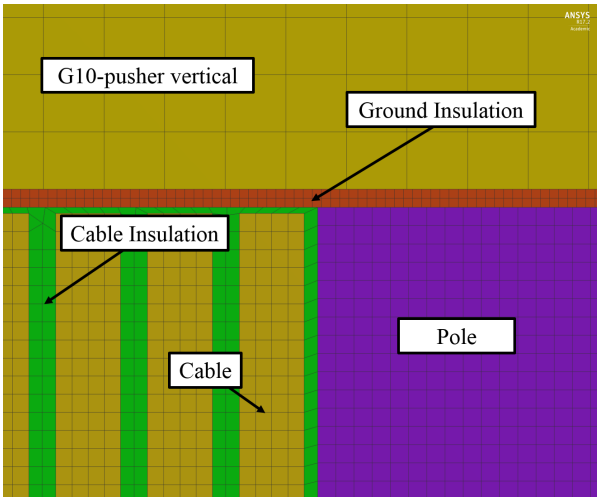

Figure 5.48: Meshing used in the SMC-11T-model

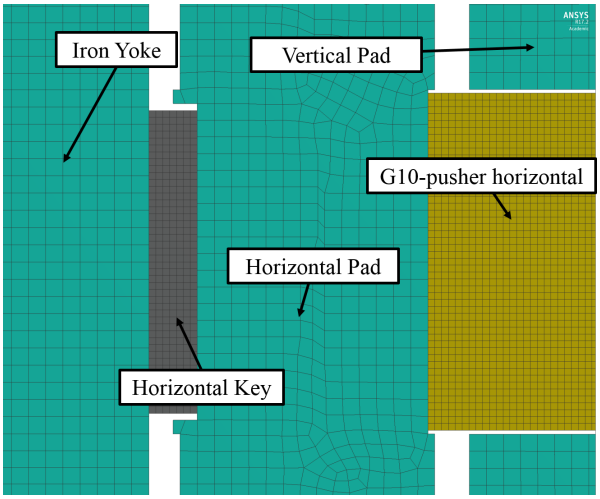

Figure 5.49: Detailed meshing

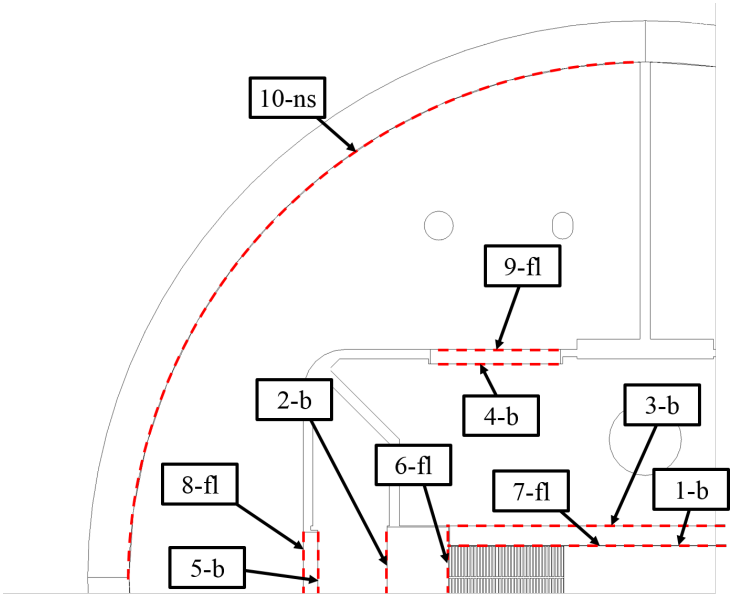

Figure 5.50: SCM-11T: overview of the contacts; b-bonded, f-frictional, fl-frictionless, ns-no separation, r-rough

iron plates. On the surface closer to the center the keys are *bonded* to the iron plates (CN 4 & 5), the opposing contact with iron yoke is *frictionless* (CN 8 & 9). The contacts 8 & 9 are also the ones which can be activated or deactivated. The aluminium shell is connected with a *no separation* contact the the iron yoke (CN 10).

5.3.1 Load Steps (LS)

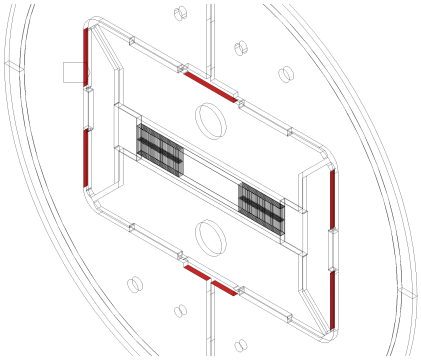

Figure 5.51: the six locations for the the pressurization of the bladders

Load Step 1 - pressurisation bladders The contact of the horizontal and vertical keys (CN 8 & 9) are deactivated. Pressure, representing the bladders, is applied on the adjacent surfaces of the bladder slots, shown in Figure 5.51. The coil-pusher assembly is only supported by the pressure boundary. The pressure linearly increases to the set maximum value.

Load Step 2 - de-pressurisation bladders, placing of the keys The pressure in the bladders gap is continuously reduced during this load step. The contact CN 8 & 9 is activated before the first iteration. During the de-pressurisation the contact checks in each iteration its status. During the de-pressurisation the all six contact surface are getting fully in contact. The remaining pre-stress in the coil is determined by the given offset to the key contacts.

Load Step 3 - idling As mentioned before no loads are applied during LS 3 in the SMC model.

Load Step 4 - cool down to 1.9K The SMC has no pressure vessel, therefore also no welding is necessary. To remain compliance with the other models the Load Step 3 is just a place holder. As in the MQXF the shell is cut in four locations, the cut in vertical direction is blocking motion in the horizontal direction, the cut in horizontal vice

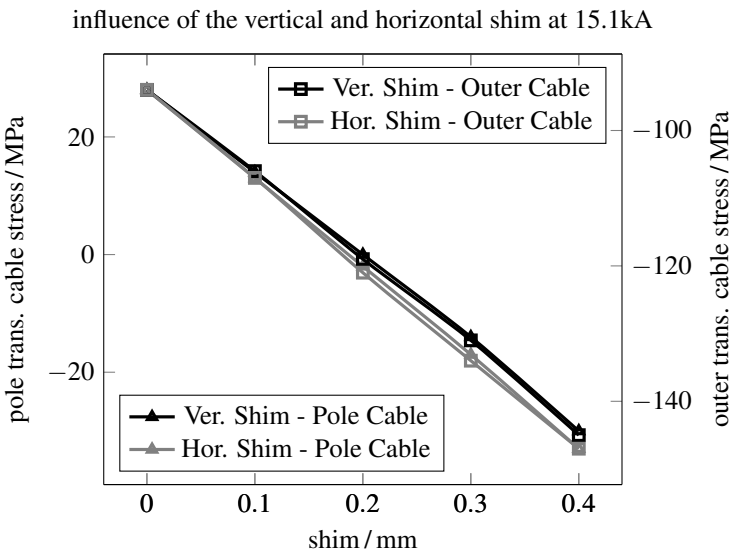

Shim / mm	Ver. Shim - Pole Cable	Hor. Shim - Pole Cable	Ver. Shim - Outside Cable	Hor. Shim - Outside Cable
0	28	28	-94	-94
0.1	14	13	-106	-107
0.2	0	-2	-119	-121
0.3	-14	-17	-131	-134
0.4	-30	-33	-145	-147

Values are the average transversal stress of the cable next to the pole and on the outer sides of the coil

Figure 5.52: SMC11T response of the average transversal stress per cable for the vertical and horizontal shim

versa. Thereby the model is constrained in all three dimensions. During the cool down the pre-stress in the coil is increasing due to the shrinkage of the aluminium shell.

Load Step 5 - excitation of the coils The imported body force is now applied on the bodies of the cable. For the SMC-11T the body force is corresponding to a powering with 15.1kA.

5.3.2 Nominal Case

The SMC has two different locations to tune the stress in the coil, one on the Vertical Key and one the Horizontal Key, Figure 5.46. As for the previous simulations both shims were varied to find the case where the pole turn are under -10MPa in compression at maximum current. Both shims were varied in a range form 0 to 0.4mm, the resulting transversal cable stresses are shown in Figure 5.52, a shim of the thickness 0 is corresponding to no interference in the keys at room temperature. The results show a linear behaviour between transversal cable stress and shim thickness. The vertical shim has a very slightly smaller influence, comparing shims of 0.4mm the difference is only 3MPa in transversal cable stress. Also should be noted that the differences in transversal stress between pole cable and the outer cable is for all cases nearly the same, 120±2MPa. To ensure that with the choice of shimming no unnecessary high EQV stresses are created the effect of the shim size was checked in Figure 5.53. It was also found that a combination of vertical and horizontal shim is resulting in the same result than individual shims with the same total thickness. For example a vertical shim of 0.1 and a horizontal shim of 0.2mm would give the same transversal pre-stress than a horizontal shim of 0.3mm. For this analysis a horizontal shim of 0.2mm and a vertical shim of 0.1mm will be used for the nominal case.

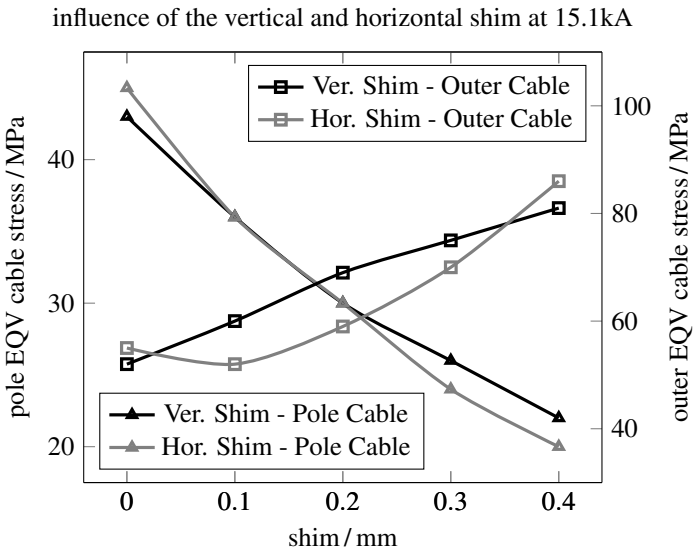

Shim / mm	Ver. Shim - Pole Cable	Hor. Shim - Pole Cable	Ver. Shim - Outside Cable	Hor. Shim - Outside Cable
0	43	45	52	55
0.1	36	36	60	52
0.2	30	30	69	59
0.3	26	24	75	70
0.4	22	20	81	86

Values are the average EQV stress of the cable next to the pole and on the outer sides of the coil

Figure 5.53: SMC11T response of the average EQV stress per cable for the vertical and horizontal shim

5.3.3 Pressurisation of the Bladders (LS 1&2)

The opening of the key slots need to be large enough to insert the keys with their specific shims. Even a key with zero interference can only be inserted with a sufficient opening of the gap. In this model a pressure of 30MPa was used for the pressurization of the vertical bladders,LS 1 and 20MPa in the horizontal bladders, LS 2, Figure 5.51. The pressure is applied in the normal direction of the surface on the yoke and the pusher. Calculating from the surface area and the pressures, a vertical force of 1980N and 2620N of horizontal force per mm thickness was applied. In Figure 5.54 and Figure 5.55 the displacement during the pressurization is shown. The minimum gap in the key gap is 0.23mm for the vertical and 0.22mm for the horizontal key.

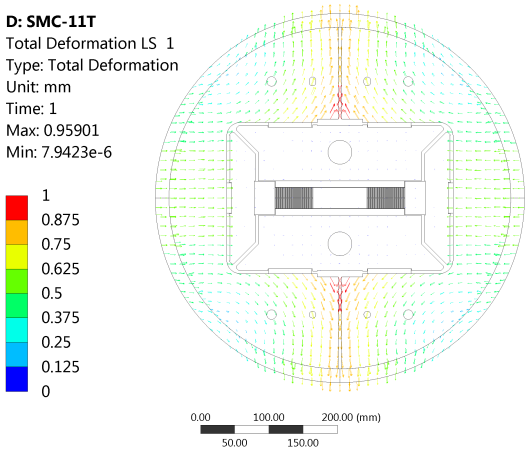

Figure 5.54: Pressurization of the vertical bladder, LS 1

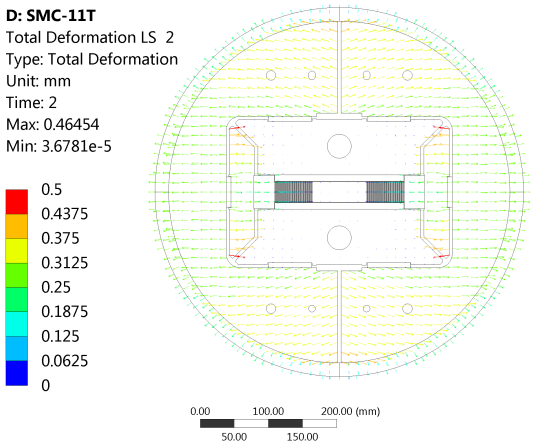

Figure 5.55: Pressurization of the horizontal bladder, LS 2

The EQV stress is concentrated in the inner corners of the yoke during LS 1, Figure 5.56, this is due to the outward bending of the yoke where the inner edges are in tension and the outer diameter in compression Figure C.64. During the pressurization of the horizontal bladders the stress is concentrated in the horizontal pushers.

During the vertical compression of the coil nearly all forces are taken by the pole, the coil is exhibit to very low stresses during this stage. The horizontal compression is acting directly on the coil causing average transversal stresses of -85MPa in the pole cable. In Figure 5.58 the EQV stress in the coil during the horizontal compression is shown.

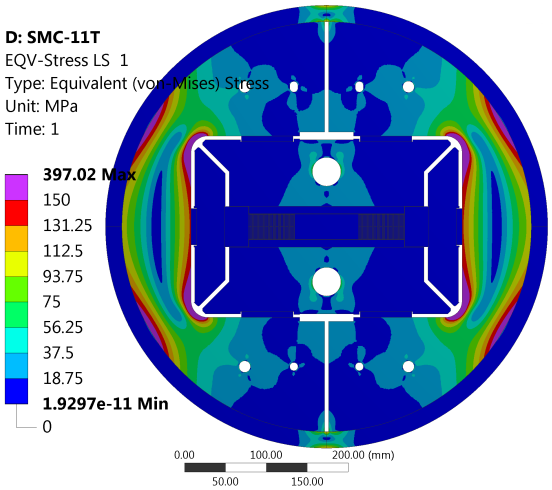

Figure 5.56: EQV stress in the magnet, vertical bladder pressurization, LS 1

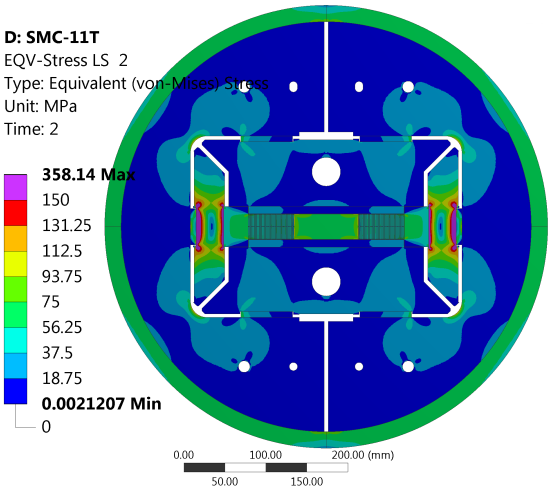

Figure 5.57: EQV stress in the magnet, horizontal bladder pressurization, LS 2

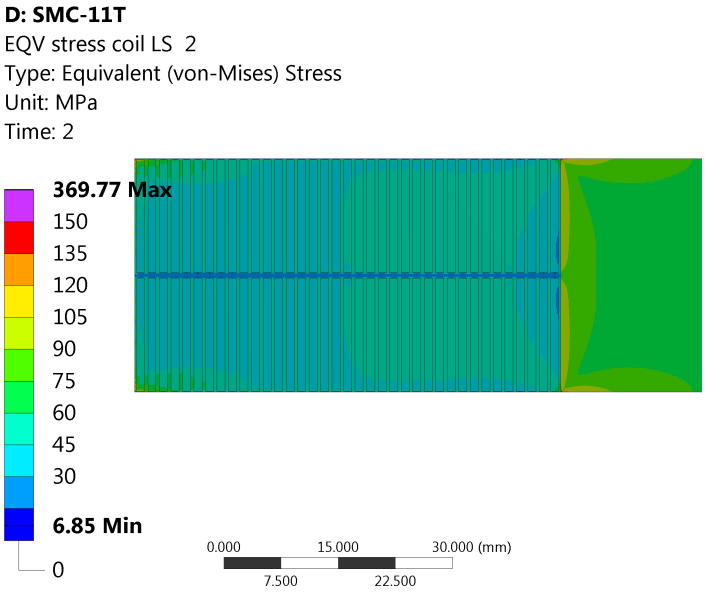

Stress / MPa	pole-cable	outer-cable
vertical pressure		
Trans.	0	0
EQV	11	7
horizontal pressure		
Trans.	-85	-80
EQV	35	53

- shown plot is for a vertical key excess of 0.2mm and a horizontal key excess of 0.1mm

Figure 5.58: SMC-11T EQV stress in the coil during horizontal compression at LS 2

5.3.4 De-pressurisation Bladders and placing of the Keys (LS 3)

After the two pressure cycles, for placing the keys, are finished the pressure is removed back to 0. This causes both key contacts to close, the magnet is at this stage completely self supported and no external forces are acting on it. The aluminium shell of the magnet is ovalized after the placing of the keys by 0.125mm radially, Figure 5.59. The EQV stress is drastically decreasing and is in the yoke concentrated around the keys, Figure 5.60.

The transversal cable stresses are reduced by -60MPa in compression compared to the horizontal pressurization. The EQV stress is decreased 43MPa in the outer cable. In Figure 5.61 the EQV stress in the coil is shown.

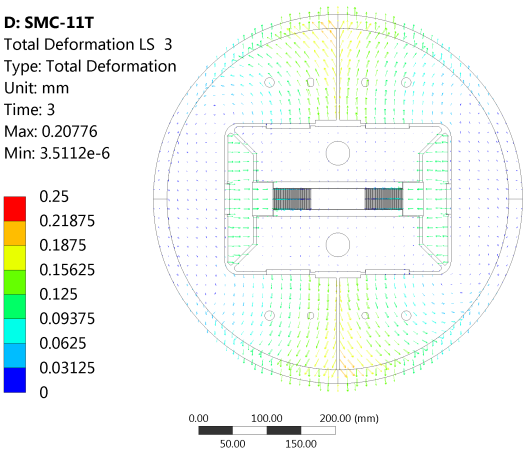

Figure 5.59: Total displacement, after the pressure is released from the bladders, LS 3

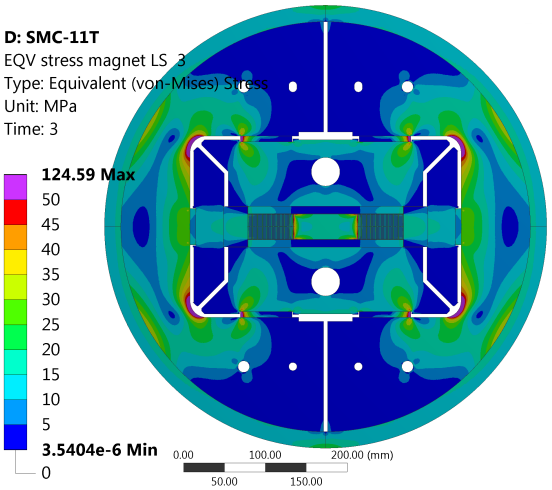

Figure 5.60: EQV stress in the magnet, after the pressure is released from the bladders, LS 3

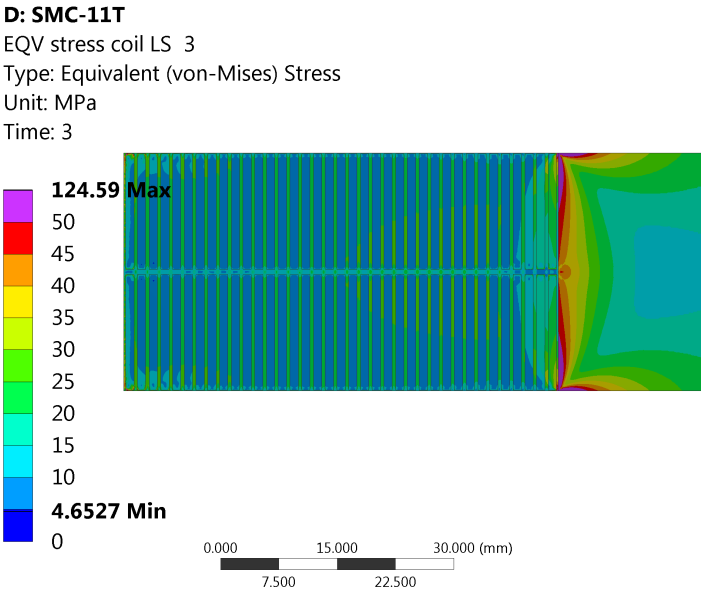

Stress / MPa	pole-cable	outer-cable
vertical pressure		
Trans.	-20	-21
EQV	23	10

- shown plot is for a vertical key excess of 0.2mm and a horizontal key excess of 0.1mm

Figure 5.61: SMC-11T EQV stress in the coil during horizontal compression at LS 3

5.3.5 Cool Down to 1.9K (LS 4)

The thermal shrinkage of the aluminium shell is compressing the whole structure which increases the pre-stress of the coils. The thermal secant coefficient of the shell is $1.44e^{-5}$ which is twice as large as the thermal coefficient of the yoke made from *Magnetil*. The thermal shrinkage of the shell is, like for the MQXF, the main contributor for the pre-stress build up in the coil. In Figure 5.62 the total displacement is shown, the previous present ovalization is still present, due to the thermal contraction the shell is contracted by nearly 1mm in the horizontal direction. In Figure C.68 and Figure C.69 the vertical and horizontal stress in the magnet is shown. The coil nearly purely loaded in the horizontal direction.

Stress concentrations occur on the outer edges of the coil, Figure 5.63. The transversal cable compression increase by approximately 100MPa to -120MPa, pole, and -132MPa on the outer cable. Apart from the stress concentration on the coil edges the stress uniformly distributed in the coil.

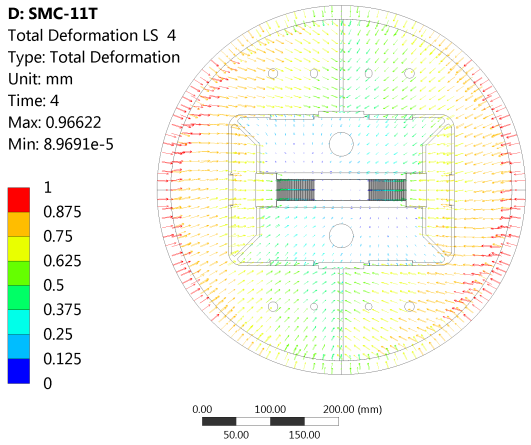

Figure 5.62: Total displacement, after the cool down to 1.9K, LS 4

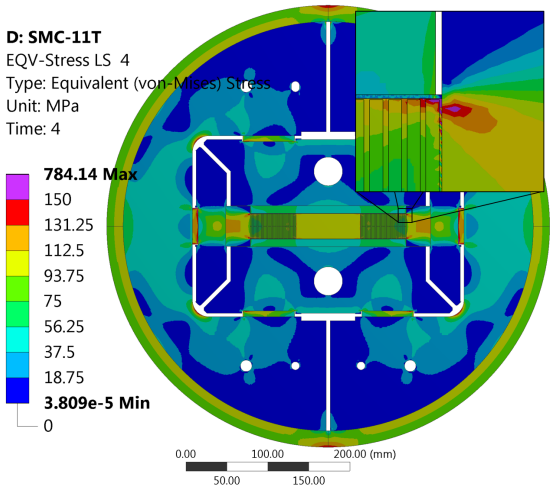

Figure 5.63: EQV stress in the magnet, after the cool down to 1.9K, LS 4

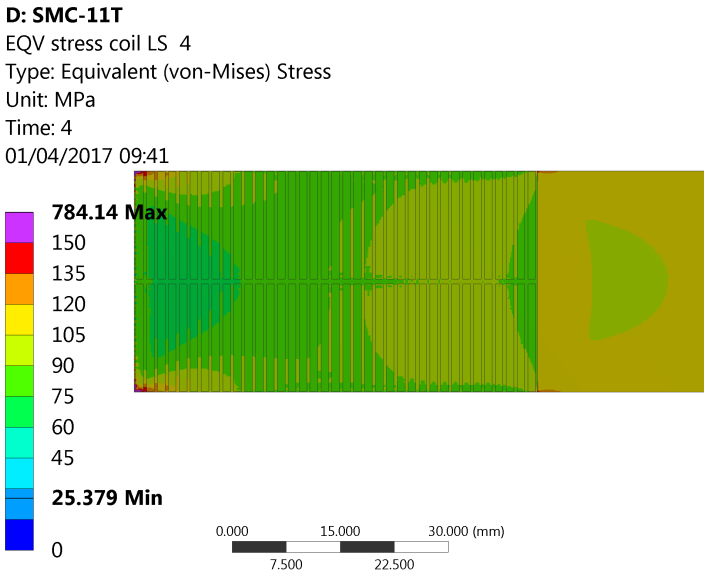

Stress / MPa	pole-cable	outer-cable
vertical pressure		
Trans.	-120	-132
EQV	80	87

- shown plot is for a vertical key excess of 0.2mm and a horizontal key excess of 0.1mm

Figure 5.64: SMC-11T EQV stress in the coil after the cool down to 1.9K, LS 4

5.3.6 Powering 15.1kA (LS 5)

The mapped EM-forces and the related magnetic field is shown in Figure C.66 and Figure C.67. The EM-forces "pull" the coil away from its pole. The resulting stress difference is shown in Figure 5.65, where the tensional stress in the pole cable increase by 120MPa.

The transversal stress in the outer cables is not changed by the EM-Forces. The EQV stress decreases in the pole cable by 53 and in the outer cable by 13MPa. Due to the EM-forces the stress state in the coil is increasingly isotropic stress, thus decreasing the EQV stress. The resulting stresses and the EQV stress in the coil are shown in Figure 5.67.

conclusion The stress distribution of the SMC-coil is very uniform after the cool down. The EM-forces cause the coil to nearly uniaxial compress, which creates a large stress difference due to the powering cycle in the pole turns. Large stress concentrations occur on the outer edges of the coil. Yielding in the mechanical structure might occur during the pressurization of the bladders in the edges of the yoke and in the keys.

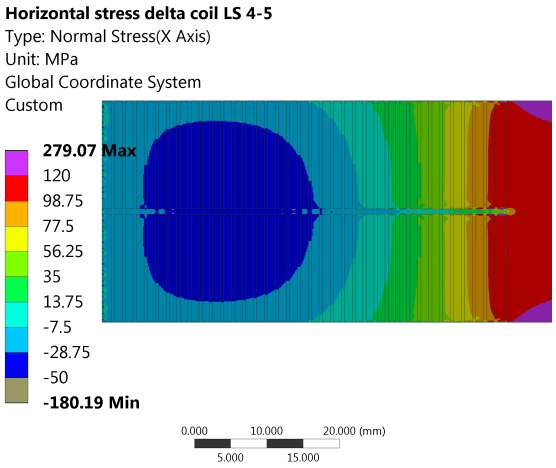

Figure 5.65: Horizontal stress delta due to the EM-forces between LS 4 and LS5

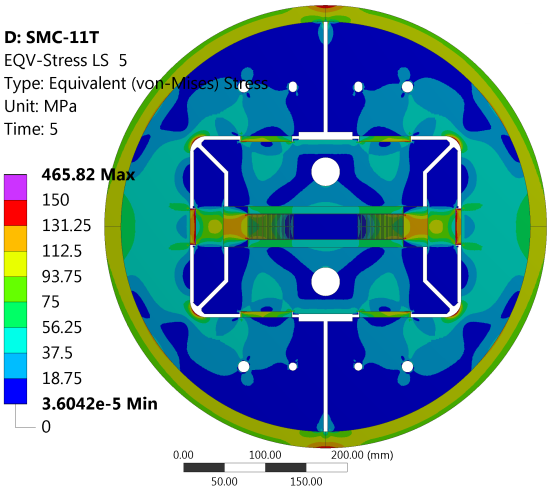

Figure 5.66: EQV stress in the magnet, powering with 15.1kA, LS 5

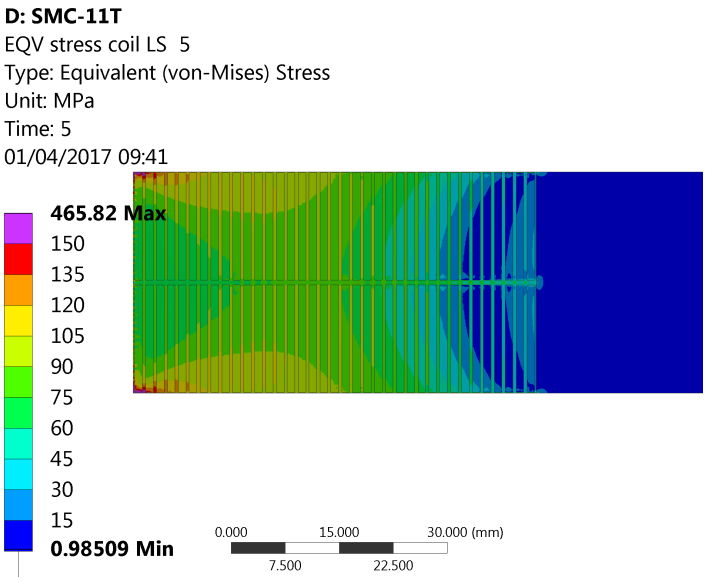

Stress / MPa	pole-cable	outer-cable
vertical pressure		
Trans.	-18	-132
EQV	27	74

- shown plot is for a vertical key excess of 0.2mm and a horizontal key excess of 0.1mm

Figure 5.67: SMC-11T EQV stress in the coil, powering with 15.1kA, LS 5

6 Comparison of the Coil-Stress and Strain

6.1 Influence of the Structure on the Coil Stress

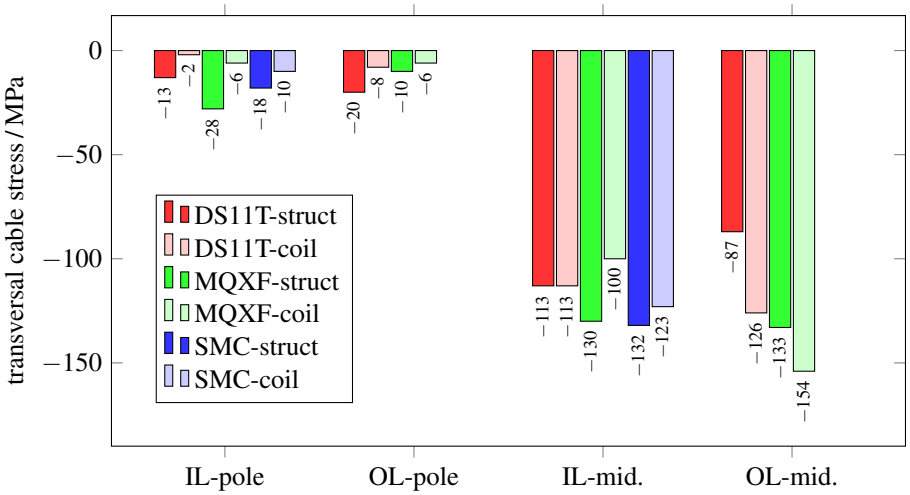

Figure 6.1: average transversal cable stress, comparison between the single coil and the coils in the structure

In section 4.2, the coil were supported by infinite rigid supports. This was done to create a baseline for the to be expected stresses due to the EM-force. Two scenarios were considered, one with the “full coil” and one with the “half coil”. Full coil meaning that both branches are attached to the pole, half that only one branch is present and the pole piece is cut in half. For this section only the half coil be considered, the results from the previous chapter have shown that the “full coil” case is not realistic and highly disadvantageous for the coil stresses. In Figure 6.1 the average transversal cable stresses are shown, for the single coil branch infinite rigid supported and for the coils in the mechanical structure. The coils were supported on the outer diameter and on the midplane, the poles were allowed to move. The same EM-forces were applied for both scenarios.

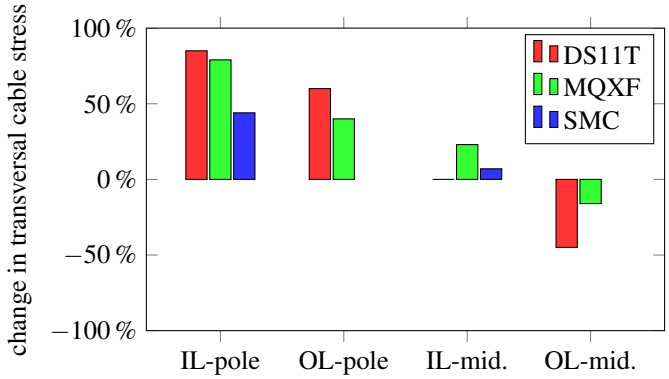

Figure 6.2: change in average transversal cable stress, comparison between the single coil and the coils in the structure

To compare the two cases, the change in percentage is plotted in Figure 6.2. A positive value means, that the compression is higher in the mechanical structure than in the infinite rigid case. For all three magnets the compression is increased in the pole turns, this is expected since the coil were not pre-compressed in the infinite rigid case. Surprisingly, the compression stresses on the midplane are very similar and decreased even on the outer layer.

conclusion Focusing on the transversal stresses, only small difference are present between the “perfect” support and the real mechanical structures. The stress delta between the poles and the midplane is nearly unchanged by the mechanical support.

6.2 Cable Stresses during Assembly and Operation

In the previous sections the stresses in the coil during the assembly and operation were shown. In this chapter the average cable stresses, transversal and EQV, will be summarized. As in the previous sections the different steps of assembly and operation are divided up in five loading steps, same as in Table 5.2. The assembly phase is differently for all three magnet, therefore the different steps will be refereed to as assembly#. For the so called operation, the powering of the magnet, the current levels from the previous section will be used. As in the previous section the average cable stress will be used, meaning that all the stresses in one cable are averaged.

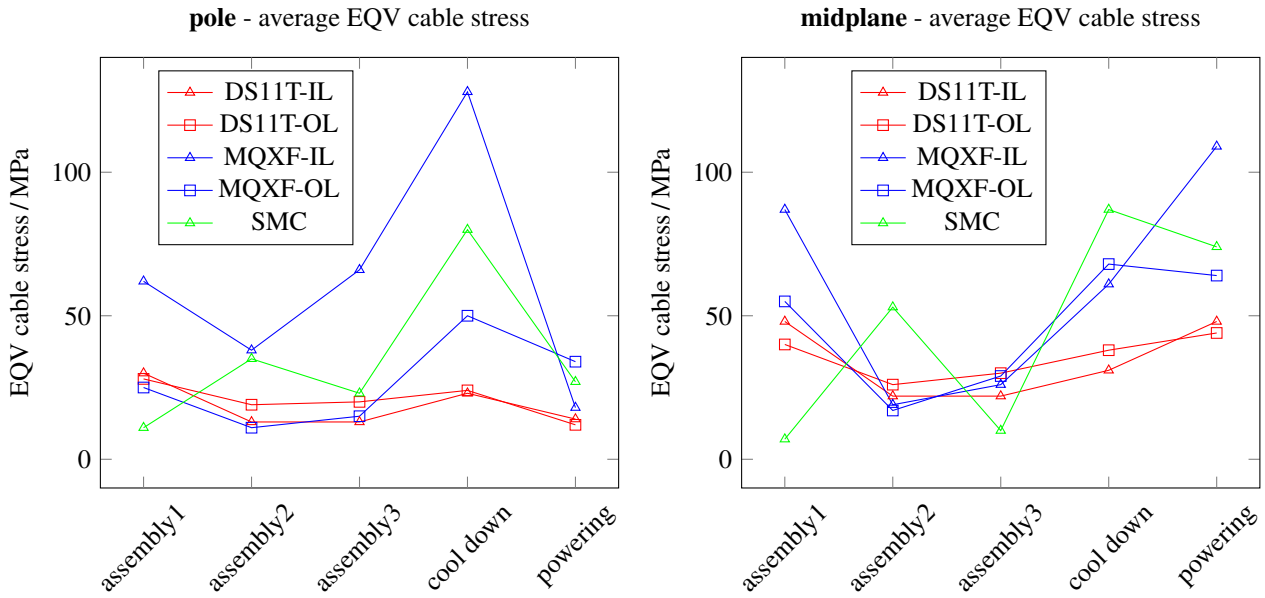

Figure 6.3: EQV stress in the pole and midplane cables

The EQV stress, for all three magnets, is shown in Figure 6.3. The highest EQV stress is seen by the MQXF inner layer pole cable after the cool down. This also the cable with highest stress difference during a powering cycle, of 110MPa. Also the difference between the inner layer and the outer layer, of the pole cable, is the largest in the MQXF. In the DS11T coil, the EQV stresses are constant through out the assembly and the operation, reaching a maximum of 48MPa in the inner layer midplane cable during collaring and operation.

The average transversal stresses of the cable are shown in Figure 6.4. The transversal stress of the SMC pole cable is oscillating throughout the loading steps, during a powering cycle the stress changes by 102MPa. A similar behaviour is observable for the MQXF inner layer pole cables, with a delta of 129MPa due to the powering. For the DS11T the maximum delta of 83MPa during the powering cycle is in the inner layer midplane cable, while the delta in the pole cables is only 36MPa.

conclusion Comparing all three magnets, the stress differences between the inner and outer layer are the largest for the pole cables in the MQXF. This is the case for both, the transversal stresses and the EQV stresses. The maximum difference in stress, between the two layers and over the full coil, in the transversal stress is similar for all three magnet. Looking at the spread throughout a coil and the differences in stress due to the powering, the DS11T seems to be the most advantageous.

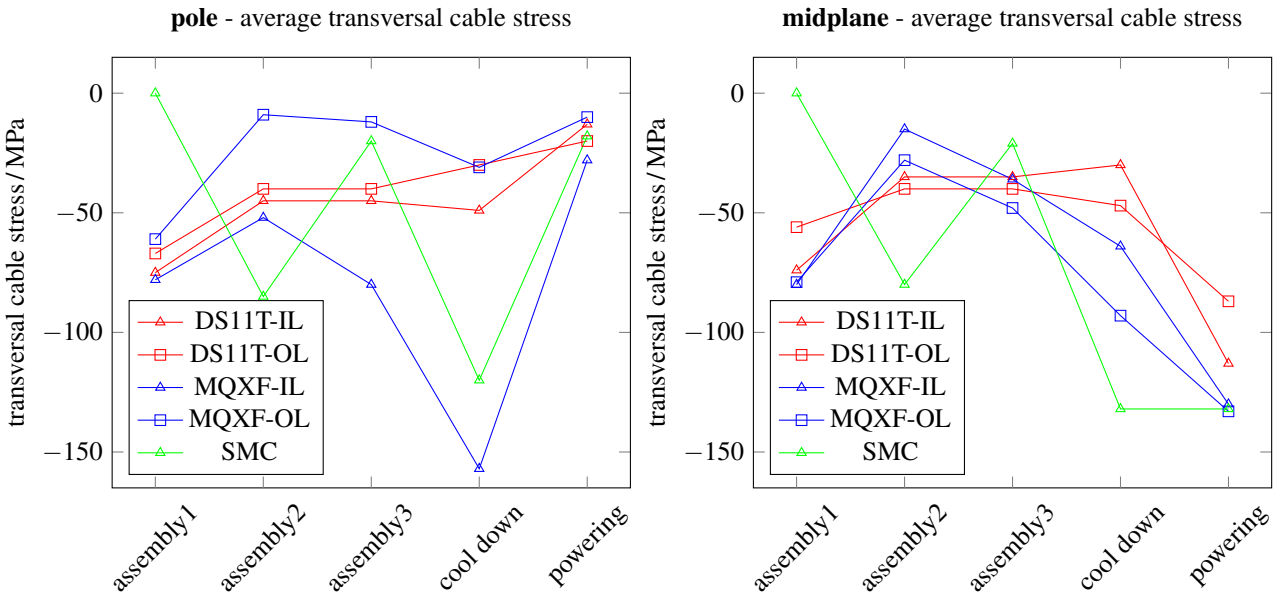

Figure 6.4: transversal stress in the pole and midplane cables

6.3 Plasticity in the Cable

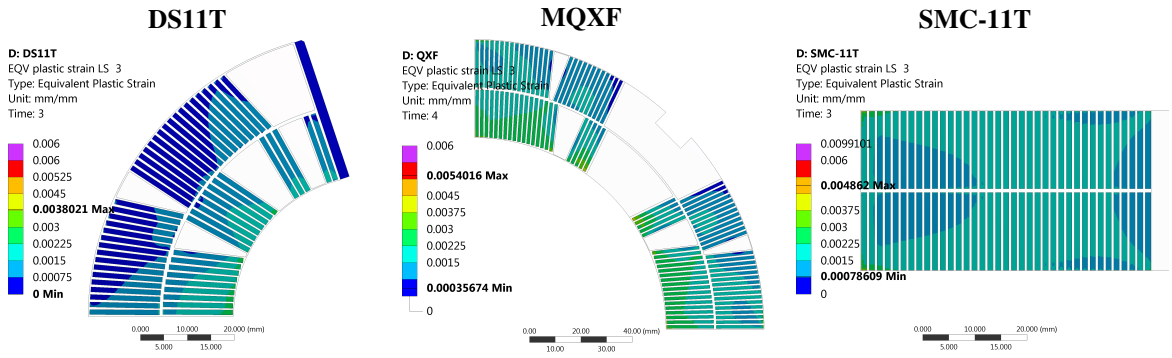

Figure 6.5: Plastic strain in the cable after the assembly of the magnet at room temperature, LS 3

The cable material used in this thesis has a bilinear hardening behaviour, as described in subsection 3.4.1. It is assumed that the cable after the thermal treatment is fully annealed, therefore a cold working mechanism takes place at even very low stresses. During the assembly the coils go through different loading and stress distributions, which influence the permanent plastic strain in the cable. The cable is modeled using an isotropic hardening behaviour, which means that the plastic strain can only increase. It is assumed that the plastic strain causes a permanent disturbance of the superconducting filaments in the strands, thereby possibly decreasing the performance of the conductor.

To make a comparison between the three different magnets plastic strain in the coils is compared after the assembly, at 1.9K and at the excitation of the coils. For the shimming of the magnets the *nominal case* is used from the previous sections. In Figure 6.5 the plastic strain after the assembly of the three magnets is shown, this is last step before the magnets are cooled down to 1.9K. For the DS11T-coil all the plasticity shown is created during the collaring process. The coils of the MQXF and the SMC-11T reach their maximum of plasticity during the maximum pressurization of the bladders, for the SMC during the horizontal loading. The shell welding has no influence on the plastic strain in the coils.

In the MQXF and the SMC the cool down to 1.9K, due to the thermal shrinkage of the aluminium shell, is the main contributor to the pre-stress in the coils. This is also observable in the plastic strain in the cable after the cool down, Figure 6.6. For the DS11T-coil the plastic strain increases slightly in the outer layer. The MQXF-coil plastifys in general but locally close to the pole on the inner layer the plastic strain doubles. In the SMC-11T coil

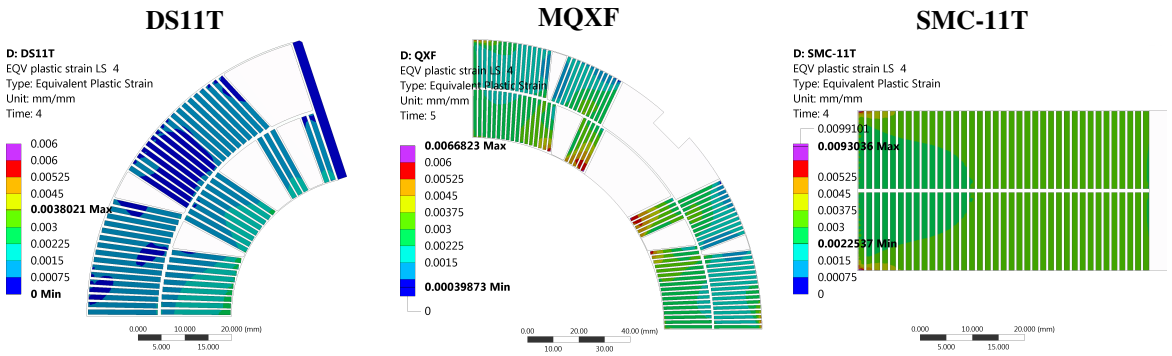

Figure 6.6: Plastic strain in the cable after the cool down to 1.9K, LS 4

the plastic strain is generally increased and evenly spread, apart from the outer corner where very high levels of 0.9% of plastic strain are reached.

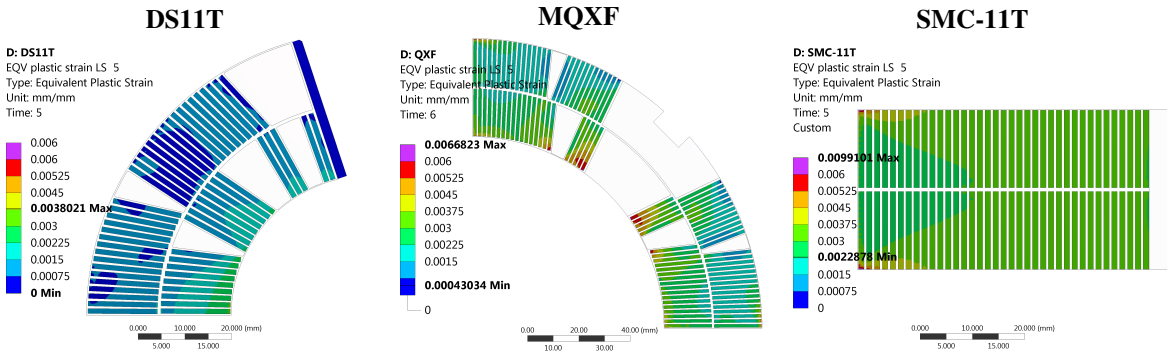

Figure 6.7: Plastic strain in the cable, excitation of the coils, LS 5

The EM-forces from the magnetic field, have a neglectable effect on the plastic strain in the MQXF- and SMC-coil, compared to the already present plastic strain. Only in the DS11T-coil a increase of plastic strain is observable on the inner layer close to the midplane.

conclusion The plastic strain in the SMC-coil is the most evenly distributed compared to the other two coils. In the MQXF the largest section, inner layer pole cable, with plastic strain higher than 0.5% is present. In the DS11T-coil the maximum plastic strain is located on the inner layer midplane, with a local maximum of 0.38%.

6.4 Possible Reduction of the Critical Current

The method presented in section 3.5 is applied on the full coil cross-section. The strain function, Equation 3.5.4, is applied on the cables in Figure 6.8. The strain function is taking all three principal strains into account. The elastic principle strains are used for this calculation. It is assumed that the plastic strains do not influence the filaments. As described in section 3.5 a correction, $s_{fac}(\varepsilon) = s(\varepsilon) - 2(1 - s(\varepsilon))$, needs to be applied to create matching results between a FE-model with single filaments and one where the cable is represented by one body with smeared material properties.

To get the information concerning the critical current degradation the magnetic field strength needs to be considered. In Equation 3.5.9 the calculation for the critical current degradation is shown. The magnetic field strength taken in to account, the resulting critical current reduction, taken the correction into account, is shown in Figure 6.9. The results shown are calculated using the “nominal case” from chapter 5. In all three magnets the critical current reduction is nearly 0% in the pole cables. The critical location is always close to the midplanes and concentrated on the edges. In the DS11T coil a large zone with a reduction of 5% is present on the inner layer midplane. In the SMC and MQXF coils large reductions on both edges of the midplane are present. The reduction in the MQXF is rather localized and can artefacts from the FEM calculation. A similar case is the SMC coil, but also large areas with a reduction of 7% or more do occur.

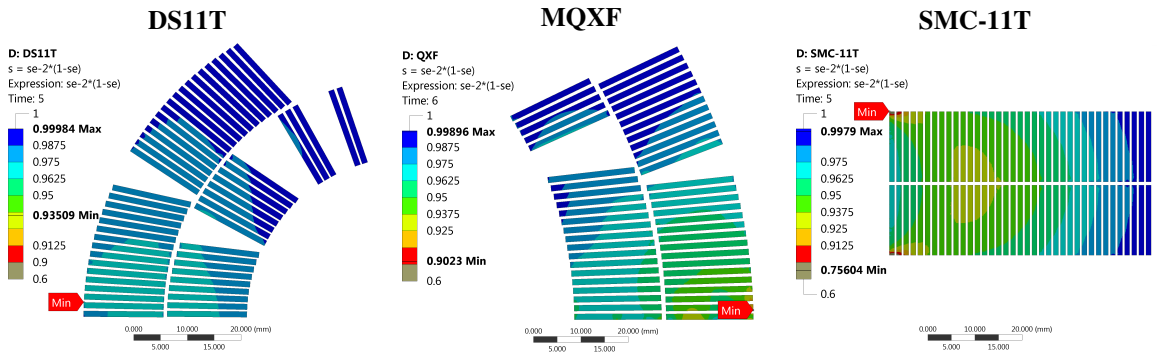

Figure 6.8: respond of the strain function s(ε), during operation, LS 5

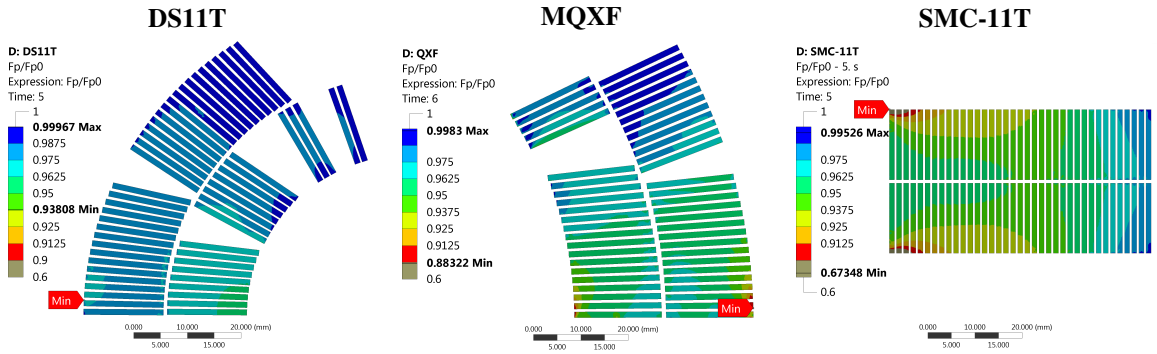

Figure 6.9: critical current reduction, during operation, LS 5

conclusion The calculation of the critical current reduction in a full magnet cross-section is a rather new approach. Many cable parameters relevant for the calculation, are not accurate and require more experimental results. Nevertheless this approach could be used to determine “hot spots”, where the performance of the magnet might be limited due to excessive strain in the conductor. The values here shown rely on a perfect geometry with perfect flat contacts, in reality impurities in the coil or in the structure itself can negatively affect these values dramatically.

7 Conclusion

The aim of this mechanical comparison of three different magnets was to find means to assess the influence of structure on the mechanical conditions of coils. Superconductivity and the challenges of designing a superconducting accelerator magnet are briefly introduced. One chapter is dedicated to the characteristics of the materials used in the magnet. This includes the definition of a non-linear material behaviour for a composite cable. An analytical model was used to determine the stiffness of the cable insulation composite. Also, the influence of single material stiffness was determined.

The electro mechanical forces acting on the coils are described in detail, focusing on the forces which act on the supporting structure and on the internal forces of the coils. An FE analysis has been done to calculate the stresses in the coil due to EM forces under the assumption of a perfect infinite rigid support. The three mechanical structures are described in detail, focusing on the occurring stresses during the assembly and the operation of the magnets. The resulting coil stresses have been compared to the coil stresses purely due to the EM forces. With this, the influence of the individual support structure could be shown. The pre-stress in the coils was set to be at least -10MPa in compression during powering.

It was found that the influence of the structures is mostly beneficial for the coil stresses during the excitation of the coils. The assembly process of the three magnets exhibits the coils to have a rather large stress variation. For example, the pole stresses of the MQXF coil have a variation of 129MPa due to the EM forces. From this analysis, it can be concluded that a significant improvement of the mechanical structure concerning the coil stresses during the powering is improbable. On the other hand, an improvement of the assembly process might be feasible. The DS11T magnets coils are exhibited to much lower stresses during the assembly phase than the SMC and the MQXF. It is also found that the freely movable pole of the DS11T magnet has a positive impact on the shimming sensitivity (pre-stress build-up at room temperature). Even when the pre-stress created at room temperature is not sufficient to maintain a cable compression of -10MPa, the pole cables of the DS11T do not go into a tension. If the created pre-stress at room temperature is not sufficient, the SMC and MQXF experience large tensile stresses in the pole cables.

The three designs have been compared in terms of the permanent plasticity of the cable. The focus is on the stages in the magnet's life where the plastification occurs. It is found that the DS11T coils mainly plastify during the collaring process, while the SMC and MQXF coils plastify during the cool down. A new approach was applied to determine the critical current reduction on a full magnet cross-section. It was found that the midplanes of all three magnets might be limiting the performance of the magnets due to excessive strain in the conductor.

Bibliography

[1] L Rossi. LHC Upgrade Plans: Options and Strategy. (CERN-ATS-2011-257):6 p, Dec 2011.

[2] Alexander V Zlobin. Superconducting magnets-principles, operation, and applications. *Wiley Encyclopedia of Electrical and Electronics Engineering*.

[3] Paul Seidel. *Applied Superconductivity: Handbook on Devices and Applications*. John Wiley & Sons, 2015.

[4] Karl-Heinz Bennemann and John B Ketterson. *Superconductivity: Volume 1: Conventional and Unconventional Superconductors Volume 2: Novel Superconductors*. Springer Science & Business Media, 2008.

[5] Geert Pieter Willering. *Stability of superconducting Rutherford cables for accelerator magnets*. PhD thesis, Enschede, May 2009.

[6] Albertus Godeke. *Performance boundaries in Nb3Sn superconductors*. PhD thesis, Enschede, July 2005.

[7] Helmut Krauth, Klaus Schlenga, Davide Nardelli, Ilaria Pallecchi, Matteo Tropeano, Roland Hott, Thomas Wolf, and Marina Putti. *Superconducting Materials*, pages 105–191. Wiley-VCH Verlag GmbH & Co. KGaA, 2015.

[8] Arnaud Devred. Insulation systems for nb 3 sn accelerator magnet coils manufactured by the wind & react technique. *IEEE transactions on applied superconductivity*, 12(1):1232–1237, 2002.

[9] M. Baier, R. Wordel, F.E. Wagner, T.E. Antonova, and V.E. Antonov. Mössbauer study of the hydrides of nb3me with a15 structure. *Journal of the Less Common Metals*, 172:358 – 365, 1991.

[10] E Barzi, D Turrioni, and AV Zlobin. Progress in rrp strand studies and rutherford cable development at fnal. *IEEE Transactions on Applied Superconductivity*, 24(3):1–8, 2014.

[11] Luca Bottura and Arno Godeke. Superconducting materials and conductors: Fabrication and limiting parameters. *Reviews of Accelerator Science and Technology*, 05:25–50, 2012.

[12] E Barzi, D Turrioni, and AV Zlobin. Progress in rrp strand studies and rutherford cable development at fnal. *IEEE Transactions on Applied Superconductivity*, 24(3):1–8, 2014.

[13] EF Holik, G Ambrosio, M Anerella, R Bossert, E Cavanna, D Cheng, DR Dietderich, P Ferracin, AK Ghosh, S Izquierdo Bermudez, et al. Fabrication and analysis of 150-mm-aperture nb 3 sn mqxf coils. *IEEE Transactions on Applied Superconductivity*, 26(4):1–7, 2016.

[14] Jean-Luc Caron. Magnetic field induced by the LHC dipole's superconducting coils.. Champ magnetique cree par les bobines superconductrices des aimants dipolaires du LHC. AC Collection. Legacy of AC. Pictures from 1992 to 2002., Mar 1998.

[15] F Toral. Mechanical Design of Superconducting Accelerator Magnets. (arXiv:1501.02932):34 p, 2014. Comments: Presented at the CERN Accelerator School CAS 2013: Superconductivity for Accelerators, Erice, Italy, 24 April - 4 May 2013.

[16] Fernando Toral. Mechanical design of superconducting accelerator magnets. *arXiv preprint arXiv:1501.02932*, 2015.

[17] RW Assmann, O Aberle, G Bellodi, A Bertarelli, C Bracco, H Braun, M Brugger, S Calatroni, R Chamizo, A Dallochio, et al. The final collimation system for the lhc. In *Proceedings of EPAC 2006*, 2006.

[18] L. Bottura, G. de Rijk, L. Rossi, and E. Todesco. Advanced accelerator magnets for upgrading the lhc. *IEEE Transactions on Applied Superconductivity*, 22(3):4002008–4002008, June 2012.

[19] RR Hafalia, PA Bish, S Caspi, DR Dietderich, SA Gourlay, R Hannaford, AF Lietzke, N Liggins, AD McInturff, GL Sabbi, et al. A new support structure for high field magnets. *IEEE transactions on applied superconductivity*, 12(1):47–50, 2002.

[20] J. C. Perez, M. Bajko, H. Bajas, B. Bordini, A. Chiuchiolo, P. Ferracin, J. Feuvrier, M. Juchno, L. Oberli, and X. Sarasola. Performance of the short model coils wound with the cern 11-t nb3sn conductor. *IEEE Transactions on Applied Superconductivity*, 25(3):1–5, June 2015.

[21] F Regis, P Manil, P Fessia, M Bajko, and G De Rijk. Mechanical design of the smc (short model coil) dipole magnet. *IEEE Transactions on Applied Superconductivity*, 20(3):204–207, 2010.

[22] P. Pugnat and A. Siemko. Review of quench performance of lhc main superconducting magnets. *IEEE Transactions on Applied Superconductivity*, 17(2):1091–1096, June 2007.

[23] ED Marquardt, JP Le, and Ray Radebaugh. Cryogenic material properties database. In *Cryocoolers 11*, pages 681–687. Springer, 2002.

[24] Gianluca De Marzi, Luigi Morici, Luigi Muzzi, Antonio della Corte, and M Buongiorno Nardelli. Strain sensitivity and superconducting properties of nb3sn from first principles calculations. *Journal of Physics: Condensed Matter*, 25(13):135702, 2013.

[25] C. Scheuerlein, B. Fedelich, P. Alknes, G. Arnau, R. Bjoerstad, and B. Bordini. Elastic anisotropy in multifilament nb3sn superconducting wires. *IEEE Transactions on Applied Superconductivity*, 25(3):1–5, June 2015.

[26] C Scheuerlein, M Di Michiel, F Buta, B Seeber, C Senatore, R Flükiger, T Siegrist, T Besara, J Kadar, B Bordini, A Ballarino, and L Bottura. Stress distribution and lattice distortions in nb 3 sn multifilament wires under uniaxial tensile loading at 4.2 k. *Superconductor Science and Technology*, 27(4):044021, 2014.

[27] A Nyilas, KP Weiss, U Balachandran, Kathleen Amm, David Evans, Eric Gregory, Peter Lee, Mike Osofsky, Sastry Pamidi, Chan Park, et al. Bi-axial strain response of structural materials and superconducting nb 3 sn wires at 295 k, 7 k, and 4 k. In *AIP Conference Proceedings*, volume 986, pages 116–123. AIP, 2008.

[28] Christian Scheuerlein, Friedrich Lackner, Frederic Savary, Birgit Rehmer, Monika Finn, and Patrick Uhlemann. Mechanical properties of the hl-lhc 11 tesla nb3sn magnet constituent materials. *IEEE Transactions on Applied Superconductivity*, 2016.

[29] Company-CTD. Ctd-101k epoxy resin system. `http://ncsx.pppl.gov/NCSX_Engineering/Materials/InsulationProperties/CTD-101K_Datasheet_2003.pdf`, 2014. 2017-01-29.

[30] F Wallenberger and P Bingham. Fiberglass and glass technology: energy-friendly compositions and applications. 2010.

[31] Deepak Reddy Chichili, Jay Hoffman, and Alexander Zlobin. Investigation of alternative materials for impregnation of nb3sn accelerator magnets. Technical report, Fermi National Accelerator Lab., Batavia, IL (US), 2003.

[32] Kamal J Araj, Theresa A Fisher, and Jan C Kronenburg. Assessment of research needs for wind turbine rotor materials technology. Technical report, National Research Council, Washington, DC (United States), 1991.

[33] HM Ledbetter and G Maerz. Temperature dependence of young's modulus and internal friction of g-10cr and g-11cr epoxy resins. *Cryogenics*, 20(11):655, 1980.

[34] Giorgio Ambrosio, Paolo Ferracin, et al. Mqxfs1 quadrupole design report. Technical report, Fermi National Accelerator Laboratory (FNAL), Batavia, IL (United States), 2016.

[35] Company-DuPont. Dec-kapton-summary-of-properties. `http://www.dupont.com/content/dam/dupont/products-and-services/membranes-and-films/polyimde-films/documents/DEC-Kapton-summary-of-properties.pdf`, 2014. 2017-01-31.

[36] AF Clark. *Advances in Cryogenic Engineering Materials*, volume 26. Springer Science & Business Media, 2012.

[37] F Bertinelli, S Comel, P Harlet, G Peiro, A Russo, and A Taquet. Production of low-carbon magnetic steel for the lhc superconducting dipole and quadrupole magnets. *IEEE transactions on applied superconductivity*, 16(2):1777–1781, 2006.

[38] MatWeb. `http://matweb.com/search/DataSheet.aspx?MatGUID=b350a789eda946c6b86a3e4d3c577b39&ckck=1`, 2011. 2017-01-29.

[39] W. Voigt. Ueber die beziehung zwischen den beiden elasticitätsconstanten isotroper körper. *Annalen der Physik*, 274(12):573–587, 1889.

[40] A. Reuss. Berechnung der fließgrenze von mischkristallen auf grund der plastizitätsbedingung für einkristalle . *ZAMM - Journal of Applied Mathematics and Mechanics / Zeitschrift für Angewandte Mathematik und Mechanik*, 9(1):49–58, 1929.

[41] DR Chichili, TT Arkan, JA Rice, et al. Niobium-tin magnet technology development at fermilab. In *Particle Accelerator Conference, 1999. Proceedings of the 1999*, volume 5, pages 3242–3244. IEEE, 1999.

[42] M Reytier, A Devred, M Durante, C Gourdin, and P Vedrine. Characterization of the thermo-mechanical behavior of insulated cable stacks representative of accelerator magnet coils. *IEEE transactions on applied superconductivity*, 11(1):3066–3069, 2001.

[43] R Bossert, G Ambrosio, M Yu, G Chjlachidze, AV Zlobin, N Andreev, I Novitski, S Krave, and A Nobrega. Recent progress and tests of radiation resistant impregnation materials for nb _3 sn coils. In *AIP Conf. Proc.*, volume 1574, pages 132–139, 2013.

[44] D Dell'Orco, RM Scanlan, CE Taylor, A Lietzke, S Caspi, JM van Oort, and AD McInturff. Fabrication and component testing results for a nb/sub 3/sn dipole magnet. *IEEE Transactions on Applied Superconductivity*, 5(2):1000–1003, 1995.

[45] N. Mitchell. Finite element simulations of elasto-plastic processes in nb3sn strands. *Cryogenics*, 45(7):501 – 515, 2005.

[46] B Bordini, P Alknes, L Bottura, L Rossi, and D Valentinis. An exponential scaling law for the strain dependence of the nb3sn critical current density. *Superconductor Science and Technology*, 26(7):075014, 2013.

[47] JW Ekin. Strain scaling law for flux pinning in practical superconductors. part 1: Basic relationship and application to nb3sn conductors. *Cryogenics*, 20(11):611–624, 1980.

[48] David MJ Taylor and Damian P Hampshire. The scaling law for the strain dependence of the critical current density in nb3sn superconducting wires. *Superconductor Science and Technology*, 18(12):S241, 2005.

[49] A Godeke, B Ten Haken, HHJ Ten Kate, and DC Larbalestier. A general scaling relation for the critical current density in nb3sn. *Superconductor Science and Technology*, 19(10):R100, 2006.

[50] Jack Ekin. *Experimental techniques for low-temperature measurements: cryostat design, material properties and superconductor critical-current testing*. Oxford university press, 2006.

[51] Tiening Wang, Luisa Chiesa, Makoto Takayasu, and Bernardo Bordini. A novel modeling to predict the critical current behavior of Nb3Sn PIT strand under transverse load based on a scaling law and Finite Element Analysis. *Cryogenics*, 63:275–281. 7 p, 2014.

Appendices

A Table Appendix

Table A.1: Tensile tests at different temperatures, samples from longitudinal and transversal rolling directions[37]

	Temperature (K)	Young's Modulus (GPa)	Yield Strength (MPa)	Ultimate Tensile Strength (MPa)	uniform Elongation (%)	Total Elongation (%)
L direction	295	205	115	249	32	52
T direction	295	200	123	282	26	44
L direction	233	196	151	260	25	50
T direction	90	210	642	653	5.9	20
-	77	221	821	828	-	10.1
L direction	7	200	-	723	0.5	0.5
T direction	7	211	-	926	0.5	0.5

Table A.2: Electro magnetic forces summary in N/mm

MQXF	*Horizontal*	*Vertical*	*Radial*	*Azimuthal*
CB-1	2221	-1026	1725	-1443
CB-2	767	-702	259	-1003
CB-3	-393	-1009	-468	-937
CB-4	525	-1799	-249	-1851
Total	**3120**	**-4536**	**1266**	**-5235**
DS11T	*Horizontal*	*Vertical*	*Radial*	*Azimuthal*
CB-1	881	-109	846	-269
CB-2	907	-159	639	-663
CB-3	401	-65	145	-380
CB-4	281	-38	48	-279
CB-5	60	-442	-43	-444
CB-6	1031	-1019	3	-1449
Total	**3561**	**-1832**	**1639**	**-3484**
SMC-11T	*Horizontal*	*Vertical*		
CB-1	1697	-1825		
CB-2	1697	1825		
Total	**3394**	**0**		

A.1 FEA of the structures

A.1.1 Contacts

Table A.3: Contacts for the DS11T model, first table

Number	**Contact Name**	**Contact Side**	**Type**	**Number Contacting**	**Penetration** / *mm*	**Geo. Gap** / *mm*	**Pinball** / mm	**Normal Stiffness** / N/mm^3	**Tangentail Stiffness** / N/mm^3
1	Collaring Keys-Collar	Contact	Bonded	276	2.3×10^{-14}	1.6×10^{-2}	1.7×10^{-3}	19198000	5957500
1	Collaring Keys-Collar	Target	Bonded	265	1.8×10^{-15}	1.6×10^{-2}	1.7×10^{-3}	16313000	4820400
2	Rivet-Collar	Contact	Bonded	588	3.9×10^{-14}	5.0×10^{-2}	3.6×10^{-2}	3655400	2568800
2	Rivet-Collar	Target	Bonded	616	3.6×10^{-12}	4.1×10^{-2}	4.6×10^{-2}	2547800	1587400
3	Kapton-Coil OD& L. Plate	Contact	Bonded	6540	4.0×10^{-14}	5.3×10^{-5}	3.6×10^{-4}	13792	3103.3
3	Kapton-Coil OD& L. Plate	Target	Bonded	2916	3.2×10^{-14}	7.5×10^{-8}	2.8×10^{-4}	13792	3131.3
4	Kapton-Lateral Shim	Contact	Bonded	1812	1.5×10^{-14}	7.5×10^{-8}	8.1×10^{-8}	13792	3103.3
4	Kapton-Lateral Shim	Target	Bonded	3600	1.5×10^{-14}	7.6×10^{-8}	8.4×10^{-8}	13792	3103.3
5	Yoke Shim-Yoke Insert	Contact	Bonded						
5	Yoke Shim-Yoke Insert	Target	Bonded	1842	1.5×10^{-14}	3.8×10^{-3}	6.6×10^{-3}	313950	70640
6	Collared Coil Shim-Yoke	Contact	Bonded						
6	Collared Coil Shim-Yoke	Target	Bonded	1986	9.5×10^{-15}	0	4.7×10^{-3}	321480	72333
7	Collared Coil Shim-Yoke	Contact	Bonded	1986	3.9×10^{-14}	1.5×10^{-3}	1.6×10^{-3}	318470	71656
7	Collared Coil Shim-Yoke	Target	Bonded						
8	Kapton-Collaring Shoe	Contact	Frictional	4908	3.5×10^{-4}	3.5×10^{-4}		13792	620.65
8	Kapton-Collaring Shoe	Target	Frictional	8832	2.7×10^{-4}	2.7×10^{-4}		13792	728.93
9	Collar-Collaring Shoe	Contact	Frictional	1099	1.8×10^{-3}	0	0	3801000	307570
9	Collar-Collaring Shoe	Target	Frictional	5071	2.2×10^{-3}	2.2×10^{-3}	1.1×10^{-7}	380100	9981.2
10	Yoke-Shell	Contact	Frictional	927	3.0×10^{-3}	3.0×10^{-3}	7.2×10^{-6}	1213100	177270
10	Yoke-Shell	Target	Frictional						

Table A.4: Contacts for the DS11T model, second table

Number	**Contact Name**	**Contact Side**	**Type**	**Number Contacting**	**Penetration** / *mm*	**Geo. Gap** / *mm*	**Pinball** / mm	**Normal Stiffness** / N/mm^3	**Tangentail Stiffness** / N/mm^3
11	Lateral Shim-Pole 1	Contact	Frictionless	900	2×10^{-1}	7.0×10^{-8}		364040	0
11	Lateral Shim-Pole 1	Target	Frictionless	549	2×10^{-1}	6.8×10^{-8}		3640400	0
12	Lateral Shim-Pole 2	Contact	Frictionless	900	2×10^{-1}	1.0×10^{-8}		360940	0
12	Lateral Shim-Pole 2	Target	Frictionless	549	2×10^{-1}	9.3×10^{-9}		3609400	0
13	Lateral Shim-Pole 3	Contact	Frictionless	900	2×10^{-1}	7.0×10^{-8}		361540	0
13	Lateral Shim-Pole 3	Target	Frictionless	549	2×10^{-1}	6.8×10^{-8}		3615400	0
14	Lateral Shim-Pole 4	Contact	Frictionless	900	2×10^{-1}	1.0×10^{-8}		360140	0
14	Lateral Shim-Pole 4	Target	Frictionless	549	2×10^{-1}	9.3×10^{-9}		3601400	0
15	Coil Midplane-Coil Midplane	Contact	Frictionless	438	1.7×10^{-16}	1.7×10^{-18}	0	58915	0
15	Coil Midplane-Coil Midplane	Target	Frictionless	438	0	0	1.7×10^{-18}	58915	0
16	Pole-Collar	Contact	Frictionless	42	0	0	0	2359500	0
16	Pole-Collar	Target	Frictionless	26	7.1×10^{-15}	0	0	2191000	0
17	Yoke-Yoke Shim	Contact	Frictionless						
17	Yoke-Yoke Shim	Target	Frictionless	0	0	0	9.6×10^{-4}	0	0
18	Yoke Insert Notch-Collar- Notch	Contact	Frictionless	0	0	0	3.1×10^{-2}	0	0
18	Yoke Insert Notch-Collar- Notch	Target	Frictionless						
19	Yoke Notch-Collar- Notch	Contact	Frictionless	0	0	0	3.0×10^{-2}	0	0
19	Yoke Notch-Collar- Notch	Target	Frictionless						
20	Collared Coil Shim / Yoke -Collared Coil	Contact	Frictionless						
20	Collared Coil Shim / Yoke -Collared Coil	Target	Frictionless	34	1.4×10^{-2}	1.4×10^{-2}	2.0×10^{-4}	5494800	0
21	Collared Coil Shim / Yoke Insert-Collared Coil	Contact	Frictionless						
21	Collared Coil Shim / Yoke Insert-Collared Coil	Target	Frictionless	430	2.5×10^{-2}	2.5×10^{-2}	1.5×10^{-4}	5494800	0
22	Yoke Symmetry Plane-Yoke	Contact	Frictionless	0	0	0		0	0
22	Yoke Symmetry Plane-Yoke	Target	Frictionless						
23	Pole Side-Collar	Contact	No Separation	66	0	9.7×10^{-4}	9.7×10^{-4}	3023100	0
23	Pole Side-Collar	Target	No Separation	32	0	9.7×10^{-4}	9.8×10^{-4}	1824400	0
24	Collaring Keys-Collar	Contact	Rough	168	1.6×10^{-2}	1.6×10^{-2}	1.6×10^{-3}	19263000	6192400
24	Collaring Keys-Collar	Target	Rough	150	1.6×10^{-2}	1.6×10^{-2}	1.6×10^{-3}	16313000	4820400

Table A.5: Contacts for the MQXF, first table

Number	**Contact Name**	**Contact Side**	**Type**	**Number Contacting**	**Penetration** / *mm*	**Geo. Gap** / *mm*	**Pinball** / mm	**Normal Stiffness** / N/mm^3	**Tangentail Stiffness** / N/mm^3
1	Kapton-Coil	Contact	Bonded	4752	1.9×10^{-14}	1.5×10^{-3}	1.0×10^{-3}	4614.6	1038.3
1	Kapton-Coil	Target	Bonded	2608	1.9×10^{-14}	1.1×10^{-3}	7.2×10^{-4}	4614.6	1038.3
2	Iron Pad-Iron Master	Contact	Bonded	236	2.0×10^{-14}	4.8×10^{-2}	5×10^{-2}	1022000	302310
2	Iron Pad-Iron Master	Target	Bonded	940	4.0×10^{-14}	6.9×10^{-2}	8.8×10^{-2}	102190	22993
3	Iron M. Inner-Radial Key	Contact	Bonded	96	0	0	0	1505600	338760
3	Iron M. Inner-Radial Key	Target	Bonded	112	0	0	0	1505600	338760
4	Iron M. Outer-Tang. Key	Contact	Bonded	48	0	0	0	1505600	338760
4	Iron M. Outer-Tang. Key	Target	Bonded	48	0	0	0	1505600	338760
5	Iron M. Outer-Yoke	Contact	Bonded	952	4.0×10^{-14}	6.9×10^{-2}	8.8×10^{-2}	104050	23411
5	Iron M. Outer-Yoke	Target	Bonded	240	3.6×10^{-14}	4.8×10^{-2}	5×10^{-2}	969970	287070
6	Yoke-Al-Shell	Contact	Frictional	262	4.7×10^{-3}	4.7×10^{-3}	2.0×10^{-5}	131700	7750.2
6	Yoke-Al-Shell	Target	Frictional	304	2.7×10^{-3}	2.7×10^{-3}	4.8×10^{-5}	414750	24625
7	Al-Shell-SS-Shell	Contact	Frictional	0	0	0		0	0
7	Al-Shell-SS-Shell	Target	Frictional	124	5.9×10^{-4}	5.9×10^{-4}		35807	1631.3
8	Coil1 - Coil2	Contact	Frictional	0	0	0		0	0
8	Coil1 - Coil2	Target	Frictional	0	0	0		0	0
9	Coil2 - Coil3	Contact	Frictional	0	0	0		0	0
9	Coil2 - Coil3	Target	Frictional	0	0	0		0	0
10	Coil3 - Coil4	Contact	Frictional	0	0	0		0	0
10	Coil3 - Coil4	Target	Frictional	0	0	0		0	0
11	Coil4 - Coil1	Contact	Frictional	0	0	0		0	0
11	Coil4 - Coil1	Target	Frictional	0	0	0		0	0

Table A.6: Contacts for the MQXF, second table

Number	**Contact Name**	**Contact Side**	**Type**	**Number Contacting**	**Penetration** / *mm*	**Geo. Gap** / *mm*	**Pinball** / mm	**Normal Stiffness** / N/mm^3	**Tangentail Stiffness** / N/mm^3
12	Keys Side-Pole	Contact	Frictionless	60	5.6×10^{-9}	5.6×10^{-9}		17097	0
12	Keys Side-Pole	Target	Frictionless	80	5.6×10^{-9}	5.6×10^{-9}		17097	0
13	Iron M. Outer-Radial Key 1	Contact	Frictionless	24	2×10^{-1}	0		1505600	0
13	Iron M. Outer-Radial Key 1	Target	Frictionless	28	2×10^{-1}	0		1505600	0
14	Iron M. Outer-Radial Key 2	Contact	Frictionless	24	2×10^{-1}	0		1505600	0
14	Iron M. Outer-Radial Key 2	Target	Frictionless	28	2×10^{-1}	0		1505600	0
15	Iron M. Outer-Radial Key 3	Contact	Frictionless	24	2×10^{-1}	0		1505600	0
15	Iron M. Outer-Radial Key 3	Target	Frictionless	28	2×10^{-1}	0		1505600	0
16	Iron M. Outer-Radial Key 4	Contact	Frictionless	24	2×10^{-1}	0		1505600	0
16	Iron M. Outer-Radial Key 4	Target	Frictionless	28	2×10^{-1}	0		1505600	0
17	Kapton-Collar	Contact	No Separation	2752	2.0×10^{-14}	1.0×10^{-3}	6.4×10^{-5}	4614.6	0
17	Kapton-Collar	Target	No Separation	832	2.0×10^{-14}	7.1×10^{-4}	2.4×10^{-8}	4614.6	0
18	Keys -Pole	Contact	No Separation	56	2.0×10^{-14}	5.6×10^{-9}	2.0×10^{-14}	76105	0
18	Keys -Pole	Target	No Separation	56	2.0×10^{-14}	5.6×10^{-9}	2.0×10^{-14}	76105	0
19	Collar-Iron Pad	Contact	No Separation	184	3.6×10^{-14}	4.8×10^{-2}	5.0×10^{-2}	875340	0
19	Collar-Iron Pad	Target	No Separation	700	3.9×10^{-14}	6.9×10^{-2}	8.8×10^{-2}	108420	0
20	Iron M. Inner Side-Tang. Key	Contact	No Separation	16	0	0	8.9×10^{-16}	1505600	0
20	Iron M. Inner Side-Tang. Key	Target	No Separation	16	0	8.9×10^{-16}	0	1505600	0

Table A.7: Contacts for the SMC-11T

Number	**Contact Name**	**Contact Side**	**Type**	**Number Contacting**	**Penetration /** *mm*	**Geo. Gap /** *mm*	**Pinball /** mm	**Normal Stiffness /** N/mm^3	**Tangentail Stiffness /** N/mm^3
1	Kapton-Coil	Contact	Bonded	1274	0	7.1×10^{-15}	3.6×10^{-15}	47814	10758
1	Kapton-Coil	Target	Bonded	2540	0	5.3×10^{-15}	7.1×10^{-15}	47814	10758
2	Horizontal Pusher-Plate	Contact	Bonded	380	1.1×10^{-14}	7.1×10^{-15}	6.2×10^{-2}	62708	14109
2	Horizontal Pusher-Plate	Target	Bonded						
3	Vertical Pusher-Plate	Contact	Bonded	98	0	2.8×10^{-14}	4.3×10^{-14}	62707	14109
3	Vertical Pusher-Plate	Target	Bonded						
4	Vertical Keys-Plate	Contact	Bonded						
4	Vertical Keys-Plate	Target	Bonded	252	0	2.8×10^{-14}	2.8×10^{-14}	165520	38707
5	Horizontal Keys-Plate	Contact	Bonded						
5	Horizontal Keys-Plate	Target	Bonded	88	0	8.5×10^{-14}	2.8×10^{-14}	164340	39474
6	Horizontal Pusher-Coil	Contact	Frictionless	203	2.8×10^{-14}	2.8×10^{-14}	1.4×10^{-14}	295860	0
6	Horizontal Pusher-Coil	Target	Frictionless	62	2.8×10^{-14}	2.8×10^{-14}	1.4×10^{-14}	295860	0
7	Vertical Pusher-Kapton	Contact	Frictionless	2528	3.6×10^{-15}	3.6×10^{-15}	3.6×10^{-15}	47814	0
7	Vertical Pusher-Kapton	Target	Frictionless	380	7.1×10^{-15}	7.1×10^{-15}	1.8×10^{-15}	47814	0
8	Vertical Keys-Yoke	Contact	Frictionless	252	2×10^{-1}	3.1×10^{-14}		164420	0
8	Vertical Keys-Yoke	Target	Frictionless						
9	Horizontal Keys-Yoke	Contact	Frictionless	88	2×10^{-1}	4.5×10^{-14}		164270	0
9	Horizontal Keys-Yoke	Target	Frictionless						
10	Shell-Yoke	Contact	No Separation	626	1.4×10^{-13}	3.1×10^{-2}	3.1×10^{-2}	71223	0
10	Shell-Yoke	Target	No Separation	808	1.2×10^{-13}	3.1×10^{-2}	3.1×10^{-2}	70439	0

B Graph Appendix

B.1 FEA of the strand

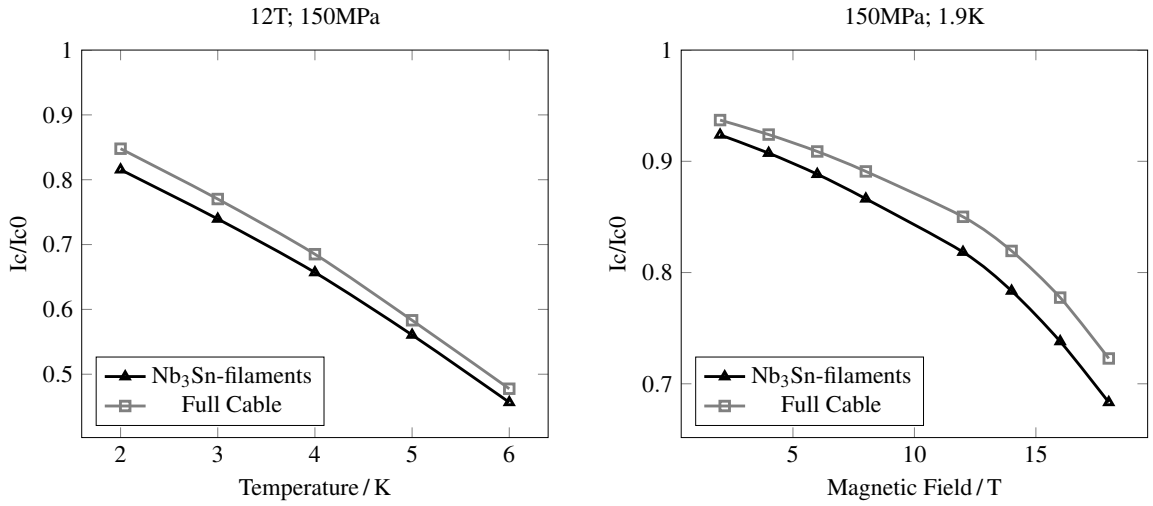

Figure B.1: Simulation results for 108/127 RRP Strand

B.2 FEA of the coils

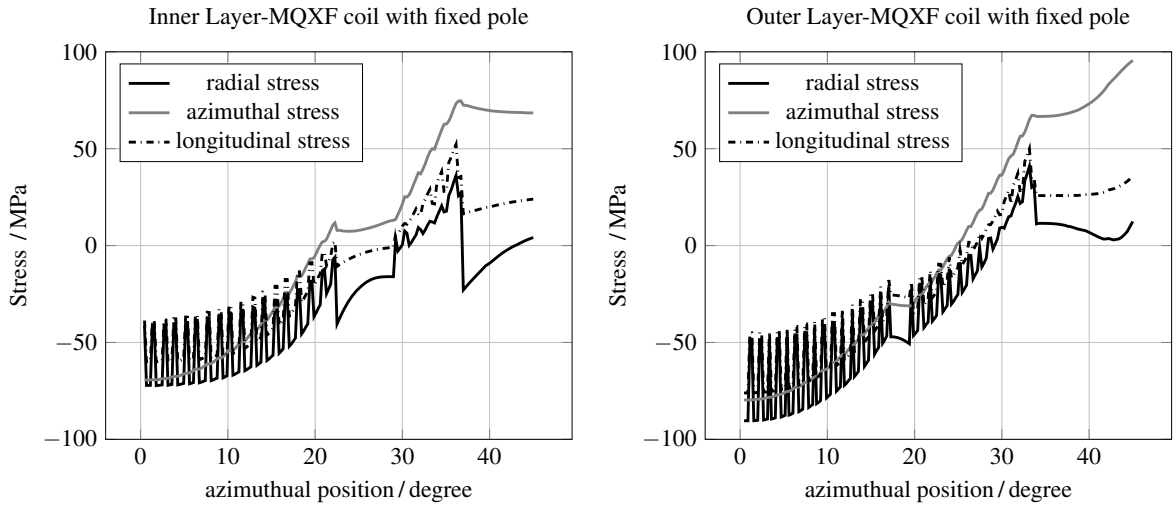

Figure B.2: Stresses in the MQXF-coil with the pole at 19.1kA, azimuthal position is 0 at the midplane

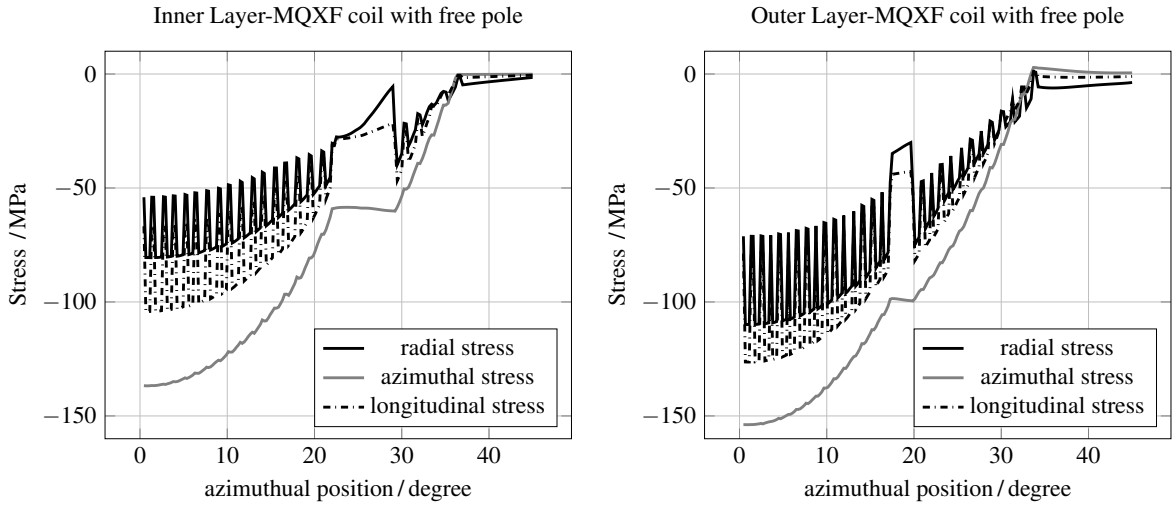

Figure B.3: Stresses in the MQXF-coil with a free pole at 19.1kA, azimuthal position is 0 at the midplane

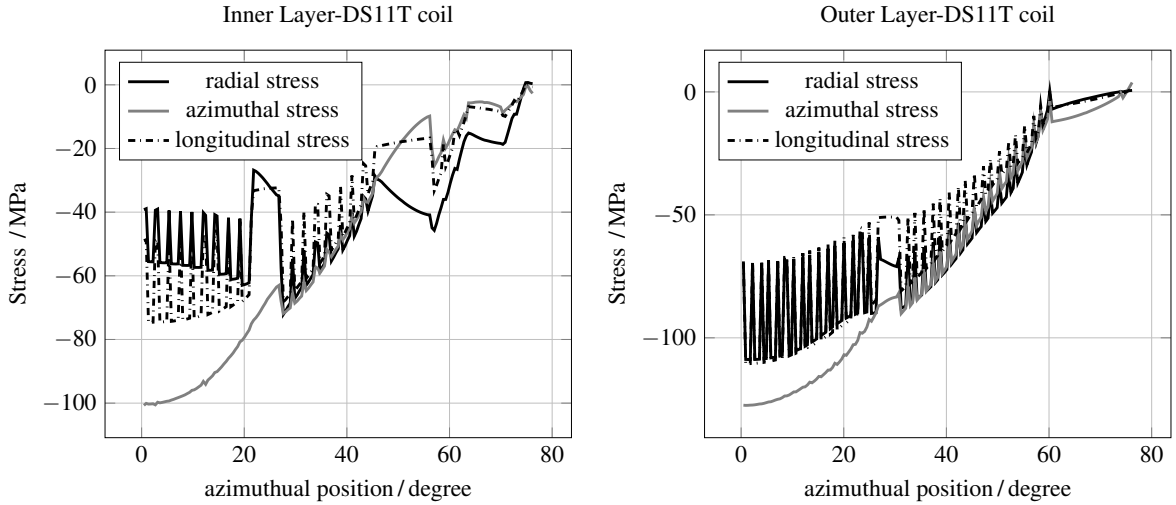

Figure B.4: Stresses in the DS11T-coil at 12.8kA, azimuthal position is 0 at the midplane

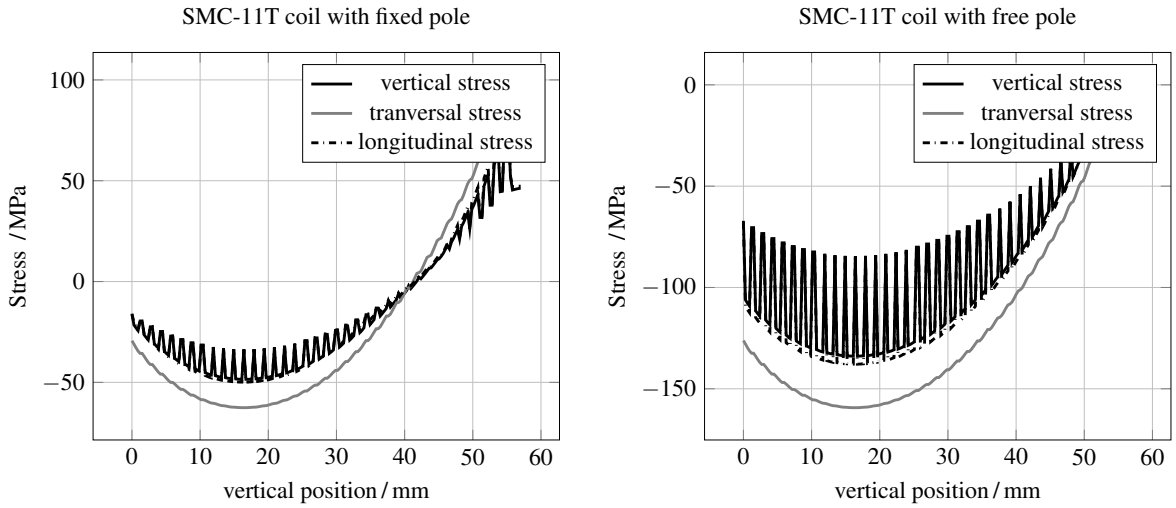

Figure B.5: Stresses in the SMC-coil at 15.1kA, vertical position is 0 at the midplane

C Figure Appendix

C.1 FEA of 10-Stacks

Von Mises / Equivalent

Stress

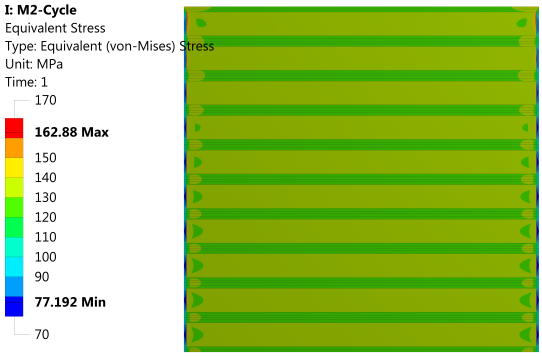

Strain

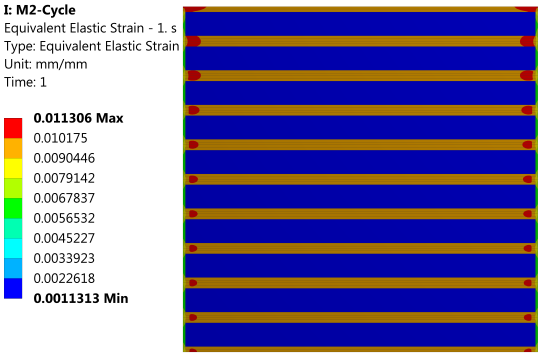

Horizontal

Stress

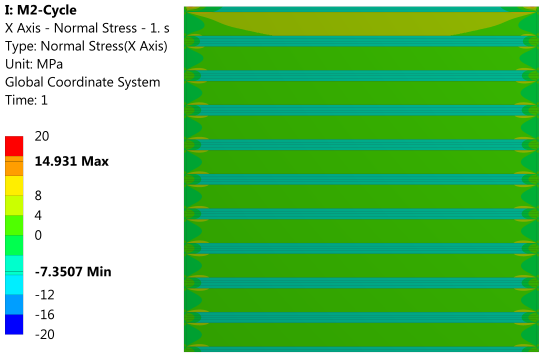

Strain

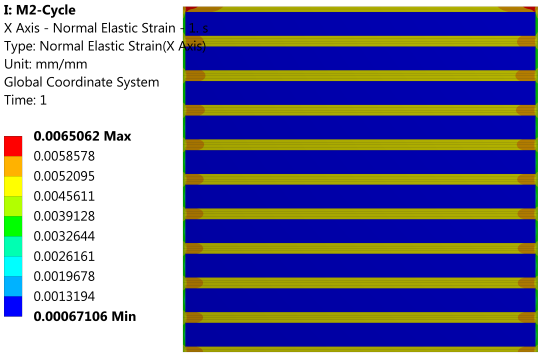

Vertical

Stress

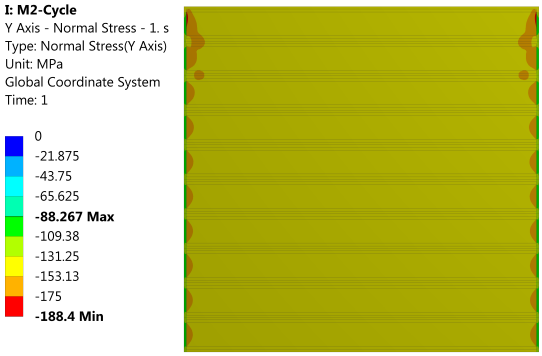

Strain

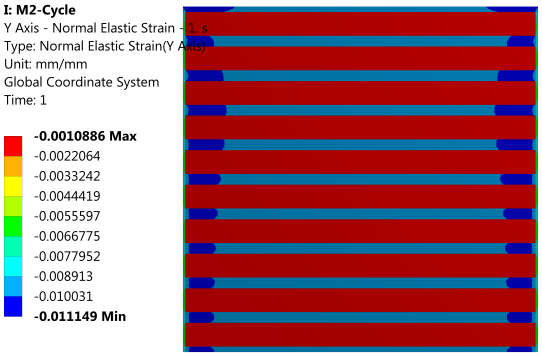

Figure C.1: Vertical loading of the M2 10-Stack model to 150MPa in compression

Von Mises / Equivalent

Stress

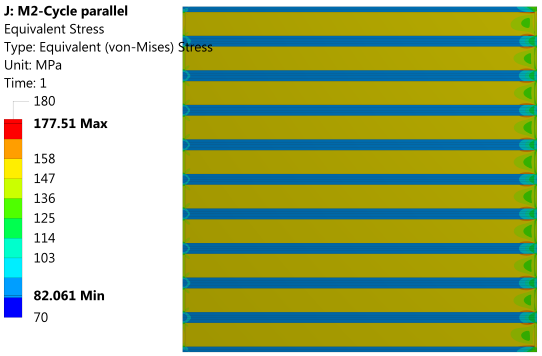

Strain

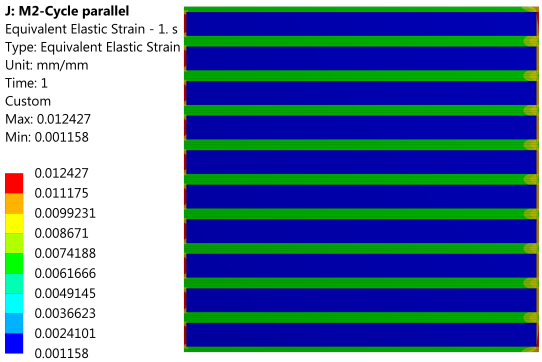

Horizontal

Stress

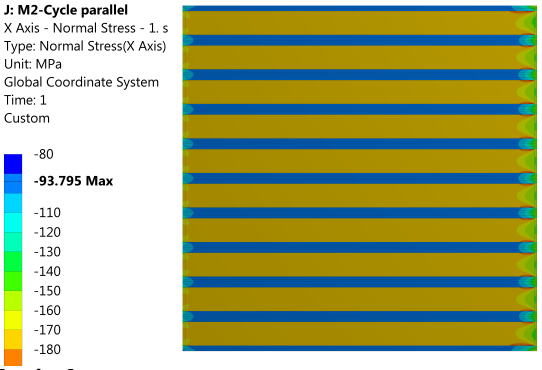

Strain

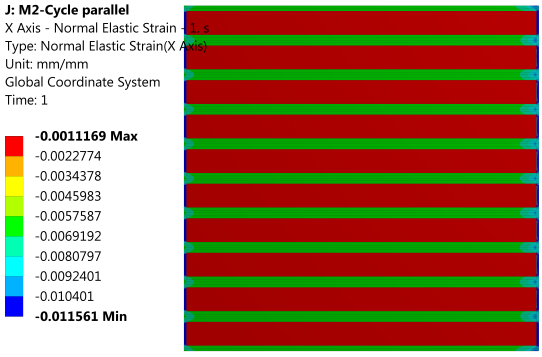

Vertical

Stress

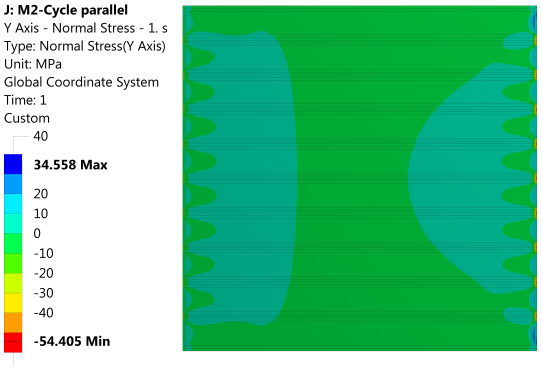

Strain

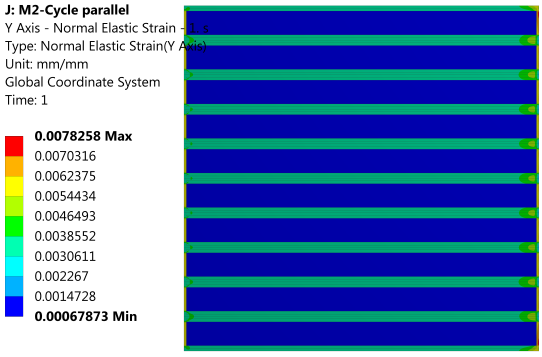

Figure C.2: Horizontal loading of the M2 10-Stack model to 150MPa in compression

Von Mises / Equivalent

Stress

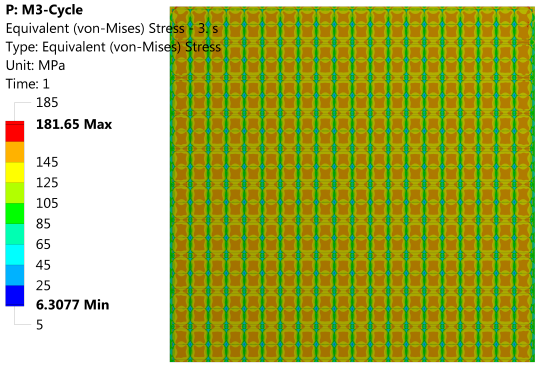

Strain

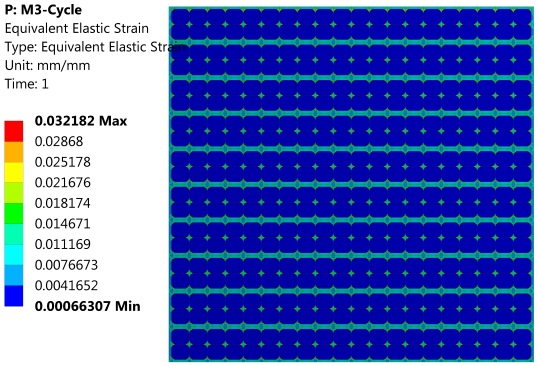

Horizontal

Stress

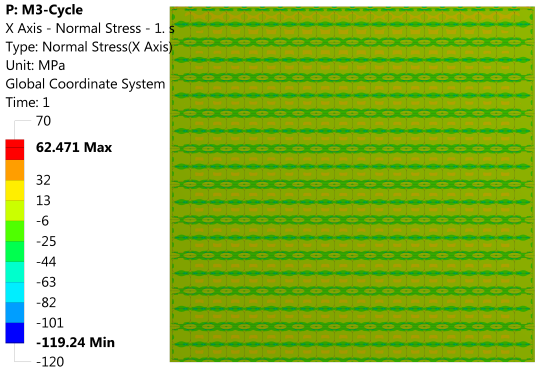

Strain

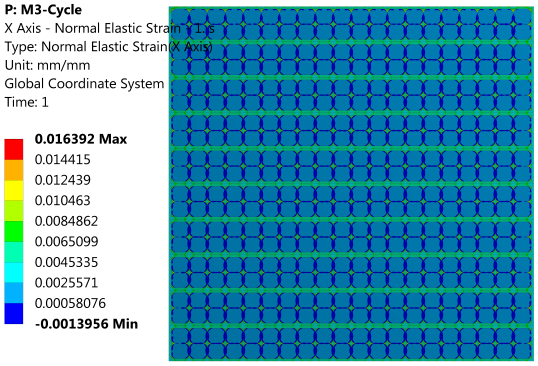

Vertical

Stress

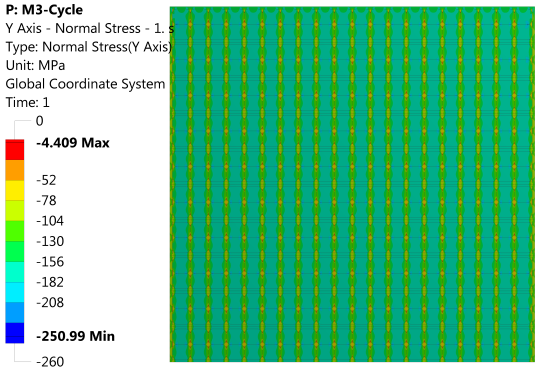

Strain

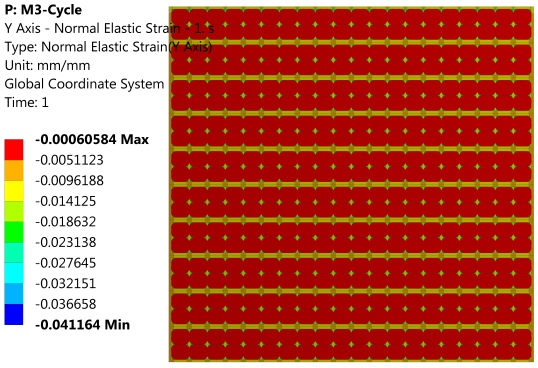

Figure C.3: Vertical loading of the M3 10-Stack model to 150MPa in compression

Von Mises / Equivalent

Stress

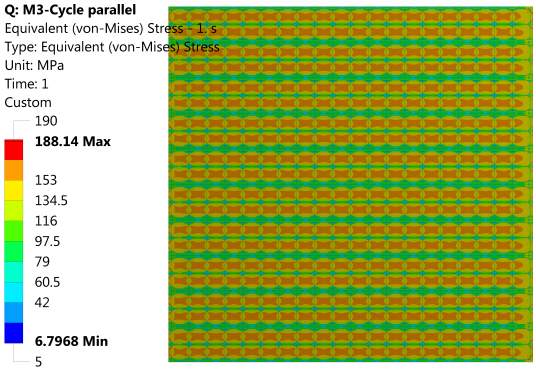

Strain

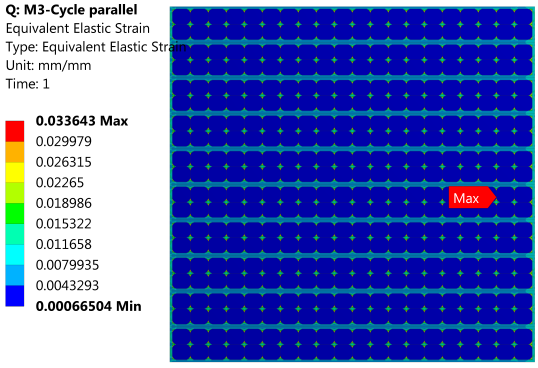

Horizontal

Stress

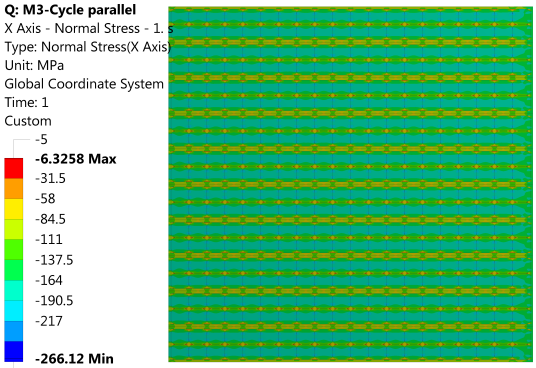

Strain

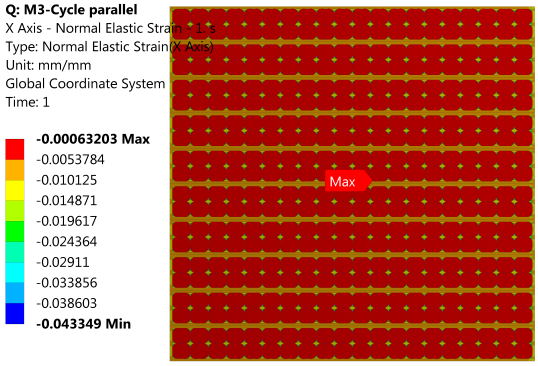

Vertical

Stress

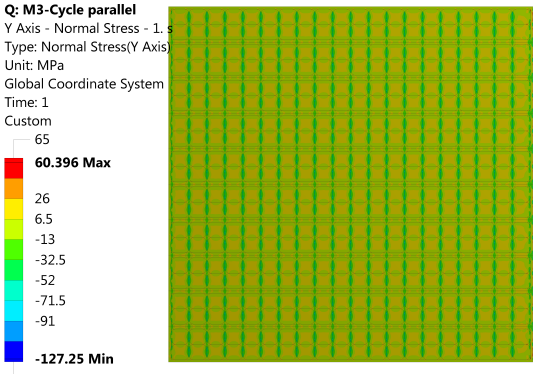

Strain

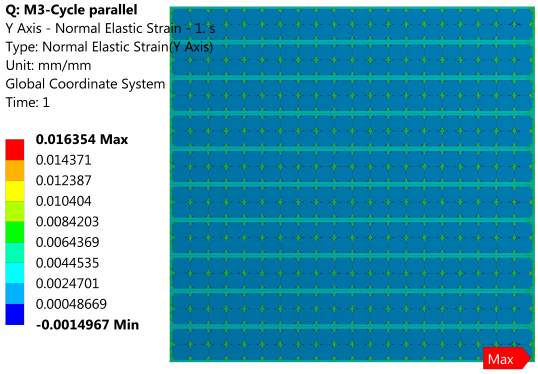

Figure C.4: Horizontal loading of the M3 10-Stack model to 150MPa in compression

C.2 FEA of the strand

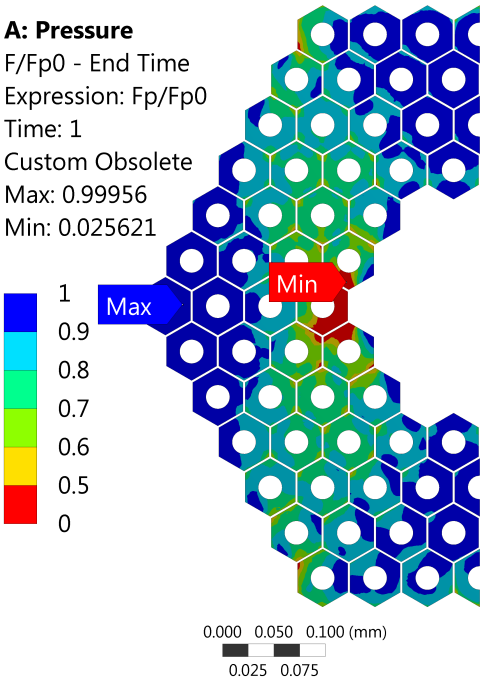

Figure C.5: critical current reduction, 108/127 RRP Strand, 12T at 1.9K

C.3 Electro Magnetic Force plots

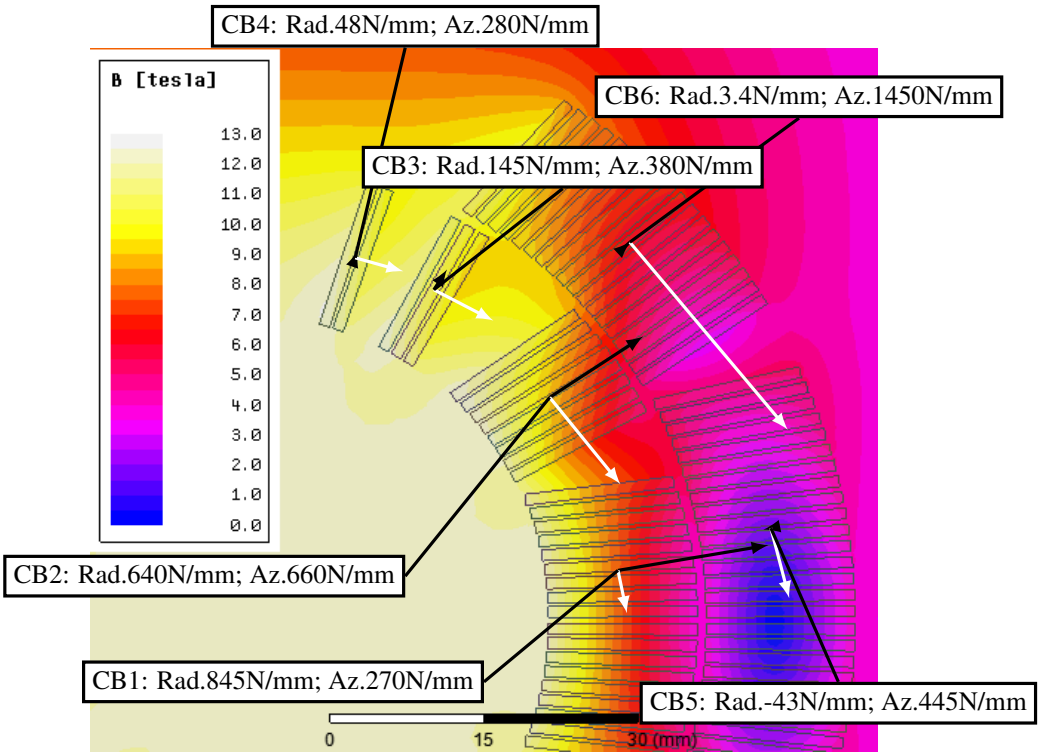

Figure C.6: Radial and Azimuthal Forces - DS11T at 12.8 kA

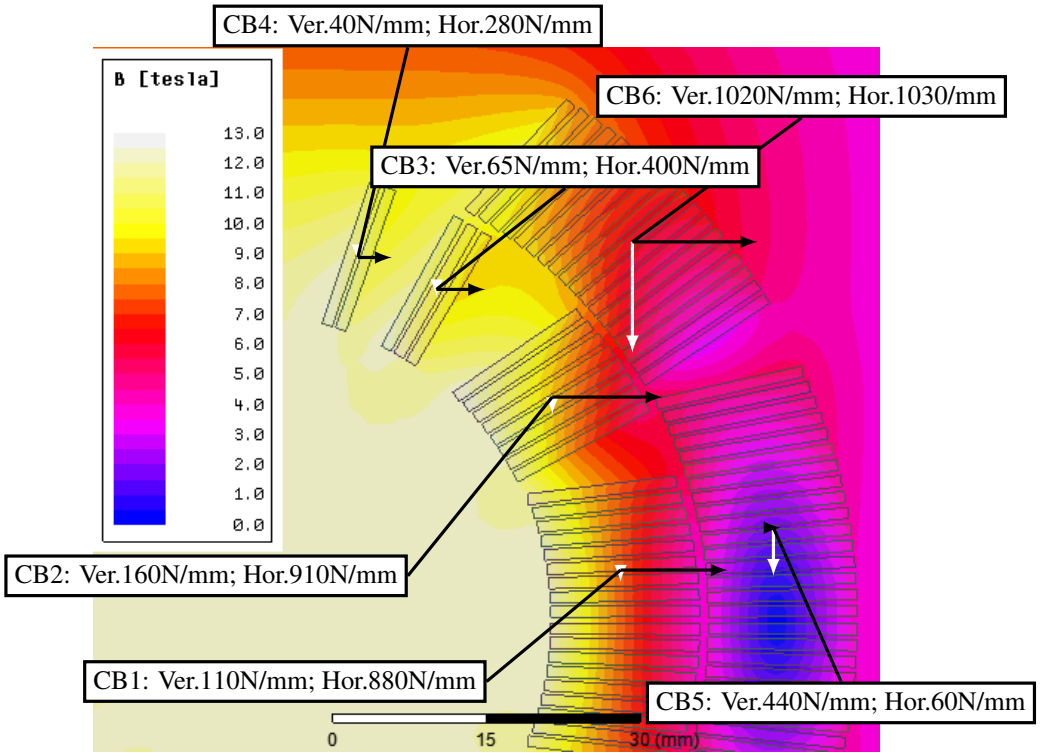

Figure C.7: Horizontal and Vertical Forces - DS11T at 12.8 kA

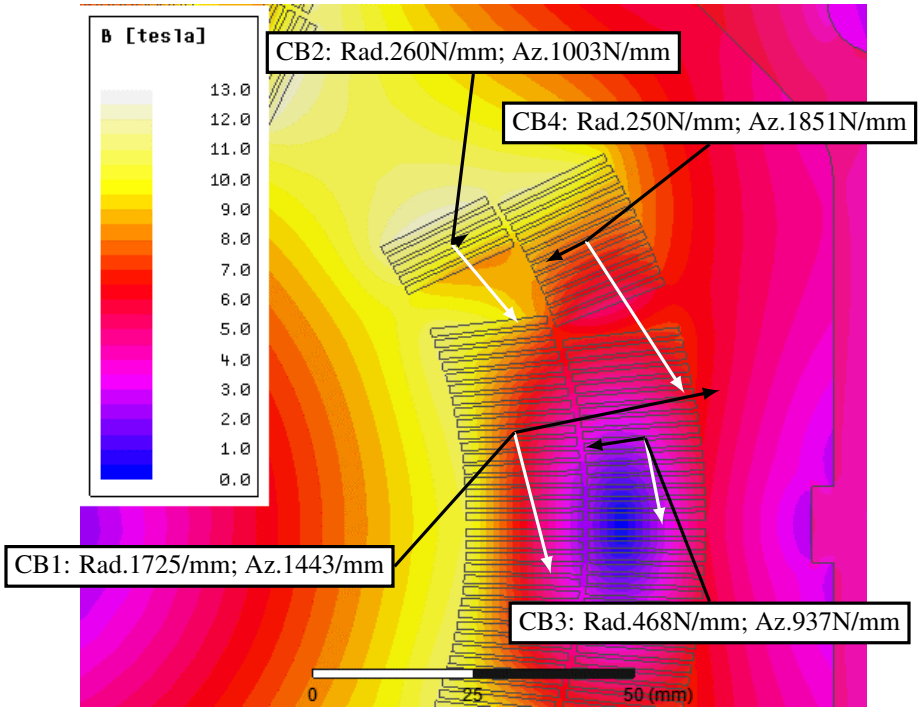

Figure C.8: Radial and Azimuthal Forces - MQXF at 19.1 kA

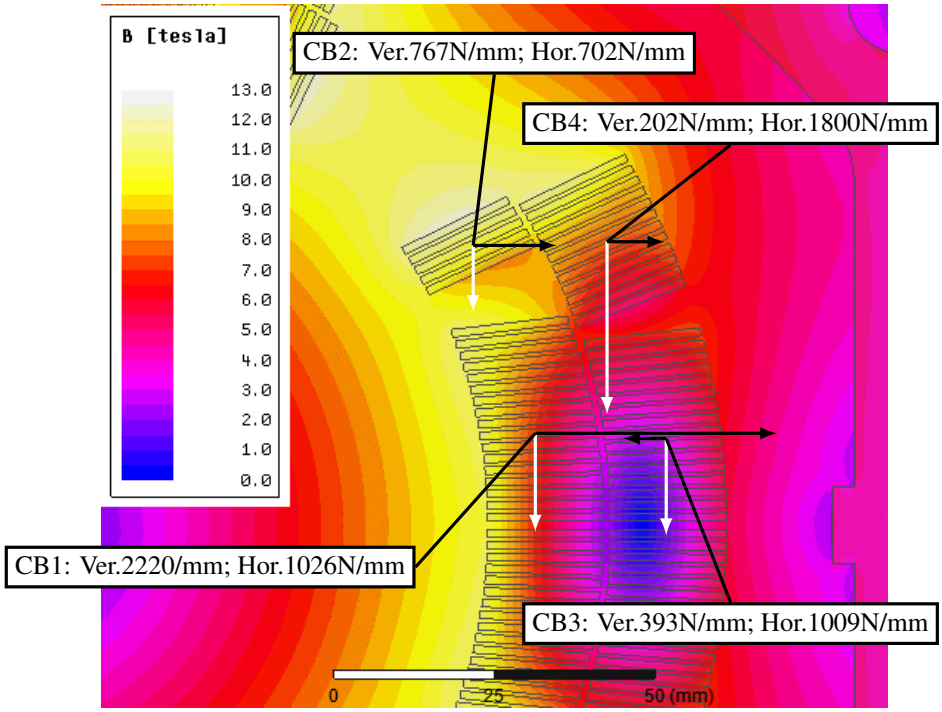

Figure C.9: Horizontal and Vertical Forces - MQXF at 19.1 kA

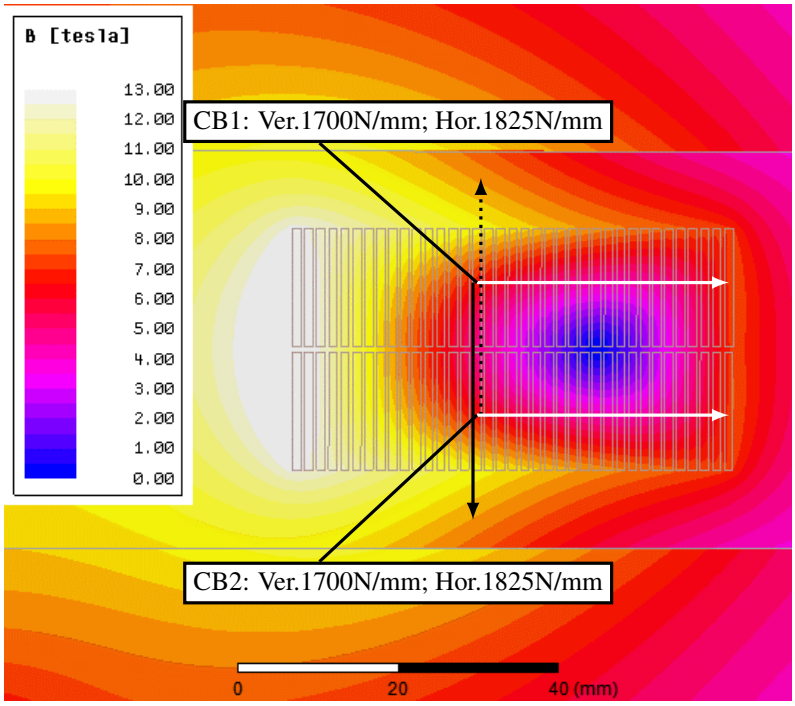

Figure C.10: Horizontal and Vertical Forces - SMC-11T at 15.1 kA

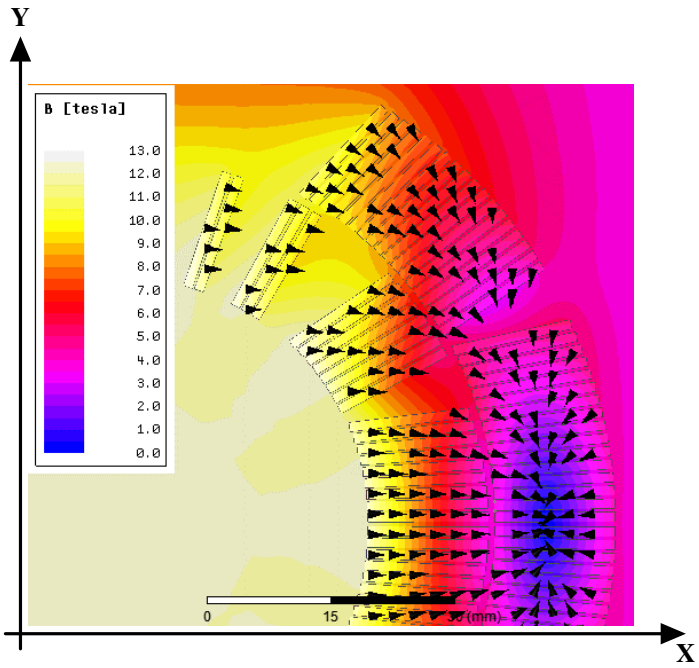

Figure C.11: 11T magnetic field an force vectors at 12.8 kA, coordinate systems origin is in the center of the bore

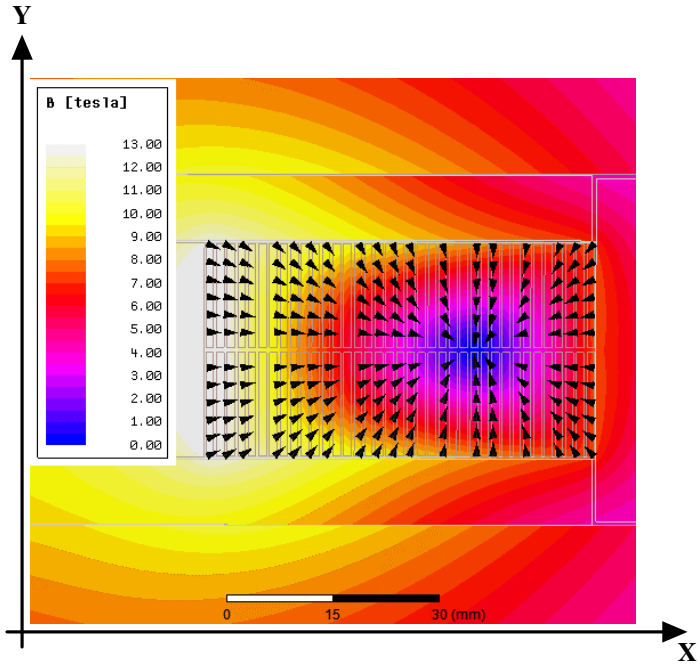

Figure C.12: SMC-11T magnetic field an force vectors at 15.1 kA, coordinate systems origin is in the center of the coil

C.4 FEA of the coils

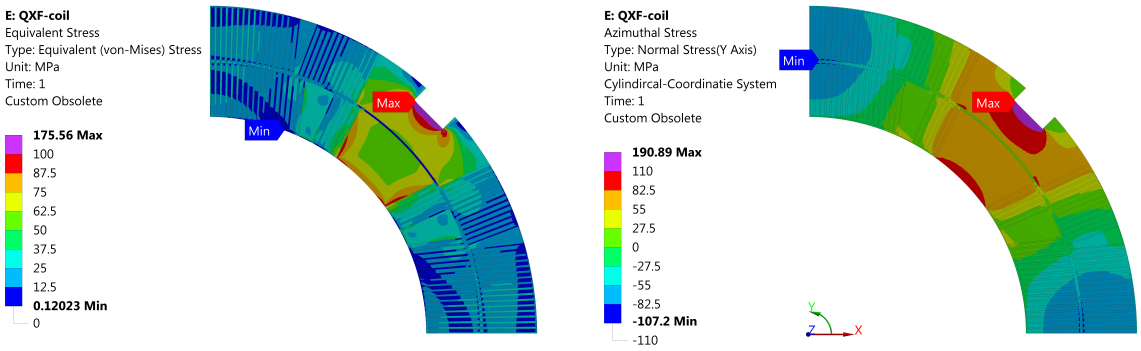

Figure C.13: MQXF - only full coil - EQV and Azimuthal Stress at 19.1kA

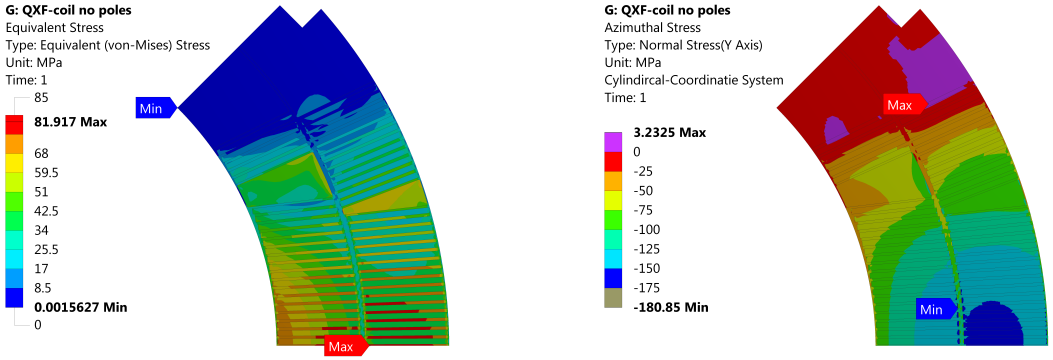

Figure C.14: MQXF - only half coil - EQV and Azimuthal Stress at 19.1kA

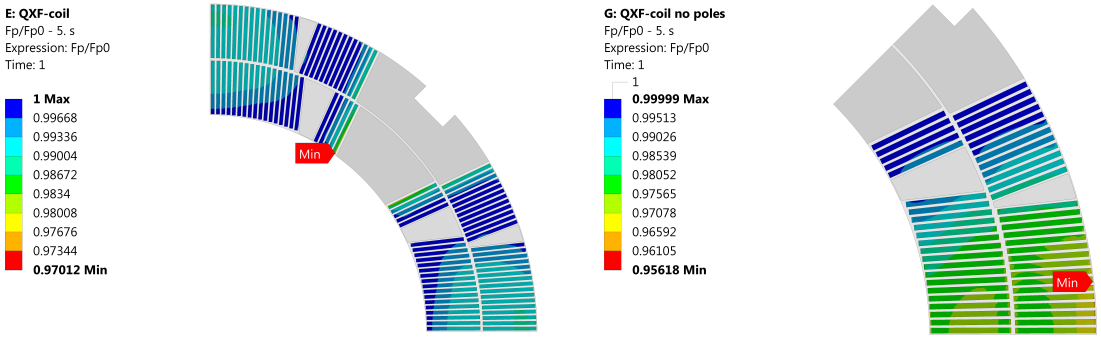

Figure C.15: MQXF - half and full coil model - critical current degradation at 19.1kA

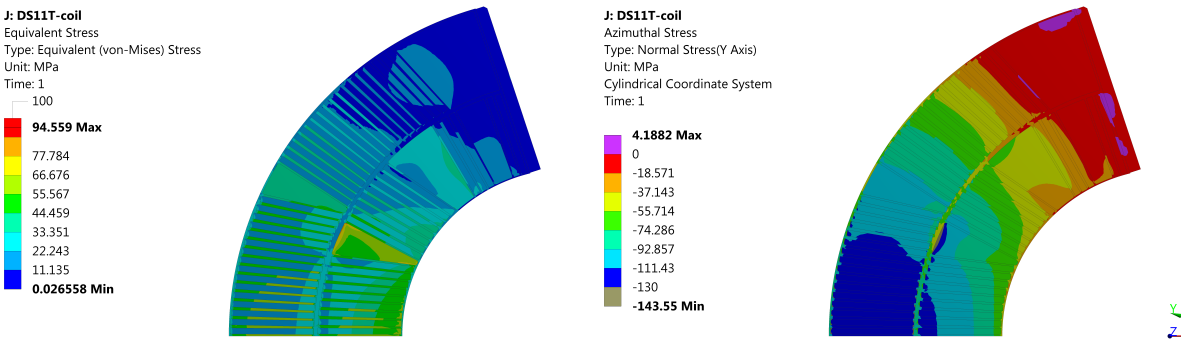

Figure C.16: DS11T - EQV and Azimuthal Stress at 12.8kA

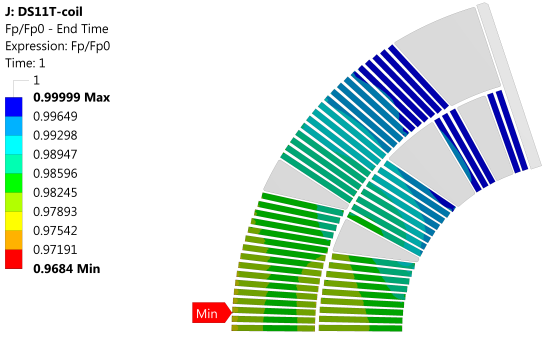

Figure C.17: DS11T - critical current degradation at 12.8kA

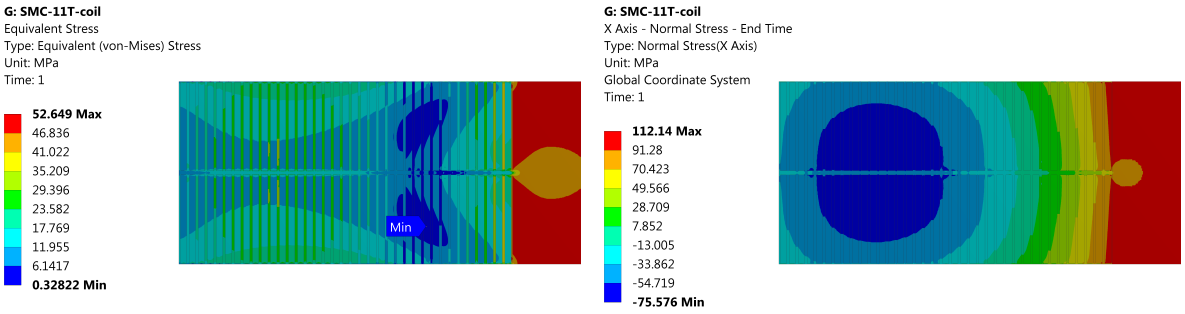

Figure C.18: SMC - only full coil - EQV and Azimuthal Stress at 15.1kA

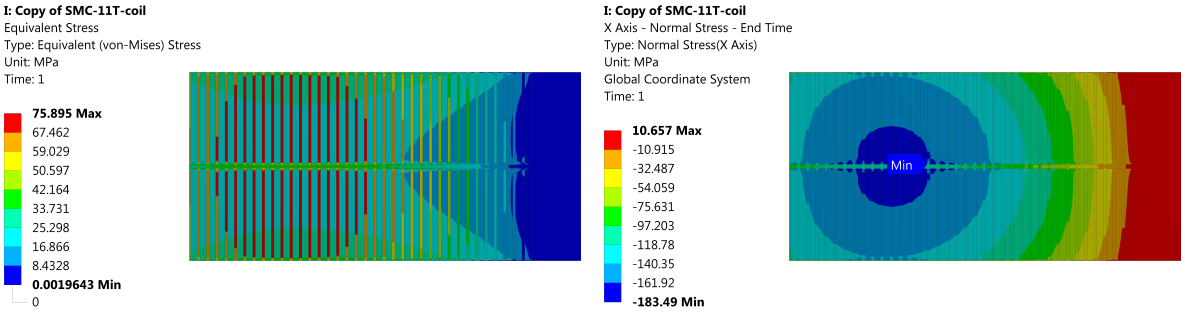

Figure C.19: SMC - only half coil - EQV and Azimuthal Stress at 15.1kA

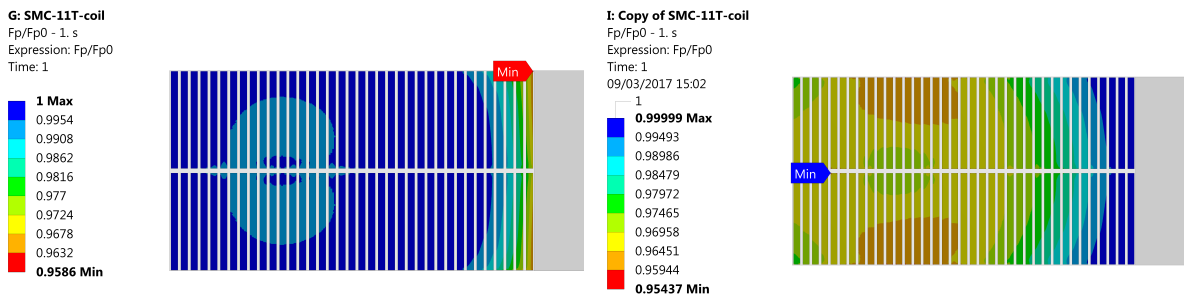

Figure C.20: SMC - half and full coil model - critical current degradation at 15.1kA

C.5 FEA of the structures

C.5.1 DS11T

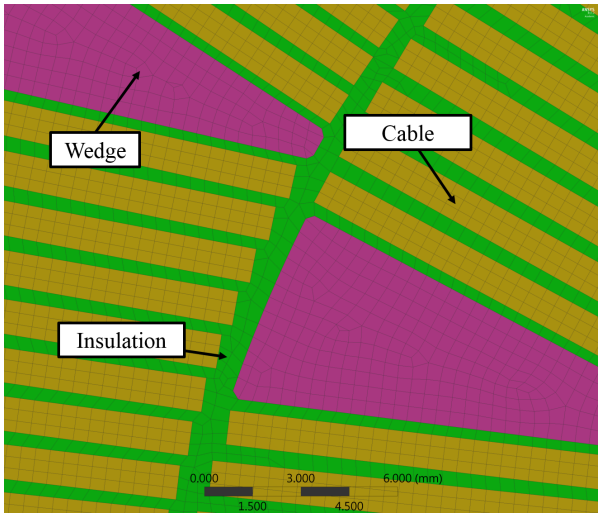

Figure C.21: Meshing used on the cable and insulation

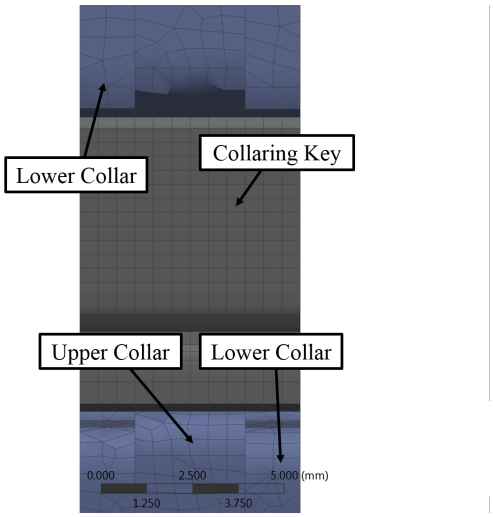

Figure C.22: Meshing of the collaring key and the three interleaving collars

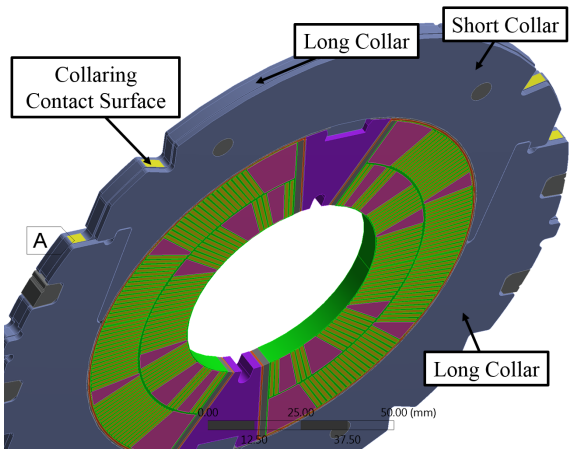

Figure C.23: Collaring Surfaces Top Collar-Pack

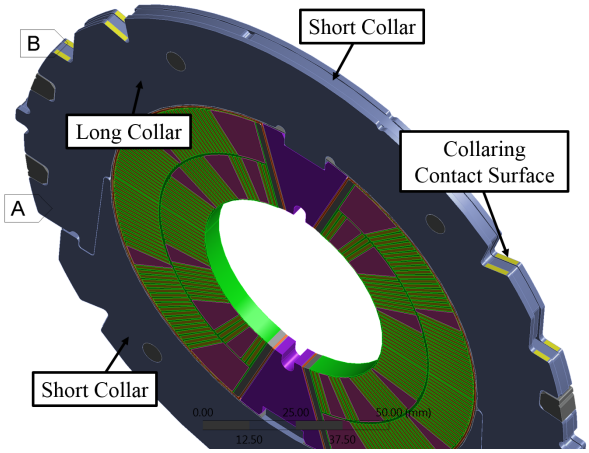

Figure C.24: Collaring Surfaces Lower Collar-Pack

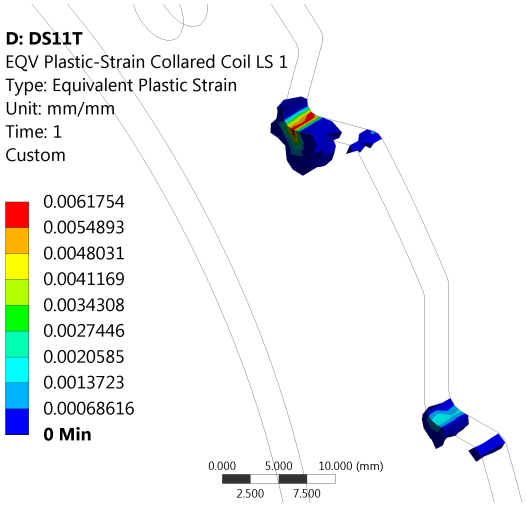

Figure C.25: EQV Plastic Strain in the long collar after collaring

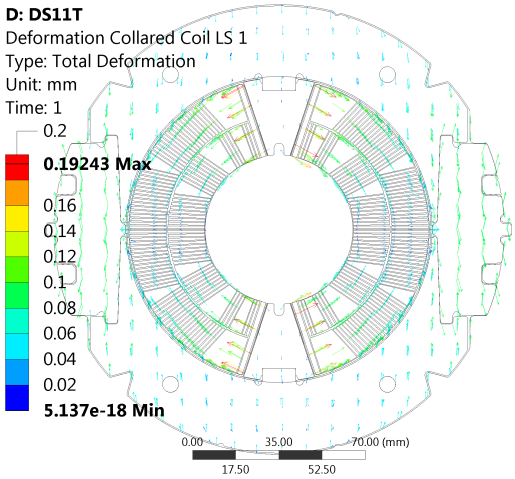

Figure C.26: Displacement vector during the maximum collaring displacement, note that the max. displacement is due to the contact offset of 0.2mm

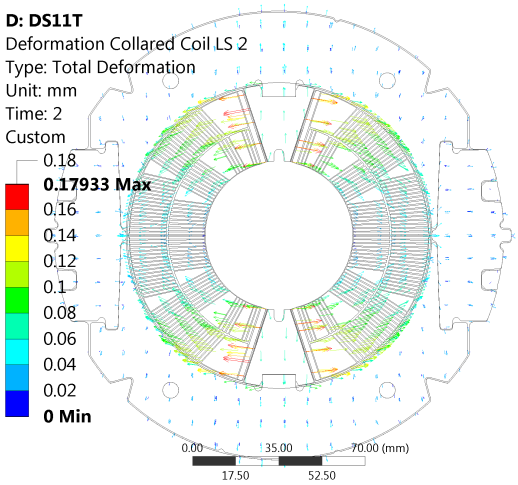

Figure C.27: Total deformation after collaring, LS 2

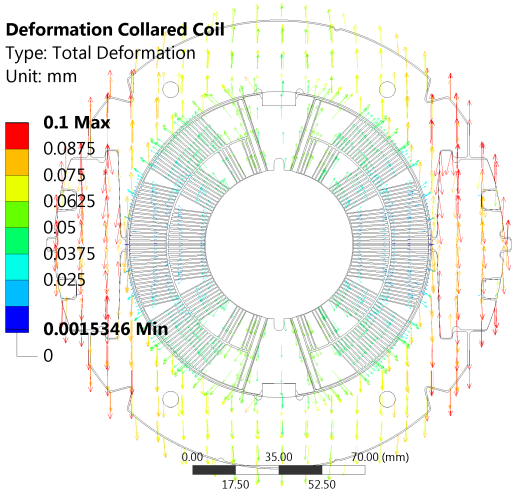

Figure C.28: Deformation due to spring back, LS 2

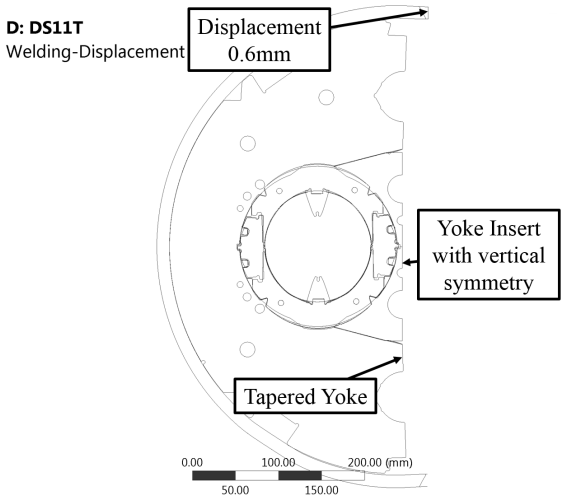

Figure C.29: "pulling" on the shell to simulate the welding, deformation scaled by factor 50, LS 3

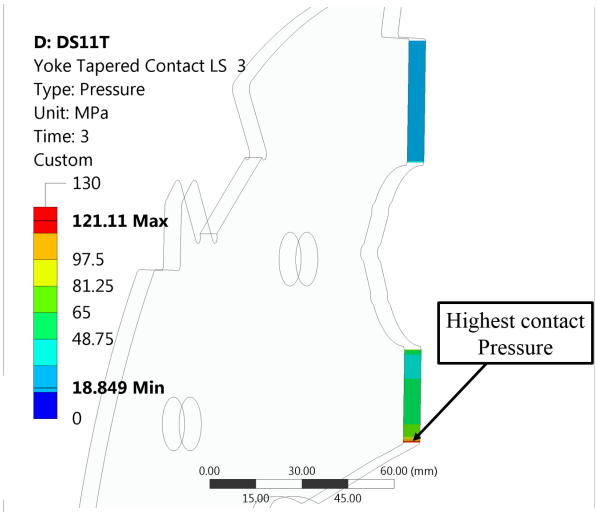

Figure C.30: Contact pressure of the yoke on the tapered edge, after welding, LS 3

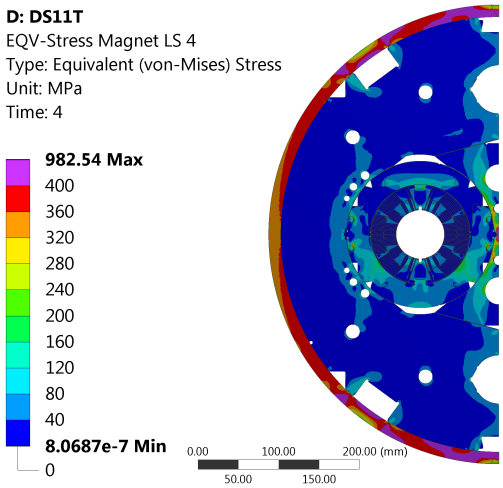

Figure C.31: EQV stress in the magnet at 1.9K

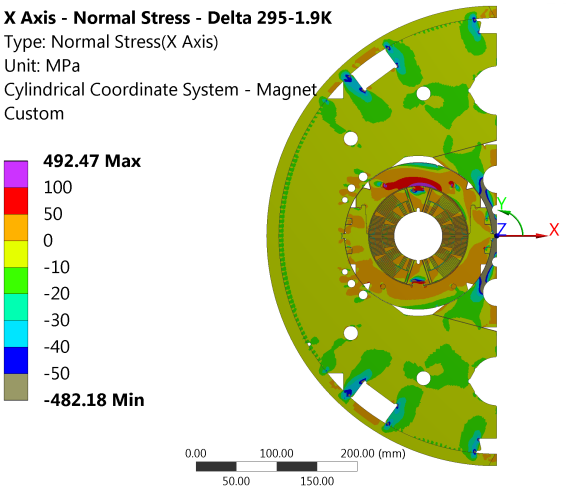

Figure C.32: Delta between 295K and 1.9K in radial pressure, CS center of the magnet

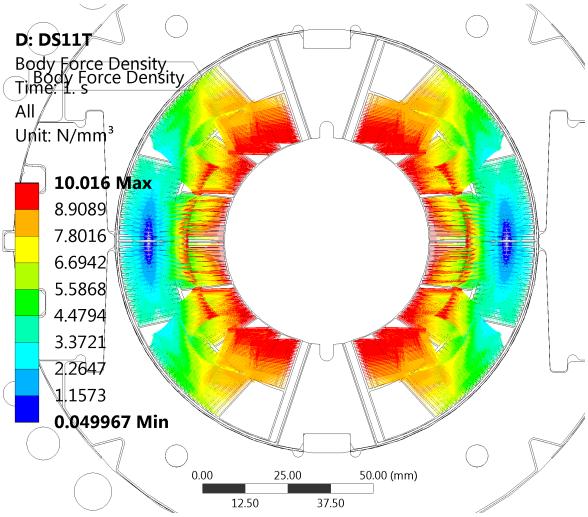

Figure C.33: Body force map of the DS11T at 12.8kA

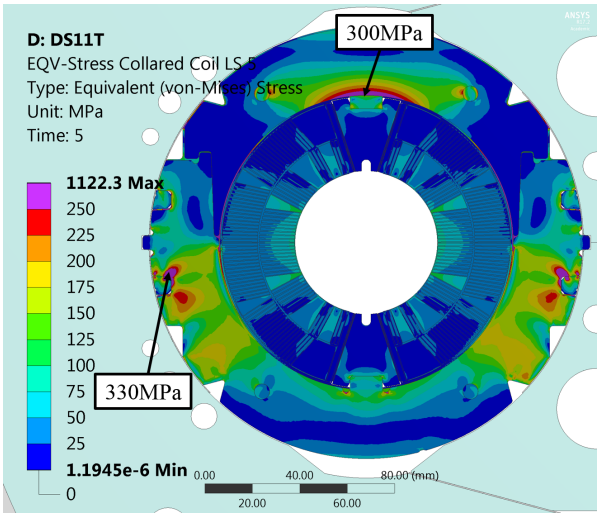

Figure C.34: EQV stress in the collared coil during powering, LS 5

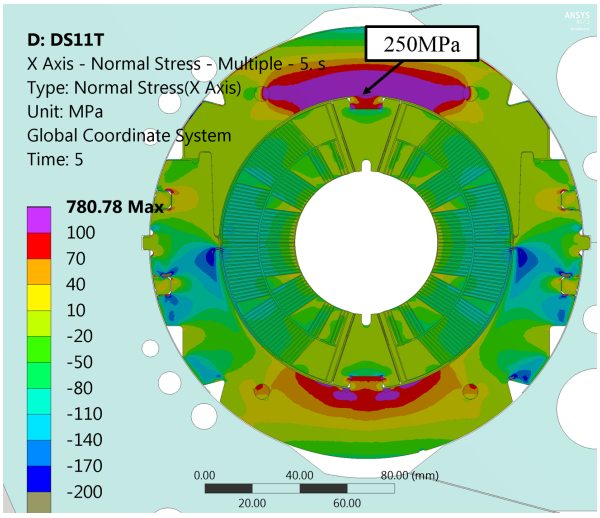

Figure C.35: Vertical normal stress in the collared coil during powering, LS 5

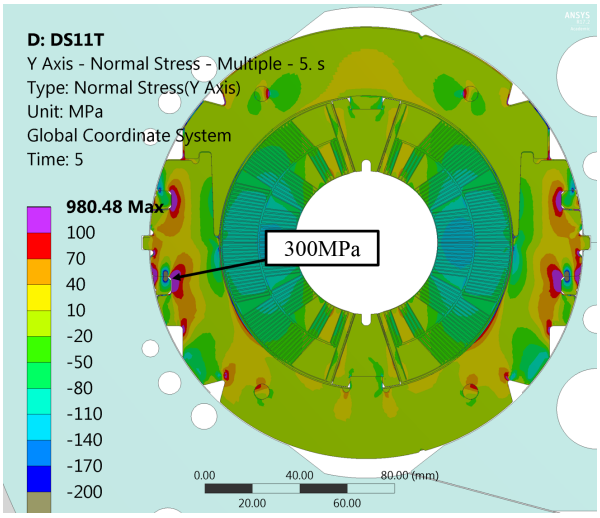

Figure C.36: Horizontal normal stress in the collared coil during powering, LS 5

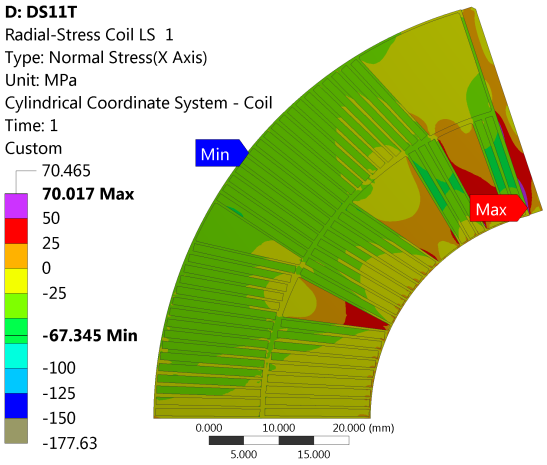

Figure C.37: DS11T radial coil stress, LS 1

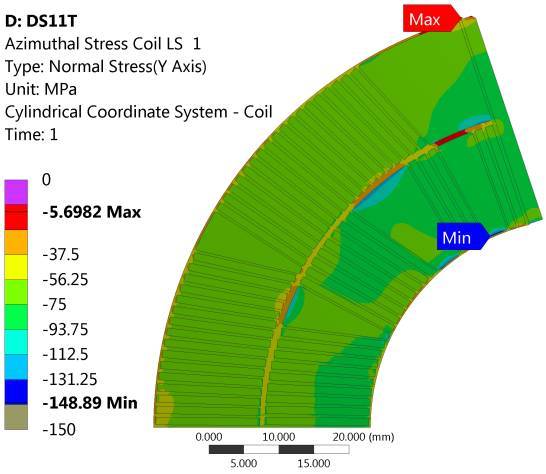

Figure C.38: DS11T azimuthal coil stress, LS 1

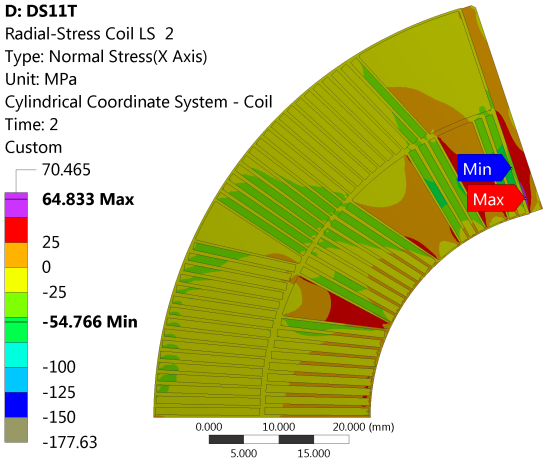

Figure C.39: DS11T radial coil stress, LS 2

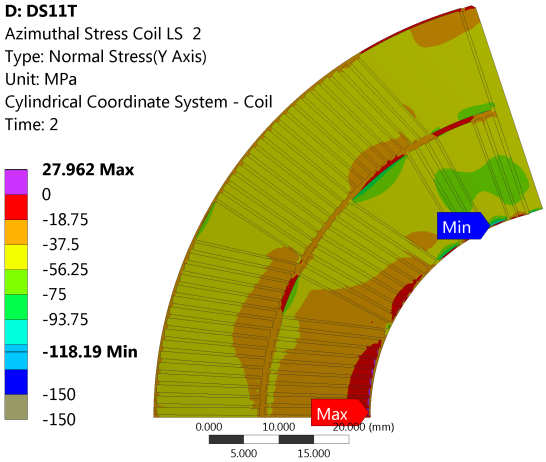

Figure C.40: DS11T azimuthal coil stress, LS 2

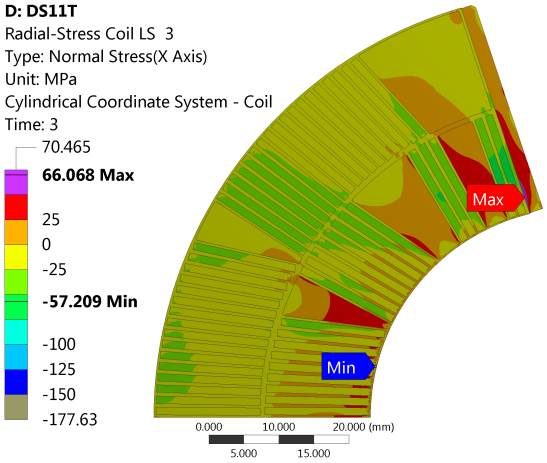

Figure C.41: DS11T radial coil stress, LS 3

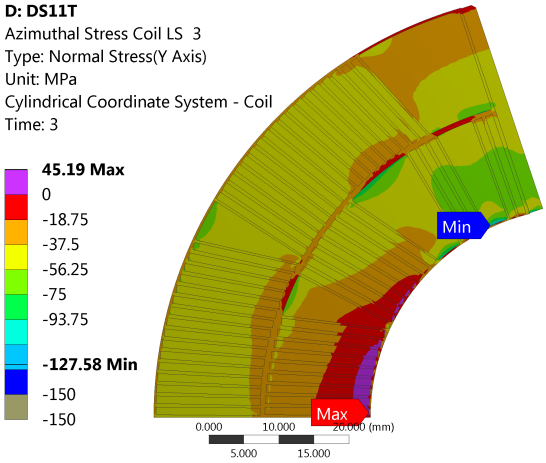

Figure C.42: DS11T azimuthal coil stress, LS 3

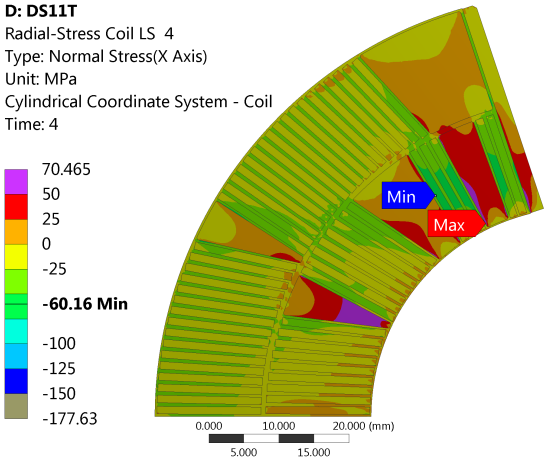

Figure C.43: DS11T radial coil stress, LS 4

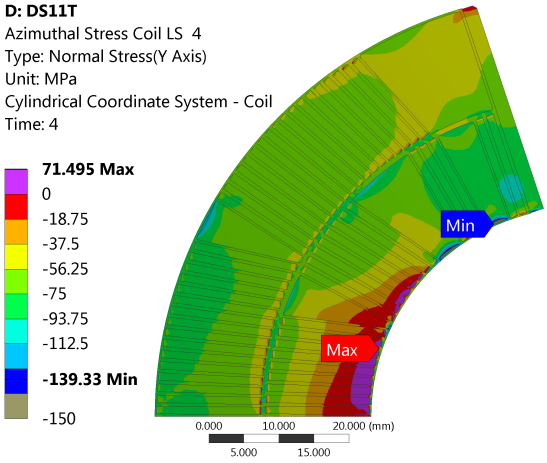

Figure C.44: DS11T azimuthal coil stress, LS 4

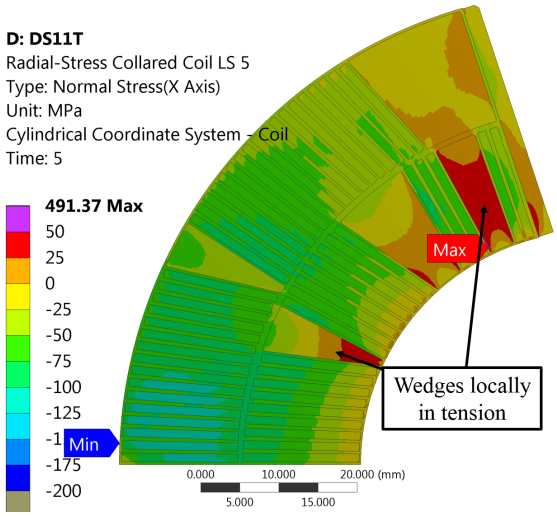

Figure C.45: Radial normal stress in the coil during powering, LS 5

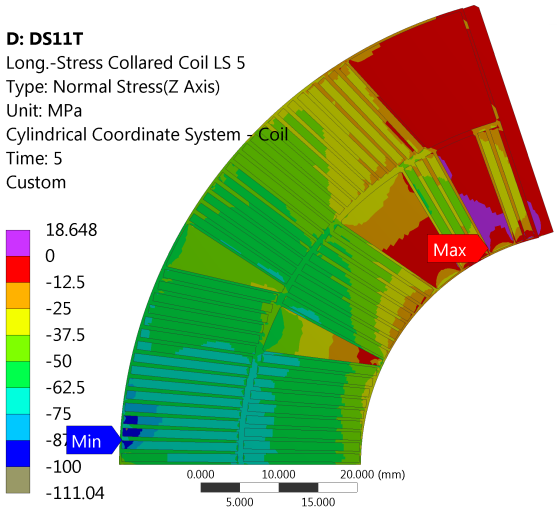

Figure C.46: Longitudinal normal stress in the coil during powering, LS 5

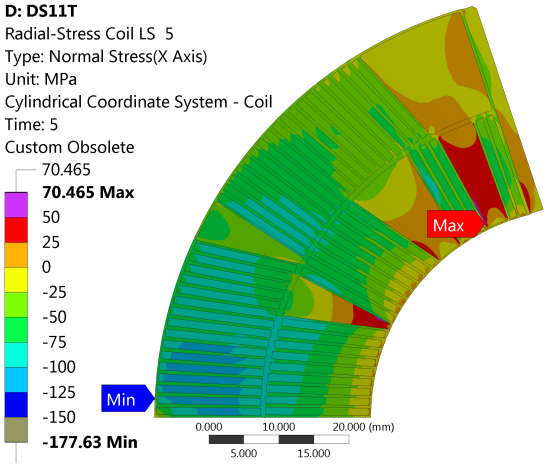

Figure C.47: DS11T radial coil stress, LS 5

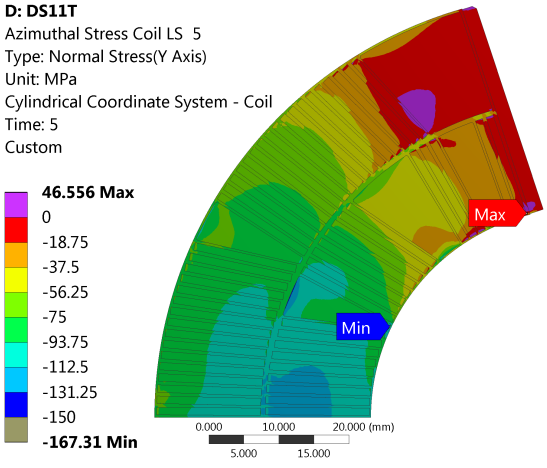

Figure C.48: DS11T azimuthal coil stress, LS 5

C.5.2 MQXF

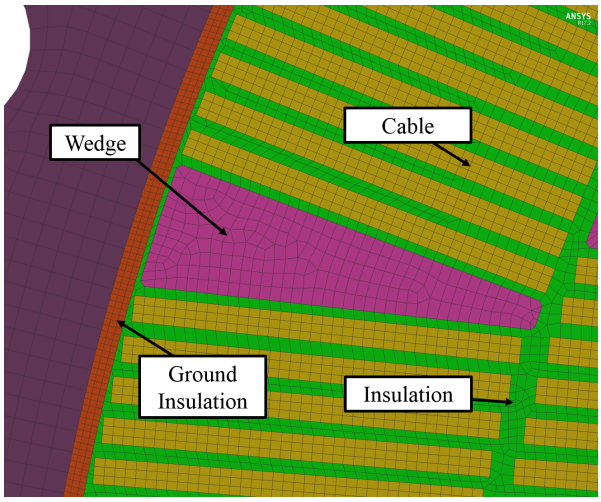

Figure C.49: Meshing used on the cable and insulation

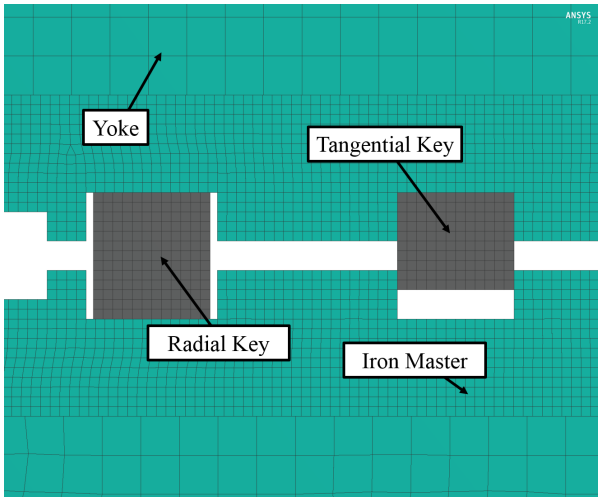

Figure C.50: Meshing of the vertical and horizontal keys

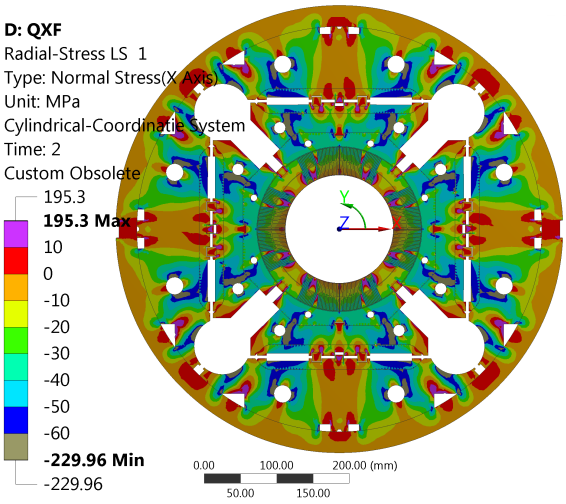

Figure C.51: Radial stress at maximum bladder pressure, LS 1

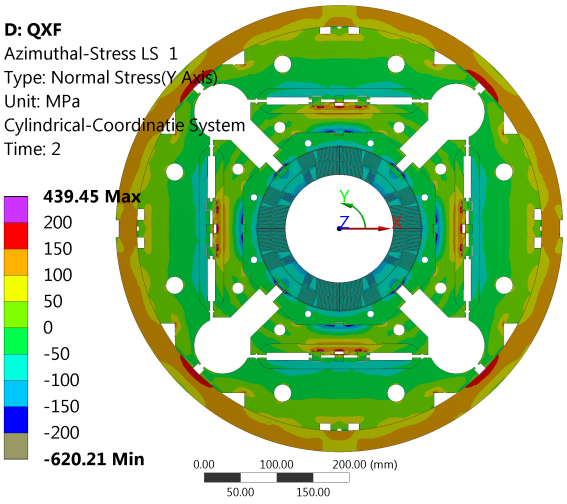

Figure C.52: Azimuthal stress at maximum bladder pressure, LS 1

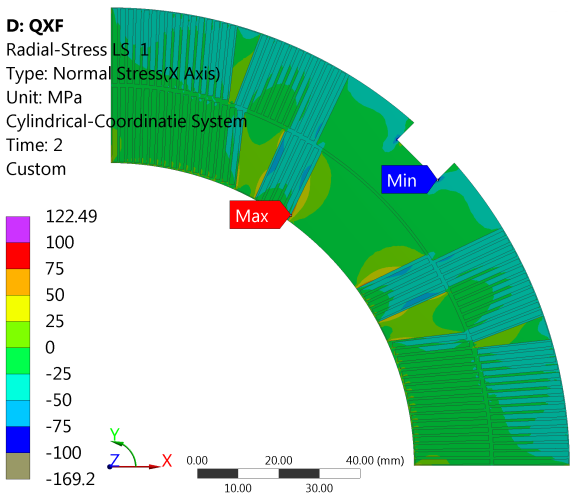

Figure C.53: MQXF radial coil stress, LS 1

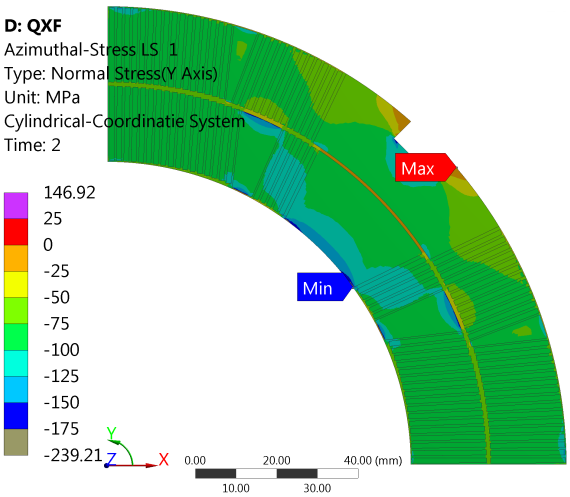

Figure C.54: MQXF azimuthal coil stress, LS 1

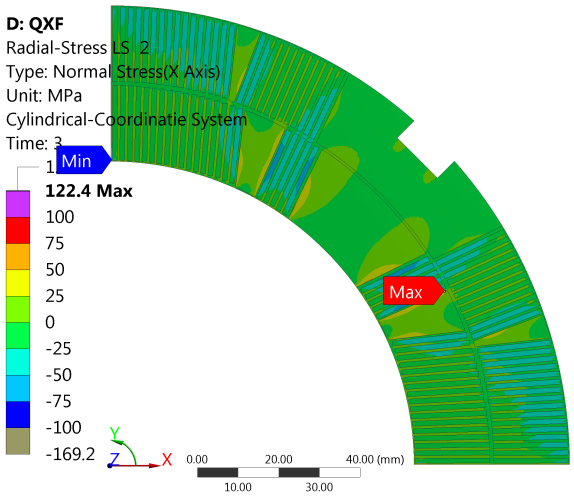

Figure C.55: MQXF radial coil stress, LS 2

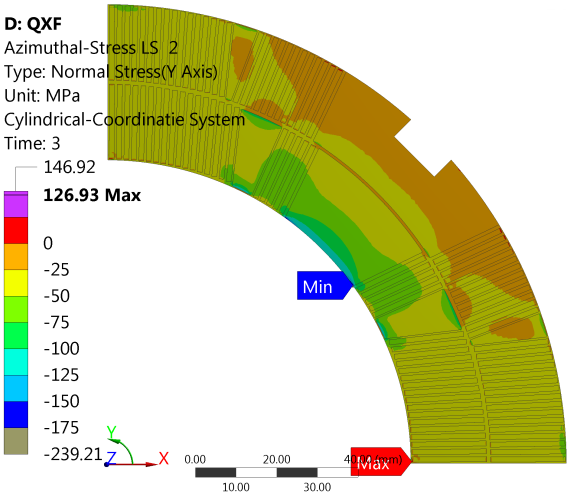

Figure C.56: MQXF azimuthal coil stress, LS 2

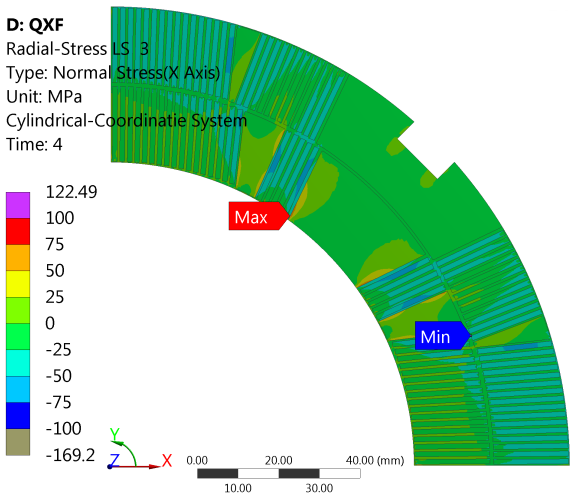

Figure C.57: MQXF radial coil stress, LS 3

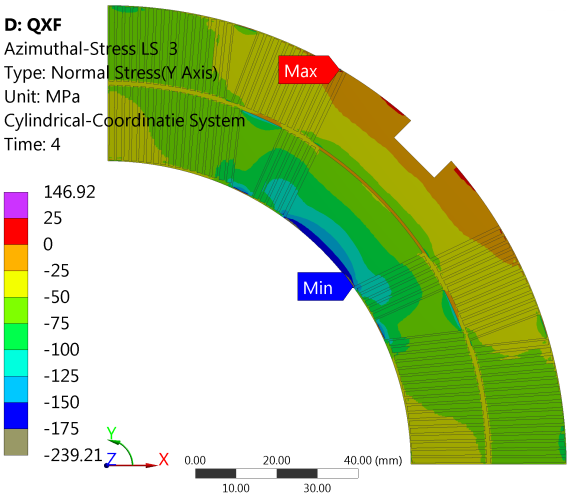

Figure C.58: MQXF azimuthal coil stress, LS 3

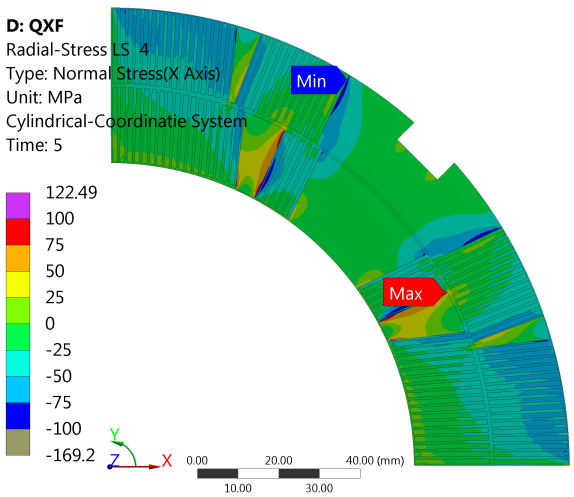

Figure C.59: MQXF radial coil stress, LS 4

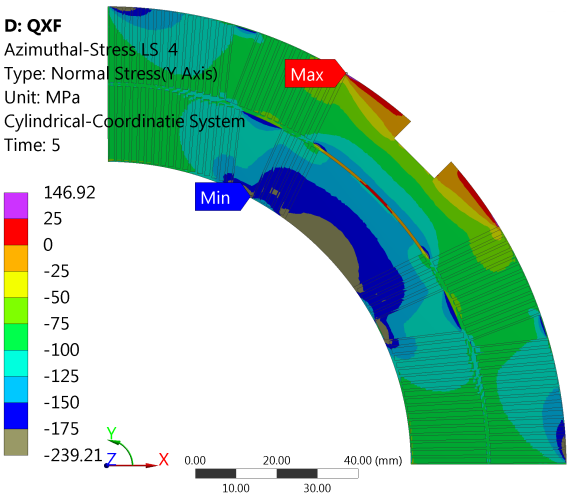

Figure C.60: MQXF azimuthal coil stress, LS 4

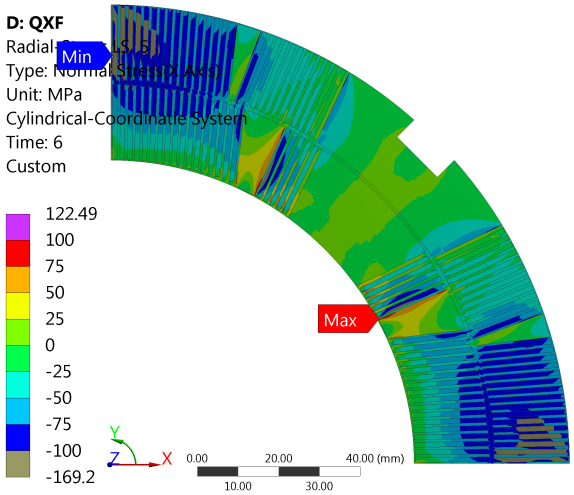

Figure C.61: MQXF radial coil stress, LS 5

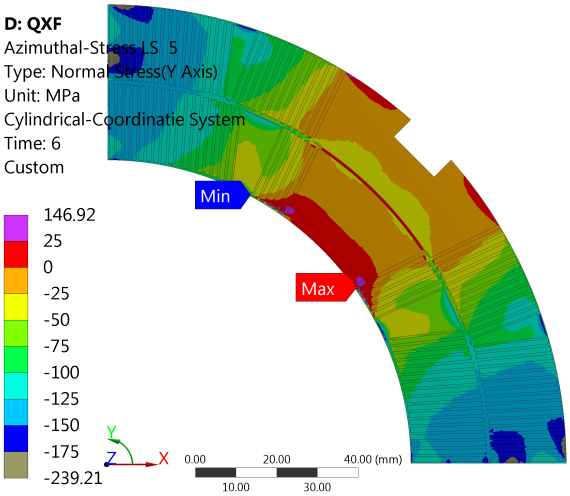

Figure C.62: MQXF azimuthal coil stress, LS 5

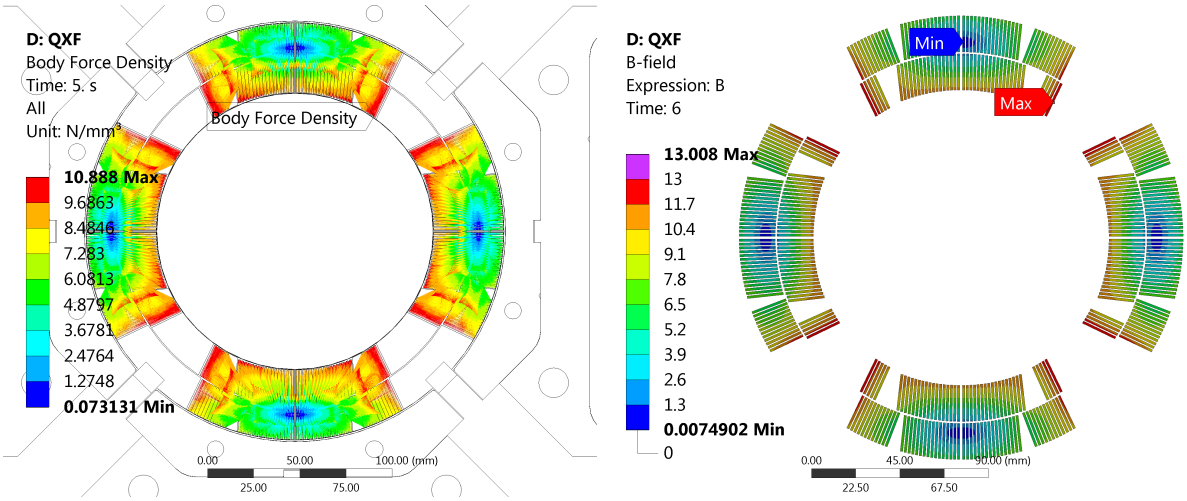

Figure C.63: Magnetic field in the condutor and body force map of the MQXF at 19.1kA

C.5.3 SMC-11T

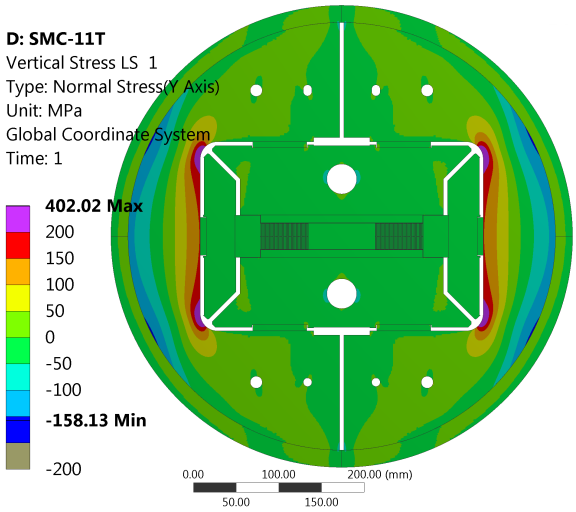

Figure C.64: SMC-11T horizontal stress, LS 1

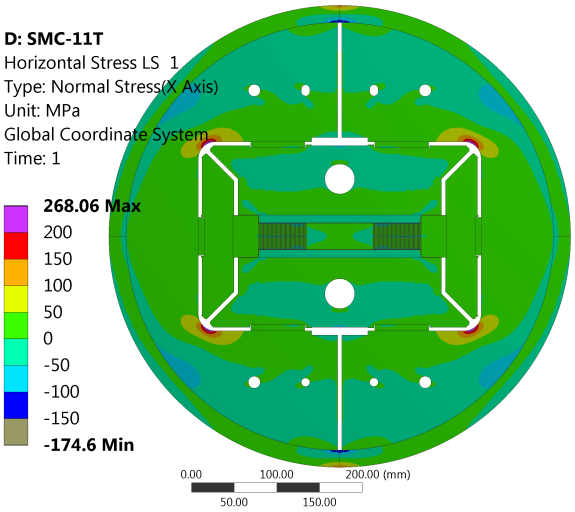

Figure C.65: SMC-11T vertical stress, LS 1

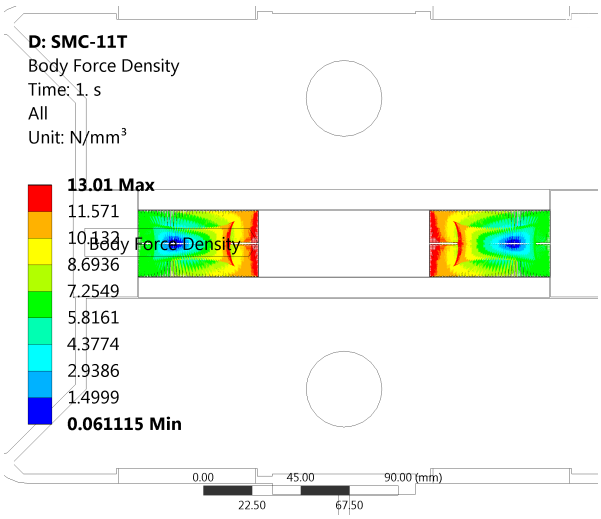

Figure C.66: SMC-11T body force density of the EM-forces

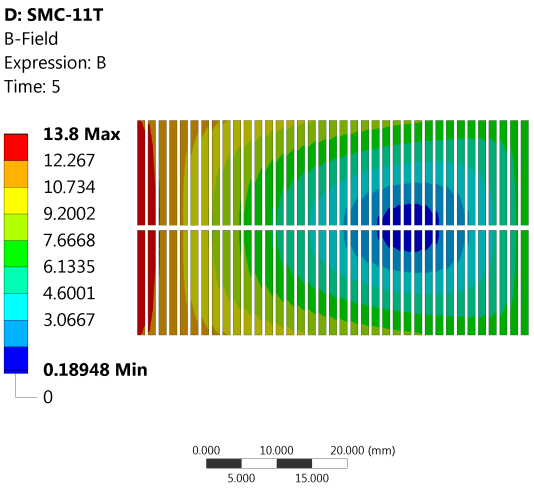

Figure C.67: SMC-11T magnetic field at 15.1kA

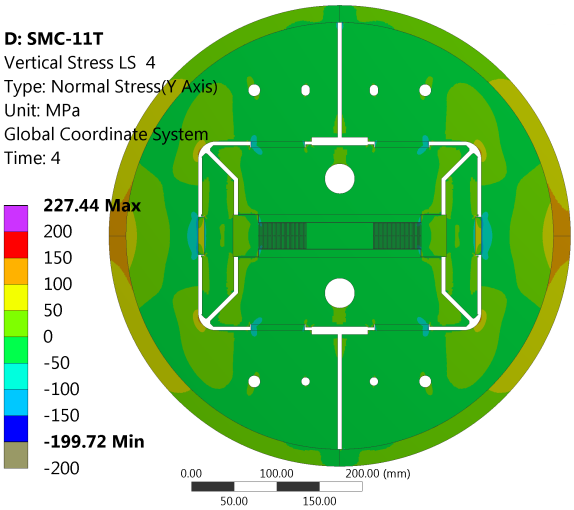

Figure C.68: SMC-11T horizontal stress, LS 4

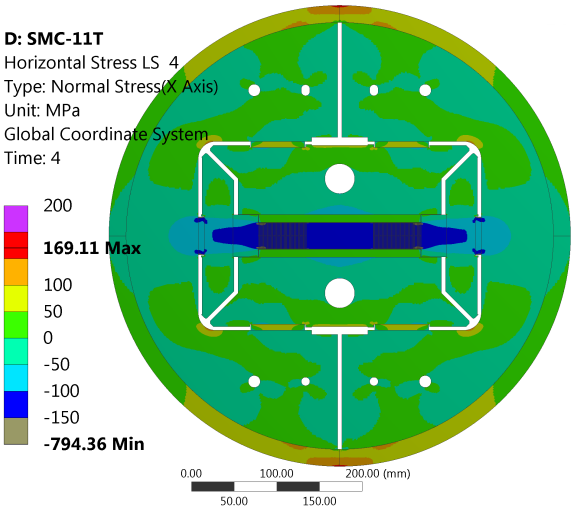

Figure C.69: SMC-11T vertical stress, LS 4

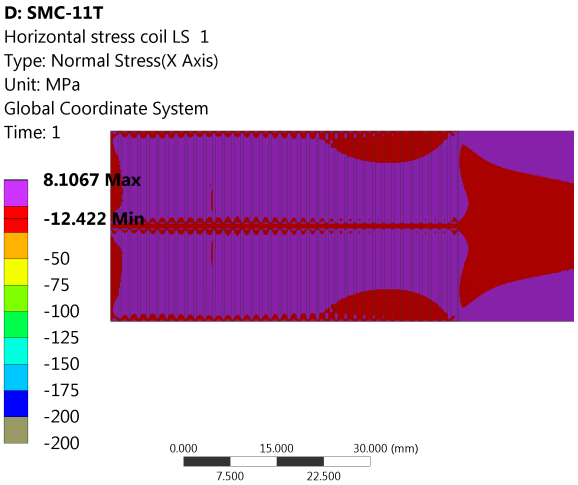

Figure C.70: SMC-11T horizontal stress, LS 1

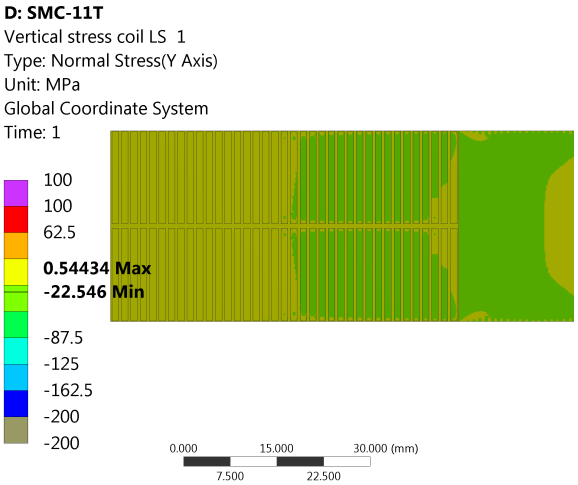

Figure C.71: SMC-11T vertical stress, LS 1

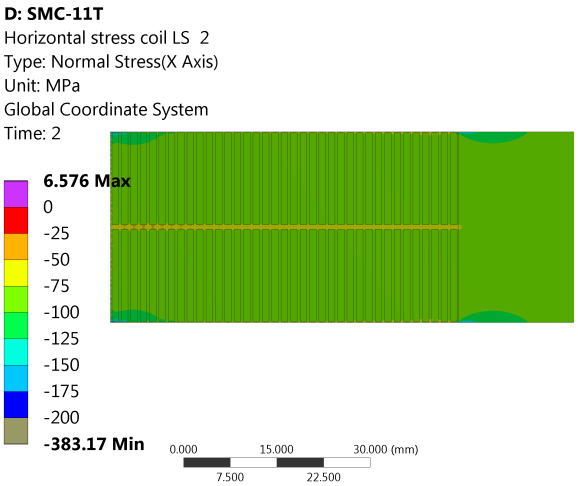

Figure C.72: SMC-11T horizontal stress, LS 2

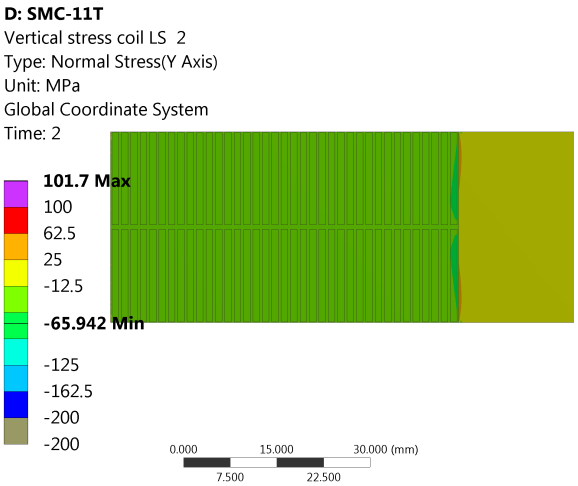

Figure C.73: SMC-11T vertical stress, LS 2

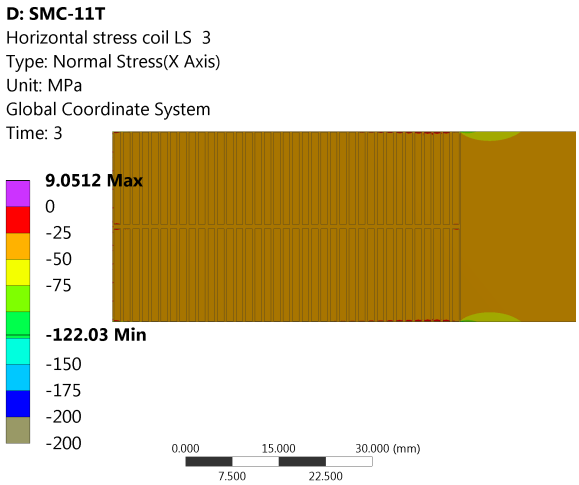

Figure C.74: SMC-11T horizontal stress, LS 3

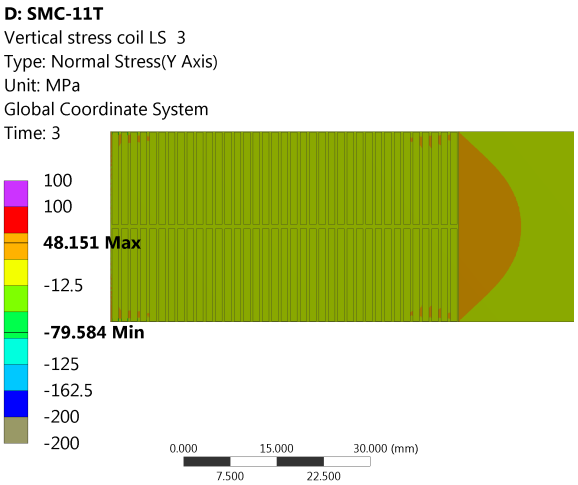

Figure C.75: SMC-11T vertical stress, LS 3

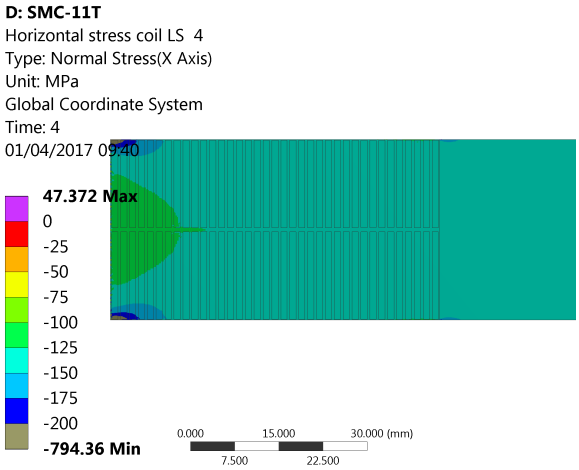

Figure C.76: SMC-11T horizontal stress, LS 4

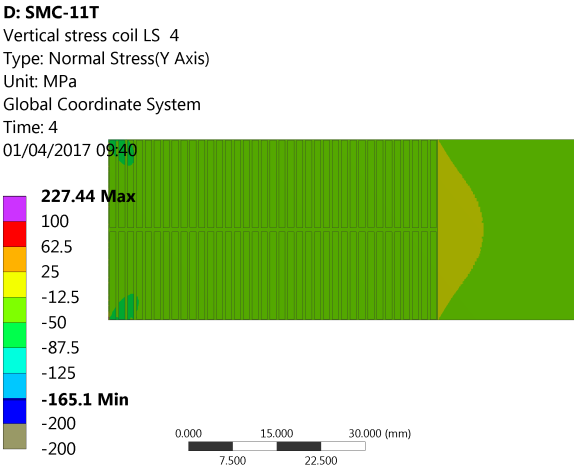

Figure C.77: SMC-11T vertical stress, LS 4

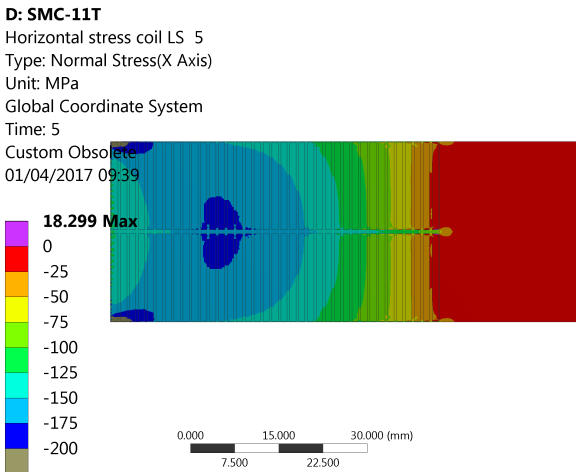

Figure C.78: SMC-11T horizontal stress, LS 5

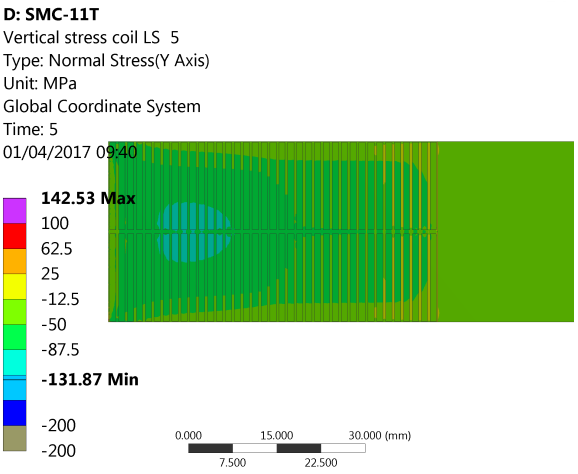

Figure C.79: SMC-11T vertical stress, LS 5

C.5.4 convergence plots

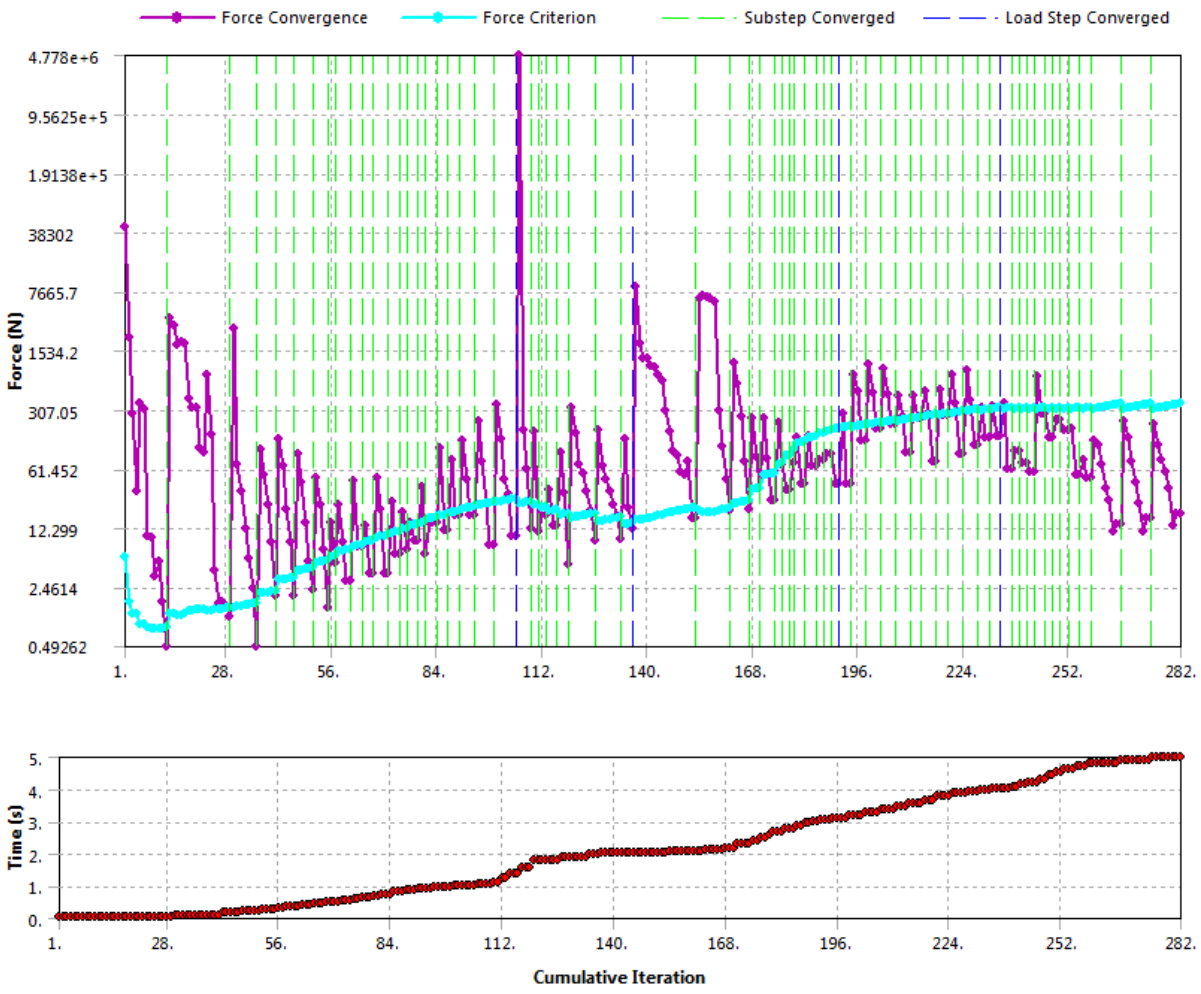

Figure C.80: convergence of the five loading steps of the nominal shimming DS11T-simulations

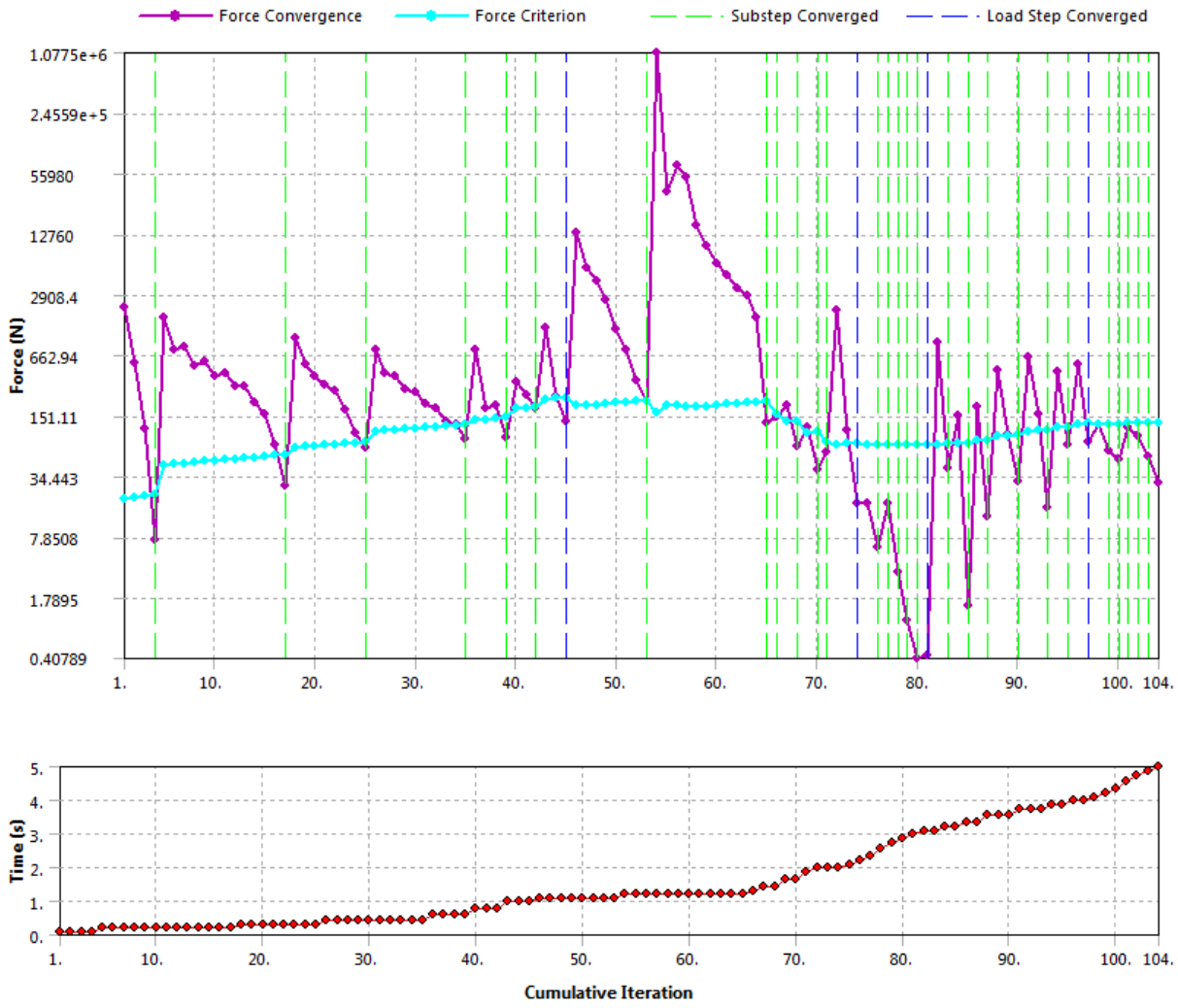

Figure C.81: convergence of the five loading steps of the nominal shimming SMC-11T-simulations

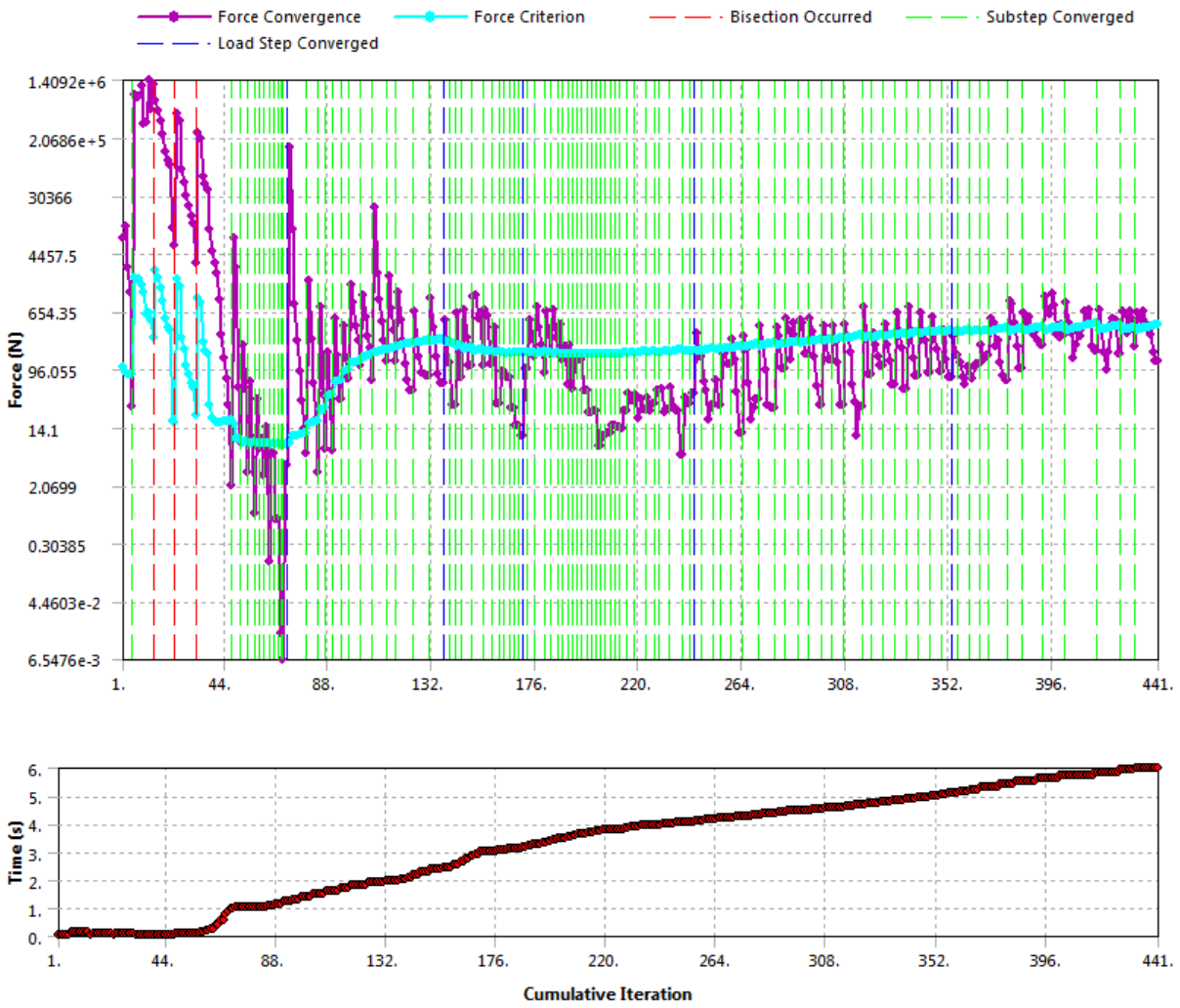

Figure C.82: convergence of the five loading steps of the nominal shimming MQXF-simulations

C.6 Geometrical Dimensions

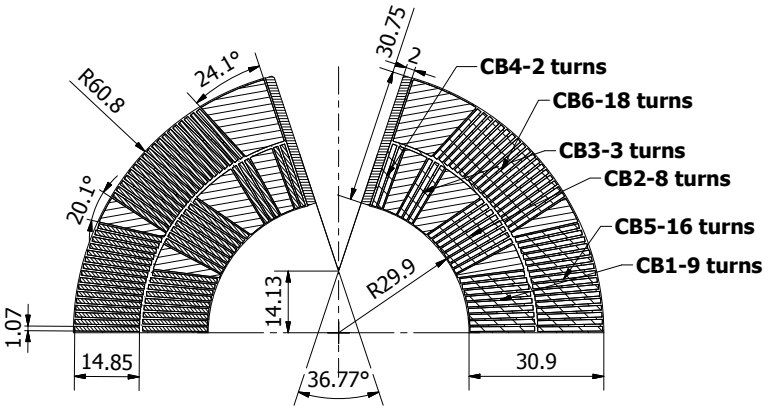

DS11T

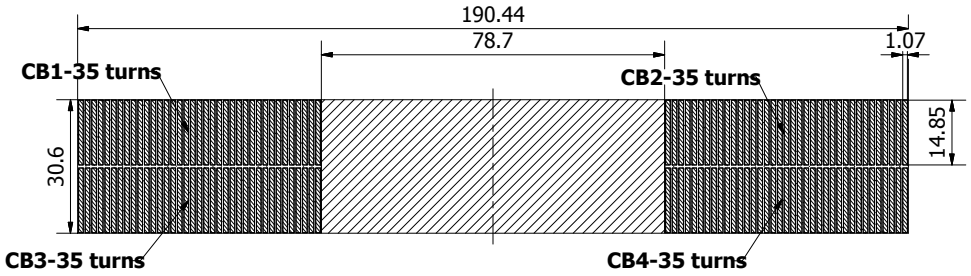

SMC-11T

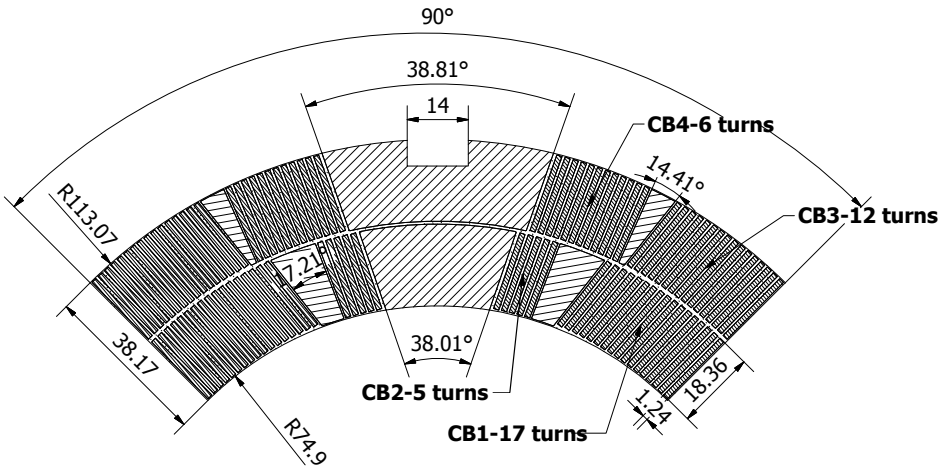

MQXF

Figure C.83: Dimension of the DS11T, SMC-11T and the MQXF coil

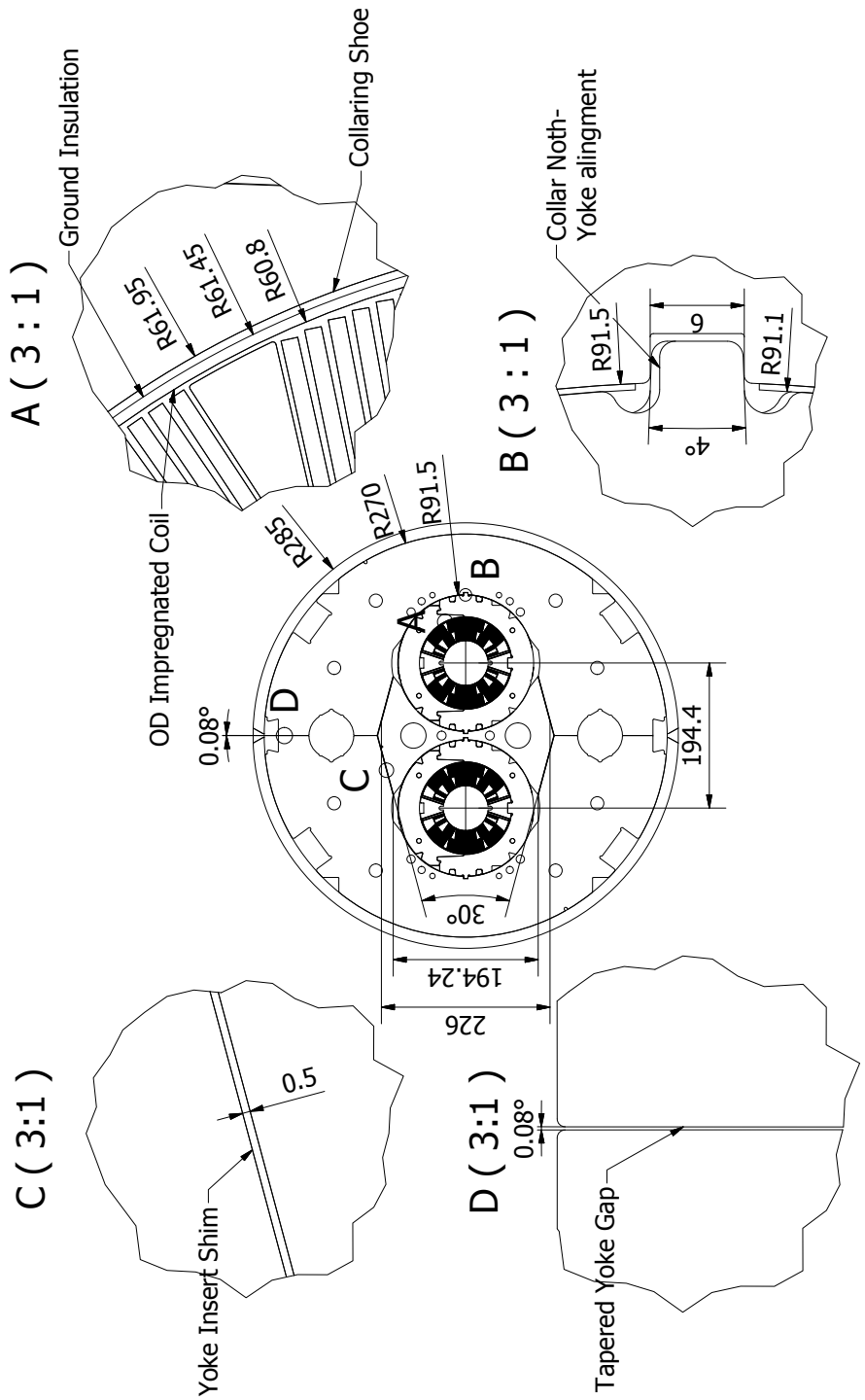

Figure C.84: Dimensions of the DS11T

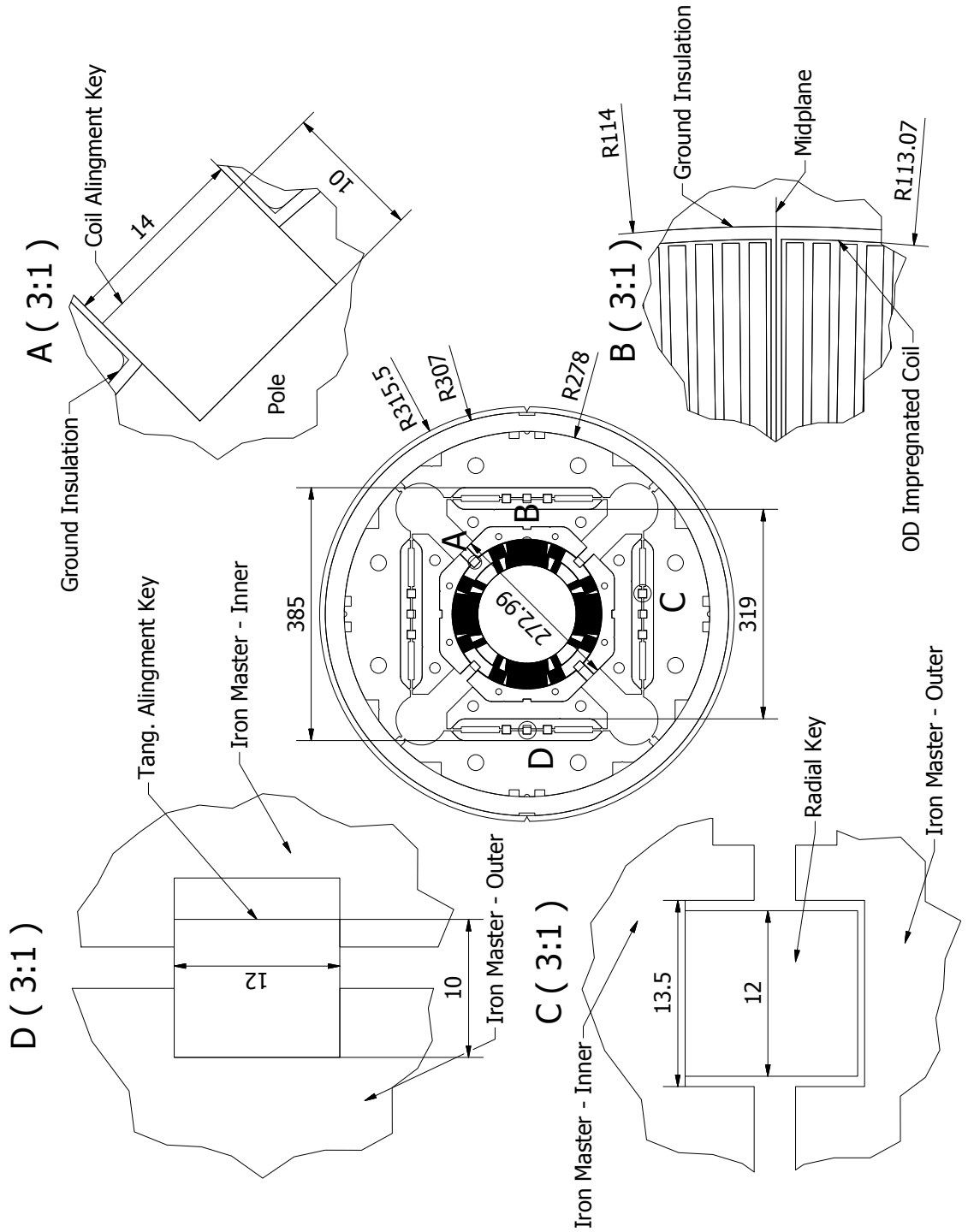

Figure C.85: Dimensions of the MQXF

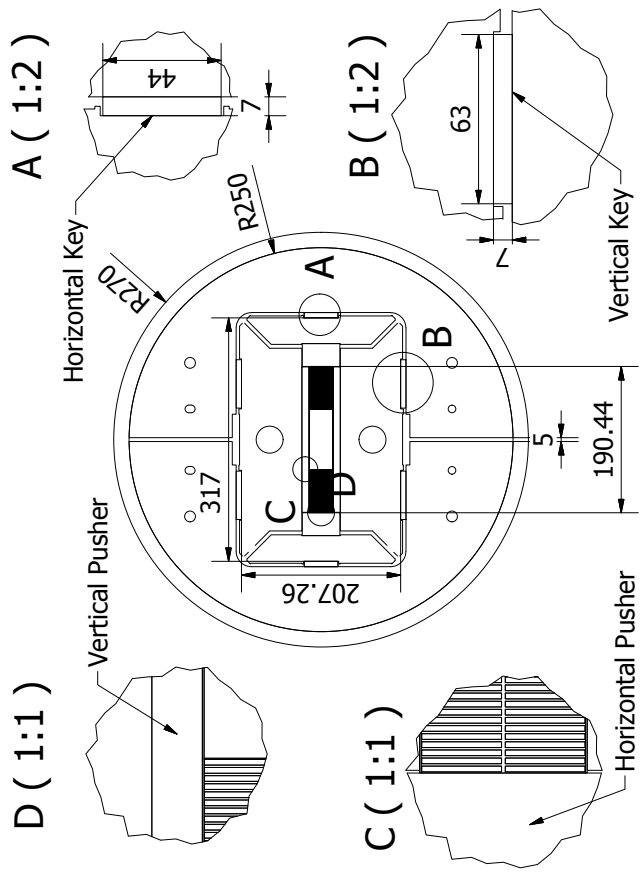

Figure C.86: Dimensions of the SMC-11T